Stony Brook University

Opportunities for Functional Oxides in $YO_{1.5}$-TiO_2-ZrO_2 System: Applications for Novel Thermal Barrier Coatings

A Dissertation Presented

by

Wesley Francillon

to

The Graduate School

in Partial Fulfillment of the

Requirements

for the Degree of

Doctor of Philosophy

in

Materials Science and Engineering

Stony Brook University

May 2009

Stony Brook University

The Graduate School

Wesley Francillon

We, the dissertation committee for the above candidate for the
Doctor of Philosophy degree, hereby recommend
acceptance of this dissertation.

Dr. Sanjay Sampath – Dissertation Advisor
Professor, Materials Science and Engineering

Richard Gambino
Professor, Materials Science and Engineering

Dr. Christopher Weyant
Assistant Professor, Materials Science and Engineering

Dr. Claire Grey
Professor, Chemistry Department
Stony Brook University

This dissertation is accepted by the Graduate School

Lawrence Martin
Dean of the Graduate School

Abstract of the Dissertation

Opportunities for Functional Oxides in $YO_{1.5}$-TiO_2-ZrO_2 System: Applications for Novel Thermal Barrier Coatings

by

Wesley Francillon

Doctor of Philosophy

in

Materials Science and Engineering

Stony Brook University

2009

This dissertation is an investigation of materials and processed under consideration for next generation thermal structural oxides with potential applications as thermal barrier coatings; wherein, high temperature stability and mechanical properties affect durability. Two notable next generation materials systems under investigation are pyrochlore and co-doped zirconia oxides. The motivation for this work is based on current limitations of the currently used thermal barrier material of yttria stabilized zirconia (YSZ) deposited by the plasma spray processes. The rapid quenching associated with the plasma spray process, results in a metastable structure that is a non-transformable tetragonal structure in the yttria partially stabilized zirconia system rather than the equilibrium anticipated two phase mixture of cubic and monoclinic phases. It has been shown that this metastable structure offers enhanced toughness and thus durability during thermomechanical cycling from the operating temperatures in excess of 1000C to ambient. However, the metastable oxides are susceptible to partitioning at temperatures greater than 1200C, thus resulting in a transformation of the tetragonal phase oxides. Transformations of the tetragonal prime phase into the parent cubic and tetragonal prime phase result in coating degradation. Several of the emerging oxides are based on rare earth additions to

zirconia. However, there is limited information of the high temperature stability of these oxide coatings and more notably these compositions exhibit limited toughness for durable performance.

A potential ternary composition based on the YSZ system that offers the ability to tailor the phase structure is based $YO_{1.5}$-TiO_2-ZrO_2. The ternary of $YO_{1.5}$-TiO_2-ZrO_2 has the current TBC composition of seven molar percent yttria stabilized zirconia, pyrochlore phase oxide and zirconia doped with yttria and titania additions (Ti-YSZ). The Ti-YSZ phase field is of interest because at equilibrium it is a single tetragonal phase. Thus, compositions are of single phase tetragonal phase, theoretically, should not undergo high temperature partitioning. Single Tetragonal phase oxides of Ti-YSZ also offer the possibility of enhanced toughness and higher temperature stability akin to those observed in yttria partially stabilized zirconia. Many pyrochlore oxides are under review because they have shown to have lower thermal conductivity than YSZ oxides.

This study focused on chemically synthesizing homogeneous starting material compositions in a metastable state (preferably amorphous), following its evolution according to the phase hierarchy under conditions of kinetic constraints. The current equilibrium diagram of $YO_{1.5}$-TiO_2-ZrO_2 is based on theoretical calculations. One of the contributions of this work is the redefined phase fields in $YO_{1.5}$-TiO_2-ZrO_2 based on our experimental results. Investigated compositions were based on tie lines of $Y_{2-x}Ti_2Zr_xO_{7+x/2}$ and $Y_2Ti_{2-y}Zr_yO_7$ representing substitution of Zr^{4+} for Y^{3+} and Zr^{4+} for Ti^{4+} respectively. More notably, we observed extended metastable phases in pyrochlore and fluorite oxides at low temperature. The significance of this result is that it offers a larger compositional range for investing pyrochlore oxides with associated high temperature phase stability for TBC applications. In tetragonal oxides, our results showed that Ti-YSZ results have slower partitioning kinetics in comparison to YSZ at high temperature.

This study also emphasized the deposition of advanced ceramic coatings by plasma spray for tetragonal and pyrochlore systems, compositionally complex functional oxides that may potentially have lower thermal conductivity values compared to current YSZ oxides. Next generation thermal barrier coatings require powders with high chemical purity, chemical homogeneity, controlled particle size/shape and pertinent phase state. Thermal spray offers an avenue to create novel materials and deposits directly from the precursor and compositionally controlled powder feedstock. This study contributed to

investigating an unexplored field that offers a variety of opportunities in materials synthesis that would not be possible by conventional methods.

Understanding processing-microstructure-property correlations is of considerable importance in thermal spray of functional oxide materials. This thesis demonstrated by radio-frequency thermal spray that the complex pyrochlore oxide $Y_2Ti_2O_7$ could be deposited by directly injecting molecularly mixed precursors to form oxide coatings. Structural analysis revealed the metastable fluorite phase; however, with thermal treatments at relatively low temperature of 700 ˚C the pyrochlore phase was obtained. For Ti-YSZ coatings, the tetragonal phase oxides were obtained with unique microstructures, however, the tetragonal prime destabilized at 1200 ˚C.

This dissertation explored novel oxide compositions through detailed structural analysis. The approach presented a comprehensive and integrated investigation as it pertains to phase evolution of oxides in powder feedstock to coating characteristics (phase/properties).

Dedicated To

My

Mother** and **Father

TABLE OF CONTENTS

LIST OF FIGURES

List of Tables

ACKNOWLEDGEMENTS

This dissertation is dedicated to my wonderful family. It is their long, hard work and willingness to sacrifice for their children that has made my education possible. Their encouragement and support has enabled me to push on through the toughest of times. I could never thank them enough for all that they have done for me. I am forever grateful.

I would like to acknowledge my advisor Dr. Sampath for his constant encouragement and allowing me to work on such a multi-disciplined research project. Other very influential people in the department of material science and (CTSR) include Dr. Herbert Herman and Dr Andrew Gouldstone and Professor Gambino.

I would also like to thank Dr. Carlos Levi at the University of California UCSB for the opportunity to work two summers in his Materials Processing Laboratory (MPL). I would also like to thank his three postdoctoral researchers; Dr. A. Ghandi, Dr. R. Leckie and Dr. T. Schaedler for all of their insightful discussions, assistance and encouragement.

For their collaborative efforts and long discussions with me, I could not have more helpful colleagues than those in the Center for Thermal Spray Research (CTSR). I thank Drs. Vasu,. A. Kulkarni, Dr. S. Desphande, Dr. L. Li, Dr. B. Ravi. and Dr. D. Otterson.

The long hours, the struggles and success will always be a moment in my life where I will always value and cherish.

Others to whom I am indebted include my strong support network at Stony Brook University; this includes the College Science Technology Entry Program (CSTEP), Alliance for Minority Participation (AMP) the Alliance for Graduate Education in the Professoriate (AGEP) and the Turner Fellowship.

This research was supported in part by MRSEC program of NSC under contract DMR 0080021.

Chapter 1: Introduction

Functional oxides, a class of materials that involve multi component systems with complex chemistries, specific composition and phase are of interest for many advanced engineering applications. Functional oxides have applications in various industries and include Magneto-resistive / piezoelectric sensors, dielectrics, fuel cells, planar inductors, superconductors and battery materials. There remain many opportunities in studying functional oxides for new areas to meet the demands of future materials structure-properties relationships. Two promising areas are in materials for Thermal Barrier Coatings (TBC) and Solid Oxide Fuel Cells (SOFC). A favorable and cost effective method to produce thick coatings is by the thermal spray process. Typical ceramic overlays are wear resistant, corrosion resistant and electrically and/or thermally insulating. Coatings of functional oxides are different from other coatings in that they must be chemically homogenous, high chemical purity, controlled particle size/shape and pertinent phase state. The presented constraints require an unprecedented level of control of starting material powders, processing conditions and post-treatment. This chapter will investigate previous research work on functional oxides deposited by thermal spray, report new class of low thermal conducting materials, and explore the potential of co-doped oxides and pyrochlore oxides as novel thermal barrier coating material.

1.1. Functional Oxides: Thermal Barrier Coatings

For gas turbine engines, current research has focused on developing and improvements in three important areas. There has been a focus on improving alloy design for turbine blades, combustion and materials. In the design and combustion, there are developments in casting technology that includes single crystal blades/veins and cooling channels to lower temperatures. There is also a need to improve the processing of thermal insulating materials that can be deposited efficiently on conformal shapes of the blades. Materials in turbines engines are moving towards compositions that are more creep and oxidation resistant. The function of TBC's is to increase the engine efficiency while reducing the surface temperature of the alloy (Figure 1). The primary benefit of a thermal barrier coating is to lower the thermal conductivity from the gas in the engine to the surface of coated alloy components[1].

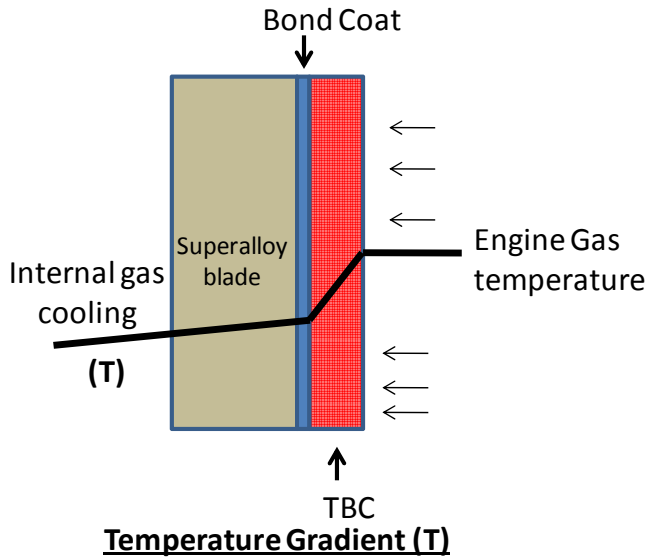

Figure 1 Temperature gradient: TBC reducing surface temperature of super-alloy by approximately 200˚C

Currently, TBC materials are multilayered systems; they are comprised of a ceramic over coat that resides on an oxidation resistant bond coat. The bond coat adheres to the underlying nickel-based superalloy (Figure 1). TBC's are deposited by the techniques of EB-PVD or plasma spray. There are three primary requirements of TBC materials. First, the materials must be a low thermal conductor. There must also be strain compliance between the coating and the alloy because of the thermal expansion and thermal cycling of the TBC. The effective strain compliance is critical for gas turbine systems because there expansion may lead to spontaneous failure of the TBC material. The third requirement is that the TBC should be thermodynamically compatible with oxides. Finally, the TBC should be prime reliant, by ultimately preventing the super alloy from exceeding its melting temperature. Due to extraordinary chemical and thermal stability, yttria stabilized zirconia (YSZ) is currently the most favored TBC material. The following section will expand on YSZ's attributes which have resulted in its dominance over the past three decades.

1.2. Materials Requirements for TBCs

Presently, thermal barrier coating materials are based on 7-8 mol% $YO_{1.5}$ in ZrO_2. The narrow range of compositions and its current use have proven to be very durable although other materials have shown to have enhanced performance. The durability of 7YSZ is based on the composition having superior cycle life over novel materials. Motivated by applications in environments with substantially higher operating temperatures; the major caveats for current thermal barrier coating of 7YSZ are aging effect on the phase stability of 7YSZ above 1200˚C, the pore content/architecture needed to achieve strain tolerance and the desirable reduction in thermal conductivity.

Material requirements for thermal barrier coatings materials:

- Low thermal conductivity
- Strain tolerance
- Erosion resistance
- Morphological stability
- Phase stability

Promising materials for TBCs must also satisfy a few conditions based on the processing by either EB-PVD or plasma spray processing. Additional material requirements that must be considered for novel TBC materials are sintering and densification. In general, porous materials suffer from densification when heat treated at high temperatures for long periods of time as a function of the pores closing by reduction in the surface energy area. Material densification increases the elastic modulus, thus, decreasing the strain compliance of the coating. Moreover, densification decreases the volume fraction and causes an increase in thermal conductivity. Studying and

characterizing the pore size and shape in the coating deposits is essential. The second most important criteria in TBC systems are phase stability in coating materials. Current TBC contain between 7-8 mol% $YO_{1.5}$. The phase of interest in yttria-stabilized zirconia is the tetragonal phase above 1050˚C under equilibrium conditions. Both EB-PVD and plasma spray have high cooling rates and are non-equilibrium process that can achieve mechanically constrained materials phases (tetragonal prime). The constrained coatings are in a metastable state and have the tetragonal prime phase. The tetragonal prime phase has been proven to reduce the crucial material transformation from the tetragonal zirconia to monoclinic phase that results in cracking and ultimately material failure. Failure modes in TBC are associated with structural instability and mechanical stresses. The high stresses originate from stresses during deposition and stresses from the TBC in service as an effect of the thermal mismatch between the ceramic coating material and the metallic substrates. Because of thermal cycling, the different heating and cooling rates of the materials cause thermal mechanical fatigue cracking that may lead to coating failure. Thus, residual stresses are critical to cracking in TBC materials and structural stability to novel materials.

1.3. Phase Stability- Structure of Binary $YO_{1.5}$-ZrO_2 Oxides

Zirconia, in its purest form can exist in three polymorphs. It adopts monoclinic crystal structure at room temperature, transforming to a tetragonal phase at 1170°C, the cubic fluorite structure at 2370°C and then finally a liquid at 2680°C (Figure 2). The fluorite crystal structure has a face centered cubic array of cations with a simple cubic-like array of anions on the tetrahedral interstices of the lattice. The second polymorph is an intermediate tetragonal phase. It has a P42/nmc symmetry. The tetragonal structure is a result of distortion of the oxygen sublattices which causes the [001] row of oxygen to be offset with respect to the fcc cation lattice[2]. The mechanical integrity of materials from pure zirconia is degraded during thermal cycling because of volume expansions of approximately 4.5% and shape changes of around 7% during the monoclinic to tetragonal phase transition. Zirconia will readily form solid solutions with many lower valence metals including alkali metals and rare earths. The dopants substituted on the zirconium cation site improve the thermo-mechanical integrity by stabilizing the high temperature phase of zirconia down to room temperature. With proper doping, the tetragonal phase is stabilized at room temperature and with increasing doping the cubic phase is made stable from room temperature up to the melting temperature. Currently, yttrium is the most common dopant used in commercial applications. Yttria stabilized zirconia coatings, whether deposited by thermal spray or electron-beam evaporation, are in a metastable state that is commonly referred as tetragonal prime. It has been shown that the maximum life of coatings occurs when coatings have compositions of approximately 7-8 mol% $YO_{1.5}$-ZrO_2. At high temperatures, the metastable tetragonal phase slowly partitions into a mixture of an yttrium-rich cubic phase (~17 mol% $YO_{1.5}$) and yttria-poor tetragonal phase (~4 mol% $YO_{1.5}$) in accordance

with the equilibrium phase diagram. The dopants also function as a means to increase the ionic conductivity by creating vacancies. A dopant ion such as Y^{3+} acts as an acceptor, since it has lower valence than the Zr^{4+} that it replaces.

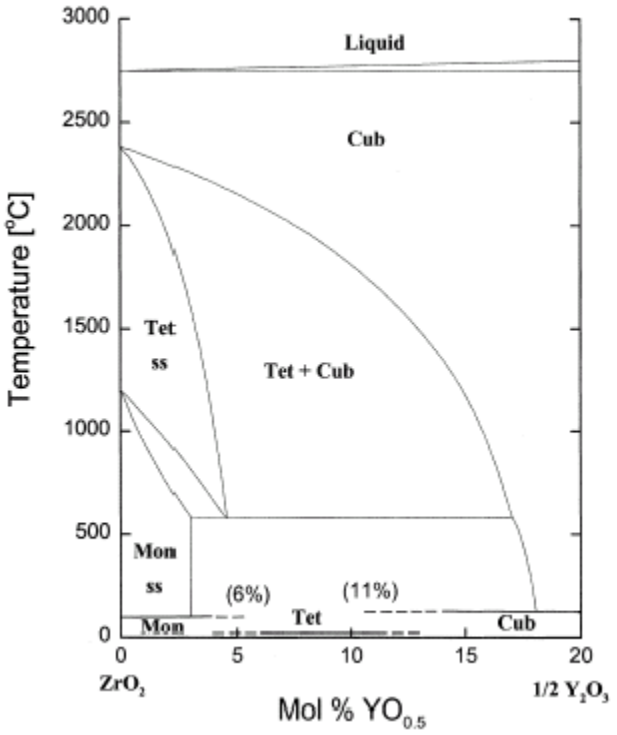

Figure 2 Binary phase diagram of ZrO_2 -$YO_{1.5}$. Mole percent $YO_{1.5}$ from 0-20% in ZrO_2[3]

1.4. Criteria for Low Thermal Conductivity

One of the first theoretical models proposed to explain thermal conductivity was by Debye [4, 5]. Debye defined thermal conductivity as the diffusivity of heat flow by phonon transport in a temperature gradient. Debye theory took into account three factors, the specific heat (c_v), the speed of sound (v_m), and phonon scattering (Λ). The relationship is expressed in equation one [6, 7].

$$\kappa = C_v v_m \Lambda / 3 \tag{1}$$

Furthermore, extending the analysis of Debye's equation considered the temperature characteristics of the material known as the Debye temperature and the size of the unit cell. The relationship between the shortest wavelength phonon to size of the unit cell is:

$$\Theta = \frac{2\hbar\upsilon v_m}{a_o k_B} \tag{2}$$

Equation 2 has the unit cell parameter (a_o) and Plancks constant ($\hbar$). M. Winter, presented guidelines suggesting that in order for materials to have low thermal conductivity they must satisfy four principle conditions; large molecular weight, complex crystal structures, non-directional bonding, large number of different atoms per molecule. M. Winter further suggested that traditional strategies for reducing thermal conductivity, inter-mixing ions of different atomic masses will only decrease the minimum thermal conductivity if it leads to an increase in the mean atomic mass[8]. The current model that best describes thermal conductivity in materials takes into account attainable and/or tabulated material properties and it is expressed as:

$$\kappa_{min} = \frac{\rho^{1/6} E^{1/2}}{(M/m)^{2/3}} \quad (3)$$

Where M is the mean atomic mass of ion in the unit cell, m is the number of ions in the unit cell, ρ is density, and E is the elastic modulus. Research has shown that introducing randomly distributed point defects into structure with sufficiently high density will cause high inelastic phonon scattering resulting in the decrease of the phonon mean path followed by a decrease in the attainable thermal conductivity[9, 10]. Results also suggest that we can effectively use alloying to create disorder on more than one sub-lattice in a crystal. In summary, the two main parameters that influence thermal conductivity are phonon scattering and atomic density.

1.5. Novel Class of TBC Materials: Pyrochlore Oxide

In 2000, M. Maloney was issued a patent for the discovery of a class of ceramic materials that has applications in the area of thermal barrier coatings [11]. The finding consists of a family of ceramic materials having a pyrochlore structure with composition of $A_2B_2O_7$. The A-cation haves valence of 3^+ or 2^+ and B cation can have a valence of 4^+ or 5^+ wherein the sum of A and B valences is 7. Maloney et al., investigated material systems in which A is selected from lanthanum, gadolinium and yttrium mixtures. The B cation was selected from zirconium, hafnium, titanium and mixtures thereof. The impact of Maloney's work was that the pyrochlore oxides have thermal insulating properties (low thermal conductivity) that exceed those of the most commonly used zirconia-based TBC materials. Additionally, pyrochlores have melting points of more than 3000°F (1650°C) and they have been shown to successfully adhere to alumina. However, the boundaries of the phase diagrams for the binary and ternary systems are currently under investigation.

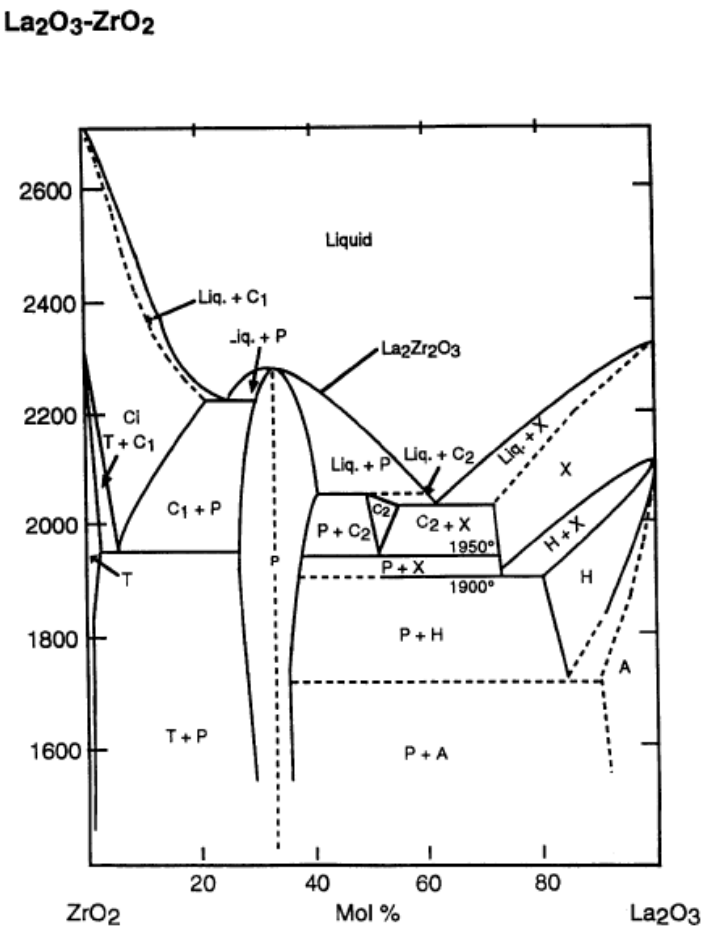

Figure 3 Pyrochlore phase found in La_2O_3-ZrO_2 phase diagram (excerpt from Patent M. Maloney 2000 [11])

Figure 3 illustrates the binary diagram for La_2O_3-ZrO_2. The stability range of the pyrochlore phase was approximately 27-37 mol%. The pyrochlore phase has a range from room temperature to 2300˚C. The significance of Maloneys work was that the pyrochlore oxide of $La_2Zr_2O_7$ thermal conductivity values decreased with an increase in temperature.

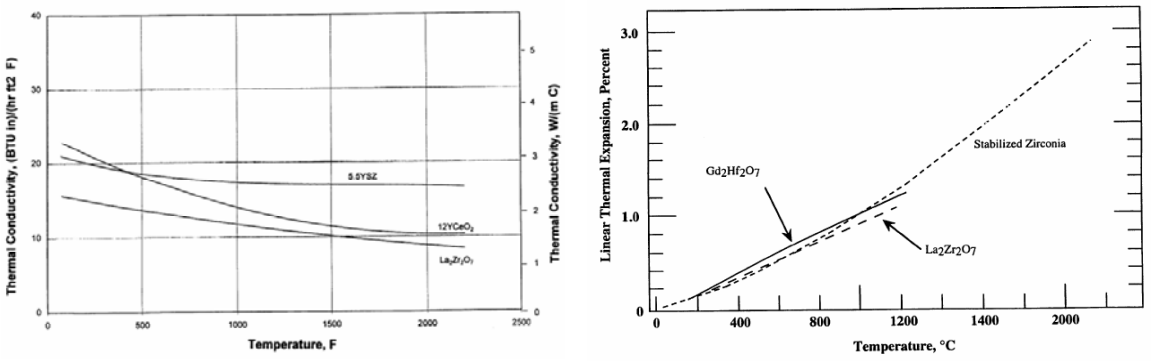

Figure 4 (a) Thermal conductivity values of lanthanum zirconate compared to stabilized (b) Thermal expansion results as compared to stabilized zirconia.[11]

Figure 4 illustrates the thermal conductivity and thermal expansion of the following pyrochlores: $Gd_2Hf_2O_7$ and $La_2Zr_2O_7$. The significance of the results is that ratio of thermal expansion to temperature are consistent with those of stabilized zirconia. Secondly, in Figure 4a, the thermal expansion values of the pyrochlores is similar to stabilized zirconia.

1.6. Low Thermal Conductivity in Pyrochlore Oxides

The rationale for low thermal conductivity in pyrochlore oxide compounds are based on crystallographic and chemical effects as described in sections 1.4. For many oxide systems, the thermal conductivity at high temperatures is determined by phonon scattering crystal imperfections and other phonons. Pyrochlore oxides have high intrinsic defect concentrations, which are associated with low thermal conductivity materials. Experimentally, it has been proven that the differences in atomic mass between constituents in a compound increases, the thermal conductivity of that compound decreases[12]. The substitution of a high concentration and high atomic mass atoms such as lanthanum, gadolinium and yttrium into the fluorite structure provides a means

to lower the thermal conductivity. Moreover, results have also shown that the same does not hold true for zirconia-based compounds because of trade-offs between the reduction in thermal conductivity and issues associated with having higher density[6]. Figure 4a compares the thermal conductivity values of $La_2Zr_2O_7$, 12 mol.% $YCeO_2$, and 5.5 mol.% YSZ. The lowest thermal conductivity values were found to be in the pyrochlore $La_2Zr_2O_7$ with 1.5W/mC at 1500˚C. To note, the thermal conductivity values continually decreases as the temperature increases. In comparison to yttria-stabilized zirconia, the thermal conductivity remains linear after 500˚C.

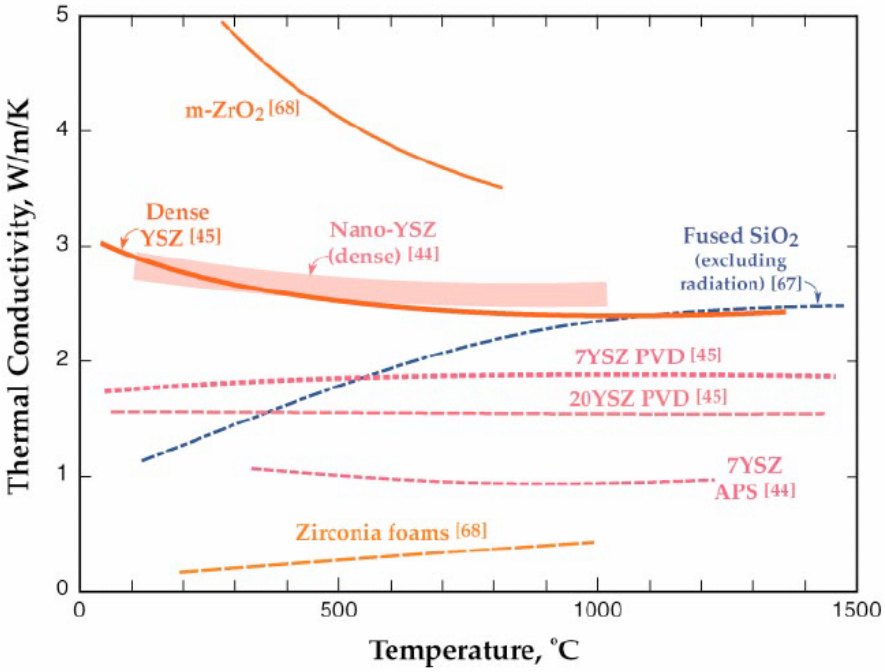

Figure 5 Thermal conductivity values of YSZ and comparisons by the depositions techniques of APS and PVD [6]

Figure 5, illustrates compiled data comparing thermal conductivity of zirconia oxides and coatings. Of interest is the comparison of dense zirconia (~2.8 W/mK) , Physical Vapor Deposition (PVD) and APS. Air Plasma Spray had the lowest thermal spray conductivity for the molar composition of 7YSZ[6].

1.7. Pyrochlore Structured Oxides ($A_2B_2O_7$)

Pyrochlore compounds form over a large compositional range due to the flexibility of the structure. Compounds of the pyrochlore structure were explained in detail in the review by Subramanian [13]. The pyrochlore compounds considered in this study are formed by combining a trivalent A^{3+} cation and a tetravalent B^{4+} cation however; pyrochlores can also form in the $A^{2+}{}_2B^{5+}{}_2O_7$ stoichiometry. The reaction for oxides in pyrochlore oxides with tri- and tetravalent cations is expressed as follows:

$$A_2O_3 + 2BO_2 \rightarrow A_2B_2O_7 \quad (4)$$

Due to their wide compositional range, pyrochlore compounds have many different properties and they have been used, or are being put forward as materials for use in diverse applications including solid electrolytes, anodes and cathodes for fuel cells and sensors, catalysts, dielectrics, thermal barrier coatings, materials for the encapsulation of actinides and other nuclear waste[14-16]. Pyrochlore ($A_2B_2O_7$) compounds are related to the fluorite/cubic structure.

The fluorite structure is described by anion cubic cage encapsulated inside an fcc lattice[17]. Each cation has eight coordinated oxygen anions and each oxygen atom has four coordinated cations. In the disordered fluorite structure, $Fm\bar{3}m$ space group, has a 7/8 occupancy of the 8c oxygen sublattice (Figure 6). The pyrochlore structure may be defined by two interpenetrating networks based on B_2O_6 and A_2O'. Thus, the A cation has an 8 fold coordination and six oxygen anions on the 48f position from the BO_6 octahedra. The A cation is at the center of a six O atoms and normal to the mean plane of this hexagon is a pair of O′ atoms. The A cation are octahedrally coordinated with 6 O anions and two O′ anions located within distorted cubes. The smaller B cation are six-fold coordinated and are located within the distorted octahedral[18]. The bond

lengths, B-O are equal in length; thus, having the BO_6 network. There are also A_2O' chains that are in a linear coordination with no primary bonds between the networks. The coordination of oxygen is four A atoms in the form of a regular tetrahedron. In the B_2O_6 octahedra, B is a distorted octahedral coordination. The pyrochlore compound tends to be cubic and ionic in nature. The structure has also tolerance for vacancies defects at the A and O sites thus, cation migration is possible. Stoichiometric pyrochlore $A_2B_2O_7$, can also adopt the defect pyrochlore structure. The defect pyrochlore structure has anion and cation vacancies in the lattice, thus having the composition of $A_2B_2O_6O'$ or $A_2B_2O_{7-x}O'$. The defect pyrochlore structure is different to the pyrochlore structure because it has vacant 8b oxygen (O') in the unit cell[19].

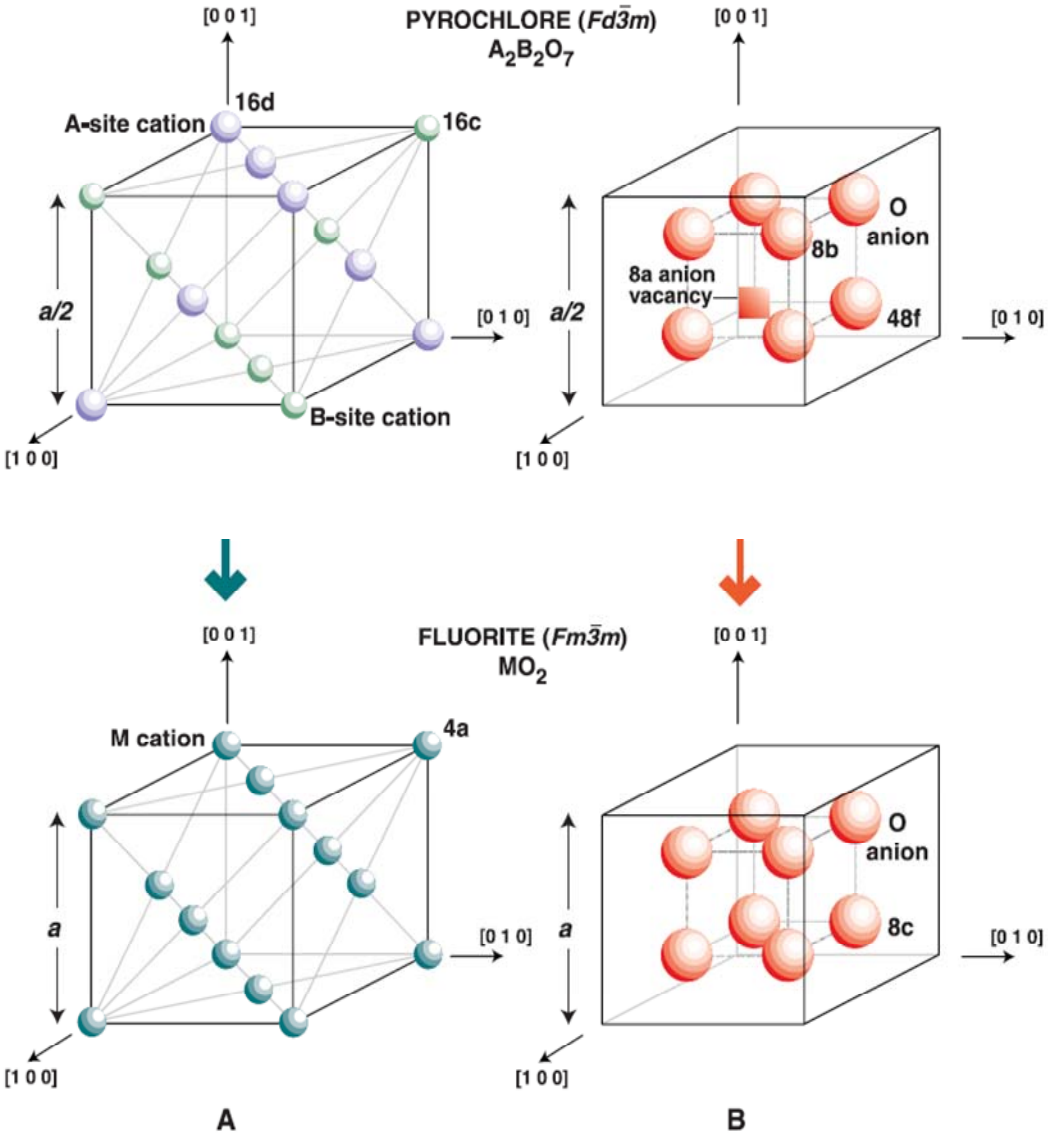

Figure 6 Illustration is a comparison between the fluorite and the pyrochlore atomic structure including (A-B) cation and anion positions within a unit cell. [18]

1.8. Diffusion Mechanism in Zirconia and Pyrochlore Structures

Oxygen migration in fluorite structures are influenced by the extra positive charge (cations) that attract the negatively charged oxygen anions, resulting in migration of the oxygen anions. Therefore, the oxygen diffusion process is the result of continuous jumps of anions. Thus, there is a continuous jump of the anions in the oxygen diffusion process in the presence of anion vacancies. The vacancies cause the position of the cations in the tetrahedron containing the vacancy to be distorted. The distortion of the cations may cause the distance to increase forming a pathway for the migration of oxygen atoms. Therefore causing the neighboring oxygen atoms to be attracted towards the excess local positive charges, thus the anions move closer to the vacant site[20]. The migrations exist due to balance between the repulsive and attractive Coulomb forces among the cations and anions[21].

In pyrochlore oxides, the vacant 8b site has a tetrahedron of four B cations and the 8a site has four A cations. The 48f site has two A and two B cations (Figure 7). Oxygen ion second nearest neighbors gives an indication of possible migration pathways for oxygen hoping because of oxygen sites have vacant oxygen sites as second nearest neighbors. Second nearest neighbors of the 8a and 8b sites are always 48f oxygen ions with neither forming a continuous network by which diffusion could proceed. The 48f sites on the other hand have 8b, 8a and 48f sites as second nearest neighbors along which oxygen vacancy hoping diffusion could occur[22]. Secondly, if the cations can vary the valence states, oxygen migration may be promoted by the valence variations, which are electron hopping.

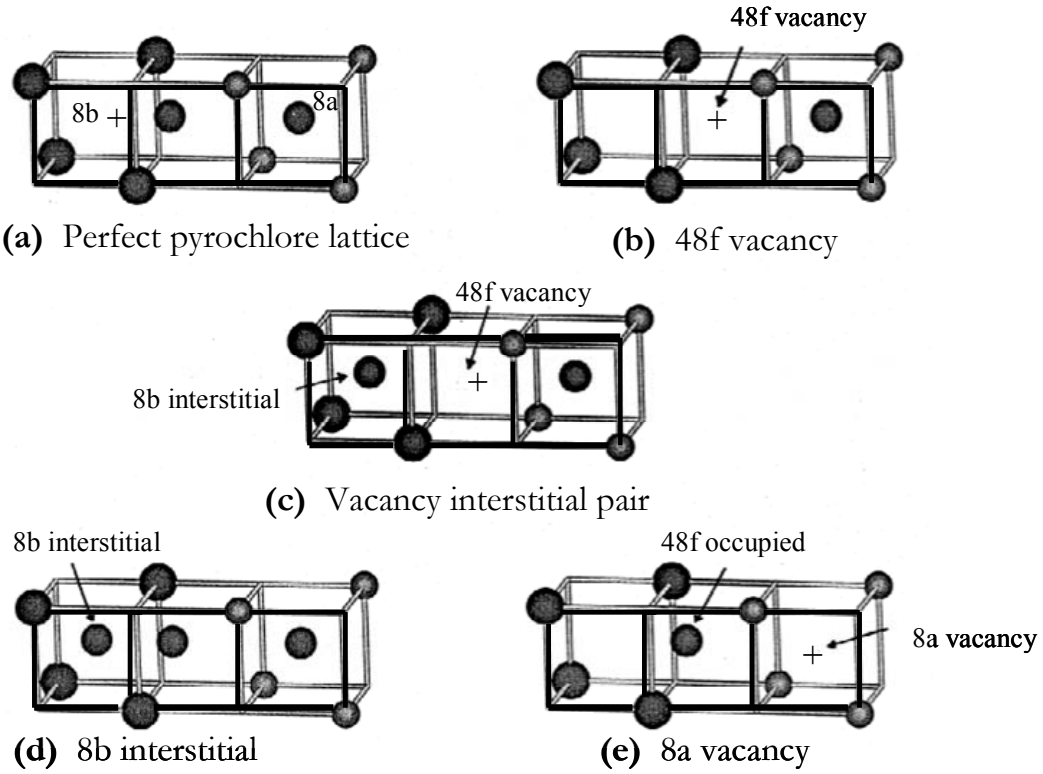

Figure 7 Anionic defects in pyrochlore structure. Vacant sites for ionic conductivity[22]

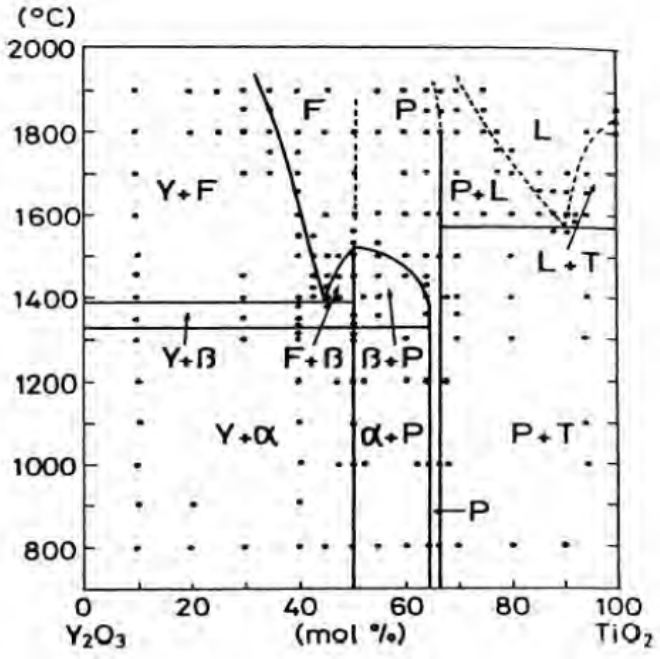

Figure 8 Phase diagram of Y_2O_3-TiO_2; Y = Y_2O_3, P = pyrochlore, T= TiO_2 rutile[23]

1.9. Extrinsic Defects in Zirconia and Pyrochlore Oxides

The discovery of solid-state oxygen ion conductors, such as Y-substituted ZrO_2, suggested the principle of substituting in a lower valence cation to form charge compensating oxygen vacancies has become the standard route to oxygen ion conducting electrolytes. Since this discovery, many oxide systems have been investigated [24]. Research has also shown that the introduction of a stabilizer decreases the thermal conductivity of pure zirconia. The stabilizers introduce vacancies to maintain the charge neutrality of the ionic lattice. Therefore, the substitution of two zirconium ions (4+) by yttria ions (3+) is accompanied by one vacancy. Equation (2), Kroger Vink notation, shows: Y_{zr} is an yttrium ion on a zirconium site (single negative charge), V_o an oxygen vacancy twice positively charged, O_o an oxygen ion on an oxygen site.

$$Y_2O_3 \rightarrow 2Y'_{Zr} + V_O^{\bullet} + 3O_O^x \qquad (5)$$

In comparison to fluorite oxides, pyrochlore oxides have shown to be intrinsic anion ionic conductors with stoichiometric compositions ($A_2B_2O_7$). Substitutions with AO_2 enter the possibility of having charge compensation due to substitutions on lattice sites. Equations 6-8 are for charge compensations resulting in vacancy defects and equations 9-11 are possible charge compensation effects for interstitial site occupancy.

$$7MeO_2 + 8A_A^x + 4B_B^x \rightarrow 7Me_A^{\bullet} + V_A''' + 4A'_B + +2A_2B_2O_7 \qquad (6)$$

$$7MeO_2 + 4A_A^x + 4B_B^x \rightarrow 3Me_A^x + 4Me_B^{\bullet} + V_A''' + 2A_2B_2O_7 \qquad (7)$$

$$7MeO_2 + 4A_A^x + 7B_B^x \rightarrow 7Me_B^x + 3B_A^{\bullet} + V_A''' + 2A_2B_2O_7 \qquad (8)$$

Equations (6) and (7) describe the solution AO_2 via the formation of charge compensating A cation vacancies. Equation (6) occupies the A site exclusively. Equation (8) assumes the occupancy of the A and B site equally. Equations 9-11 define the same charge compensation in pyrochlore materials as in equation 6-8 except they are for interstitial sites formation rather than vacancy.

$$4MeO_2 + 4A_A^x + 2B_B^x \rightarrow 4Me_A^{\bullet} + 2A_B' + O_i'' + A_2B_2O_7 \quad (9)$$

$$4MeO_2 + 2A_A^x + 2B_B^x \rightarrow 2Me_A^{\bullet} + 2Me_B^x + O_i'' + A_2B_2O_7 \quad (10)$$

$$4MeO_2 + 2A_A^x + 4B_B^x \rightarrow 2B_A^{\bullet} + 4Me_B^x + O_i'' + A_2B_2O_7 \quad (11)$$

1.10. Thermal Spray

Thermal Spray is essential to many technological industries because it provides thick coatings that are crucial in protective materials, biomedical, wear resistant coatings, microelectronics and thermal barrier coatings. One of the technological benefits of thermal spray is the ability to use a variation of feedstock materials from ceramics, refractory to intermetallic compounds. Thermal spray is also an economically more viable deposition technique in comparison to other techniques such as (EB-PVD). Thermal spray offers a high degree of process variability that affects the material coating properties. A characteristic of thermal spray is imperfections (defects) in the form of interlamellar pores, cracks and gas porosity. Imperfections in coatings are responsible for variations in the material properties. The imperfections are a function of the process where the powders in-flight are subjected to high temperatures in excess of 10,000°C. The high temperature plasma causes the powder feedstock to become molten and additionally, the powder is accelerated towards a substrate by a hot jet of combusting or plasma gas. When these molten droplets collide onto the surface, they spread to form splats. A coating is therefore formed a combination of splats adhering to each other in a brick-like structure. The high velocity particles in-elastically adhere onto the surfaces and rapidly cool forming coatings (Figure 9b). Thermally sprayed coatings are applicable in a variety of engineering applications. One of the primary applied areas is the aerospace industry where the coatings provide protection within advanced gas turbines and high performance internal combustion engines. The motivation for utilizing thermal spray in turbine/combustion engines is to improve performance. Currently, the aerospace industry uses as their thermal barrier coating material zirconia-based oxides. Current TBC materials increase

the engine operating temperature that allows engines to run at higher temperatures, thereby enhancing performance. The plasma spray process is divided into sub-systems such as Vacuum Plasma Spray (VPS) or Low Pressure Plasma Spray (LPPS) that offer controlled environments in the form of vacuum chambers that are back filled with a protective gas at low pressure. More commonly is Air Plasma Spray (APS) which is sprayed under atmospheric conditions. Figure 9a is a typical plasma spray gun and its components used in industry and research applications.

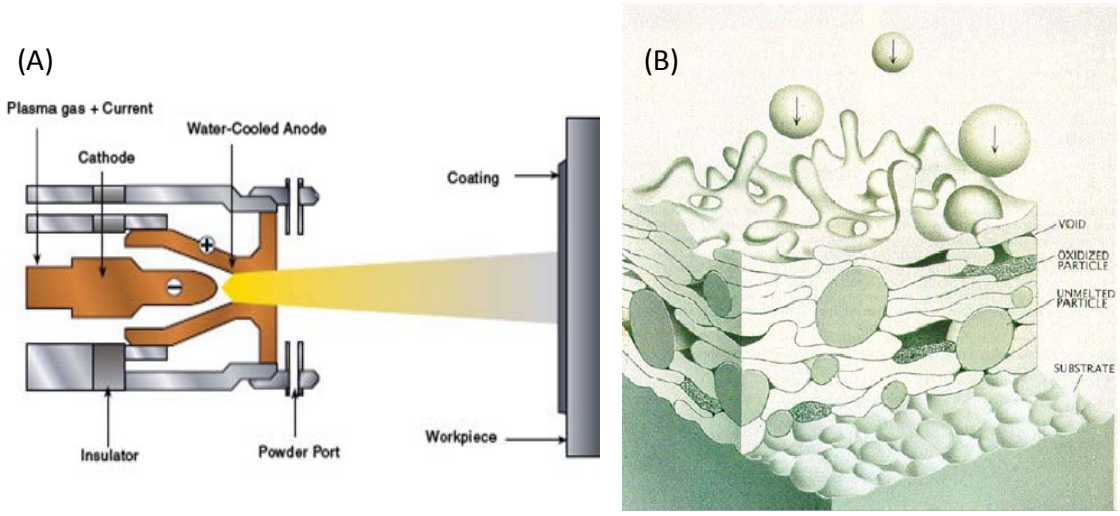

Figure 9 (A) Typical cross-section of plasma spray gun (B) Representation of coating build-up from powder feedstock in typical plasma spray deposited materials.[25]

1.11. Advancements: Precursor Plasma Spray

Studies have shown that altering the multitude of process variables in instrumentation/particle-diagnostics influences coating microstructure and properties. Controlling these variables such as gases, stand-off distance, velocity and pressure have led to highly tailored coatings. Due to the aforementioned advances, thermal spray has evolved into a viable and advanced fabrication technique for the deposition of functional oxides. Recently, there has been an increase in the demand to have coatings that are chemically and compositionally homogenous. Moreover, as these functional oxide chemistries become more complex, it is necessary to have greater control of the phase state. Other important characteristics that are beneficial for depositing functional oxides are powders with high chemical purity, more uniform particle size and shape distributions[26]. Knowledge of the chemistry and phase will enhance our understanding of future functional oxides coatings. One of the most promising advancements is in the utilization of thermal spray of solution precursors[27]. Ultimately, thermal spray synthesis from precursors provides an avenue of novel oxide compositions for rapid coating evaluation and compositional control[28]. Precursor methods are promising due to the difficulties to use powder methods to produce multi-component oxides and inhomogenity and impurities in powders. The inability to rapidly screen and assess structure-property relationships by traditional methods led to new avenues in powder preparation methods. Scientifically, the implication of precursor development is that it provides opportunities for applications where current approaches are prohibited.

Additional advantages of precursor plasma spray include:

- Greater flexibility in materials/processes
- Allowing exploratory chemical synthesis
- Utilize extreme thermal gradients to produce metastability (non-equilibrium phases)
- Control of composition

1.11.1. Soft chemistry methods for powder development

As an alternative to directly depositing solution/precursor by thermal spray, one may also use solution chemistry routes as a method to prepare very fine chemically homogenous powders. It is a strategic method to quickly screen and create powders and investigate novel compositions. The solutions and/or powders may be prepared by combining acidic nitrates solutions with a high pH solution of ammonium hydroxide. In solution chemistry preparation, one can add either the acidic nitrate solution to the precipitation solution (co-precipitation) or the adding the ammonium hydroxide to the acidic cation solution (reverse co-precipitation). Both methods produce different powder morphologies. With the addition of the acidic solution to the ammonium hydroxide, a gelatinous amorphous precursor material forms. However, when properly dried, it yields sharp-edged irregularly shaped agglomerates that are dense and strong. The second method, reverse co-precipitation, yields fine and loosely agglomerated crystallites. However, reverse co-precipitation may cause segregation in multi component systems. Figure 10 describes the advantage of molecularly mixed precursors. Homogenous solutions and/or sols (colloid; solid particles dispersed in a solvent) may be dried at low temperatures to from an

amorphous oxide. The amorphous oxides were subsequently thermal sprayed and the results are presented in this dissertation.

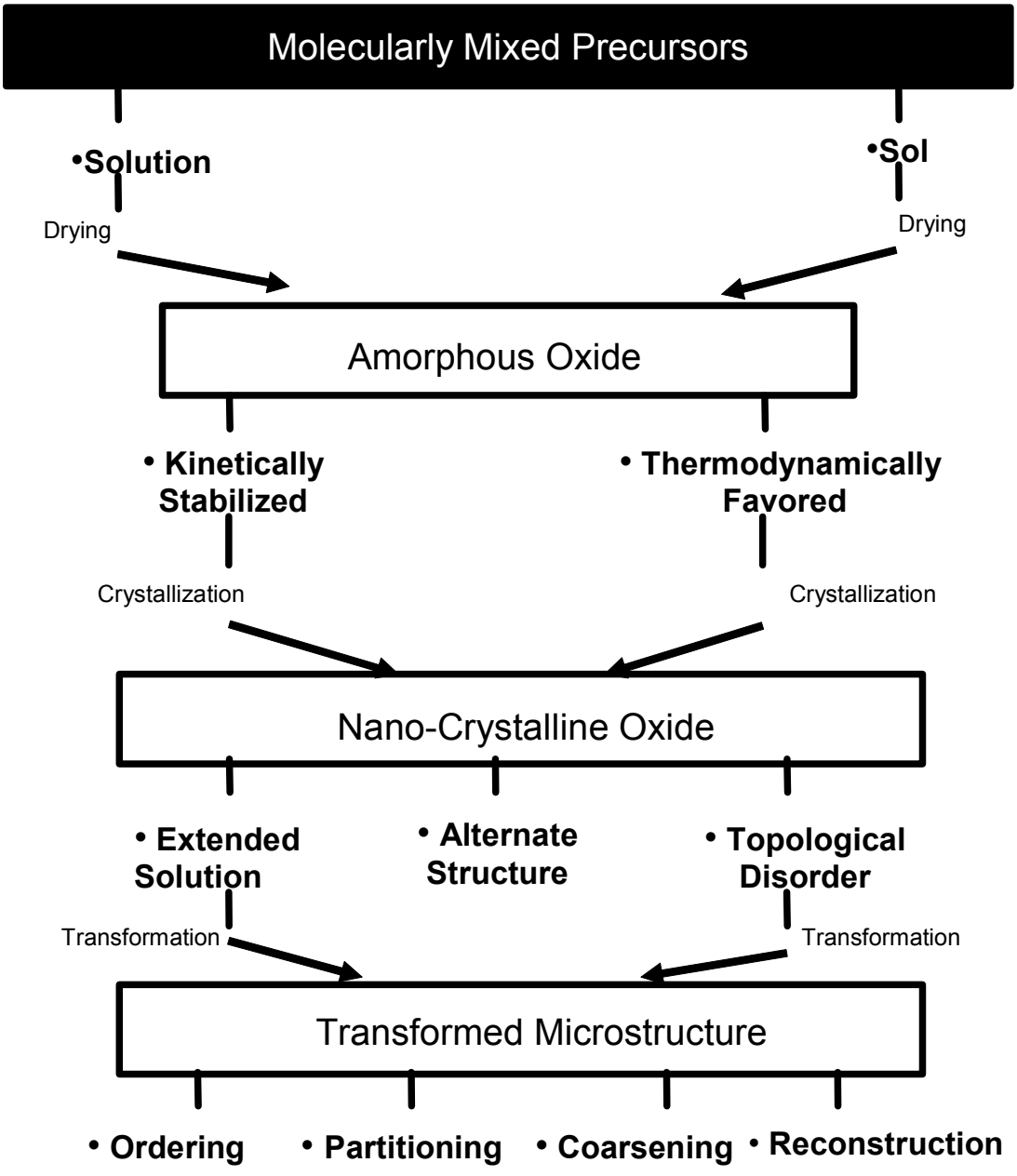

Figure 10 Hierarchy of molecularly mixed precursors and its influence on the transformed microstructure of oxides

Chapter 2: Statement of the Problem

There have been recent demands for developing complex functional oxide coating materials via inexpensive processing methods that offer materials of unique characteristics. Potential applications for such materials are fuel electrodes/electrolytes, high temperature electrochemical devices such as solid oxide fuel cells (SOFCs), catalytic materials, luminescent phosphor and thermal barrier coatings. One of the most recent areas of interest is in depositing these functional oxides using the thermal spray process given its rapid solidification rates, provides a method of producing metastable phases. For instance, in current thermal barrier coating materials, metastable phases such as tetragonal prime, are attributed to the high quench rates in the plasma-spray process leading to a substantially long-cycle life of coatings in comparison to equilibrium phases. Thermal barrier coatings are a highly established technology based on a limited selection of materials that are primarily based on yttria stabilized zirconia. The desire to further reduce the thermal conductivity and to improve the microstructure stability at high temperature is emerging as a key enabler for advanced TBC materials. The current trend used in YSZ materials for lowering thermal conductivity and microstructure stability are based upon modifications of the chemical compositions, pore content/architecture, and topology of coating (layering modifications, grain size, etc) by variations in processing parameters. The current TBC materials, doped-zirconia oxides (7YSZ), have limited stability range of the tetragonal prime phase that is a necessity for high temperature stability and low thermal conductivity. There has been a lot of research on improving reliability of the current materials; however, an increase in our understanding is necessary for a successful route to significant improvements.

There are current improvements in the development of mechanical based models and diversifying materials to address the performance and durability demands of next generation engines.

Two candidate systems for next generation thermal barrier coating with emphasis on reducing the thermal conductivity are based on co-doped YSZ with one or more Rare Earth Oxide (REO) and pyrochlore type zirconates ($M_2Zr_2O_7$).

2.1. Tetragonal Phase Oxide in $YO_{1.5}$-TiO_2-ZrO_2

In multi-doped oxides, there is renewed interest due to the higher combinations of material compositions and materials in the ternary systems with tetragonal oxide phases. Ternary oxide systems, particularly with single tetragonal phase fields are of interest because they offer the possibility of producing tetragonal prime phases in rapid-solidification process such as plasma spray. This dissertation will explore a composition with tetragonal phase with the molar composition of $7.6YO_{1.5}$ - $15.2TiO_2$ – $77.2ZrO_2$ (Ti-YSZ) in $YO_{1.5}$-TiO_2-ZrO_2. Previous research work has shown that the addition of Ta_2O_5, Nb_2O_5 and HfO_2 enhances transformability of yttria stabilized zirconia indicated by an increase in phase transformability and fracture toughness. Enhanced transformability is attributed to an increase in tetragonality (c/a axial ratio) in coatings deposited by plasma spray. There remain many opportunities to investigate transformability in compositions in $YO_{1.5}$-TiO_2-ZrO_2 such as the composition Ti-YSZ.

2.2. Pyrochlore Phase Oxide in $YO_{1.5}$-TiO_2-ZrO_2

Recently, pyrochlore oxides have been shown to have thermal insulating properties (low thermal conductivity), that exceed those of the most commonly used zirconia based thermal barrier coating materials. Initial research work has investigated pyrochlore oxides in binary systems. The first available patent suggesting that pyrochlore oxides may be used as thermal barrier coatings was reported by Maloney et al. for $La_2Zr_2O_7$. Since the initial findings, there have been contributions in binary systems such as $Eu_2Zr_2O_7$, $Sm_2Zr_2O_7$ and $Gd_2Zr_2O_7$ with lower thermal conductivity values in comparison to YSZ. Due to high possible combinations of cations for pyrochlore oxides, there remain opportunities in systems such as $Y_2Ti_2O_7$. Although pyrochlore have intrinsically low thermal conductivity, substitutions with AO_2 (ZrO_2) offer the possibility of introducing charge compensation which would introduce vacancies to maintain the charge neutrality of the ionic lattice, hence increasing defect sites and lowering thermal conductivity. The principle of substituting valence cations to form charge compensation has been used as a technique to increase oxygen ion conduction and reducing thermal conductivity in YSZ and other electrolyte and/or TBC materials. Finally, pyrochlore with substitutions of AO_2, satisfy the current model to reduce thermal conductivity in oxides such as large molecular weight, complex crystal structures, large number of different atoms per molecules and intermixing ions of different atomic masses.

2.3. Synopsis of the Dissertation

This dissertation will investigate compositions in the ternary system $YO_{1.5}$-TiO_2-ZrO_2 and the stability range of selected phases. A practical approach to studying the structure of thermal sprayed functional oxide coating materials is by studying systematically the phase constitution and phase evolution of sprayed material powders and coatings. The motivation is to investigate the feasibility in depositing complex oxides by thermal spray. The scientific interest is to extend the understanding of metastable phase transformations as it pertains to low thermal conducting pyrochlore oxides and tetragonal oxides (YSZ with TiO_2 additions) phases in the ternary $YO_{1.5}$-TiO_2-ZrO_2 system. The findings detail the phase stability of selected complex oxides compositions for applications that are relevant for thermal barrier coating materials and in solid oxide fuel cells (SOFC). This thesis presents a study of the phase evolution in powder and phase stability in coatings for compositions of complex oxides of $Y_{2-x}Ti_2Zr_xO_{7+x/2}$ (0.2, 0.4, 0.8, 1.2) and Ti-YSZ ($7.6YO_{1.5} - 15.2TiO_2 - 77.2ZrO_2$). Understanding the phase evolution in the complex oxide powders has led to improved comprehension in phase stability in coatings.

Tetragonal phase oxides will be explored in order to address the following;

The distinctive existence of a stable non-transformable tetragonal region in the ternary oxide system ($YO_{1.5}$-TiO_2-ZrO_2) allows for phase stability to high temperature; promising in the area of next generation thermal barrier coating materials.

- Understanding phase evolution in compositions within tetragonal phase of $YO_{1.5}$-TiO_2-ZrO_2
- Determining if the tetragonal prime phase can be created in thermal sprayed coatings with titania additions to YSZ
- Identification of the decomposition temperature of the tetragonal phase of Ti-YSZ in comparison to YSZ
- Structural analysis for powder and coatings with co-dopants
- Understand thermal conductivity for both YSZ and Ti-YSZ coatings
- Investigate high temperature phase stability in coatings

Pyrochlore phase oxides will be explored in order to address the following;

As an alternate material to zirconia doped oxides, pyrochlores have shown to have lower thermal conductivity, thus the potential as a next generation thermal barrier coating material.

- Phase evolution in compositions with A and B cation substitutions in yttria-titanate oxides for phase stability fields in ternary system
- Thermal conductivity of oxide compositions in pyrochlore region
- The extend of metastability in pyrochlore region; address if pyrochlore phase is metastably extended beyond compositions proposed by equilibrium diagram
- Phase stability in coatings; report the effect of processing on coating microstructure and structural analysis

2.4. Investigated Ternary Systems: $YO_{1.5}$-TiO_2-ZrO_2

Figure 11 is the theoretical ternary diagram proposed by Yokokawa in 1991. The ternary diagram illustrates the defined phase fields for single, binary and ternary phase fields in the $YO_{1.5}$-TiO_2-ZrO_2 system. Figure 11 shows the regions of interest for (i) YSZ (7.6 mol. %$YO_{1.5}$), (ii) Ti-YSZ (7.6 mol. %$YO_{1.5}$ -15.2mol. %TiO_2 - 72.8 mol. % ZrO_2), (iii) compositions in the pyrochlore region. This dissertation will expand on the ternary diagram based on experimental results for high temperature phase stability.

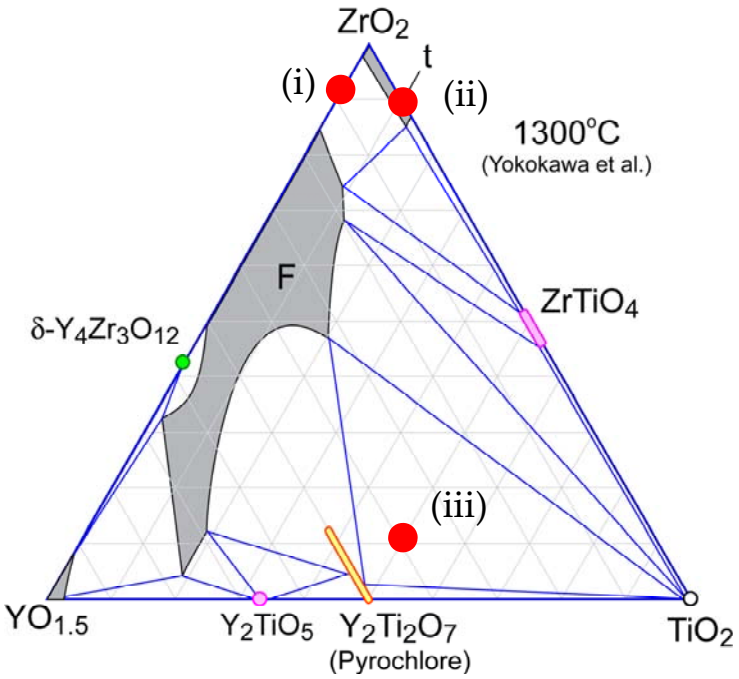

Figure 11 Ternary phase Diagram of $YO_{1.5}$-TiO_2-ZrO_2 at equilibrium (1300˚C)[29]; (i) YSZ (7.6 mol. %$YO_{1.5}$), (ii) Ti-YSZ (7.6 mol. %$YO_{1.5}$ -15.2mol. %TiO_2 - 72.8 mol. % ZrO_2), (iii) compositions in the pyrochlore region

Chapter 3: Materials and Methods

3.1. Soft-Chemistry Processing

Traditional thermal spray coatings are produced by the following variations in starting powders: Hollow Spheres (HOSP), Fused and Crushed (F&C), Agglomerated and Sintered and (A&S) or Sol-gel (Figure 12). Preparations of HOSP powders utilize spray drying and plasma densification to produce globular hollow spheres. Agglomerated and sintered powders involve using a binder at high temperature to produce angular and polyhedral particles. The fabrication of sol-gel derived powders, by a wet chemical process produce particles that are spherical morphology. The investigated oxides coatings presented in this thesis were not by commercially available powder feedstock; however, they were prepared at Stony Brook University Center for Thermal Spray laboratory (CTSR) by a precipitation-based method. The powders have significantly different particle microstructures compared to other thermal spray techniques. After sols are dried on a hot plate at temperatures of 200-400°C, they result in large precipitate cakes. The remains after low pyrolizing temperature are solid agglomerates that must be carefully ground. Several sieving steps were used to reduce the particle size and avoid over-grinding. Compared to commercial powders, sol-gel prepared powders need to be crushed and ground to appropriate particle size. The following section describes the detailed methodology for powder chemistries investigated in this study.

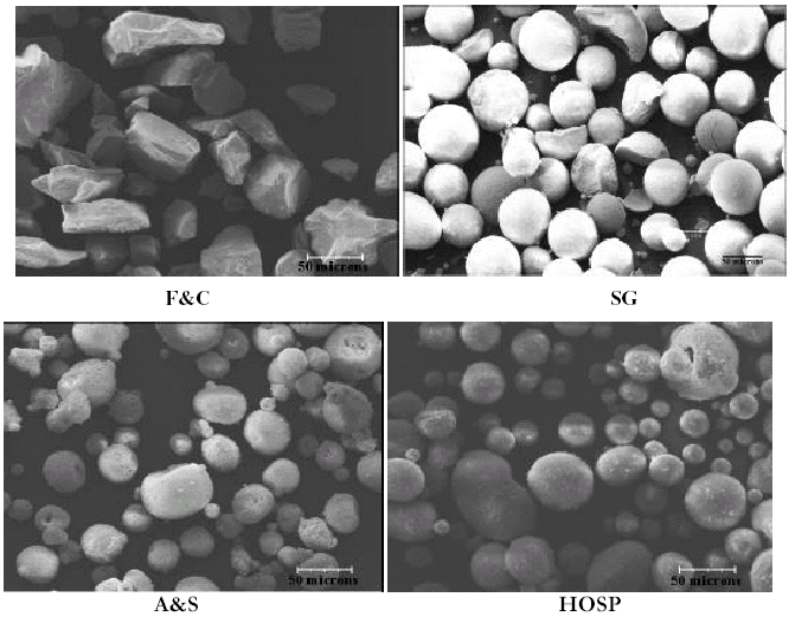

Figure 12 SEM images of YSZ powders morphologies (A. Kulkarni 2003)

Compositions of interest were prepared by a soft chemistry method. The synthesized powders were obtained by mixing precursors of yttrium nitrate [$Y(NO_3)3{\cdot}6H_2O$] , titanium iso-propoxide [$TiC_{12}H_{28}O_4$] and zirconium nitrate [$ZrO(NO_3)_2$] in iso-proponal. Gelatinous amorphous precursor precipitates were subsequently prepared by the addition of the mixture to an aqueous solution of ammonium hydroxide (28-30%NH_3). To avoid component segregation a pH of 10 was maintained by the addition of NH_4OH and monitored by an electronic pH meter. The advantage of this route is to achieve mixing of the components on an atomic scale. Zirconia precipitates at a pH between 2-2.5 while yttrium precursors precipitate at a pH of 6.5-7.0 [30]. The remaining suspension was then vacuum-filtered with a Buchner funnel and dried on a hotplate at approximately 110˚C overnight. The agglomerates were crushed with a mortar and pestle. The powders were then calcined at 700˚C (Figure 13). Sample compositions of x= 0.4, 0.8, 1.2 and 1.6 were investigated by this method for pyrochlore oxides. Powders

were also created for the compositions of ($7.6YO_{1.5}$ - $15.2TiO_2$ – $77.2ZrO_2$) for Ti-YSZ and ($7.6YO_{1.5}$-$92.4ZrO_2$) by the same precursor methodology.

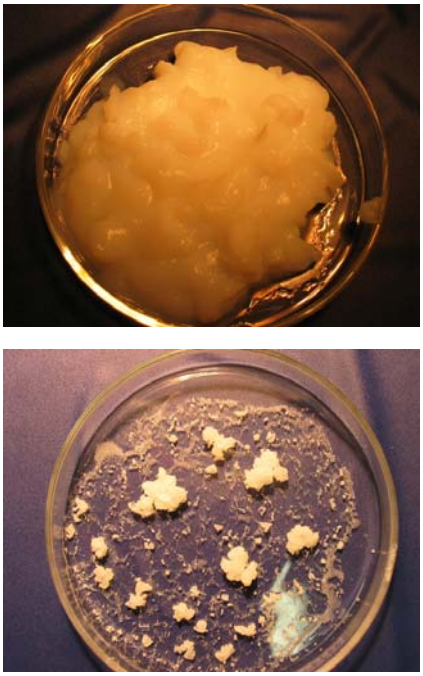

Solution Gel

- Ammonium hydroxide solution was used in order to achieve gelatinous amorphous precipitate
- Gel was vacuum filtered through a Buchner funnel in order to achieve a precipitation cake

Agglomerated Particles

- Precipitate resin is slowly dried on a hot plate for approximately five hours in order for the organics to evaporate. Remains are a dry precursor powder in the form of "chunks". Furthermore, these chunks are crushed into fine powders using a mortar and press. Sub-micron powders are achieved.

Figure 13 Co-precipitation of solutions gel before and after heat treatment

Figure 13 shows the methodology of creating powders by reverse co-precipitation. A typical amorphous precipitate cake is observed after filtration separating ammonia from solution gel. The precipitation cakes are dried low temperature (~ 150°C). After a low heat treatment, there remain dry "chunks" of powder that are agglomerated powders (Figure 13: bottom).

Figure 14 Batch processing was required to create over one kilogram of desired powders. Photograph depicts mixing container, chemical mixer and large filtration used to produce precipitation cakes.

Powder batches of approximately one pound were necessary in order to create coatings for the thermal spray coatings investigated in this thesis. For large batches, mixing of solutions required a minimum of eight hours in order to ensure homogeneity. Precipitate cakes, samples were filtered for approximately twelve hours. For large batches drying on hot plates also required twelve to fourteen hours. Filtration removed the sol-gel precipitation cakes from ammonia required approximately 12 hours for large batch process.

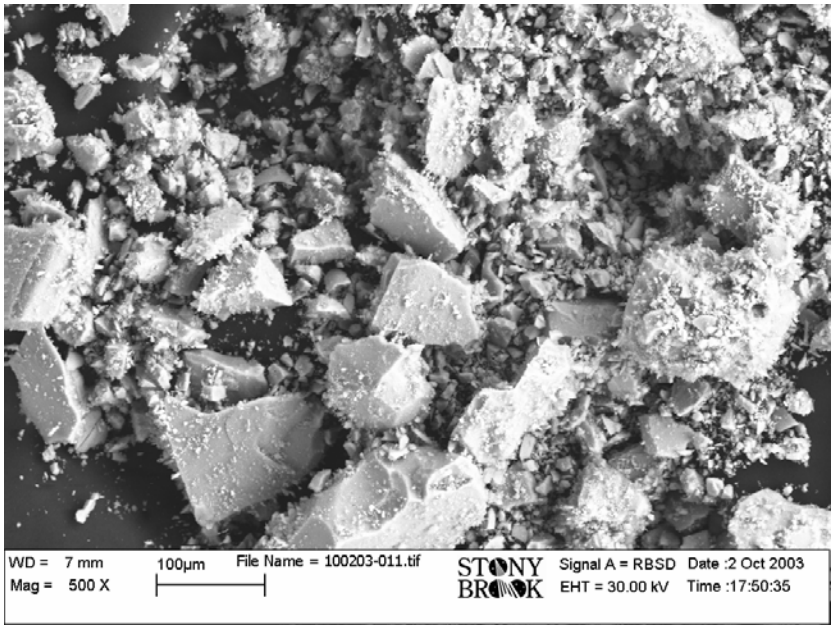

Figure 15 Final powder particles from pyrochlore oxides after crushing and grinding with mortar and pestle. Particles morphology depicts powders that are sharp and jagged.

After the samples were dried, crushed the particle sizes were measured by a Beckman coulter particle analyzer. Particles sizes were of the order of 200 um in size (Figure 15). For large batches the particles required manual grinding using a mortar and pestle for approximately five hours for the one pound of powder in order to achieve particles that were sub 100 um. After short grinding sessions, the powders were carefully sieved in order to separate larger particles from smaller particles. Figure 15 illustrates an example of the particle morphology for powders used in this dissertation dericved from co-precipitation processing. The images depict raw-paritcles after crushing and grinding and prior to sieving steps.

3.2. Analytical Techniques

3.2.1. Time Resolved XRD

Time resolved X-ray diffraction experiments were conducted on the X7B beamline in the National Synchrotron Light Source (NSLS) at Brookhaven National Laboratory. The wavelength of the synchrotron beam was 0.920 Å. An image plate (IP) detector (Mar345, 2300x2300 pixels) along with an *in-situ* heating cell was used to heat the samples from room temperature to 950 °C. Precursor powder was crushed into a fine powder using a mortar and pestle. Fine powders were inserted into 0.5 mm amorphous quartz capillary that was subject to atmospheric conditions. The heating source was a horse shaped heater and for this experiment the temperature regime had a heating rate of 5 °C/min. Temperature calibration was determined by a silver-standard with a predetermined thermal expansion value. For scanning and storage, an imagining plate was exposed for 30 s for each frame without slits, and a readout time of approximately 80 s was applied. Finally, the data was integrated using the FIT2D program. The powders investigated by this in-situ method were compared to the X-ray diffraction (XRD) results at temperature.

3.2.2. Magic Angle Spinning Nuclear Magnetic Resonance (MAS NMR)

Detailed sample preparations for the ^{17}O NMR were found elsewhere; by N. Kim et al. Samples were prepared by enriching the compounds in $^{17}O_2$ gas (40% ^{17}O, Isotec.) at 550°C for 24 hours. The powders before and after enrichment were characterized by XRD. MAS NMR experiments were conducted using a 4 mm Chemagnetics probe on a CMX-360 spectrometer. ^{17}O MAS NMR data were collected at Larmor frequencies of 48.816 MHz, and at a spin rate typically of ~15kHz. The spectra were obtained by using either a one

pulse or Hahn echo sequence (90°- γ - 180° - γ-acquisition) with pulse widths of typically 2.0-3.0 μs, γ of one rotor period and a pulse delay of 1s. The chemical shifts were referenced to distilled $H_2{}^{17}O$ (= 0 ppm) as an external reference.

3.2.3. X-Ray Diffraction

Powders and coatings were evaluated by SCINTAG/PAD-V diffractometer. The operating conditions were at a scan rate of 2° /min using CuKα radiation with a wavelength (λ) of 1.5408 Å. Phases were identified using the JCPDS powder diffraction files.

3.2.4. Scanning Electron Microscopy (SEM) and Energy Dispersive Spectroscopy (EDS)

Energy Dispersive X-ray Spectroscopy (EDS) analyzed the compositions of the powder and coatings. The EDS detector was made by EDAX Corporation is built into the SEM system. (JEOL6400) Morphological analysis of coatings and powders were performed on a field emission gun, Scanning Electron Microscope by LEO. (1550) Cross section of coatings was embedded in epoxy under vacuum conditions. Rough and fine polishes were used to reach the area of interest by using a polishing wheel until the 0.05 um diamond paste solution blend.

3.2.5. Transmission Electron Microscopy (TEM)

TEM is unique among materials characterization techniques in that it enables simultaneous examination of microstructure features through high resolution imaging and the acquisition of chemical and crystallographic information from a few nanometer regions of the specimen. High image contrasts are due to mass differences or structure differences. A Phillips CM

200kV microscope with a field emission gun was used. The probe area ranges from hundred of microns to 1.5nm and the magnification is 1.6 million times.

3.2.6. Focused Ion Beam (FIB)

A Focused Ion Beam (FIB), was the preferential sample preparation technique for TEM samples of thermal spray coatings investigated in this dissertation. The FIB machine was designed by FEI model number 830. Before samples were mounted into the FIB holder, they were manually cut into the following dimensions; 2.85 x 0.180 x 0.50 mm. The specific dimensions are found of the FIB thermal spray sample are on Figure 16. An illustration of a sample YSZ air plasma spray coating is on Figure 17. (a) Is a top down view of the sample, while (b) sample tilted at approximately 55 degrees. Samples were milled down to a thickness of approximately 50nm for electron transparency.

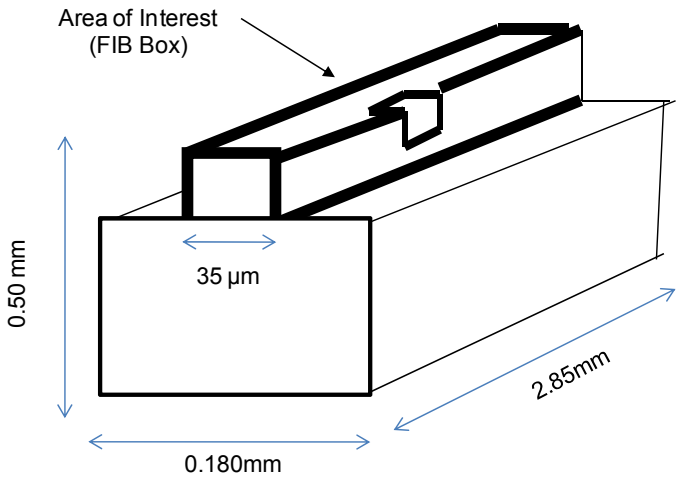

Figure 16 Schematic of H-Bar sample preparation and dimensions for plasma spray coating TEM samples

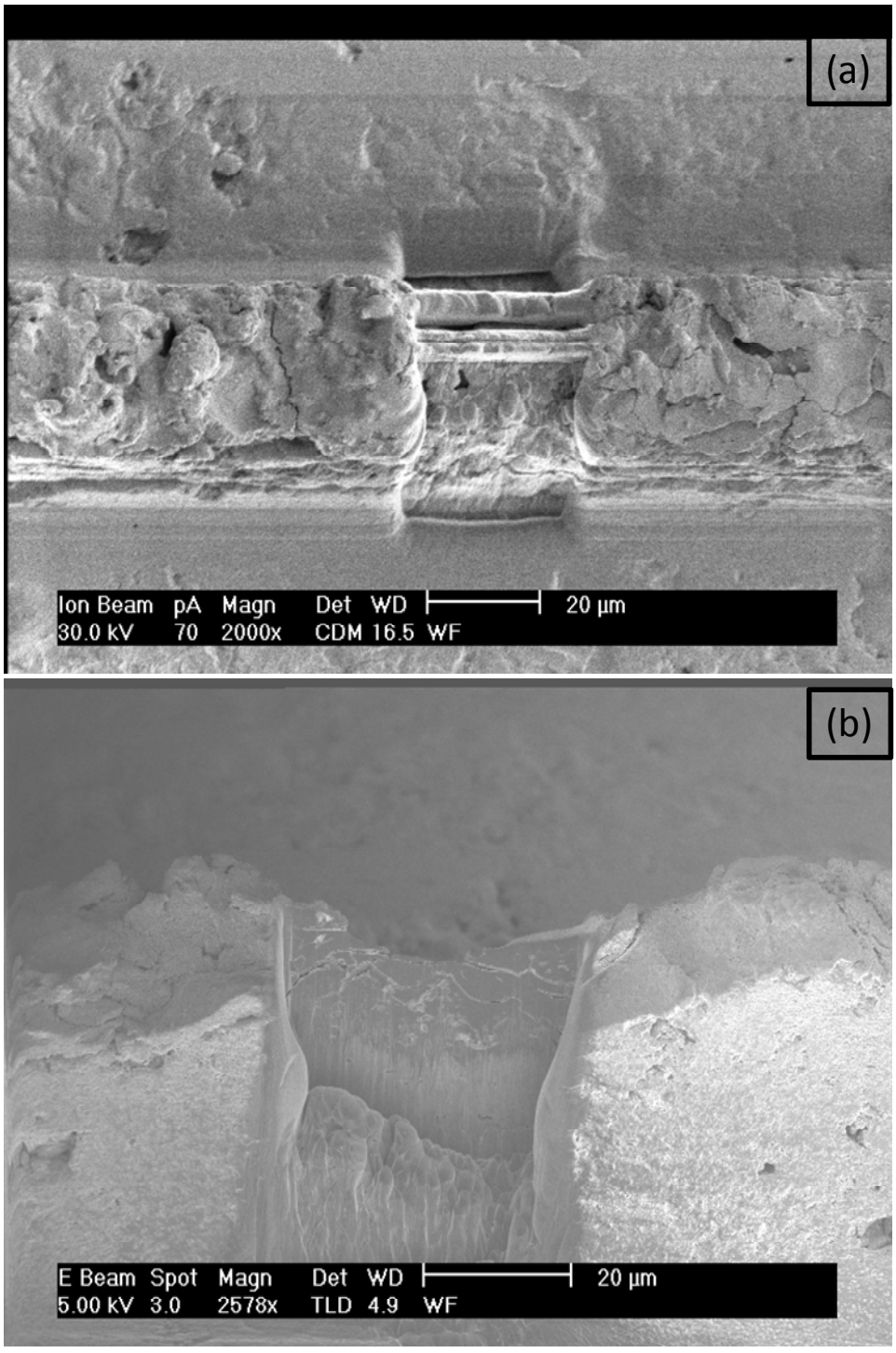

Figure 17 H-Bar sample of YSZ/Ti-YSZ (a) top down SEM image of sample. Center is ion-milled with an area of ~30um for TEM (b) 55 degree tilt of YSZ sample.

3.2.7. Particle Size Distribution

Powder particle sizes were measured by LS Particle Size Analyzer (Beckman Coulter). The laser based technology is based on both the Franhofer and Mie theories of light scattering[31]. Light scatter is a popular technique for determining the particle size and distribution of a material. In general, the scattering intensity detected by a detector placed at a distance much larger that the size of the particle is the resultant of the scattered electromagnetic radiation from different portions of the particle illuminated by a monochromatic light source. This scattering intensity pattern is specific to a material with certain physical properties and particle size distributions. Rigorous analytical solutions to determine the particle size distribution of materials are only available for spherical and rod shaped particles using the Maxwell's equations. The Mie theory is the rigorous solution for light scattered from a sphere. For particles smaller than the wavelength of light, the Mie theory is reduced to the Rayleigh theory. When particles are much larger than the wavelength of the incident light, the Mie theory simplifies to the Fraunhofer theory.

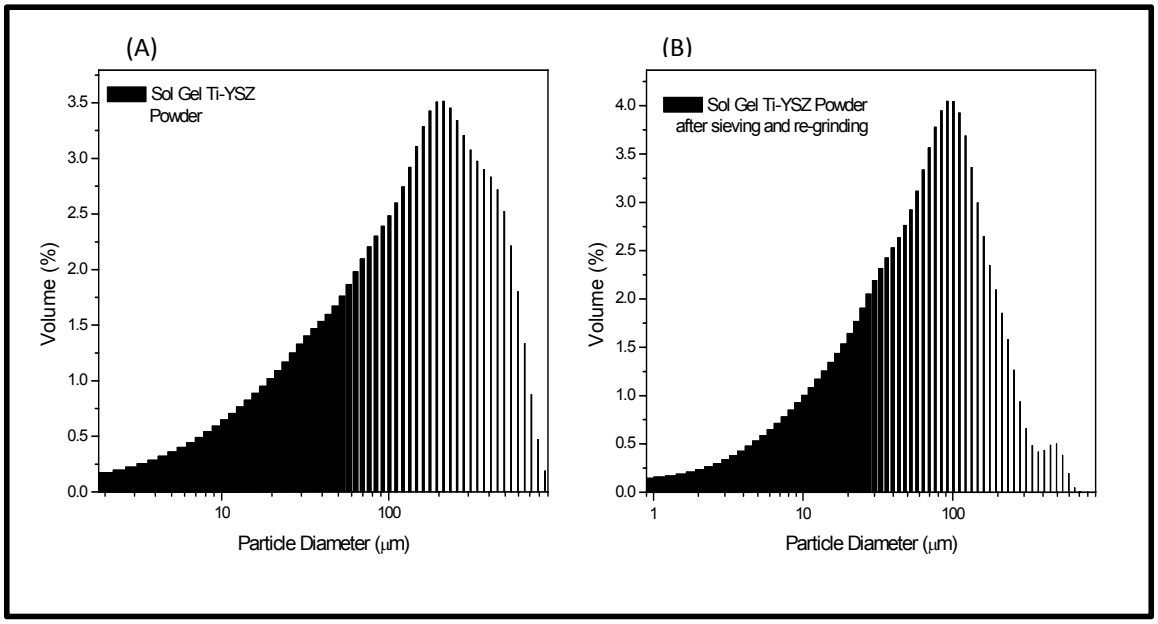

Figure 18 Precursor derived powder - Particle size distribution: Ti-YSZ (A) After powders were crushed and grinded. Particle diameter~ 200μm (B) Particle diameter after re-grinding and sieving to reduce average particle size to 97 μm

3.2.8. Atmospheric Plasma Spray

Chemical co-precipitation derived powders were plasma sprayed using a Plasma Technik F4MB gun. Atmospheric plasma spray conditions were used in order to obtain thin (50 um) and thick (500 um) coatings on various substrates (Table 1). During the spraying process, the substrates were rotated and air cooled.

Table 1 Air Plasma Spray (APS) process parameters

Parameter(s)	Value
Gun Nozzle	6 mm
Gun Amperage	650 amps
Gun Voltage	65 volts
Primary Argon Flow	40.0 slpm
Secondary Hydrogen Flow	8.0 slpm
Argon Carrier Flow	3.0 slpm
Powder Feed Rate	30 g/min
Substrate Rotational Speed	160 rpm
Gun Traverse Speed	10 mm/sec

3.2.9. Combined digital thermal analysis (DTA/DSC)

Combined digital thermal analysis is a technique that combines two common thermal analytical techniques, differential scanning calorimetry (DSC) and thermal gravimetric analysis (TGA). These experiments were carried out on a Netzsch (Burlington, MA) STA 449 C Jupiter™ model combined DSC/TGA device. The device is equipped with an electromagnetically compensated top-loading balance that has a resolution of ±0.1 μg. This test requires that a background file be generated for the specific set of conditions under which the samples are to be tested. To do this, two empty alumina crucibles with lids were placed into the test and reference positions in the sample chamber, the chamber was closed and the nitrogen purge gas and protective gases were set to 50ml/min

and 10ml/min, respectively. The system equilibrated for 5 minutes and then the balance was tarred. The chamber was then heated from ambient temperature to 1500 °C at rate of 5 °C/min. Clean, new crucibles were used to test between 10 and 15 mg specimens of each sprayed sample under these same conditions[32].

3.2.9.1. Differential Scanning Calorimetry

Differential Scanning Calorimetry measures the difference in heat flow into or out of a sample versus the heat flow to and from a reference as a function of temperature or time. For polymers, the device is used to determine glass transition temperatures, melting temperatures, heat of fusion/melting and decomposition temperatures. The DSC curve can then be further analyzed to extract information about the crystallinity of the polymer being examined.

3.2.9.2. Thermal Gravimetric Analysis (TGA)

Thermal gravimetric analysis determines a sample's mass as a function of either temperature or time as it is subjected to a controlled temperature program. It was necessary to perform a baseline correction for each sample as the scale tended to linearly add or subtract an apparent mass as a function of time regardless of what the temperature program was doing.

3.2.10. Thermal Conductivity

Thermal conductivity measurements were taken on a Holometrix laser flash thermal diffusivity instrument. Thermal conductivity measurements of thermal spray samples were taken on free-standing films. Two methods were used to create freestanding films substrates were removed by polishing off the substrates or substrates were removed by mechanically separating films from substrate by a bending technique. The measurements of the freestanding

thermal spray coatings were carried on a carbon coated 12.5 mm diameter disk. Prior to coating measurements, a reference sample was irradiated uniformly by a laser beam pulse on one side of the disk. On the other side of the disk, the temperature rise caused by the laser flash was recorded as a function of time by an infrared detector. The difference in the temperature rise and coating thickness is used to calculate thermal diffusivity. From this measurement technique, the specific heat may be calculated when it is compared to the reference sample. It is from the measurements of thermal diffusivity and specific heat coupled with the bulk density where it is possible to compute the values of thermal conductivity. In solids materials, the heat transfer is controlled by three mechanisms; electrons, phonons and photons. However, in YSZ the thermal conductivity is based on the contributions of phonons and radiative transfer. Heat transfer by electrons is considered negligible because these ceramic oxides are electrical insulators and their conductivity is dictated by oxygen ion diffusion at high temperature. The thermal conductivity can be expressed as:

$$\kappa = \rho C_p k \tag{12}$$

$$\kappa = \left(\frac{1}{3}\right) CvL \tag{13}$$

K is the thermal conductivity, C is the mean phonon velocity *v* is the mean phonon velocity and L is the phonon mean path. Thermal conductivity values for thermal barrier coating application deposited by APS are approximately 1.0 W/mk for 7YSZ (figure 15). This dissertation present thermal conductivity results of pyrochlore structured materials and Ti-doped YSZ in comparison to 7YSZ coatings and powders.

3.2.11. Mechanical Properties (Micro-indentation)

Traditionally, thermal spray coating mechanical properties have been measured by tensile or bending test. However, these measurement techniques provide average coating information about material properties in comparison to current indentation techniques that extract local material characteristics[33]. The depth sensitive indentation approach involves simultaneous measurement of force and penetration depth. Micro-indentation has been shown to be a useful technique for measuring the elastic modulus of coatings [34-37]. With the micro-indenter instrumentation, a general solution describing the load, displacement and contact area have been expressed by Sneddon [38]. The dependence of the load and displacement elastic solution may be written as:

$$P = kh^m \tag{14}$$

Where P is the load, h is in the indentation depth and k and m are constants. The expression defining the spherical indenter can be written as:

$$F = \frac{2\sqrt{2}}{3} E^* D^{\frac{1}{2}} h^{3/2} \tag{15}$$

The indenter diameter is D, and the reduced elastic modulus is E* that takes into account the properties of the indenter and the intended material. The indenter has a finite elastic constant and the deformation contributes to the overall displacement given by:

$$E^* = \left[\left(\frac{1-\nu^2}{E} \right)_{sample} + \left(\frac{1-\nu^2}{E} \right)_{indenter} \right]^{-1} \tag{16}$$

The elastic modulus for the sample and indenter are treated separately as observed in the equation with υ, poissions ratio. When the sample is unloaded,

the load/displacement does not follow the same path as the loaded material. The total displacement consists of an elastic and plastic portion of displacement[39]. The characteristic of the load/displacement curve (P-h) are the following: load maximum P_{max}, maximum displacement (h_{max}) residual plastic depth (h_p), the residual depth and the unloading slope (dF/dh) (Figure 19). From an elastic loading, only the elastic modulus may be achieved. However there remain many difficulties in exclusively indenting in the plastic regime. The relationship between the initial unloading slopes is expressed as:

$$\frac{dF}{dh} = B\frac{2}{\sqrt{\pi}}\sqrt{A}E^* \tag{17}$$

With the load F, the indentation depth h, contact area A and E* being the reduced modulus. For flat, spherical and parabolic indentors, the factor B is equal to 1.0. For triangular (e.g. Berkovich indenter) and square (e.g. Vickers indenter) indentars B is 1.034 and 1.012 respectively[40]. The equation represents the relationship allowing direct modulus evaluation from the unloading stiffness (dF/dh) and contact area[41].

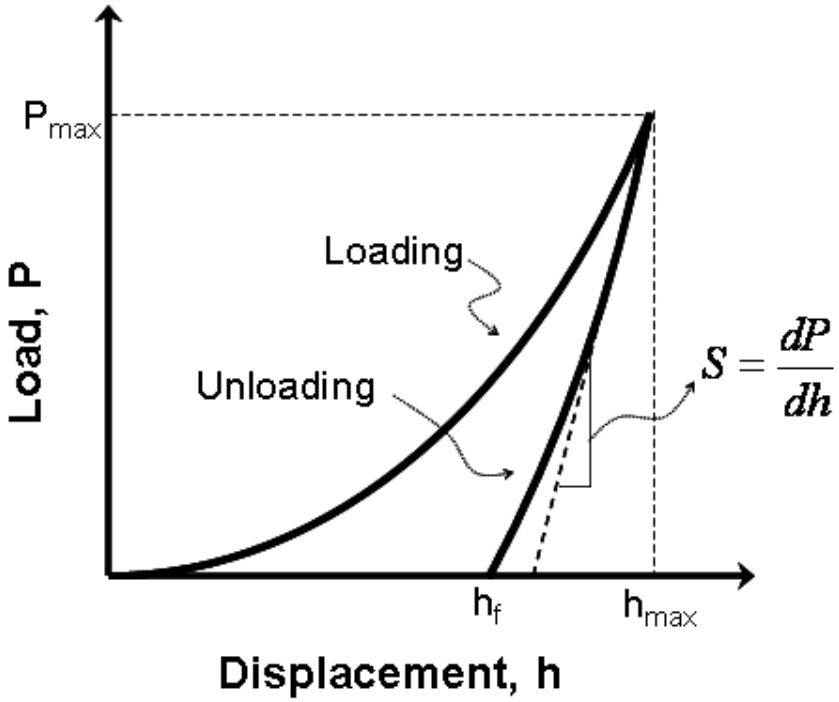

Figure 19 Characteristic load displacement curve for elastic plastic materials

3.2.12. Small Angle Neutron Scattering (SANS)

SANS measurements were conducted at the National Institute of Standards (NIST) in Gaithersburg, Maryland. The 30m instrument at the Cold Neutron Research Facility was used. For the experiment, a monochromatic beam of cold neutrons passes through the specimen in transmission geometry and the scattered neutrons are recorded on a two-dimensional detector(Figure 20)[42]. Details on the experimental set-up are found in previous reports[43]. It has been shown that SANS may provide information on microstructure of porous ceramic oxides including thermal sprayed coatings. The main advantage in comparison to other techniques is that SANS can provide size of closed pores on a nanometer scale[44, 45]. The pores are measured as the total void surface area per unit sample volume contributing to the total surface area. Other advantages include the anisotropic porod scattering. The scattering is based on variations with the sample and the beam orientation, in the intensity of the terminal slope of the small angle scattering at large scattering angles can be related to the anisotropic void surface area distribution.

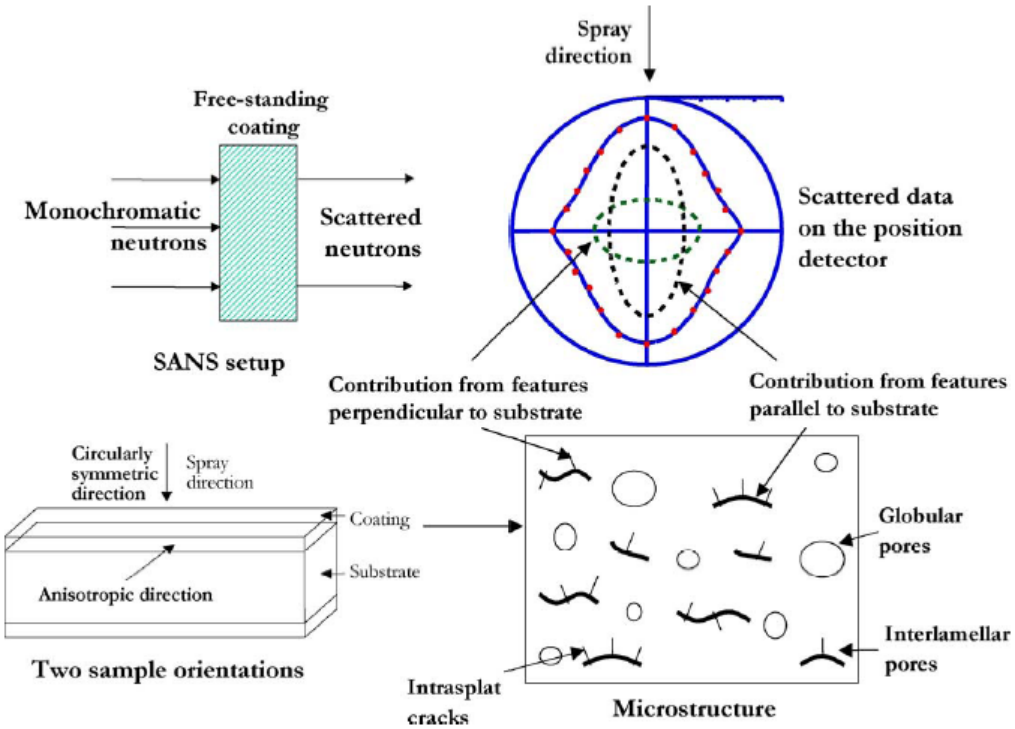

Figure 20 SANS experimental setup and model representation (excerpt from A. Kulkarni)[42]

Chapter 4: Phase Evolution in precursor-derived powders of pyrochlore and tetragonal phase oxides in $YO_{1.5}$-TiO_2-ZrO_2

Yokokawa published the first ternary diagram on $YO_{1.5}$-TiO_2-ZrO_2 based on calculated thermodynamic data compiled from literature; including estimates for the oxides based on correlation between interaction parameters and ionic radii [29]. Figure 21 are the binary diagrams of Y_2O_3-TiO_2 and ZrO_2-TiO_2. There are few published reports on experimental data for the ternary systems defined phase fields; therefore providing opportunity for investigating material compositions and properties. This chapter will address metastability and phase transformations for select material compositions as they are synthesized from precursor precipitations methods. The precursor syntheses method is beneficial as a non-equilibrium approach in order to investigate phase transformations as the material crystallizes from an amorphous oxide towards its final equilibrium phase[46]. The transformation paths will contribute to phase evolution maps for select composition up to their equilibrium temperatures. The motivation is to determine phase equilibria in $YO_{1.5}$-TiO_2-ZrO_2 systems on compositions that are have potential applications as next generation thermal barrier coatings, aiming to lower thermal conductivity and/or to improve high temperature performance and durability.

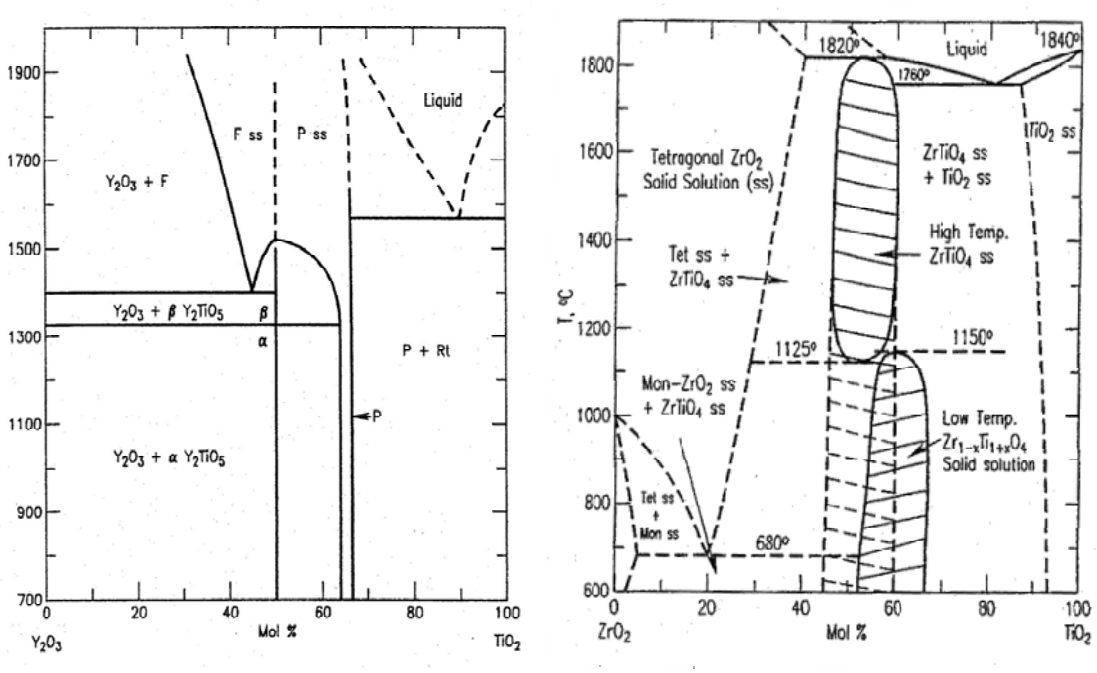

Figure 21 Proposed binary diagram of Y_2O_3-TiO_2 and ZrO_2-TiO_2[23]

This thesis reports the investigation of YSZ and two compositions (Figure 22) within the ternary System of $YO_{1.5}$-TiO_2-ZrO_2 that have potential applications as thermal barrier coating Phase evolution of powders will be explored in the following three regions:

(i) The benchmark composition, 7.6 mol.% YSZ, is currently used commercial thermal barrier coating materials due to its durability

(ii) Tetragonal phase in $YO_{1.5}$-TiO_2-ZrO_2 for composition (7.6 mol. %$YO_{1.5}$ -15.2mol. %TiO_2 - 72.8 mol. % ZrO_2)

(iii) Pyrochlore region ($Y_{2-x}Ti_2Zr_xO_7$) in $YO_{1.5}$-TiO_2-ZrO_2 (x=0.2, 0.4, 0.8, 1.2)

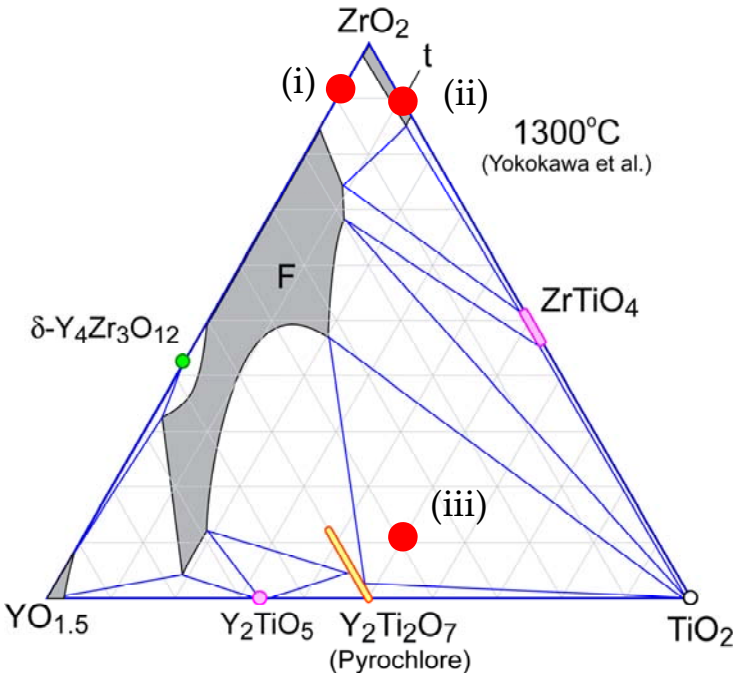

Figure 22 Ternary diagram for $YO_{1.5}$-TiO_2-ZrO_2 Red circles indicate compositions investigated in this dissertation

The following three sections highlight the motivation for selecting the compositions within $YO_{1.5}$-TiO_2-ZrO_2 as a thermal barrier coating material.

(i) Yttria stabilized zirconia compositions in $YO_{1.5}$-TiO_2-ZrO_2

In current thermal barrier coatings systems, yttria stabilized zirconia (YSZ) remains the most prominent material system. YSZ has exceptional high cycle-life when its composition is between the ranges of 7-8 mol. % $YO_{1.5}$. Much of the phase stability in this system has been thoroughly investigated. One of the main unresolved questions is why this particular composition has such high cycle life and low thermal conductivity. (Chapter 1.3 explores the phase stability of this binary system ($YO_{1.5}$-ZrO_2)). In this dissertation, YSZ will be used as the benchmark oxide for high temperature phase stability in powders and in coatings investigated.

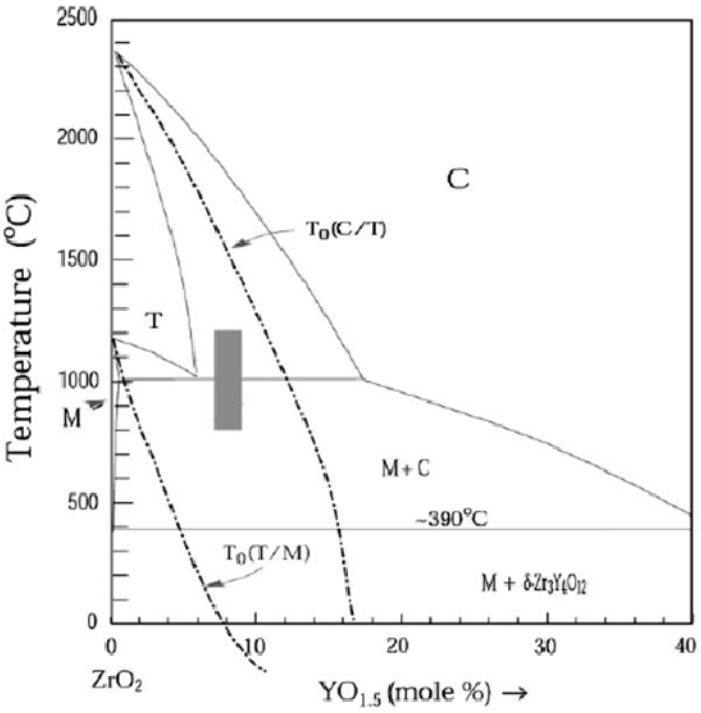

Figure 23 Binary diagram of $YO_{1.5}$-ZrO_2 with defined compositional area of tetragonal prime phase [6]

(ii) Tetragonal oxides compositions in $YO_{1.5}$-TiO_2-ZrO_2

The high temperature stability of YSZ is limited by the temperature of decomposition of the tetragonal prime phase. There has been renewed interest in the use of both alternative stabilizers and the use of co-stabilizers (additions of stabilizer to YSZ). Although there has been some research on alternate stabilizers there has been little work on determining the high temperature compositional phase stability of select oxides. One promising area for research is in the investigation of zirconia with two co-dopants. A promising two co-dopant systems is that of ZrO_2-$GdO_{1.5}$-$YO_{1.5}$ reported by R.M.R. Leckie [47](Figure 24). Leckie reported the decomposition temperature for tetragonal prime phase for multiple compositions. His results signified that for compositions fabricated from precursors, there was a metastable extension of the tetragonal prime phase

at high temperature up to 1500 ˚C. Secondly, for tetragonal phase oxides, Leckie reported the decomposition temperature for select compositions. The ternary diagram was based on binary diagrams of $GdO_{1.5}$-ZrO_2 and $YO_{1.5}$-ZrO_2.

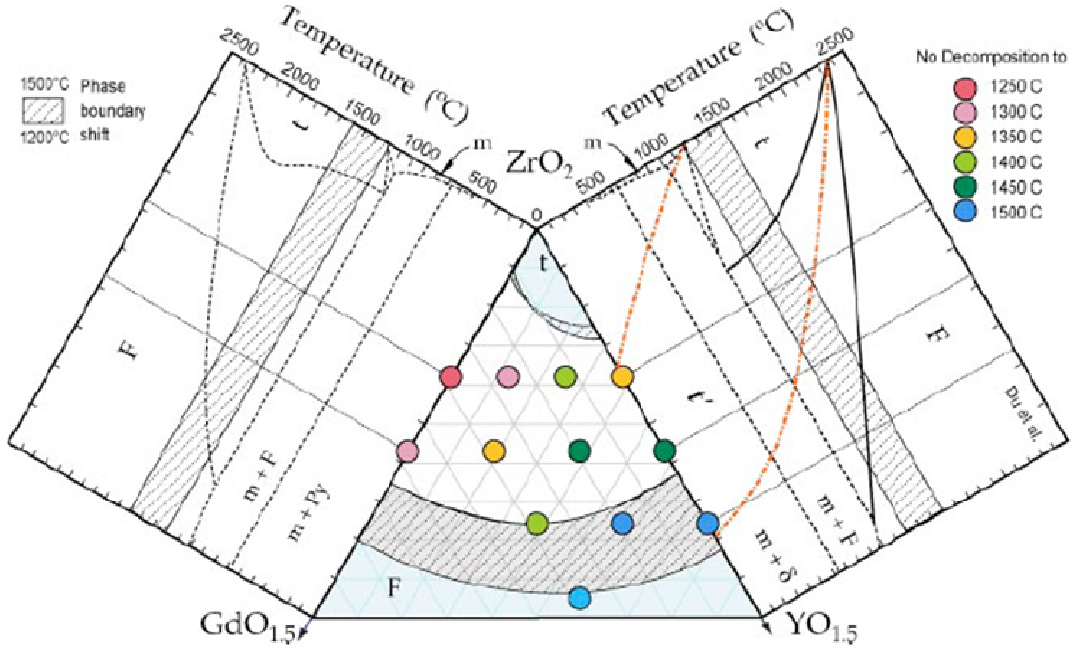

Figure 24 Ternary diagram of ZrO_2-$GdO_{1.5}$-$YO_{1.5}$ system. Temperatures for zirconia rich portion of diagram where colored dots represent where no decomposition of the tetragonal prime phase exist [47]

In comparison to $GdO_{1.5}$-$YO_{1.5}$-ZrO_2, the ternary system of $YO_{1.5}$-TiO_2-ZrO_2 is very promising because at equilibrium temperatures, select compositions may be rapidly quenched to form the tetragonal prime phase. The addition of the co-dopant TiO_2 is promising because it may potentially increase the decomposition temperature of the standard YSZ oxide. Therefore, there are many opportunities in determining phase stability in this system. A candidate composition that is within the equilibrium tetragonal phase is that of 7.6 mol.% $YO_{1.5}$ -15.2 mol.% TiO_2 77.2mol.%-ZrO_2 (Ti-YSZ). Another important factor is that the substitution of TiO_2 for ZrO_2 has been found to increase the toughness in zirconia oxides up

to two-fold in comparison to YSZ. Recently, there has been a link between tetragonality (ratio of c-axis to a-axis) to an increase in toughness.

(iii)Pyrochlore compositions in $YO_{1.5}$-TiO_2-ZrO_2

There remains many opportunities to investigate co-stabilizers in future TBC systems. The pyrochlore phase in some oxide systems has recently proven to be of interest due to their reported low thermal conductivity values in comparison to YSZ (Figure 25). One of the first findings of low thermal conductivity was reported by Maloney in $La_2Zr_2O_7$ system and its potential application as a thermal barrier coating. Since Maloney's findings, there have been investigations into the low thermal conductivity in systems of $Gd_2Zr_2O_7$, $Eu_2Zr_2O_7$ and $Sm_2Zr_2O_7$. A compilation of thermal conductivity results were compiled by C.G. Levi in for pyrochlore oxide values in comparison to stabilized zirconia. It was reported that the thermal conductivity of the dense pyrochlores was approximately half the density of yttria stabilized zirconia. The stoichiometric pyrochlore composition of $Y_2Ti_2O_7$ line composition is found in $YO_{1.5}$-ZrO_2-TiO_2 ternary system. In addition, to the stoichiometric pyrochlore phase, $Y_2Ti_2O_7$, the pyrochlore phase extends in non-stoichiometric compositions with additions of ZrO_2. The ternary system of $YO_{1.5}$-ZrO_2-TiO_2 is fairly unexplored presenting opportunities for phase stability and the extent of metastability in the pyrochlore region. Schaedler et al. reported phase transformation on the tie line extending for compositions of$Y_2Ti_{2-y}Zr_yO_7$ in the ternary diagram (pyrochlore to fluorite phase). This chapter will focus on investigating the pyrochlore region along the tie line of $Y_{2-x}Ti_2Zr_xO_{7+x/2}$ (pyrochlore to zirconium titanate phase) to study high temperature phase transformations.

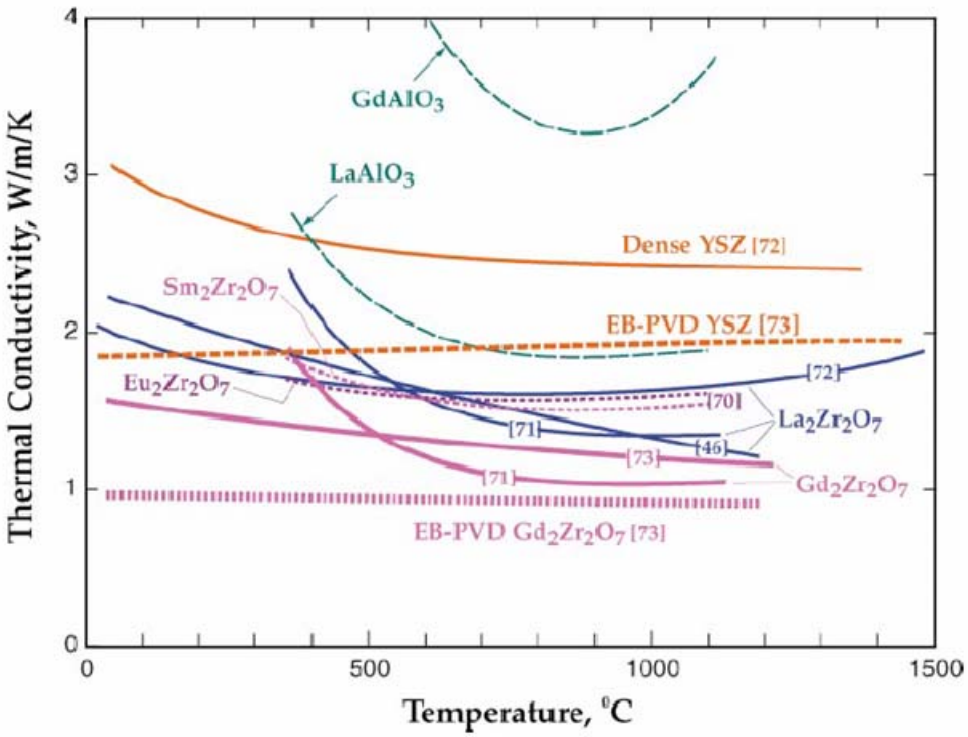

Figure 25 Thermal conductivity of pyrochlore oxides ($Gd_2Zr_2O_7$, $La_2Zr_2O_7$, $Sm_2Zr_2O_7$) and YSZ[6]

Due to limited research on phase equilibrium diagrams, this chapter will address detailed phase stability in compositions in aforementioned compositions in $YO_{1.5}$-TiO_2-ZrO_2. The strategy was to study phase transformations from amorphous oxides to their equilibrium temperature. Powders were synthesized from precursor pyrolysis methods. Advantages include non-equilibrium approach and control of compositions. Soft chemistry methods will also contribute to phase evolution maps and the investigation into the extendibility of metastable phases. Thus, the results are based on quenched-in states of thermal aged powders. The results of the quenched-in states enhance our understanding of the plasma sprayed coatings. This chapter will be divided into two sections focusing on phase evolution in; (A) pyrochlore region oxides and (B) tetragonal phase oxides.

(A) Phase Evolution in Pyrochlore Oxides in the $YO_{1.5}$-ZrO_2-TiO_2 System

- Understand the effect of substitutions (A and B-site) on crystallization
- Understand the stability range near pyrochlore phase and its constituents
- Phase evolution from amorphous to equilibrium temperature phase in precursor derived oxide compositions
- Experimentally determine phase for compositions in $Y_{2-x}Ti_2Zr_xO_{7+x/2}$

(B) Phase Evolution in Tetragonal Oxides in the $YO_{1.5}$-ZrO_2-TiO_2 System

- To understand and evaluate the effects of substitutions of Ti^{4+} for Zr^{4+} on high temperature stability of tetragonal phase
- Report the resistance to de-stabilization of tetragonal phase
- Link structural analysis results to thermal conductivity values in coatings
- Investigate trends in phase stability of ZrO_2 -7.6$YO_{1.5}$ precursor derived powders in comparison to ZrO_2-7.6$YO_{1.5}$-15.2TiO_2
- Report the tetragonality values of titania additions on 7YSZ oxides (high tetragonality has been proven to result in higher toughened materials)

4.1. (A) Pyrochlore Oxide compositions in Y_2O_3-ZrO_2-TiO_2 system

The pyrochlore oxide of the general type $A_2B_2O_6O'$ displays a large variety of physical and chemical properties that have many important applications depending on its chemical elements and composition. The ternary oxide system $YO_{1.5}$-ZrO_2-TiO_2 and its resulting pyrochlore compound, $Y_2Ti_2O_7$, have received attention because of its electro-chemical properties. Moreover, in solid solution with Ti^{4+} partially substituted by Zr^{4+} has shown ionic conductivity of the same order of magnitude as that of yttria stabilized zirconia. This phenomenon is promising because of its ability to be a Mixed Ionic-Electronic Conductor (MIEC)[48]. In the $Gd_2(Zr,Ti)_2O_7$ pyrochlore structure it was found that varying its chemical composition leads to in principal ionic or the mixed ionic-electronic conduction depending on the dopant concentrations[49]. The pyrochlore structure is typically described as two interpenetrating three-dimensional networks, a B_2O_6 network composed of corner sharing BO_6 octahedra and a A_2O' network[50]. The interactions between these two networks are weak and vacancies on the O' are common. Structurally, the pyrochlore has the A cations, rare-earth ion, located at the Wyckoff position 16c (0 0 0), B cations at 16d site (½ ½ ½), O at 48f (x 1/8 1/8) and O' at (1/8 1/8 1/8)[51]. The 8b site is vacant for the completely ordered pyrochlore type structure. The A cation, (Y^{3+}) and B-cations (Ti^{4+}, Zr^{4+}) are 8- and 6-coordinated by oxide ions, respectively[52]. There are several published reports on the synthesis of pyrochlore oxides, however they focus on conventional solid state reactions requiring processing of the oxides of TiO_2, ZrO_2 and Y_2O_3 in the appropriate molar ratios, at high temperatures (> 1200°C) accompanied by a grinding step resulting in large particles on the order of tens of micrometers. Reports have shown that soft chemistry routes such as

reverse co-precipitation provide precursors that are sub-micron to nano-crystalline powders and are advantageous because they allow lower synthesis temperatures (700˚C to 1000˚C) depending on the trivalent cation element. Soft chemistry also allows for the study of homogenous mixtures, the observation of metastability and extended solid solutions for fixed compositions.

Studying the structures of phases at different temperature intervals, from an amorphous precursor by rapidly cooling powders, cause kinetic suppression of long-range diffusion. We can kinetically suppress long range diffusion by rapidly cooling powders and study their phase at different temperature intervals. This study may translate knowledge to thermal spray technology because the occurrence of metastable phases are frequent in thermal spray materials and are result of large solidification rates which suggest massive or partition-less solidification by under-cooling.[25] We address the local bonding environment for the complex chemistries in $YO_{1.5}$-TiO_2-ZrO_2 by studying affects of heat treatments on different material compositions. An investigation of the gradual structural transformation from an amorphous to ordered material has been investigated by XRD, Raman spectroscopy and NMR. X-ray diffraction results represent long-range order in the solid solution. However, MAS NMR determines the short-range order by its ability to probe at the atomic level. In this work, ^{17}O MAS NMR is employed for it has high sensitivity to the local oxygen environments in these compounds. The determination of the differing bonding environments of yttrium, titanium, and zirconium cations, is critical to understanding the mechanism of ionic conductivity.

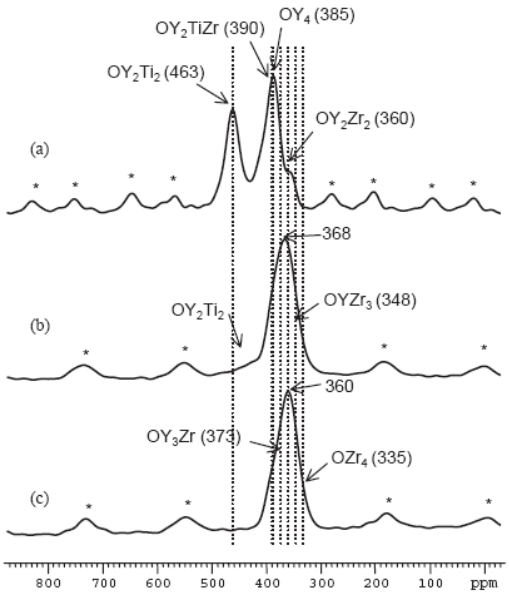

Figure 26 ^{17}O MAS NMR spectra $Y_2(Zr_{0.3}Ti_{0.7})_2O_7$, (b) $Y_2(Zr_{0.3}Ti_{0.7})_2O_7$(c) $Y_2Zr_2O_7$ [53]

N. Kim et.al, investigated short-range order in fluorite ($Y_2Zr_2O_7$) and pyrochlore oxides[53]. The pyrochlore compositions were of $Y_2(Zr_{0.3}Ti_{0.7})_2O_7$ and $Y_2(Zr_{0.3}Ti_{0.7})_2O_7$ and their phases were confirmed by neutron diffraction. The compositions reflect mixing only on the B cation site with Ti^{4+} and Zr^{4+}. Kim's results showed that there were four resolved resonances in the spectra. Assigned peaks are 463 ppm for ($O1T_2Y_2$), 385 ppm (OZY_4), 360 ppm ($O1ZrY_2$) and 390 ppm due ($O1Y_2TiZr$) (Figure 26). The significance of his results was that he reported the local environment of fluorite oxides and with additions of Ti^{4+}, reflecting a wider range of compositions that signify the transition to the pyrochlore phase. Each resonance peak is an assignment based on oxygen's local environment. The preliminary NMR results in this chapter present mixing of the A and B cations and its effect of the local oxygen environment. M. Glerup et. al. was the first to report structural transformations from pyrochlore structures to the defect fluorite structure in $Y_2Ti_{2-y}Zr_yO_7$(Figure 27)[54]. Their work focused on the stoichiometric composition doped with Zr^{4+} on B- cation site.

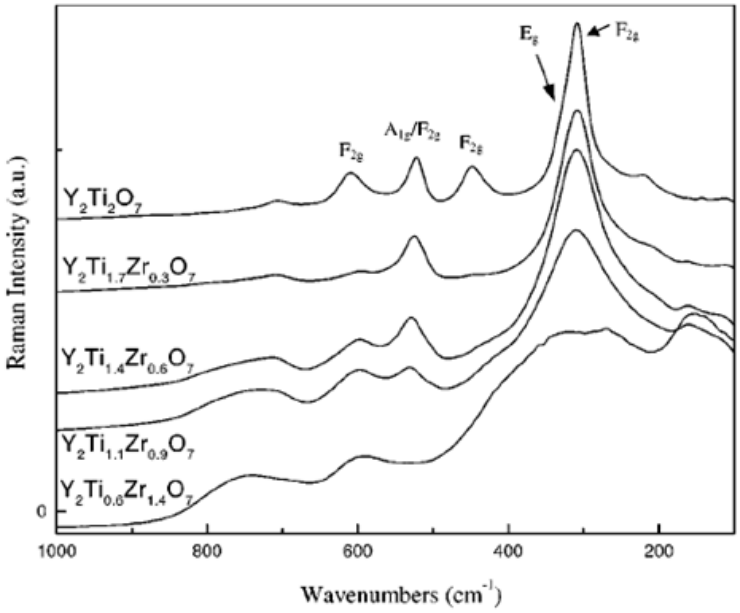

Figure 27 Raman spectra of un-doped ($Y_2Ti_2O_7$) and Zr^{3+} doped pyrochlore oxides[54]

4.2. Results and Discussion

This section presents an investigation into the effect of Zr^{4+} substitutions for Y^{3+} in the $Y_{2-x}Ti_2Zr_xO_{7+x/2}$ system measured by thermal analysis, X-ray Diffraction (XRD), NMR and Raman spectroscopy. T. Schaedler contributed to the experimental results for the tie-line that investigated the effect of substitutions of Zr^{4+} for Ti^{4+} (B-cation substitution only) in the ternary diagram (equation 18). The crystallization temperatures and phase formations were investigated by *ex-situ* XRD at desired temperatures and *in-situ* XRD at heating rates of 5°C/min. The results presented in this section specifically address cation substitutions (Y^{3+} for Zr^{4+}) in $YO_{1.5}$-TiO_2-ZrO_2. This chapter will also explore the affect of cation substitutions on crystallization (Y^{3+} for Zr^{4+}). Comparisons between both methods were investigated in order to detect changes in the structure and present data on phase hierarchy of select compositions. The select compositions provide fundamental data on the stability range of phases in the ternary system. Studying the effects of cation substitutions provide an understanding of the stability range of the phases with variations in the chemistries. Experimental results are presented as follows: thermal analysis emphasized the crystallization temperatures and the effects of substitution on phase formation; detailed phase analysis by XRD to determine transformation paths; Raman spectroscopy and NMR results presented short range ordering with varying compositions.

4.2.1. Crystallization kinetics in precursor derived powders

Figure 28 and Figure 29 are thermal analysis results of DSC measurements from amorphous powder oxides prepared by soft-chemistry and heat treated from ambient temperature to 1500˚C. Two separate tie lines were investigated within the ternary system. The first tie-line represents substitutions of (Zr^{4+} for Ti^{4+}) in $Y_2Ti_{2-y}Zr_yO_7$. The second tie-line represents Zr^{4+} for Y^{3+} in $Y_{2-x}Ti_2Zr_xO_{7+x/2}$. Results in Figure 28 display the effects of substitutions in $Y_2Ti_{2-y}Zr_yO_7$ (Zr^{4+} for Ti^{4+}) and Figure 29 were taken to study the effects of Zr^{4+} for Y^{3+} in $Y_{2-x}Ti_2Zr_xO_{7+x/2}$. In Figure 28; the exothermic peak observed between 250 to 350˚C are the results of the decomposition of organic species introduced by the reverse co-precipitation process. The second sets of exothermic peaks found between 750 to 850˚C are the result of a phase transformation from an amorphous to a crystalline material. There were peak shifts when substituting Zr^{4+} for Ti^{4+}. The crystallization temperatures decreased from 843 to 817˚C. In addition to peak shifts in the crystallization temperature, there was a reduction in the exothermic peak height and peak broadening as the amount of Zr^{4+} increases from 0.2 – 1.2. Figure 30 illustrates the dependence of the A^{3+} and the average B^{4+} cation ratio on crystallization as noted in equation four on the effect of stoichiometric compositions.

$$Y_2Zr_2O_7 \xleftrightarrow{Composition} Y_2Ti_2O_7 \qquad (18)$$

The results were quantified by averaging B-cation ionic radii for Ti^{4+} and Zr^{4+} by the following equation:

$$r(B_{av}^{4+})=(1-0.5x)r(B^{4+})+0.5xr(B^{4+}) \qquad (19)$$

As there is an increase in the ionic radius ratio $r(A^{3+})/r(B_{av}^{4+})$ there is also an increase in the crystallization temperature (Figure 30). In Figure 29, the onset of crystallization was observed for temperatures between 715°C to 843°C when substituting Zr^{4+} for Y^{3+} ($Y_{2-z}Ti_2Zr_zO_{7+z/2}$, $0 < z < 2$). All phase transformation from amorphous to crystalline materials was very sharp and did not illustrate any reductions in the exothermic peaks or any significant peak broadening.

Results indicate that substitutions of Zr^{4+} for Y^{3+} caused little or no change in the exothermic peak in $Y_{2-z}Ti_2Zr_zO_{7+z/2}$ compared to substitutions of Zr^{4+} for Ti^{4+} in $Y_2Ti_{2-y}Zr_yO_7$. Figure 30 is a graph of the ionic radius ratio $r(A^{3+})/r(B_{av}^{4+})$ on the phase transformation from a fluorite to a pyrochlore phase. The transition temperature was determined by XRD results. Below the trend line a fluorite phase was observed and above the trend line a pyrochlore phase was present. The greater the ionic radius ratio, of A to B cation, the higher the occurrence of the pyrochlore phase field, however, at low ionic radius ratio values the larger the fluorite phase field. This suggests that the transformation to the fluorite phase is kinetically favored as the ratio of the cation on the B-site approach unity. Compared to the substitutions Zr^{4+} for Y^{3+} in $Y_{2-z}Ti_2Zr_zO_{7+z/2}$ there are little or no reduction in the area of the exothermic peaks. When the samples were heated at 10°C/min it was found that the onset for crystallization decreased from 834 °C to 817 °C when substituting Zr^{4+} for Ti^{4+} ($Y_2Ti_{2-y}Zr_yO_7$, $0 < y < 1.2$) Larger changes in the onset of crystallization (activation energy) with substitutions of Zr^{4+} for Y^{3+} compared to Zr^{4+} for Ti^{4+}. The data also implies that less energy (enthalpy of crystallization) is required for crystallization when substituting Zr^{4+} for Ti^{4+} as seen in Figure 28 as evident with the decrease in the exothermic energy needed to cause a phase transformation. In other words, the energy required for atomic mobility to form the fluorite phase is kinetically favored as the ratio of the

B-site approaches unity. Dependence of the ionic radius ratio was observed in the $Y_2Ti_{2-y}Zr_yO_7$. The DSC experiment revealed that there is a strong relationship in the system as a function of the $r(A^{3+})/r(B^{4+})$.

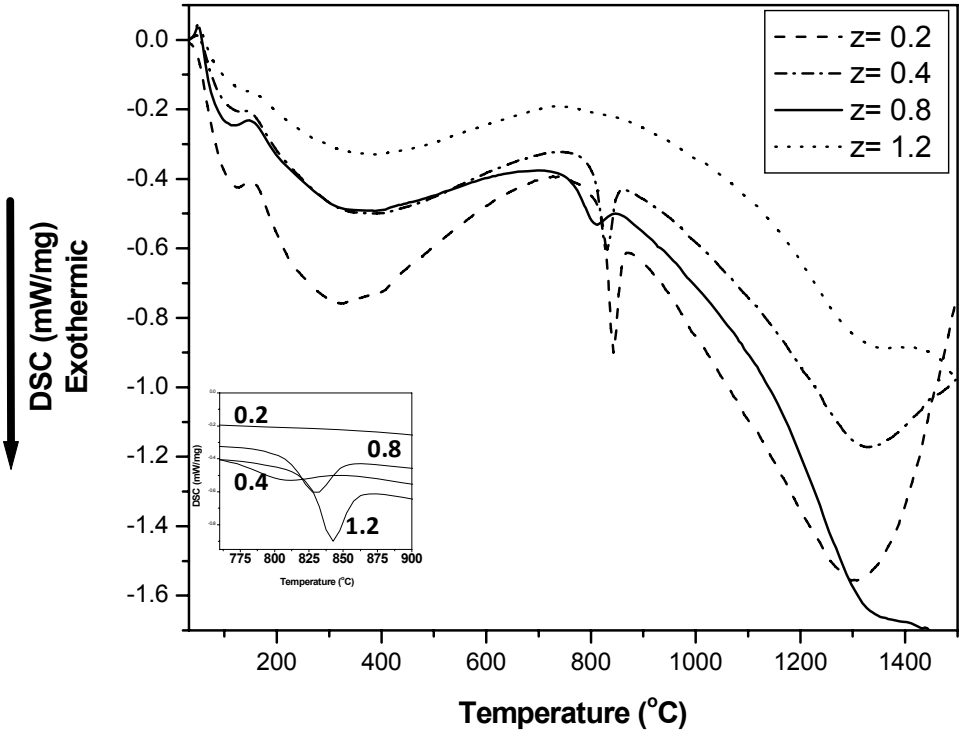

Figure 28 DSC results for substitutions of Zr^{+4} for Ti^{+4} in $Y_2Ti_{2-y}Zr_yO_7$. A heating rate of 5°C/min was used from ambient to 1500°C

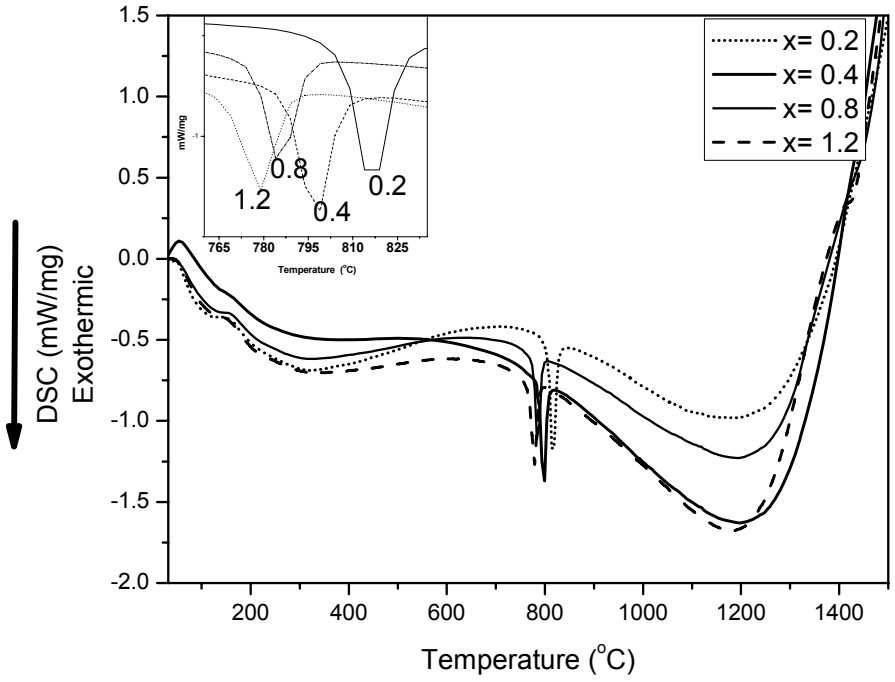

Figure 29 DSC results for substitution of Y^{3+} for Zr^{4+} in $Y_{2-x}Ti_2Zr_xO_{7+x/2}$. A heating of rate 5˚C/min was used from ambient to 1500˚C

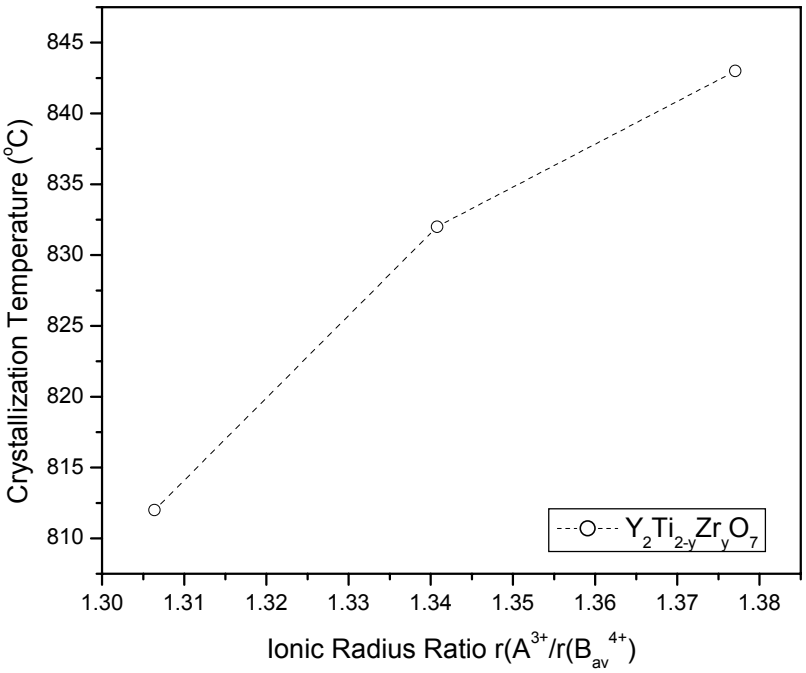

Figure 30 Crystallization temperature versus ionic radius ratio $r(A^{3+})/r(A^{4+})$ in $Y_2Ti_{2-y}Zr_yO_7$.

4.2.2. Quantitative compositional analysis of precursor powders

A conversion table for the chemistries investigated in dissertation is found in Table 2 for chemical formulas to molar percentages. EDS results provided compositional analysis for the derived powders by reverse co-precipitation processing (Table 3). Results showed that desired compositions averaged had weight percent values that were within 2-4 percent error in comparison to starting composition. Figure 31 shows the morphology of the powders by synthesized by precipitation processing. Powders morphology described as jagged edged, cylindrical and average 100 μm in size. The morphology is the result of multiple mortar and grinding steps using a mortar and pestle. There were no distinctive differences in the powder morphologies for the four sample compositions.

Table 2 Chemical formula to mole percentage conversion table

Chemical Formula	Mol. %
$Y_{1.6}Ti_2Zr_{0.4}O_{7.2}$	50Ti-40Y-10Zr
$Y_{1.2}Ti_2Zr_{0.8}O_{7.4}$	50Ti-30Y-20Zr
$Y_{0.8}Ti_2Zr_{1.2}O_{7.2}$	50Ti-20Y-30Zr
$Y_{0.4}Ti_2Zr_{1.6}O_{7.2}$	50Ti-10Y-40Zr

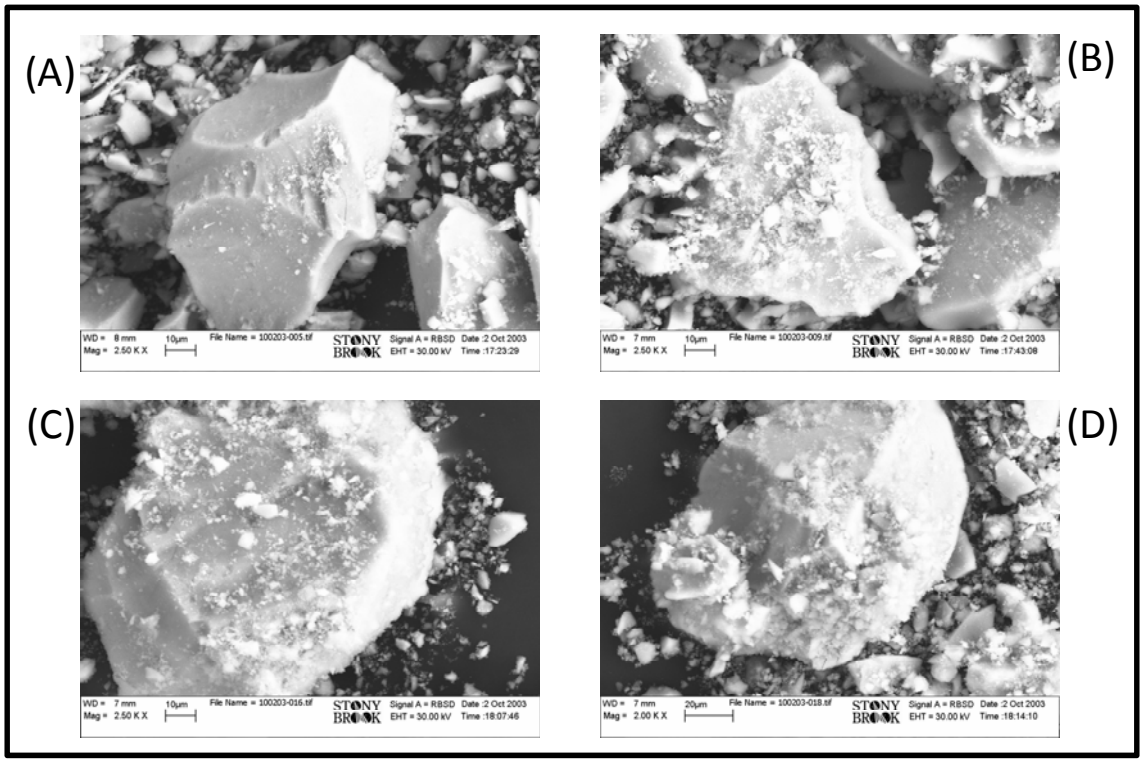

Figure 31 Morphology of powder particles synthesized from reverse co-precipitation processing. Samples after crushing using a mortar and pestle; followed by low pyrolysis temperature of 700˚C. Powder samples are (A) $Y_{1.6}Ti_2Zr_{0.4}O_7$ (B) $Y_{1.2}Ti_2Zr_{0.8}O_7$ (C) $Y_{0.8}Ti_2Zr_{1.2}O_7$ (D) $Y_{1.6}Ti_2Zr_{0.4}O_7$

Table 3 EDAX ZAF Quantification for compositional analysis for compositions derived by reverse co-precipitation processing

	50Ti-40Y-10Zr		50Ti-30Y-20Zr		50Ti-20Y-30Zr		50Ti-10Y-40Zr	
Element	**wt%**	**at%**	**wt%**	**at%**	**wt%**	**at%**	**wt%**	**at%**
Ti K	51.1	66.1	51.6	66.6	49.3	64.7	52.3	67.5
Y K	39.3	27.4	28.8	20.1	20.6	14.6	11.2	7.82
Zr K	9.59	6.49	19.6	13.3	30	20.7	36.5	24.7
Total	100		100		100		100	

4.2.3. Structural evolution of oxide compositions from amorphous to equilibrium phase in $YO_{1.5}$-TiO_2-ZrO_2

Figure 32 represents a series of ex-situ experiments for the pyrochlore region composition of $Y_{1.6}Ti_2Zr_{0.4}O_{7.2}$. All samples were subjected to high temperature heat-treatments at temperature followed by rapid quenching of oxides in air. The samples were quenched after a thirty minute heating regime. This was followed by XRD of powders between each heating/time interval. The results were graphically summarized for ex-situ XRD for low and high temperature compositions in Figure 33 and Figure 34 respectively. Figure 33 is a ternary diagram summarizing experimental results for compositions at low thermal exposures. With pyrolizing temperatures at 600 ˚C we obtained the amorphous phase for all oxide compositions. With low heat treatments of 700 ˚C, we observed large fluorite domains in phase diagrams suggesting metastable fluorite for multiple compositions in the ternary system. In addition we observe metastably extended tetragonal phase oxides. Figure 34 is a summary of heat treatments near equilibrium temperatures in the ternary system. Summary includes results from T. Schaedler to develop domains at heat-treatment temperatures and the equilibrium temperature of selected compositions within the ternary diagram. Phase diagram emphasis observations of the extended fluorite/rutile phases for temperatures at 1000 ˚C. For heat treatments of oxides at 1400 ˚C we observe Fluorite/Pyrochlore + rutile + $ZrTiO_4$ phases for compositions along $Y_{2-x}Ti_2Zr_xO_{7+x/2}$. For compositions along the compositional tie-line of $Y_2Ti_{2-y}Zr_yO_7$, pyrochlore and fluorite phase were observed. Samples were heated at 1400 ˚C for one hour and initial results were similar to Yokokawa's theoretical diagram. However, with extended heat treatments of twenty four hours, our results contradicted the theoretical phase diagram.

Samples for $Y_2Ti_{2-y}Zr_yO_7$ did not undergo any significant changes, however, samples for $Y_{2-x}Ti_2Zr_xO_{7+x/2}$ did not agree with the equilibrium diagram by Yokokawa.

A second study involved heating samples by an in-situ XRD. Compositions were subjected to a ten degree per minute steps with simultaneous XRD data collections. Figure 35, x = 0.4, in $Y_{1.6}Ti_2Zr_{0.4}O_{7.2}$ the spectrum showed that the structure was amorphous until 450 ˚C. After 450˚C the fluorite phase field peaks were present by observing the indices of (111) (200) and (220). The fluorite phase was stable until 650˚C. The pyrochlore phase was identified by the (331) indices between 650 to 725˚C. At 725˚C observation of the characteristic (110) plane indicating the rutile peak. A two phase region of pyrochlore and rutile was observed until 930˚C. Figure 36, x = 0.8, the *in-situ* XRD spectra of $Y_{1.2}Ti_2Zr_{0.8}O_7$ remains amorphous from room temperature to 450˚C. After 450˚C the crystalline phase, fluorite is observed and identified by the (111) and (200) indices. The fluorite stability range is between 450 and 725˚C. From 750 to 930˚C, the pyrochlore and zirconia titanate phase are present. For Figure 37, z= 1.2, the amorphous phase is present from room temperature until 400˚C. The fluorite phase is observed from 400˚C to 650˚C. Following the fluorite phase, rutile and anatase form and the peaks are apparent up to 700˚C. The pyrochlore phase field was present from 700 to 750˚C. However they lose their intensity and become broader as the temperature increases. At 825˚C, the zirconia titanate phase, (011) is observed. In comparison to dynamic in-situ XRD results from the National Synchrotron Light Source (NSLS-BNL); ex-situ experiments were evaluated. Experiments were based on short time exposures at high temperature at fifteen-minute intervals. XRD spectrums were taken for pyrolyzed powder to 1200˚C. An example of the phase evolution is found on Figure 32 for the composition of $Y_{1.6}Ti_2Zr_{0.4}O_{7.2}$. Figure 38 summarizes the results for three

compositions of the system $Y_{2-z}Ti_2Zr_zO_{7+z/2}$ for the comparison of the phase hierarchy for both static and dynamic experiments.

An advantage of *in-situ* XRD is the ability to observe and determine the phase formation of the structure from ambient temperature towards the select compositions to the equilibrium temperature. In-situ XRD determined phase formation of oxides because it is a more sensitive technique than isothermal XRD experiments. In comparison to the conventional diffractometer results that were taken for constant temperatures at defined time intervals, *in-situ* XRD provides information on preferential phase formation at temperatures. *Ex-situ* diffractometer XRD results showed that all the material compositions were amorphous up to 800˚C followed by a phase transformation to a crystalline phase. Amorphous to crystalline transitions were detected by a 150˚C or less by *in-situ* XRD. Results from the composition of $Y_{1.6}Ti_2Zr_{0.4}O_{7.2}$ by conventional XRD at 1400˚C showed that a three phase system consisting of pyrochlore, zirconia titanate, and rutile were observed. This three phase system was also observed in the *in-situ* XRD results at 900˚C. The composition of x=0.8 ($Y_{1.2}Ti_2Zr_{0.8}O_{7.4}$) also had a three phase system consisting of P+Z+R compared to only pyrochlore in the *in-situ* results. In x= 1.2 ($Y_{0.8}Ti_2Zr_{1.2}O_{7.6}$) 1400˚C XRD results show phases of P+R while in *in-situ* show P+R+Z. Results of *in-situ* XRD show a stronger influence of the TiO_2 and $ZrTiO_4$ phase at lower temperatures compared to conventional XRD. Results also indicate that transformations from an amorphous precursor do not always lead to fluorite phases. In fact, *in-situ* results show the appearance of the pyrochlore phase. Amorphous to crystalline transition temperatures were determined at lower temperature in in-situ XRD by approximately 400˚C. The results proved experimentally and the theoretical phase diagrams were not in agreement. The crystallite size dependence on the annealing temperature is shown in Figure 39. There was a linear increase in the

crystallite size as the temperature increased for the synthesized powders. Crystallite sizes were determined by the Scherer equation:

$$D = 0.9\left(\frac{\lambda}{\Delta\cos(\theta)}\right) \tag{19}$$

Results are from isothermal powder XRD experiments. As temperatures increased for all powder compositions, the crystallite sizes also increased. The slope of crystallite size versus annealing temperature was highest in compositions of 50Ti-30Y-20Zr; corresponding to a transformation from fluorite to a pyrochlore phase and zirconate phase. In comparison, the structural transformations for to the composition of 50Ti-40Y-10Zr were from fluorite to pyrochlore and 50Ti-20Y-30Zr transformed to pyrochlore and rutile phases.

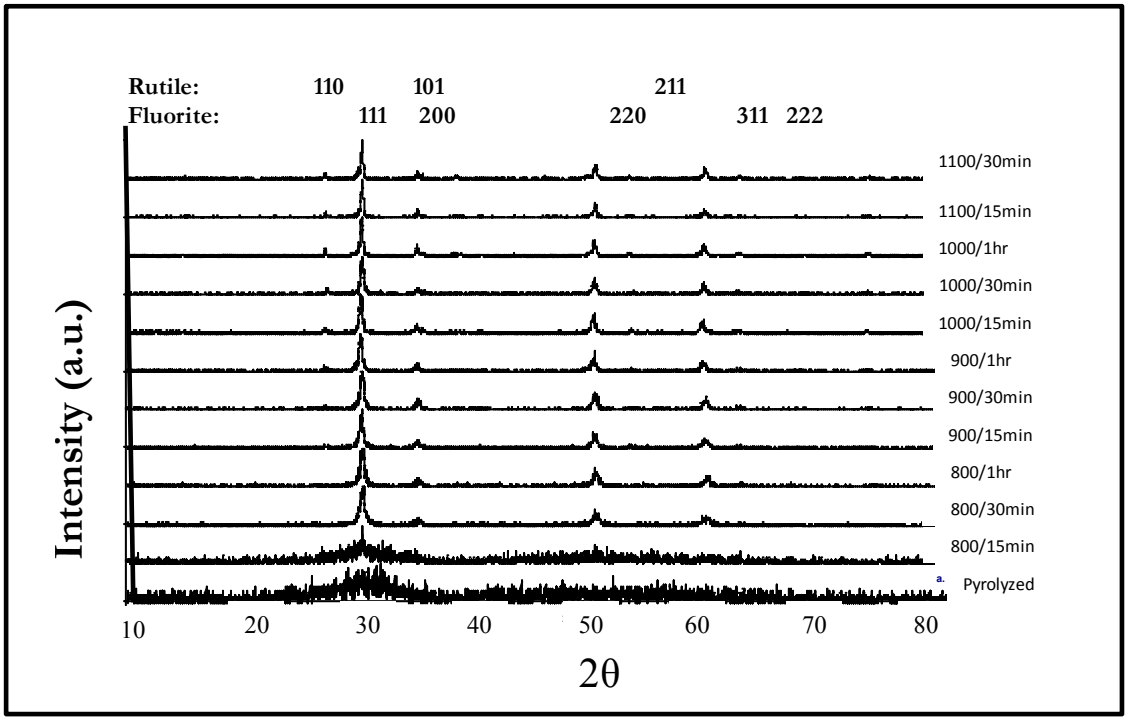

Figure 32 Series of X-ray diffraction patterns for $Y_{1.6}Ti_2Zr_{0.4}O_{7.2}$ powder under static isothermal conditions. Combinations of spectrums at short thermal intervals reveal the progression of fluorite and rutile phases up to 1100°C.

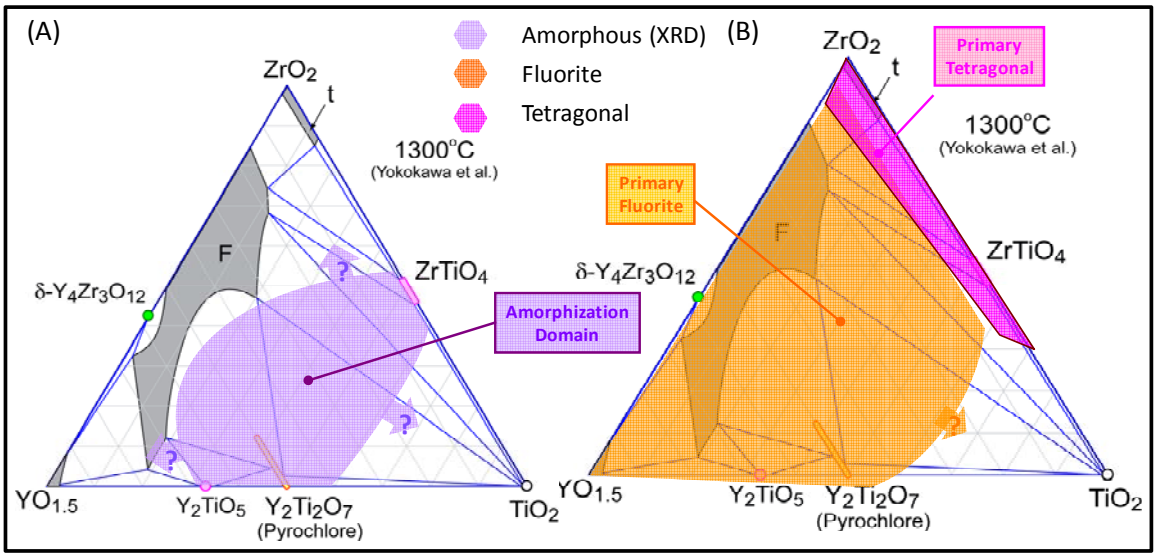

Figure 33 Low temperature pyrolysis of oxide compositions (A) Amorphization domain for pyrolysis temperatures of 700˚C (B) Extended fluorite and tetragonal phase in ternary phase diagram

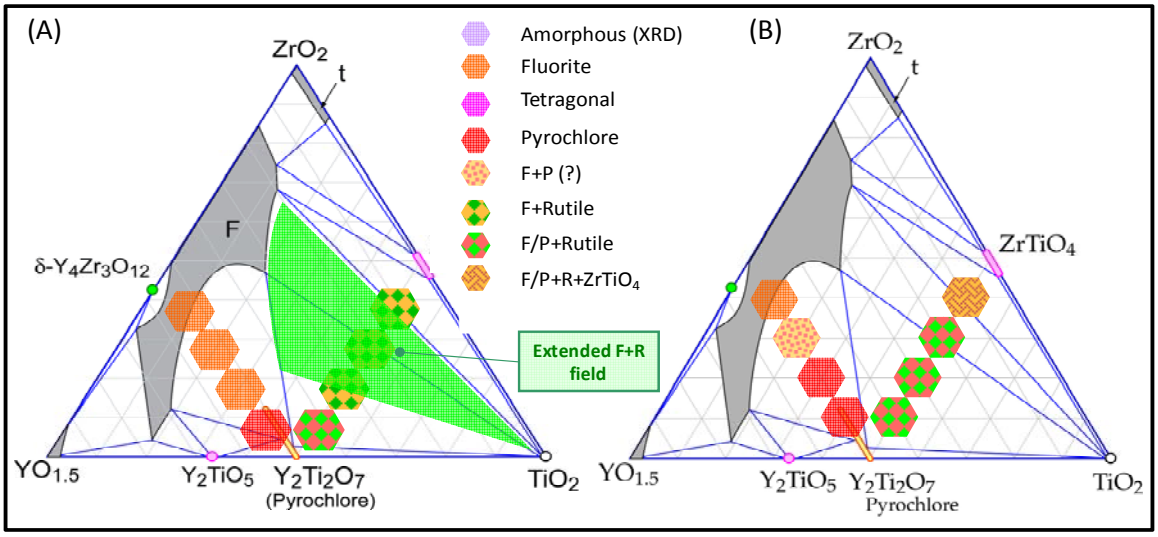

Figure 34 Summary of high temperature structural evaluation of oxide compositions (A) 1000˚C with extended fluorite and tetragonal phases (B) 1400˚C In ternary diagram for select compositions

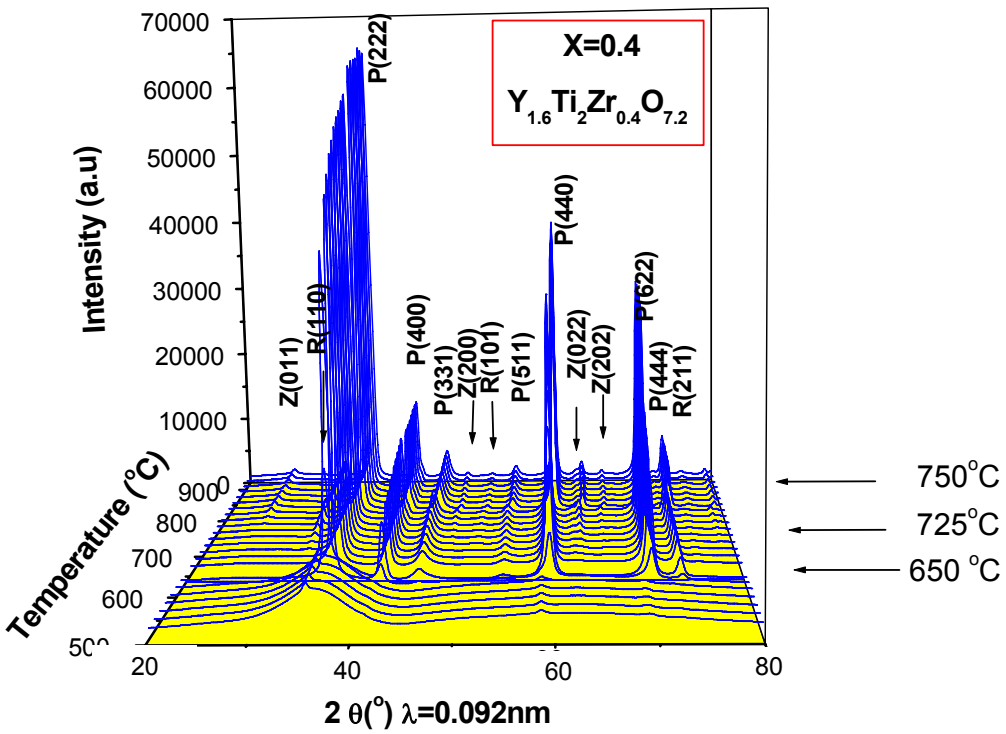

Figure 35 In-situ XRD spectra of $Y_{1.6}Ti_2Zr_{0.4}O_{7.2}$. The transition from the amorphous phase to pyrochlore phase occurs at 650°C. The $ZrTiO_4$ phase was detected at 725°C. Rutile peaks were observed at approximately 750°C (Z=Zirconate, R= Rutile and P=Pyrochlore)

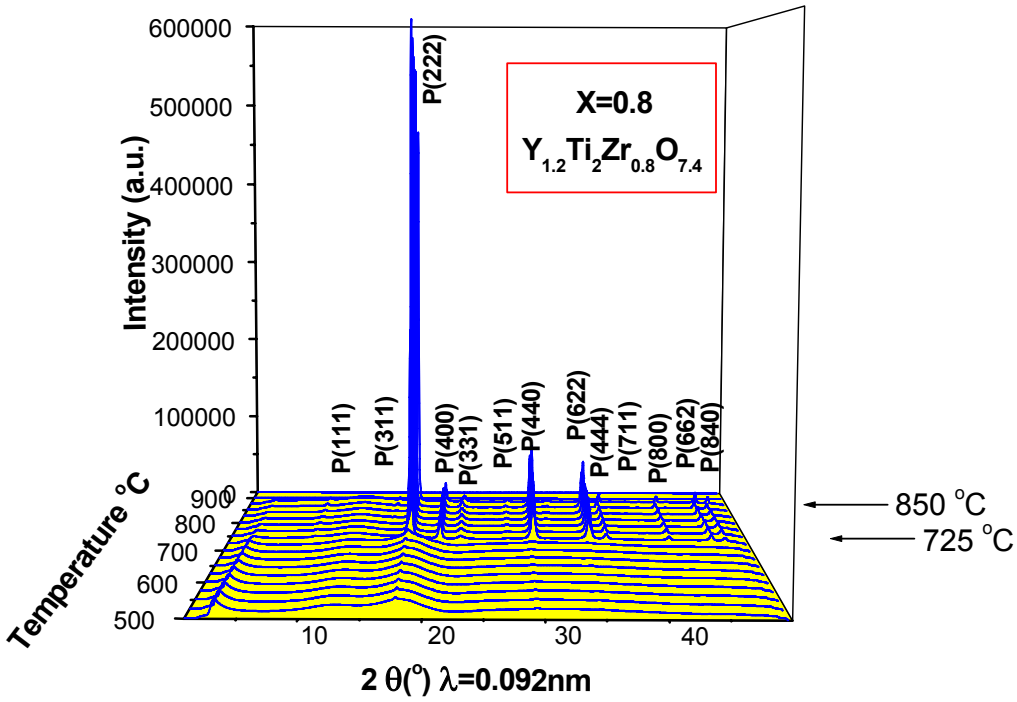

Figure 36 *In-situ* XRD of $Y_{1.2}Ti_2Zr_{0.8}O_{7.4}$. Phase transformation from the amorphous to fluorite phase occurred at 725˚C. The transformation from the fluorite to pyrochlore occurred at 850˚C. (Z=Zirconate, R= Rutile and P=Pyrochlore)

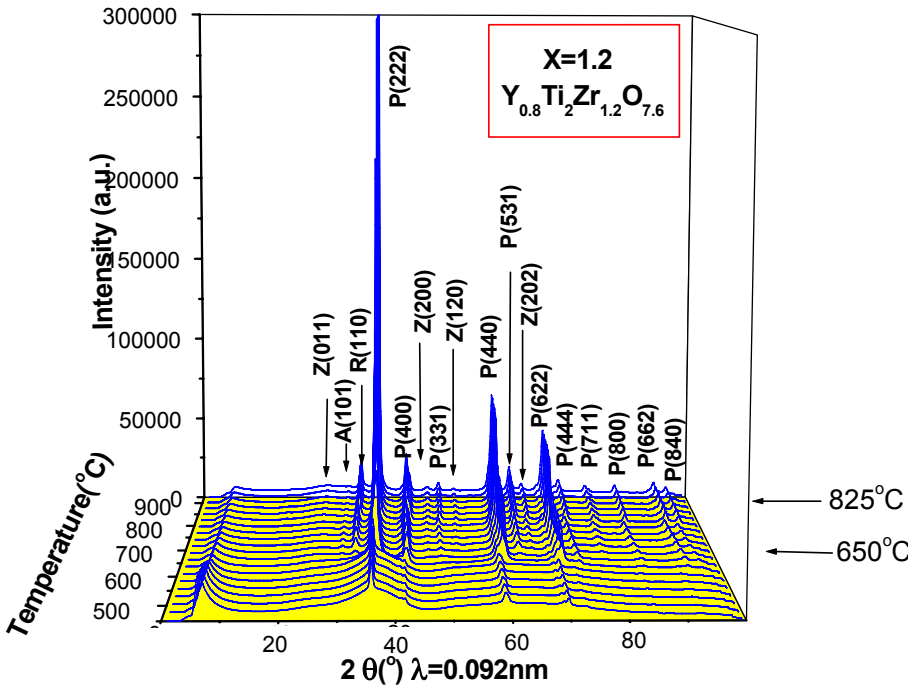

Figure 37 The *in-situ* XRD spectra of $Y_{0.8}Ti2Zr_{1.2}O_{7.6}$. Amorphous to fluorite temperature was observed at 650˚C. The transformation to the pyrochlore and zirconate phase was observed at approximately 825˚C. (Z=Zirconate, R= Rutile and P=Pyrochlore)

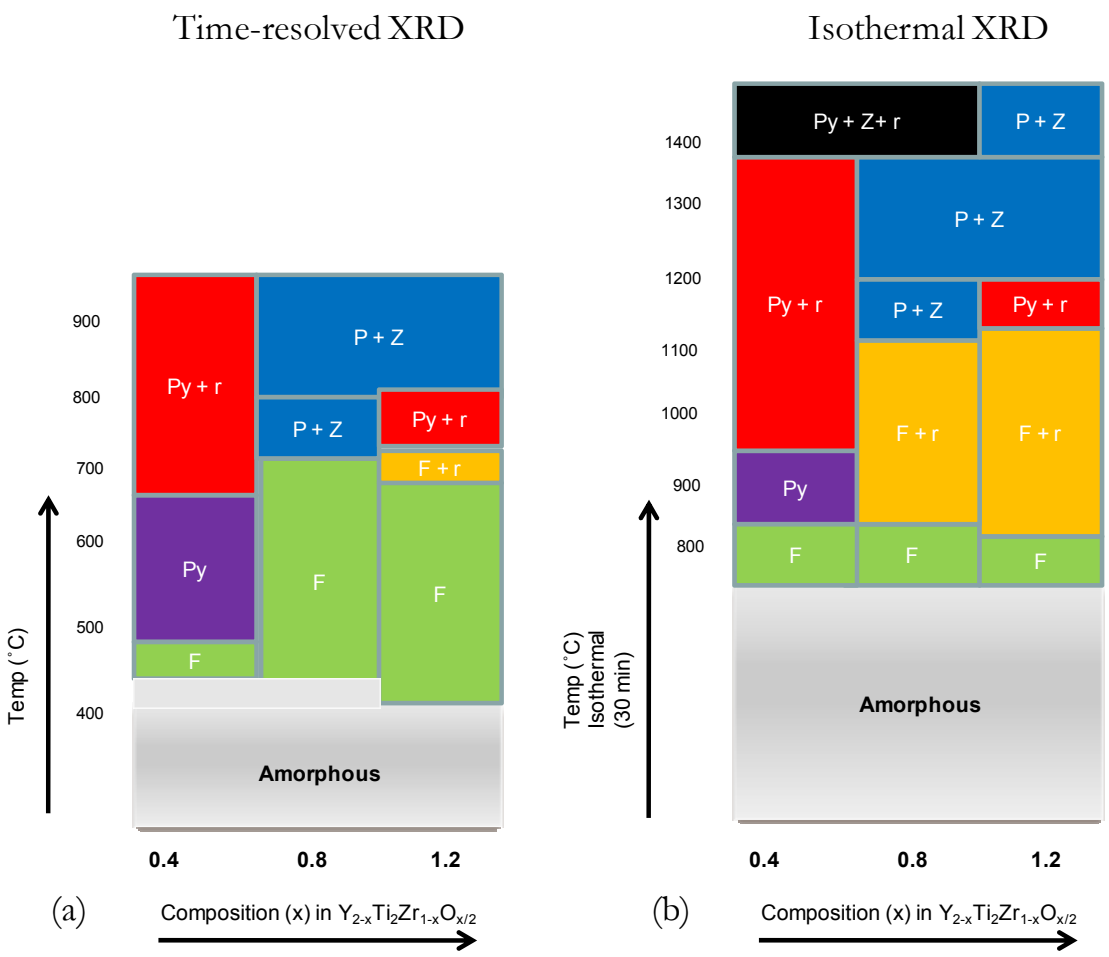

Figure 38 Summary of phase evolution in (a) *In-Situ* synchrotron XRD and (b) conventional XRD. In-situ results are heat treated to 930˚C and conventional XRD heat treatment reached an equilibrium temperature at 1300˚C.

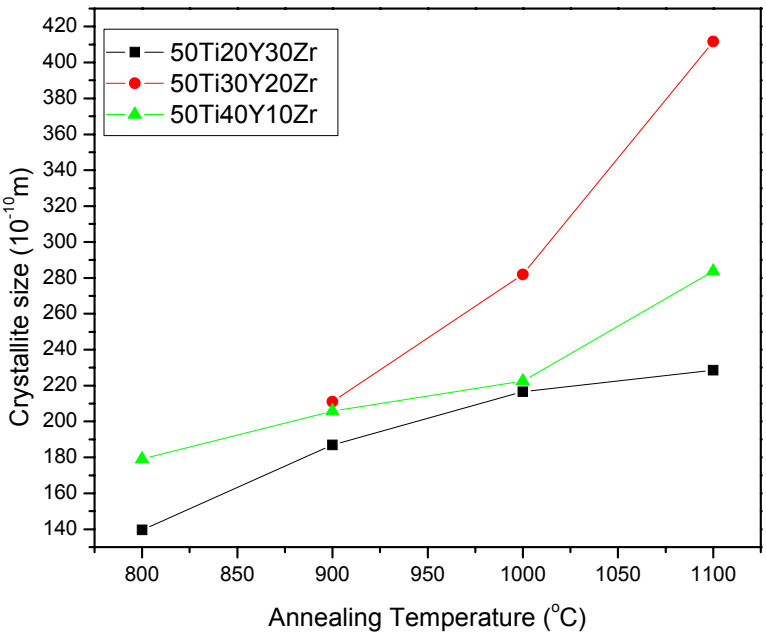

Figure 39 Crystallite size versus heating temperature for compositions of $Y_{2-z}Ti_2Zr_zO_{7+z/2}$

4.2.4. Short range ordering transformation via Raman Spectroscopy

This section reports the temperature dependence of crystallization by the phase evolution of four compositions within the $Y_{2-x}Ti_2Zr_xO_{7+x/2}$ system by Raman spectroscopy. The prepared Raman samples are precursor derived powders for compositions of 50 mol.% titania. The percentage of yttria increased by ten molar percentage from (10-40mol.%) while the zirconia content decreased correspondingly. Raman spectroscopy was used to investigate the structural changes with yttria and zirconia content (A and B cation substitutions). Vibrational spectra of pyrochlore structures have well resolved frequencies. Distinct changes in the Raman Spectra were observed and are found on Figure 41-Figure 44 and the peaks were reported on Table 4-Table 6. Raman spectroscopy was used to explore the effects, if any, of the substitution of trivalent ions for tetravalent ions, respectively, on the 16c and 16d sites of the pyrochlore structure. From factor group analysis of $A_2B_2O_7$ pyrochlores, there are six Raman-active modes and seven infrared-active modes for the Fd3m space group[55, 56].

Raman active modes: $\Gamma = A_{1g} + E_g + 4_{2g}$ (20)

IR active modes: $7F_{1u}$ (21)

Inactive Mode: $2F_{1G} + 3A_{2u} + 3E_u + 4F_{2u}$ (22)

Acoustic mode: $1F_{1u}$ (23)

Previous studies have shown that the $A_2Ti_2O_7$ pyrochlores are dominated by two intensities at approximately 310 and 512cm^{-1}. The two intensity bands have been assigned to O-A-O (E_g) bending and A-O (A_{1g}/F_{2g}) stretching modes, respectively (A corresponding to Y cations)[57]. Raman spectroscopy is a proven technique useful to study the disorder-order transition in pyrochlore materials.

In the B-site of the pyrochlore series, (Ti and Zr) it was shown by Vandenborre that the force fields are transferable, therefore the observed Raman band assignments are derived from previous published results[54]. There were three to four well-resolved Raman bands for the $Y_{2-x}Ti_2Zr_xO_{7+x/2}$ system. The results are in agreement with the literature for pyrochlore based oxides [58, 59]. Figure 41, displays the spectra for compositions in the range of x=0.4 - 1.2 heat treated to 1300˚C for 74 hours representing isothermal conditions. As the concentration of Zr^{4+} increases the peaks at ~320 cm^{-1} significantly decreases followed by a decrease in the 530cm^{-1} peak. Peaks at 450 cm^{-1} experienced some peak broadening as the composition of Zr^{4+} increased. There was also an observed increase in the peak at ~620 cm^{-1}. In Figure 42 for the composition of $Y_{1.6}Ti_2Zr_{0.4}O_{7.2}$ illustrated ordering from a fluorite to a pyrochlore phase up to 1000˚C and agree with our findings in our previous XRD study (Chapter 3). Peak profiles show that peaks intensities become sharp at 1100˚C. After 1100˚C, they broaden and the intensities weaken, therefore indicating that the O-A-O is observing some signs of disordering at this temperature. Figure 43, displays the spectra for x=0.8 in $Y_{1.2}Ti_2Zr_{0.8}O_{7.4}$, at 800˚C there are no observed peaks, however at 900˚C the spectra was well resolved and were also similar to XRD results. The two most intense peaks were at ~320 cm^{-1} and ~620cm^{-1} respectively. As the temperature increased the peak at 620 cm^{-1} decreased and the intensity of the peak at 320cm^{-1} decreased. Peak at ~420cm^{-1} broadened and there was no measurable change in the peak at ~530cm^{-1}. Fig.37, there was no distinguishable peaks for x= 1.2 in $Y_{0.8}Ti_2Zr_{1.2}O_{7.6}$ at 800˚C. At 900˚C there was two large peak observed at ~620 cm-1 and ~420 cm^{-1}. There was no observed peak at ~320cm^{-1} and ~520cm^{-1}. At 1000˚C at peak at approximately 320 cm^{-1} observed. The intensities decreased as there was in an increase in all three peaks to the maximum temperature of 1300˚C when peak at ~320cm^{-1} begins to dominate the

spectrum. The observed Raman frequencies for the spectra of $Y_{2-x}Ti_2Zr_xO_{7+x/2}$ and their peak positions are summarized on Table 4-Table 6. Raman spectroscopy was used to investigate the structural changes as a function of substitutions of Zr^{4+} for Y^{3+}. It was observed that with an increase in the Zr^{4+} content there is a reduction in the O-A-O bonding peak (~310 cm^{-1}). Secondly, as Zr^{4+} increased (Decrease in Y^{3+}) in the system the A_{1g} mode increased. Results show the distinct Raman pyrochlore spectra for compositions when x=0.4 and 0.8 but not when compositions of x in 1.2. As the samples were heat treated from amorphous oxides, structural ordering was detected in $Y_{2-x}Ti_2Zr_xO_{7+x/2}$ for each composition. The results of thermal history are in agreement with the conventional XRD data by showing the crystallization transition temperature after 800°C. However, the difference between the fluorite and pyrochlore phase could not be determined. The disorder at low temperatures, sub 1000°C are caused by Y^{3+} and Zr^{4+} cation randomly occupying the same 4a site. From the results of $Y_{1.6}Ti_2Zr_{0.4}O_{7.2}$ and $Y_{1.2}Ti_2Zr_{0.8}O_{7.4}$ we observe that the pyrochlore spectra in all heat treated samples from 800 to 1300°C. This supports the XRD data from this work that the pyrochlore phase is metastably extended from its stoichiometric composition. Spectra of broad features are indicative of the disorder existing in the oxygen lattice after the partial substitution of Zr^{+4} by Y^{+3} cations and the subsequent oxygen vacancies. Moreover, as the Y^{+3} content increase reflects an increase in the disorder in the material.

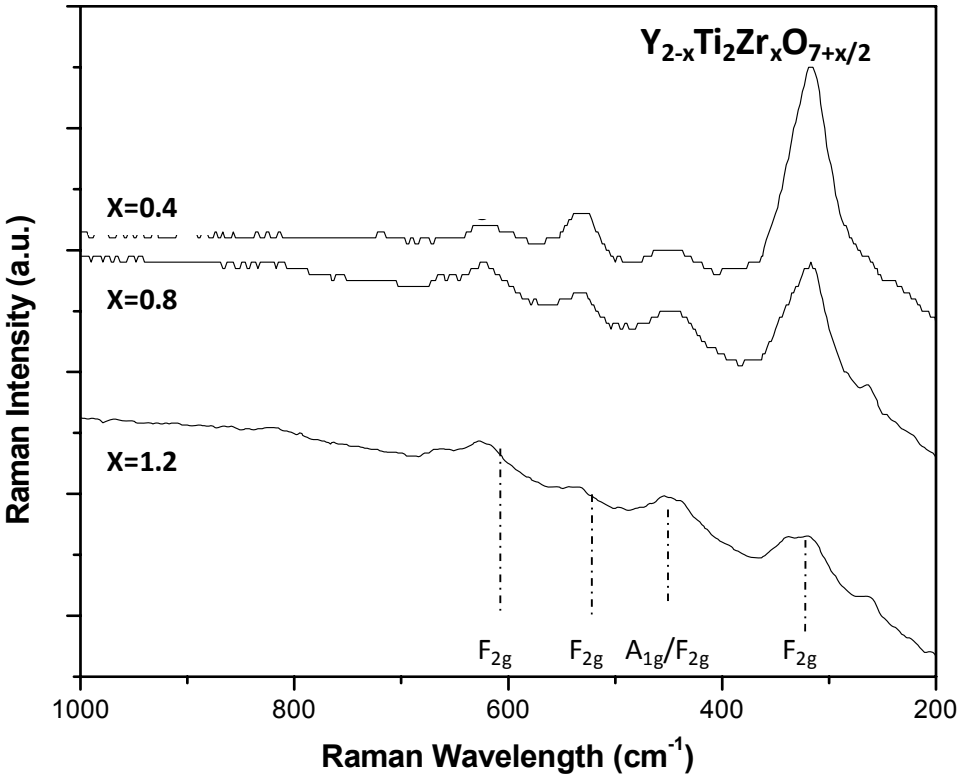

Figure 41 Raman spectra of $Y_{2-x}Ti_2Zr_xO_{7+x/2}$ with Zr^{4+} content increasing from 0.4 – 1.2. Samples were heat treated at 1300°C for 74 hours. (Isothermal conditions)

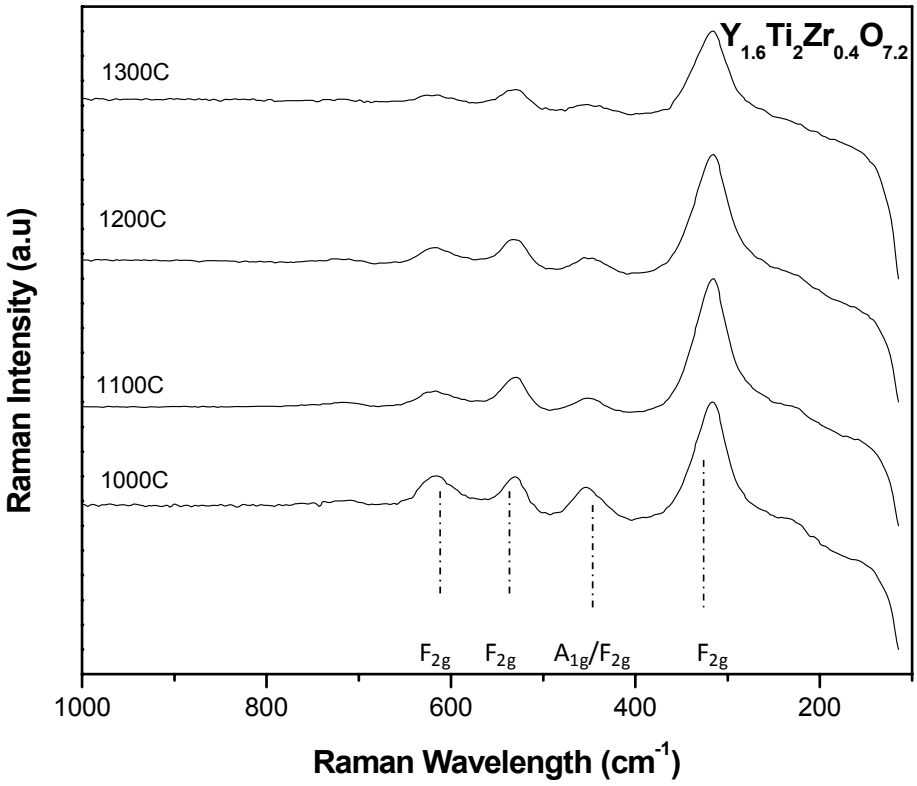

Figure 42 Raman spectra of composition $Y_{1.6}Ti_2Zr_{0.4}O_{7.2}$ from 800 to 1300˚C

Table 4 Observed bands in $Y_{1.6}Ti_2Zr_{0.4}O_{7.2}$ (50Ti40Y10Zr)

Assignment	800˚C	900˚C	1000˚C	1100˚C	1200˚C	1300˚C
			(cm^{-1})			
A_{1g}	—	—	316	316	316	317
F_{2g}	—	—	451	452	451	449
A_{1g}/F_{2g}	—	—	530	530	531	530
F_{2g}	—	—	616	618	618	618

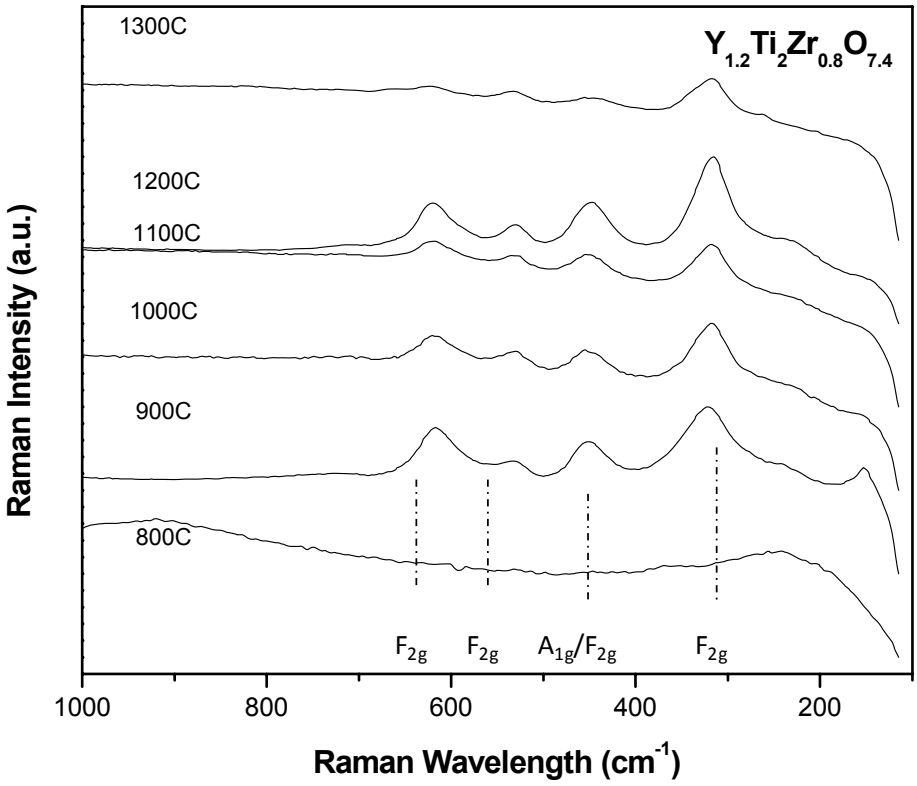

Figure 43 Raman spectra of composition $Y_{1.2}Ti_2Zr_{0.8}O_{7.4}$ from 800 to 1300˚C

Table 5 Observed bands in $Y_{1.2}Ti_2Zr_{0.8}O_{7.4}$ (50Ti-30Y-20Zr)

Assignment	800˚C	900˚C	1000˚C	1100˚C	1200˚C	1300˚C
				(cm^{-1})		
A_{1g}	—	—	321	317	316	317
F_{2g}	—	—	451	456	448	449
A_{1g}/F_{2g}	—	—	531	530	530	533
F_{2g}	—	—	617	619	620	624

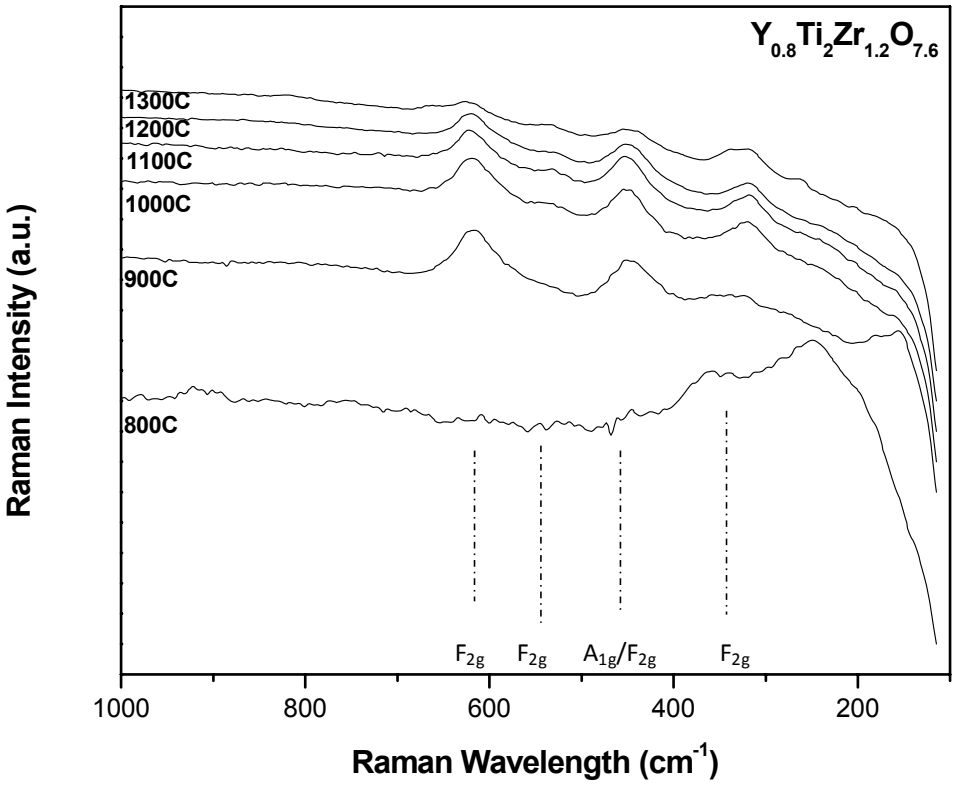

Figure 44 Raman spectra of $Y_{0.8}Ti_2Zr_{1.2}O_{7.6}$ heat treated from 800˚C to 1300˚C.

Table 6 Observed bands in $Y_{0.8}Ti_2Zr_{1.2}O_{7.6}$ (50Ti-20Y-30Zr)

Assignment	800˚C	900˚C	1000˚C	1100˚C	1200˚C	1300˚C
			(cm^{-1})			
A_{1g}	—	324	319	319	319	323
F_{2g}	—	449	450	450	450	450
A_{1g}/F_{2g}	—	—	533	531	532	535
F_{2g}	—	617	620	620	620	626

4.2.5. Short range ordering via Nuclear Magnetic Resonance (NMR)

X-ray diffraction results represent long range order in the solid solution. However, Nuclear Magnetic Resonance Spectroscopy (NMR) studies represent determination of short-range order. NMR was used due to its sensitivity to determine the distribution of the yttrium, titanium, and zirconium cations. Distributions of cations is critical to the understanding the role in conductivity (Ionic conductivity). NMR may be used to identify the different local environments in a solid solution while there is a variation in y, which represents substitution of zirconia for yttria and by phase transformations based on the phase evolution map discussed earlier. This is due to the chemical shifts that may be observed in ^{17}O NMR and its high sensitivity to the oxygen local environments. Contributions to this section were made by John Palumbo from the Department of Chemistry at SUNY Stony Brook. J. Palumbo contributed to the experimentation of the NMR and evaluation of the data. Figure 40 illustrates a NMR spectrum of $Y_{1.2}Ti_2Zr_{0.8}O_{7.4}$ amorphous powder and the same powder heat-treated in a ^{17}O oxygen environment at a temperature of 800°C for one hour. The amorphous peak illustrates that initially the material composition are equally rich with Y-Ti (left) and Y-Zr (right) phase suggesting that the material is predominately amorphous. Without low levels of ordering there is a large hump around 450 PPM. When the material is heat treated for one hour at 800°C, XRD results confirm the fluorite crystal structure and the NMR spectrum we observed a strong peak at 380 PPM. The peak at 380 PPM is associated to Y-Zr bonding for the fluorite phase. As the material is heat-treated, our XRD results confirm that the material transforms to a fluorite crystal phase. The NMR spectrum showed a strong peak at 380 PPM. This peak indicates dominance in Y-Zr; which is associated with the fluorite phase of this composition. Figure 41 shows an amorphous and a heat treated powder of 800°C for one hour for $Y_{1.2}Ti_2Zr_{0.8}O_{7.4}$.

There is an apparent spectral-hump that illustrates the Y-Ti rich and the Y-Zr rich region when the material is in the amorphous state and is in agreement with the XRD results. For heat treated samples the material shows two distinct peaks at 375 PPM and 475 PPM. The peak at approximately 475 PPM corresponds to the fluorite phase while the peak at 375 PPM Y_2Ti_2O corresponds to the pyrochlore phase[53]. XRD results of 700°C heat-treated powder, for static XRD had amorphous and in-situ XRD results indicated start of fluorite phase. However, due to the peak intensity difference between the fluorite and pyrochlore phase, 375 PPM and 475 PPM respectively, the fluorite phase is the most dominant.

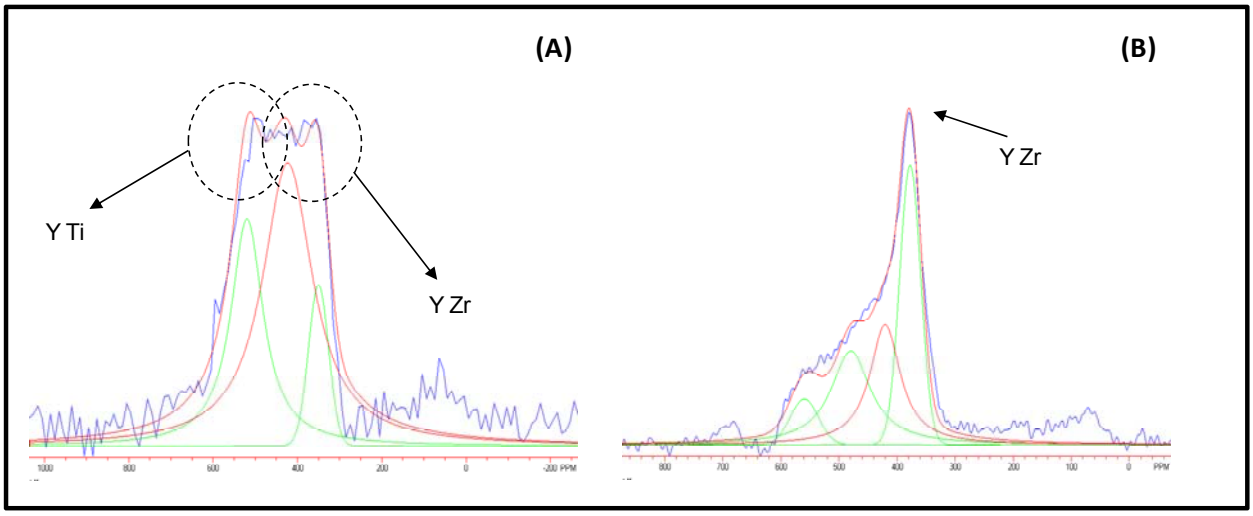

Figure 45 NMR spectrums of $Y_{0.8}Ti_2Zr_{1.2}O_{7.6}$ (A) amorphous powder and (B) heat treated powder at 800˚C/1hr

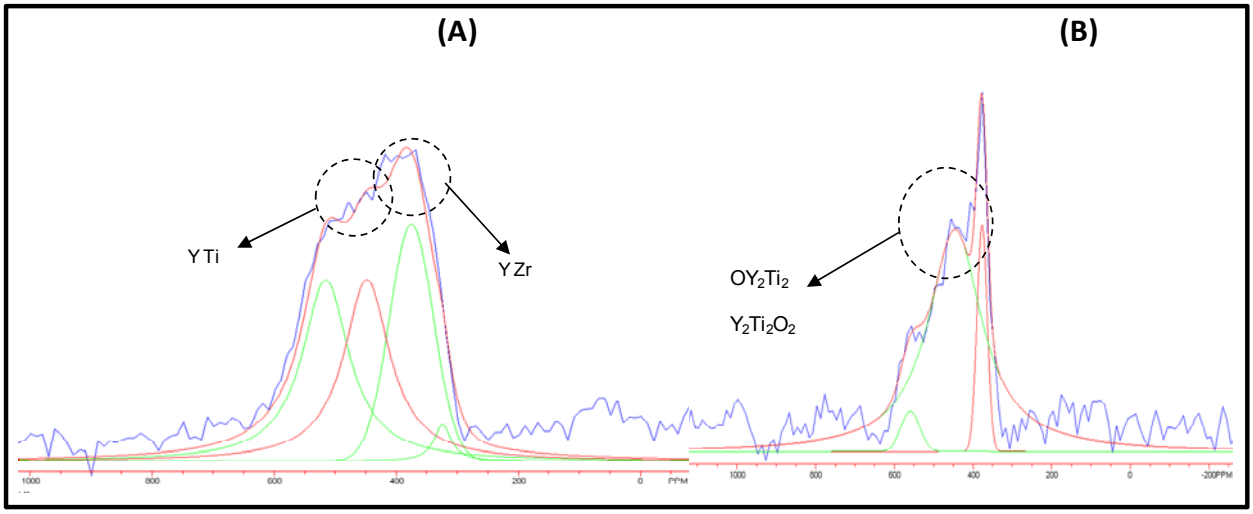

Figure 46 (A) NMR spectra of Amorphous powder of $Y_{1.2}Ti_2Zr_{0.8}O_{7.4}$Illustrates a Y-Ti rich and Y-Zr rich peak. (B)Heat treatment illustrates a dominant Y-Zr rich peak of the fluorite crystal structure

4.3. Summary and Conclusion

This chapter contributed to modifying the theoretical phase diagram by experiments based on detailed phase evolution of select compositions. The experimental results, utilized a combination of *ex-situ* and *in-situ* diffraction methodologies in order to modify the ternary diagram. The *in-situ* diffraction provided the most detailed analysis of long range order for the crystal phase due to sensitivity of the detector and more importantly the synchrotron light source. The cation substitutions essentially are modification of the ionic radii within the pyrochlore phase field that ultimately affect the crystallization behavior of oxides. In addition, short range ordering was detailed by Raman spectroscopy and Nuclear Magnetic Resonance (NMR). The results showed that the preferential local environments of oxide at low temperatures. Thermal conductivity results were promising for oxide compositions near the pyrochlore phase. Initial results showed that thermal conductivity for pressed sintered pellets were lower than the yttria stabilized zirconia oxides. The results are summarized in detail in the following sections.

4.3.1. Transformation Paths in Pyrochlore Region of $Y_{2-x}Ti_2Zr_xO_{7+x/2}$

Time-resolved XRD provided higher resolutions in determining the preferential phase formation for the system of $Y_{2-x}Ti_2Zr_xO_{7+x/2}$. Varying the amounts of x in $Y_{2-x}Ti_2Zr_xO_{7+x/2}$ represents cation substitutions of Y^{3+} and Zr^{4+} in the pyrochlore compound of $Y_2Ti_2O_7$. The higher resolution helped differentiated the pyrochlore from the fluorite phase as well as identify minority phases such as rutile. Detailed phase analysis has contributed to a revision of the ternary diagram as illustrated in Figure 47. The first published ternary diagram

was based on computational modeling in comparison to our experimental results. Results of the phase evolution study contributed to redefined phase fields for compositions in $Y_{2-x}Ti_2Zr_xO_{7+x/2}$ system as they structurally evolved from amorphous materials to their final equilibrium temperatures.

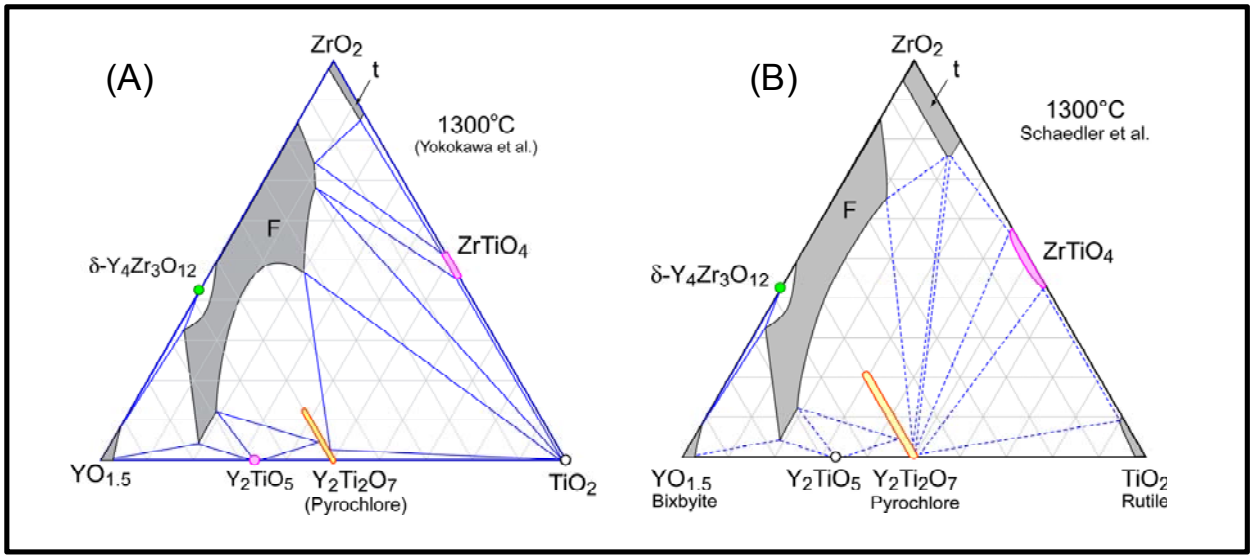

Figure 47(a) First proposed ternary diagram by Yokokawa et al. based on computed theoretical values [29] (b) Modified ternary diagram based on experimental results [60]

Short range order in oxides was studied with NMR and Raman spectroscopy in conjunction with XRD. Results in NMR suggest fluorite structure formation in oxides for low heat treatment. Results in Raman spectroscopy illustrated that increasing Zr^{4+} resulted in increasing in the disorder of the structure. Low Zr^{4+} resulted in spectrums that were pyrochlore like while high concentrations have spectrums indicative of fluorite structures. Thermal conductivity values of approximately 1.6 W/mk were measured for sintered pellets similar to reported values of sintered oxides for $Gd_2Zr_2O_7$, $Nd_2Zr_2O_7$ and

$Sm_2Zr_2O_7$. In comparison, reported values for the commercially available composition of 7YSZ for sintered pellets are approximately 2.3(W (m K)$^{-1}$). Lower values in pyrochlore oxide are promising as a material candidate in thermal barrier coatings.

4.4. (B) Tetragonal oxides compositions in Y_2O_3-ZrO_2-TiO_2 system

4.4.1. Transformation Paths in YSZ and YSZ with Titania Additions (Ti-YSZ)

For thermal barrier systems, novel materials must address fundamental issues that will improve current high temperature stability and/or lower the thermal conductivity. This section focuses on the single phase of tetragonal oxide in $YO_{1.5}$-TiO_2-ZrO_2. We investigate the high temperature stability of zirconia with additions of TiO_2 with the composition of 7.6 $YO_{1.5}$ – 15.2 TiO_2 – 77.2 ZrO_2 within the equilibrium phase field. Motivation is placed on the phase evolution in powders as well as the resistance of the oxides to partitioning from metastable tetragonal (t') phase into the equilibrium phase proposed by the ternary diagram by Yokokawa. Based on prior literature, durability of thermal barrier coatings has been based on high toughness[61]. Research has shown that the additions of TiO_2 affect the mechanical properties of 7YSZ TBC materials[62]. In the case of single phase tetragonal 7YSZ there are reports that there is a two-fold increase in toughness with additions of dopants such as TiO_2. The ternary diagram of TiO_2-Y_2O_3-ZrO_2 provides excellent opportunities to investigate novel compositions that have both the tetragonal phase of zirconia oxides with TiO_2 additions. One particular composition that satisfies the tetragonal phase and addition of TiO_2 is 7.6 $YO_{1.5}$ – 15.2 TiO_2 – 77.2ZrO_2. Zirconia doped with yttria and one or more rare earth oxide has been proven to be a strong candidate in lowering the thermal conductivity values of novel thermal barrier coatings. Current research for TBC materials utilizes the standard partially stabilized zirconia (7YSZ) compositions (~7.6 mol% $YO_{1.5}$) with rare earth oxides additions. The standard molar composition (7.6YSZ) retains the metastable tetragonal

single phase when deposited on thermal spray or EB-PVD instead of the tetragonal and cubic phase dictated by the equilibrium binary diagram.

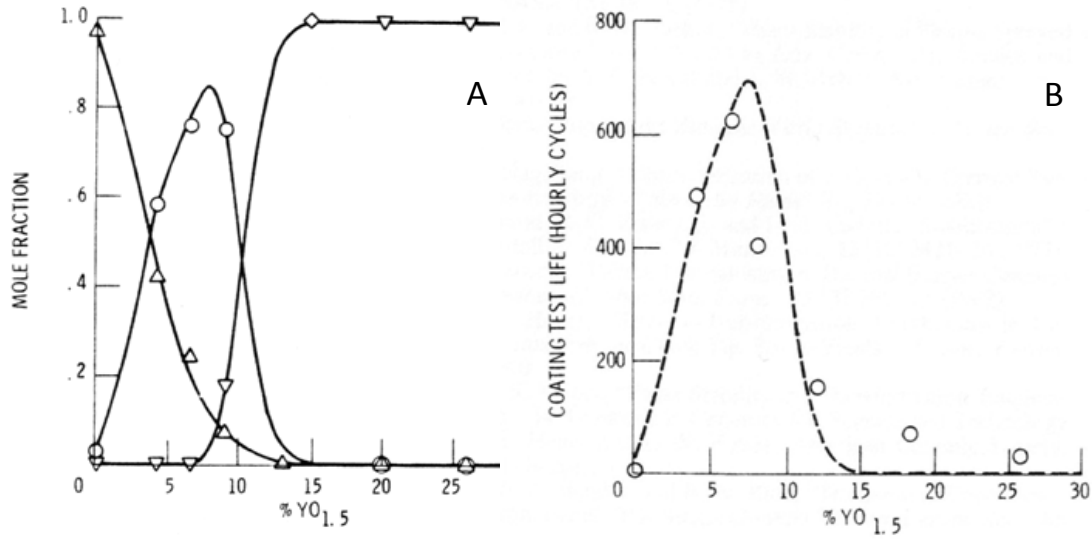

Figure 48 Figure (A) Calculated mole fraction of monoclinic (▲)cubic(▼))and tetragonal phases (○) Figure (B) coating life cycle test versus mole faction of $YO_{1.5}$ [63]

Miller et al reported that in thermal barrier coating materials, the mole fraction of $YO_{1.5}$ was related to optimal coating life cycles[63]. Figure 48 (A) are calculated mole fractions for monoclinic, tetragonal and cubic phases of zirconia doped with yttria ($YO_{1.5}$) mole percents from 0 to 25%. The yttria content and the monoclinic, cubic and tetragonal mole fractions correspond to the binary phase diagram of $YO_{1.5}$-ZrO_2. The results correspond to the binary phase diagram for $YO_{1.5}$ and ZrO_2. In figure 47 (A), as $YO_{1.5}$ is in the range of 5-10 mol%, the tetragonal phase is at a maximum. In Figure 48 (B) within the range of 5-10 mol% $YO_{1.5}$ displayed the highest coating life. Millers finding illustrated the relationship of the tetragonal phase and coating performance. The results from this study by Miller contributed to our understanding of the effect of yttria molar percentage on coating life in plasma sprayed coatings. Optimized coatings based

on life cycle; increase coating life by slowing the destructive transformation from cubic to the equilibrium phase of tetragonal and monoclinic. The microstructure may also be driven to its equilibrium two-phase system when it is exposed to temperatures at or greater than 1200˚C.

4.4.2. Enhanced Toughness in Zirconia Oxide Systems

There have been significant advances in improving coating durability of thermal barrier coatings. However coatings are still susceptible to various types of damage including erosion, oxidation and attack from environmental contamination. Impact damage may eventually cause spallation and loss of the thermal barrier coating. Accordingly, it would be desirable to improve the impact resistance of thermal barrier coatings to avoid spallation. Thus, a major limitation in ceramic structures is their poor fracture toughness. The fracture toughness of brittle materials depends on the interactions of the crack tip stress field with microstructure. Toughening mechanisms are classified in two areas: (1) process zone around crack tip (by modifying compositionally and raising intrinsic properties) (2) crack bridging by reinforcements (fibers, whiskers, particulates, etc). Process zone mechanisms are considered raising the intrinsic properties. In thermal spray coating of zirconia oxide systems, structures have the tetragonal prime phase. The tetragonal prime phase is formed by a cubic-tetragonal displasive transformation which is known to be a ferroelastic transformation. Crystallographically the t′ phase is identical to the tetragonal phase, but the morphology is distinctly different. In the tetragonal prime phase grains consist of domains in three mutually orthogonal directions wherein the domain is on the order of 0.1 um or less. The extremely fine size of the domains makes the tetragonal prime phase highly resistant to martensitic transformation.

The tetragonal prime phase has the unique attributes of excellent resistance to destructive martensitic transformation which is common in large grained tetragonal phase materials, excellent toughness, good strength and excellent creep resistance in comparison to tetragonal phase materials[64]. Transformation toughening occurs when metastable retained t-ZrO_2 transforms to the monoclinic ZrO_2 phase in the tensile stress field around a propagating crack. The volume expansion of (4-5%) characteristic of the t-m transformation induces a net compressive stress in the process zone around the crack tip. This reduces the local crack stress intensity and hence the driving force for crack propagation therefore increasing the effective toughness of the material. The transformability is generally understood as the ability of the t-ZrO_2 to transform to m-ZrO_2 in the crack tip stress field. The additions of the trivalent-ZrO_2 stabilizers such as Y_2O_3, Tb_2O_3 and Gd_2O_3 increases the tetragonal zirconia lattice constant in a-axis and decreases the c-axis. Decrease in the c/a ratio (tetragonality) of tetragonal zirconia with Y_2O_3 content decreases the ratio of the room temperature tetragonal lattice parameters of c and a axes (c/a). The decrease in c/a ratio of t-ZrO_2 with Y_2O_3 is consistent with the increase in the stability of Y-TZP which is related to the difficulty of the t-m transformation. Therefore, the results suggest that an increase the c/a ratio caused an increase in the fracture toughness. The currently used 7YSZ composition has a single-phase tetragonal prime phase with a tetragonality (ratio of c-axis to a-axis lattice dimensions) of c/a-1=1.1%. In the binary system of $YO_{1.5}$-ZrO_2 compositions with high yttria concentrations/Cubic-phase (20 mol.% YSZ) have toughness values of approximately of $\Gamma = 6\ Jm^{-2}$. Tetragonal phase compositions (4 mol.% YSZ) have the highest fracture toughness values of $\Gamma \cong 210\ Jm^{-2}$. Seven mol. % YSZ has been found to experimentally have toughness values of 45-150 Jm^{-2}. Recently, ferroelastic domain switching has been recognized as an additional toughening

mechanism in zirconia ceramics containing t'ZrO_2[65]. The tetragonal prime phase, a product of c-ZrO_2, is non-transformable and has a poly-domain structure with each domain having tetragonal structure symmetry. The c-axis of each tetragonal domain can lie along any of the three <100> axes of the parent c-ZrO_2 phase. Ferroelastic toughening differs from stress induced transformation in that there is no change in the crystal structure[66, 67]. However, there is a reorientation of the ferroelastic domains. Ferro elastic toughening occurs when an unstrained material has equal proportions of domains with the orthogonal variants separated by 90° (110) twin boundaries. When the material is loaded unidirectionally one set of variants can switch orientations. It has been found that the switching is irreversible resulting in permanent strain. The presence of a crack may cause one of these variants to switch and cause an associated toughening of the material. In ferro-elastic toughening when the material is under stress, the domains can reorient their c-axis direction better to accommodate the ferroelastic strain. Dissipated energy will reduce the crack tip stress resulting in the toughening of the material. When a tensile stress, coercive stress, is applied along the crystallographic a-axes, causes it to become the c-axes.

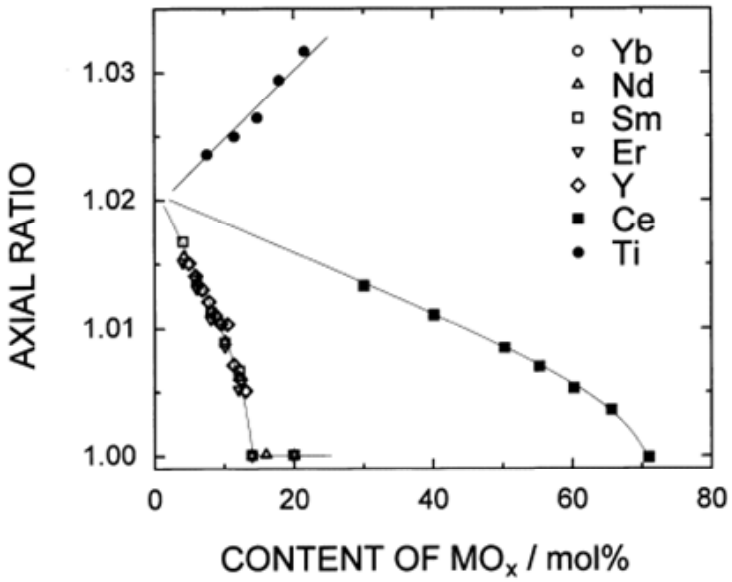

Figure 49 Relationship between c/a axial ratio and the composition in ZrO_2-R_2O_3, ZrO_2-CeO_2, and ZrO_2-TiO_2 binary systems [2]

Figure 49 shows the compositional dependence of the c/a axial ratio of tetragonal zirconia in the system of ZrO_2-R_2O_3, ZrO_2-CeO_2, and ZrO_2-TiO_2. In binary systems the reduction of the c/a ratio results in the stabilization of the cubic zirconia. Increase in the tetragonality is a result of stabilization of the tetragonal zirconia structure. The phase stability of the cubic zirconia structure is proposed to be a function of the reduction of coulomb electrical repulsive forces between neighboring oxygen ions with doping of cations[2]. Research by N. Shibata found that doping of Re^{3+} ions results in the decrease of coulomb electrical repulsive force, fc[2]. With doping with Ti^{4+} ions tend to increase the coulomb electrical repulsive force. The reduction is presumed to be a result of the electric repulsive force between neighboring oxygen ions is relaxed with the addition of Re^{3+} or Ce^{4+}. One of the first observations correlating tetragonality and toughness was reported in a patent by T. Tien et.al[68]. He reported a method for improving the ease of transformability of the tetragonal to

monoclinic phase in stabilizing t-ZrO_2 polycrystals by adding an amount of transition metal oxide sufficient to cause the ratio of the lattice parameters to increase. The stabilizing agent is Y_2O_3 and the toughening agent is Ta_2O_5. The ternary diagram is presented in Figure 50 for $TaO_{2.5}$-ZrO_2-$YO_{1.5}$. Martensitic transformation (T→m) may be induced by cooling (thermal) or by external loading (stress) under isothermal conditions. (1) Thermal induced transformations will dictate the amount of tetragonal phase that may be retained by thermal cycling. (2) Stress induced martensitic transformation enhances the toughness of zirconia ceramics. The transformation of t→m takes place in two stages. The first stage is the transition of the lattice structure from tetragonal to monoclinic by shear displacement. The second stage involves diffusional migration of oxygen to oxygen sites in the monoclinic lattice. The fracture toughness and the impact resistance performance have been found to be related to zirconia lattice stability equivalent based on the calculated zirconia lattice parameters c and a using the equation.

$$\frac{c}{a} = k_1 \sum_i (r_i - r_{Zr}) \times m_i + k_2 \sum_i (V_i - V_{Zr}) \times m_i \qquad (24)$$

Where c and a are the zirconia lattice parameters, r_i is the ionic radius of the first metal oxide, v_i is the metal ion (volume) of the metal oxide added, m_i is the molar fraction of the metal oxide added and k_1 and k_2 are constants[69]. The prior studies are based on pre-existing domains capable of switching in the crack field. Current studies by C. Mercer et al. have found through microscopy studies that there are no visible domains in APS or vapor deposited coatings for tetragonal prime YSZ[65]. Mercer found that in sintered materials that the domains found the toughening mechanism is possibly due to the nucleation of domains rather

than pre-existing domain boundaries. Mercers work illustrated that oxides with high levels of tetragonality have the potential of higher toughness than t' 7YSZ.

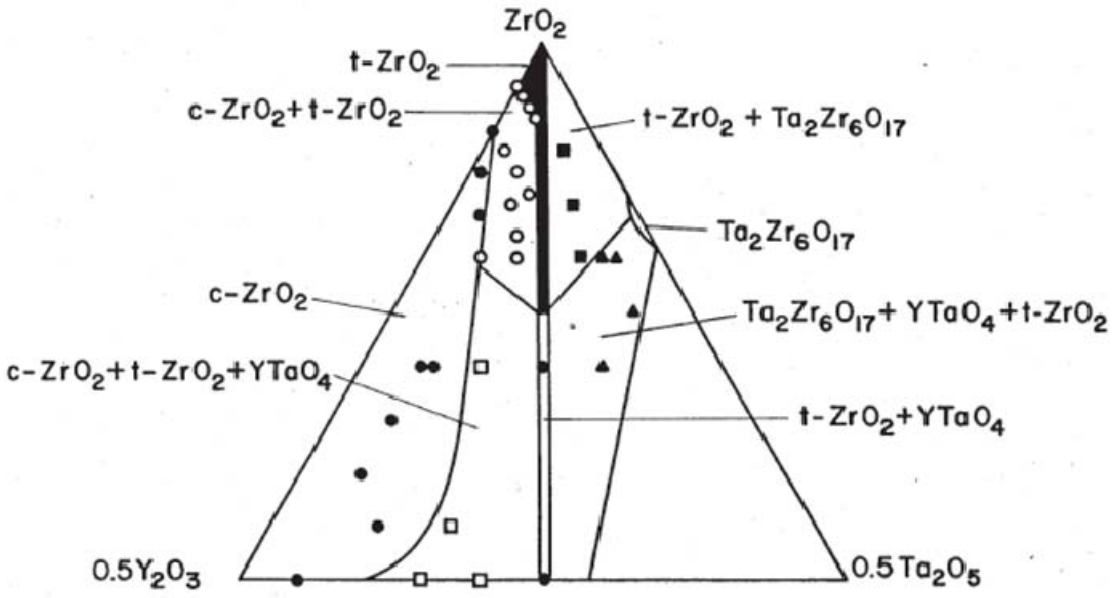

Figure 50 $YO_{1.5}$-ZrO_2-$TaO_{2.5}$ ternary phase diagram. Single phase tetragonal zirconia with enhanced toughness in comparison to YO1.5-ZrO2 was observed in this system.(1300C)[68]

In the proposed ternary diagram of $YO_{1.5}$-TiO_2-ZrO_2 on Figure 51 the tetragonal phase is found with TiO_2 concentrations from 0-20 mol%. Of particular interest is the composition 7.6% $YO_{1.5}$- 15.2% TiO_2 - 77.2% ZrO_2; where at equilibrium conditions falls within the tetragonal phase. The motivation for this chapter is to determine if the tetragonal phase in $YO_{1.5}$-TiO_2-ZrO_2 can be used as a thermal barrier coating. Unresolved issues include the destabilization of the tetragonal phase and the resistance to partitioning of the metastable tetragonal phase (t')[70]. In this dissertation, the experiments are based on preparing powders by soft-chemistry methods. Precipitation processing method produces powders that are initially supersaturated single-phase solid solutions. There are no published reports on the transformation paths in the tetragonal phase of

$YO_{1.5}$-TiO_2-ZrO_2. The addition of TiO_2 requires further research to investigate the transformation paths. Secondly, we need to further our understanding of the effect of the TiO_2 on the stability range of the different polymorphs. One of the advantages of titanium oxide is that it exhibits solid solubility in zirconia. Current research is investigating the effects of these additions on the transformation toughening mechanism and mechanical properties of the material. One of the main areas of interest is the resistance to the destabilization of the tetragonal phase.

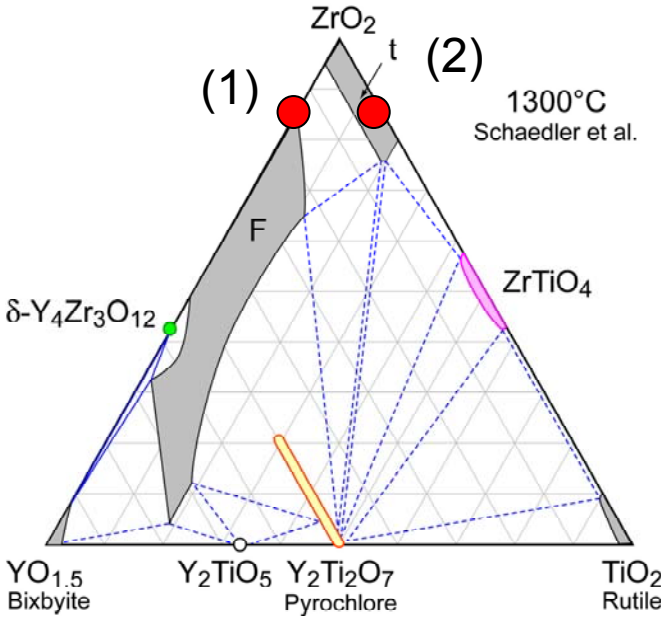

Figure 51 Equilibrium phase diagram of $YO_{1.5}$-TiO_2-ZrO_2 at 1300˚C. Compositions of interest: (1) 7.6 mol% $YO_{1.5}$. (2) 7.6 $YO_{1.5}$ – 15.2 TiO_2 – ZrO_2 mol%.

Summary of literature review for the TiO_2 in functional oxide YSZ:

- One of the main areas of interest is the resistance to the destabilization of the tetragonal phase and resistance to low temperature ageing
- Extended solid solubility in zirconia with corresponding co-dopants
- TiO_2 addition has been shown to effect the electrical properties of yttria stabilized zirconia through the reduction in the mobility of oxygen vacancies
- TiO_2 addition has been shown to affect the mechanical properties of YSZ thermal barrier coatings by effecting increasing durability in comparison to YSZ (Doubles the toughness compared to 7.6YSZ)
- TiO_2 effects the sintering, phase stability and room temperature mechanical properties

4.5. Results and Discussion

Compositions of 7.6 mol% $YO_{1.5}$ and 7.6% $YO_{1.5}$- 15.2% TiO_2 - 77.2% ZrO_2 were synthesized by precipitation methods as described in chapter three. The results are divided into low temperature synthesis and phase evolution of oxides to its equilibrium temperature. The results in this chapter contributed to our understanding of structural transformations in the material system by thermal analysis and detailed structural analysis. Therefore, the results contribute from the basis of a more complete understanding of effect of starting material and the effect of co-doping in zirconia in comparison to the commercially available 7.6 mol% $YO_{1.5}$.

4.5.1. Thermal Analysis

Thermal analysis measurements, via DSC results presented the percent weight loss as well as exothermic/endothermic reactions for Ti-YSZ and YSZ oxides synthesized from precursors from ambient to 1200˚C. The DSC spectrum for Ti-YSZ, Figure 52 showed a 50% weight loss for the precipitation prepared oxides at approximately 400˚C. Following this temperature, the weight loss is stabilized indicating decomposition of the organics. Endothermic peaks at ~250˚C indicate decomposition and vaporization of organics. The observation of an exothermic peak at 675˚C signified a transition from an amorphous to fluorite phase. The crystallization temperature from amorphous to the fluorite phase occurred at approximately 675˚C. Post 675˚C, there were no exothermic or endothermic peaks observed. A small exothermic peak was observed at approximately 500 C. The results are in agreement to XRD crystallization for the transition temperature from amorphous oxide to a crystalline oxide. Additionally, exothermic at 270˚C indicates oxidation of organics.

Figure 53 is the DSC spectrum for YSZ precursor powders without pyrolysis. YSZ samples lost approximately ten percent of its starting weight after 600 ˚C. Most of the organic compounds were evaporated at temperatures less than 300 ˚C. A small exothermic peak was observed at approximately 550 ˚C. The results are in agreement with XRD for phase transformation from an amorphous to a fluorite structure.

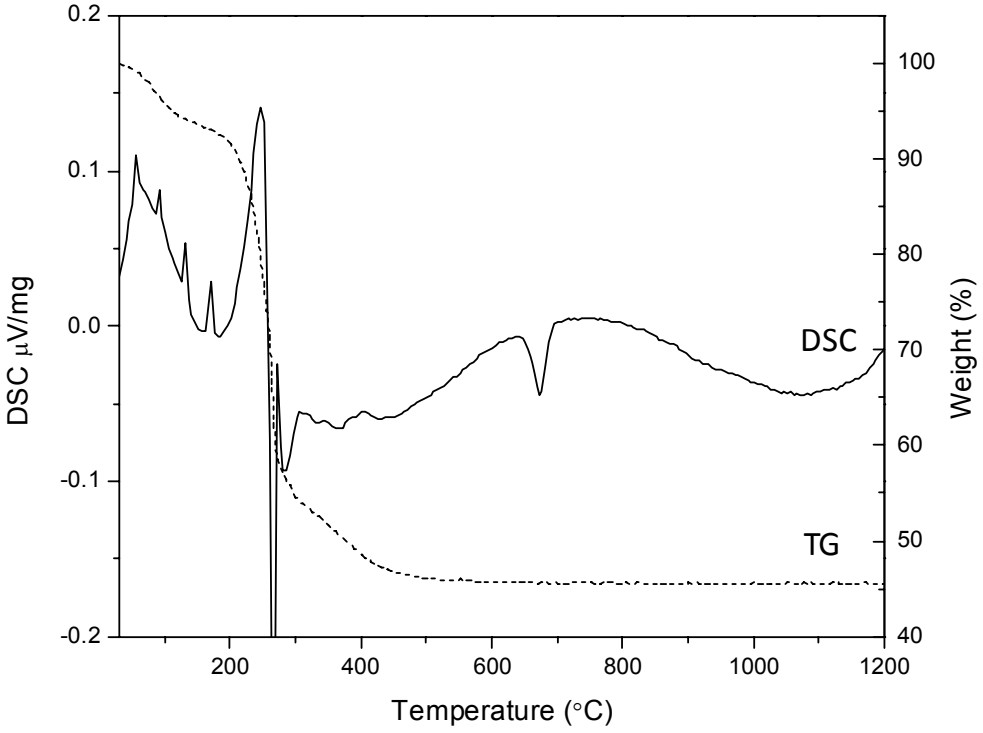

Figure 52 DSC and TG spectra for precipitation derived Ti-YSZ powders. Samples heated from ambient to 1200˚C at a heating rate of 10˚C/min. Exothermic peak observed for a phase transition at 675 ˚C.

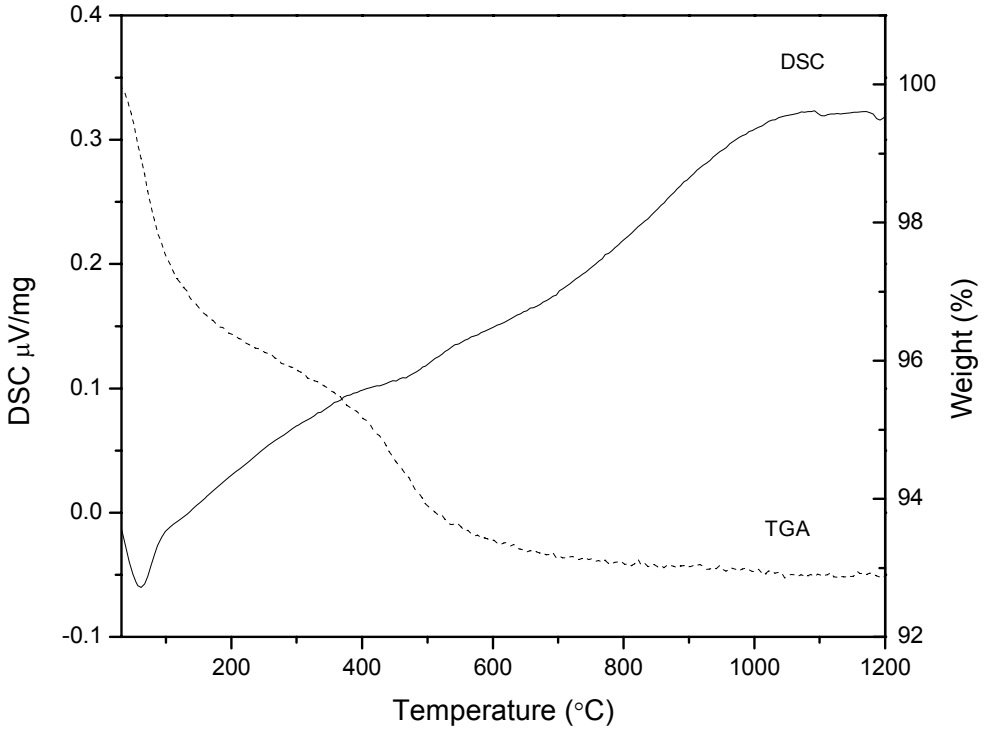

Figure 53 DSC and TG spectra for precipitation derived YSZ powders. Samples heated from ambient to 1200˚C at a heating rate of 10˚C/min. Small exothermic peak for phase transition detected at approximately 500 ˚C.

4.5.2. Partitioning Kinetics in Oxides of YSZ and Ti-YSZ

Phase evolution of heat treated powders for 7.6 mol% $YO_{1.5}$ and $7.6YO_{1.5}TiO_2$-ZrO_2 were investigated by XRD. The sintered powders were exposed to short time scales at temperature followed by quenching in air. The powders were also left at equilibrium temperature (1500˚C) under isothermal conditions to determine the final crystals structure. The diffraction patterns were analyzed extensively in the (111) and the (400) regions. The (400) region was selected because it is specific to the non-equilibrium phase; the region around (111) pertains to observations of second phases such as monoclinic and/or rutile. Figure 54 shows the XRD spectrums for powders prepared by reverse co-precipitation processing heat treated at temperature and rapidly quenched in air. Prepared powders were amorphous after 600˚C for one hour. At 700˚C, powder materials began to crystallize into the cubic fluorite phase. The observed (200) and (220) peaks are broad. The monoclinic peak at (111) was not identified at this temperature. At 1100˚C, a shoulder on the cubic fluorite (200) peak was observed. At 1300˚C it is clear that there is a split of the (200) (220) and (311) peaks. The c(200) peak splits into the (110)t' tetragonal peaks while the crystallographic cubic peak at (220), splits into the (200)t'. We also observe the c(311) splits into the tetragonal t'(211). Results suggest that the reverse co-precipitated prepared powders at 1300˚C are a combination of both the tetragonal and cubic phase. Figure 54 is a compilation of heat treated powder samples for XRD full spectrums of Ti doped YSZ powders prepared from the reverse co-precipitation powders. After the powders were pyrolysis at 600˚C, the observed structure was amorphous. After a heat treatment of 700˚C, the crystalline cubic-fluorite phase was observed. This was indicated by the observed broad peaks at (111) (200) (220) and (311). There was a considerable reduction in the amorphous hump at 1100˚C by narrow peak widths. At 1300˚C,

no monoclinic or tetragonal peaks were observed. The structure is primarily the cubic fluorite phase. At high temperature, 1400˚C for 24 hours, XRD indexed peaks revealed that the structure was cubic, tetragonal and monoclinic. In comparison, YSZ held at temperature for 24 hours revealed that the powders were crystalline and were primarily cubic phase (Figure 56).

$$\xrightarrow{600^{\circ}C}\ Amorphous\ \xrightarrow{900^{\circ}C}\ Cubic\ \xrightarrow{1100^{\circ}C}\ Tetragonal\ \xrightarrow{1300^{\circ}C}\ Tetragonal + Cubic$$

Both YSZ and Ti-YSZ follow the partitioning kinetics from amorphous to cubic at 900˚C. Following this transition, the non-transforming tetragonal phase was detected at 1100˚C. With further heat treatment, the cubic and tetragonal phase was detected.

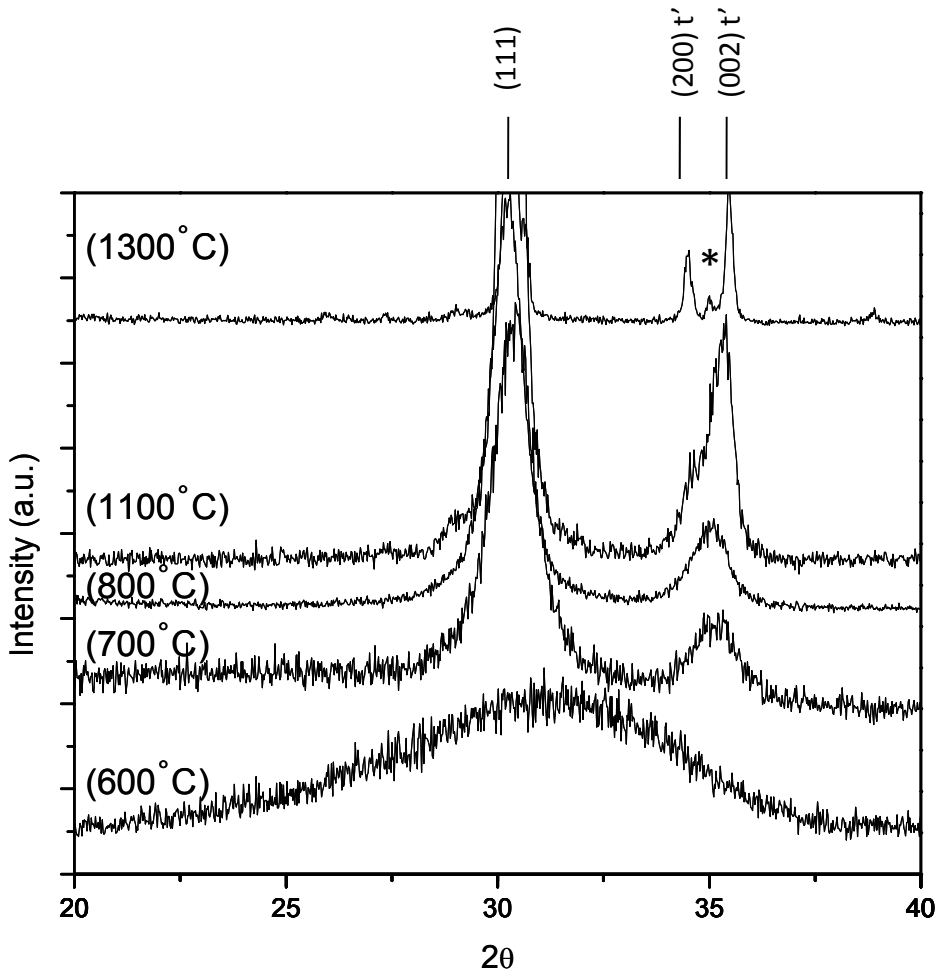

Figure 54 Phase Evolution of YSZ prepared by precursor processing for powders heat treated for temperatures between 600-1300°C

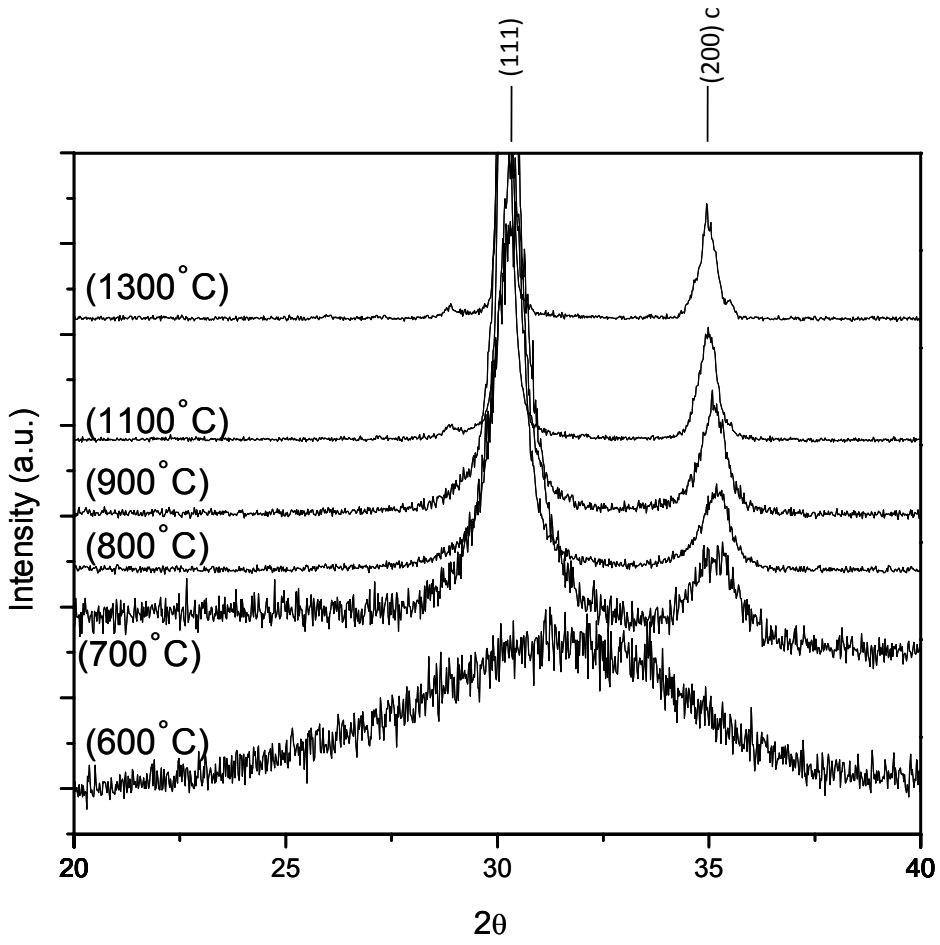

Figure 55 Phase Evolution of Ti-YSZ prepared by precursor processing for powders heat treated for temperatures between 600-1300˚C

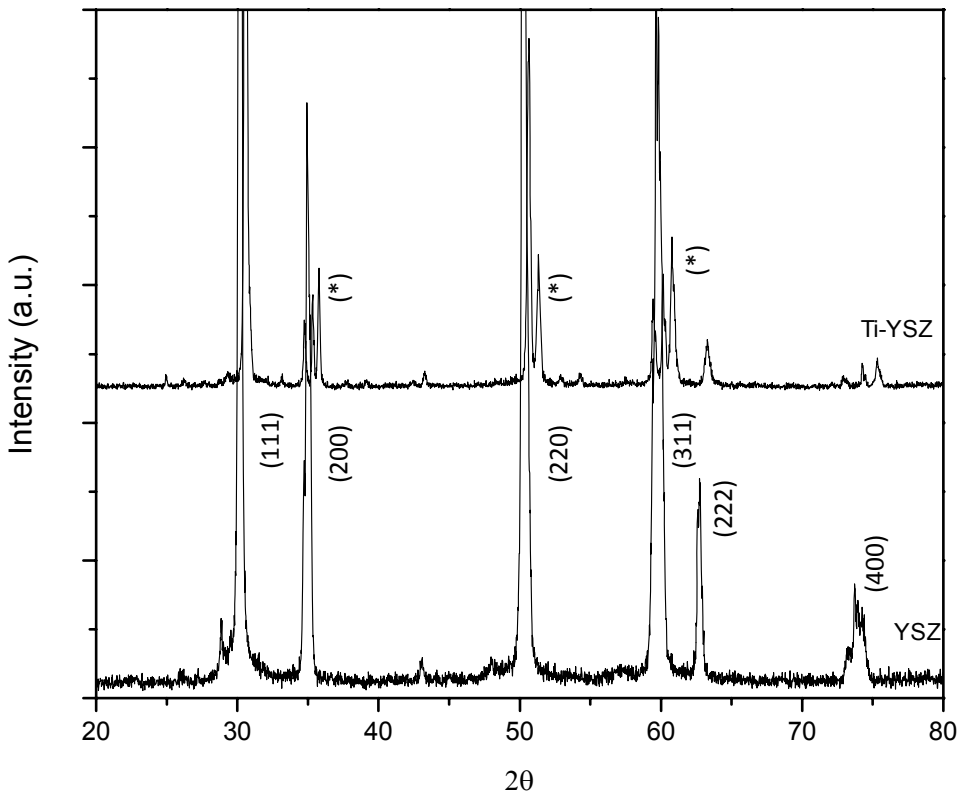

Figure 56 20-80˚ XRD spectrum heat treated to 1400˚C for 24 hours: Bottom YSZ; Top Ti-YSZ ((*) indicated tetragonal phase)

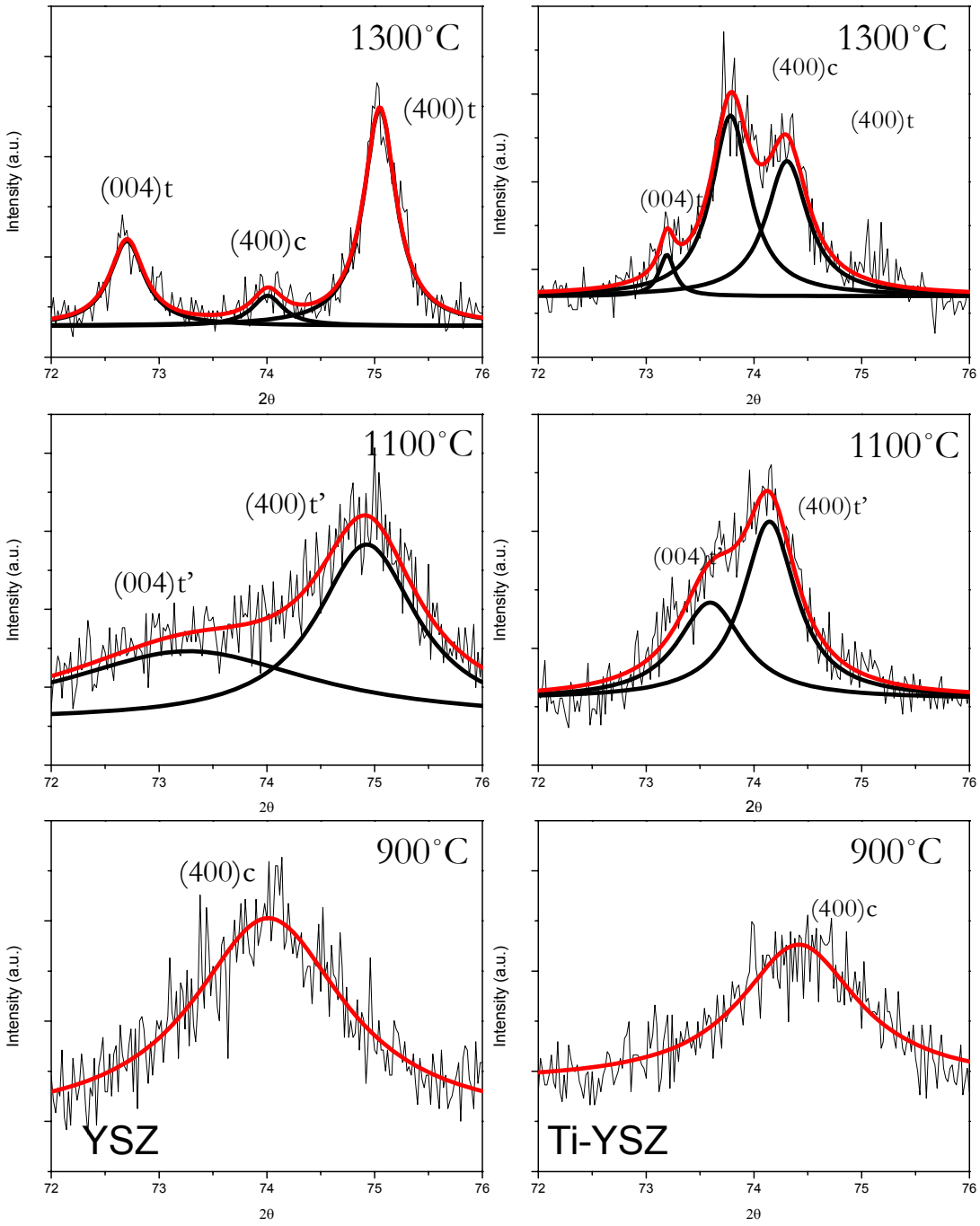

Figure 57 Phase evolution in YSZ and Ti-YSZ powders by XRD in the (400)/(004) region 72-76°

Table 7 Lattice parameter values and identified phases in heat treated YSZ and Ti-YSZ powders

Powder Heat treatment	Identified Phase	$d_t(400)$ (A)	$d_t(004)$ (A)	c (A)	a (A)	c/a (A)
YSZ1300	C+t	1.264	1.299	5.20	5.06	1.028
YSZ1100	t'	1.266	1.292	5.17	5.07	1.020
YSZ 900	C	-	-	-	-	-
TiYSZ1300	C+t	1.275	1.292	5.16	5.09	1.013
TiYSZ1100	t'	1.277	1.286	5.14	5.10	1.007
TiYSZ900	C	-	-	-	-	-

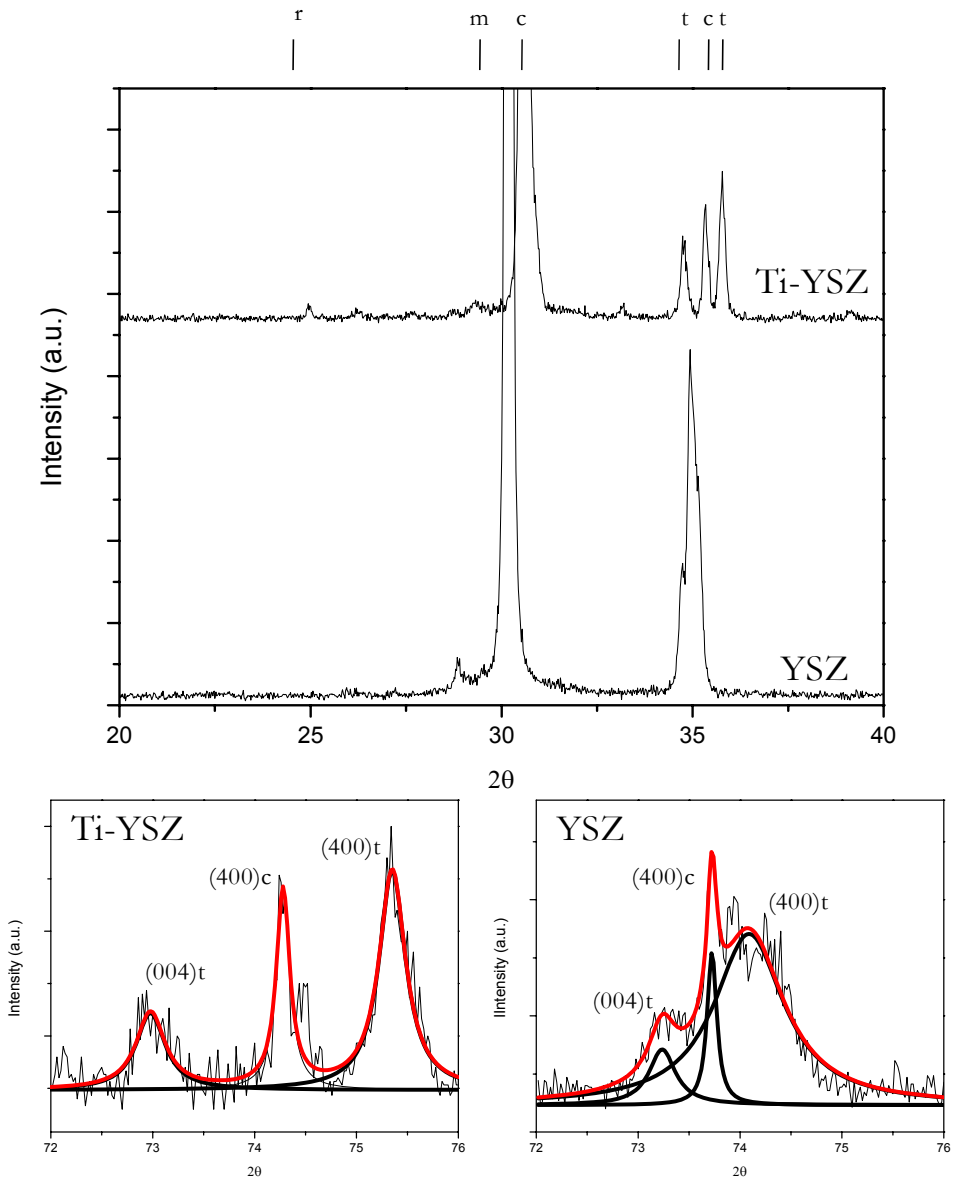

Figure 58 Powders heat treated to 1400˚C for 24 hours (A) 20-40 degree XRD spectrum for YSZ (bottom) and Ti-YSZ top (B) 72-76 degree for Ti-YSZ (C) 72-76˚ for YSZ

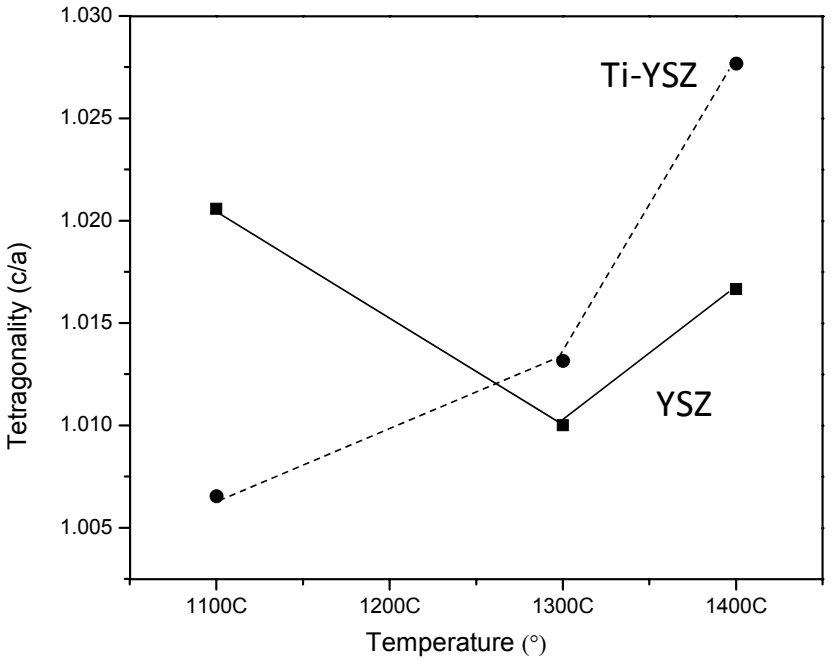

Figure 59 Tetragonality (c/a) versus temperature in precursor derived powders. Linear relationship for tetragonality in Ti-YSZ with increase in temperature.

4.6. Conclusion (Pyrochlore Oxides, YSZ and YSZ with TiO_2 additions)

4.6.1. Pyrochlore Oxide

In this chapter a combination of structural analysis techniques comprising of XRD (static and in-situ), Raman spectroscopy and NMR were used to investigate cation substitutions in the ternary system of $YO_{1.5}$-TiO_2-ZrO_2. The resulting XRD spectrums were used to derive phase evolution maps for compositions of interest. The soft-chemistry method of precipitation processing was used to produce amorphous starting oxides with the objective of studying phase formation and crystallization kinetics of oxide compositions. Precipitation processing methods ensured that we have homogenous chemistries for the oxides investigated in this study allowing for the observation of phase formation from amorphous to equilibrium temperatures. Our findings contributed to a modification of the original ternary diagram proposed by Yokokawa. We selected multiple compositions in the ternary system $YO_{1.5}$-TiO_2-ZrO_2. The first series of compositions represented substitutions of B-cations in $Y_2(Zr_yTi_{1-y})_2O_7$. .The second series of compositions represented substitutions of A and B cations in $Y_{2-x}Ti_2Zr_xO_{7+x/2}$. At low temperatures of crystallization we observe preferential ordering in oxides. All compositions near the pyrochlore regions crystallized from an amorphous to fluorite phase. The results for compositions for the tie line $Y_2(Zr_yTi_{1-y})_2O_7$ were similar to the phase fields projected by Yokokawa, however for compositions of $Y_{2-x}Ti_2Zr_xO_{7+x/2}$ the phase fields were different due to multiple competing phase scenarios. The novel ternary diagram is presented in Figure 47. We are motivated by the phase evolution results because the pyrochlore phase can be metastably extended beyond the narrow composition in the stoichiometric composition. Furthermore, the results are promising because changing level of disorder in anion and cation sites while

preserving pyrochlore structure allows for the measurement of multiple properties including ionic and thermal conductivity. We also are encouraged by low thermal conductivity in oxide compositions comparable to other pyrochlore systems such as $La_2Zr_2O_7$ and $Gd_2Zr_2O_7$. Our results found that the fluorite and pyrochlore phase are capable of achieving thermal conductivity values less than 1W/mk for sintered oxides.

Summary of pyrochlore oxide structural investigation:

- Low thermal conductivity results are attainable in the pyrochlore structure. ($Y_{2-x}Ti_2Zr_xO_{7+x/2}$.)
- Phase evolution for powders in pyrochlore regime of $Y_{2-x}Ti_2Zr_xO_{7+x/2}$ was determined
- The high temperature stability range of the pyrochlore phase was also determined for selected composition (approximately 1200˚C)
- Measure properties for non-equilibrium phases
- Extended solid solution of pyrochlore away from stoichiometric compositions

4.6.2. Yttria Stabilized Zirconia (YSZ) and Co-doped with Ti^{4+} (Ti-YSZ) Oxides

Structural analysis was performed on oxides prepared by a soft chemistry method, precipitate processing, yielding in amorphous starting oxides. As a benchmark and industrial thermal barrier coating material, the molar ratio of 7.6 mol. % $YO_{1.5}$ stabilized zirconia was thoroughly investigated. Ti-YSZ with the following molar ratios ($7.6YO_{1.5}$-$15.2TiO_2$-$77.2ZrO_2$) was investigated by x-ray diffraction and differential scanning caliometry. The Results were compared to the industrial standard of YSZ with the molar ratio of 7.6 mol% $YO_{1.5}$. Structurally, the addition of titania reduces the crystallization temperature. XRD results indicate that the addition of titanium lowers the crystallization temperature of the system. Soft chemistry methods of precursor processing resulted in starting amorphous oxides. Both YSZ and Ti-YSZ crystallized from an amorphous to the cubic phase. Ti-YSZ results indicate that there were two phases, tetragonal and cubic. At high temperature, we are capable of observing that the YSZ powders, destabilized to primarily the cubic phase. However, the Ti-YSZ powder remained the tetragonal crystal structure. This suggest that cubic structure is either in a two phase system or that kinetically, titania constrains the cubic phase.

Summary of tetragonal oxide structural investigation:

- The addition of Ti^{4+} increased the transformability in heat treated powders
- Results indicate slower partitioning in Ti-YSZ powder compared to YSZ
- In the isothermal heat treatment of 1400°C for 24 hours, the tetragonal phase remained. However, at the same temperature and time constraints; YSZ destabilized to the cubic structure

4.7. Summary of Phase Evolution in Oxides

Detailed phase evolutions data for compositions in the $YO_{1.5}$-TiO_2-ZrO_2 system are reported. The investigated compositions reflect candidate material systems and as a benchmark, 7YSZ. The motivation was to investigate phase stability in a highly unexplored ternary system. The initial investigation of phase stability for YSZ and Ti-YSZ was promising. From amorphous oxides, powders for both systems had the tetragonal prime phase. We observed slower partitioning kinetics in Ti-YSZ in comparison to YSZ. However, small amounts of rutile phase were present at low temperature but it was not observed during high heat treatments. In pyrochlore region, identified that pyrochlore phase is metastably available for compositions away from ternary equilibrium diagram phase. Cation substitutions sites are crucial in on crystallization of these investigated oxides. Additionally, observed low thermal conductivity values that are promising for thermal barrier coatings.

Chapter 5: Select compositions of pyrochlore and tetragonal phase oxides within $YO_{1.5}$-TiO_2-ZrO_2 ternary diagram deposited by Plasma Spray

5.1. Introduction

Thermal spray has been evolving from a surface technology to a materials processing technology. Historically, as a surface technology, typical materials coatings are resistant to heat, wear, erosion, and/or corrosion. As a material process technology, thermal spray is pertinent for new areas such as functional oxide materials. Functional oxides, with their complex chemistry materials provide opportunities to study the relationship between processing, phase structure and coating properties. Thermal spray of solution precursors offers an attractive method to produce functional oxides in a single deposition step due to high temperature and velocity (kinetic energy) to synthesize solution precursor to coatings. The advantage of using thermal spray is that it offers an avenue to screen compositions of interest and investigate structure property relations and fewer inhomogeneity and impurity in powders. Although favored for versatility in compositions, in our study, deposition directly from precursor solutions by RF/DC methods did not lead to dense coatings (Figure 60a). An alternative, Figure 60b, to depositing coatings directly by solution precursor is to convert solution precursors to powders for plasma spray. By utilizing low pyrolizing temperature powders can be prepared in their amorphous state, structurally similar to precursor oxides, therefore simulating amorphous precursors. However, the amorphous powders are advantageous because they can produce denser coatings by traditional plasma spray in order to measure properties (mechanical/thermal).

5.1.1. Thermal Spray of Complex Oxides

As described in chapters one and four, the ternary diagram of $YO_{1.5}$-TiO_2-ZrO_2, provides excellent opportunities to investigate compositions of materials that are promising TBC materials: (1) pyrochlore oxide compositions (2) tetragonal oxide compositions. The oxide compositions near the pyrochlore phase investigated in the study were $Y_{2-x}Ti_2Zr_xO_{7+x/2}$ and $Y_2Ti_{2-x}Zr_xO_7$. The chemical formula of $Y_2Ti_{2-x}Zr_xO_7$ represents the substitution of Zr^{4+} for Ti^{4+} on the B-cation site. $Y_{2-x}Ti_2Zr_xO_{7+x/2}$, represents the substitutions of Zr^{4+} for Y^{3+} on both the A and B cation sites of the pyrochlore/fluorite structure. Tetragonal oxide compositions were synthesized by precipitation processing for desired tetragonal oxides. The molar ratio of 7.6 mol.% $YO_{1.5}$-ZrO_2, which is the conventional composition for thermal barrier coatings were prepared. In addition compositions of yttria and titania co-doped zirconia were synthesized. The molar ratios with titania additions was $7.6YO_{1.5}$-$15.2TiO_2$ $77.2ZrO_2$ and it is referred throughout this dissertation as Ti-YSZ. Chapter four presented a detailed structural analysis of the pyrochlore and tetragonal oxide phase evolution from amorphous oxides. The significance of the results was that the proposed ternary diagram by Yokokawa based on theoretical calculations needed to be revised based on our experiments (chapter 4). Yokokawa diagram was based on theoretical models and our experimental results argued the phase fields and stability ranges for different compositions. The novel ternary diagram based on experiential results is illustrated in Figure 61. This chapter addresses the feasibility of using thermal spray to fabricate coatings that require complex-chemistry oxides in pyrochlore and tetragonal phase oxides found in Figure 61. In our first study, chapter four, we presented phase evolution for compositions under ideal conditions with controlled temperature and time constraints.

However, in this chapter we investigate the thermal spray process, which utilizes extreme thermal gradients and short exposure time for in-flight particles offer possibilities to produce metastable phases. Thermal spray is very advantageous for creating metastable phases as in the current YSZ thermal barrier coating material, but questions arise to:

As we continue to modify chemistries, how does this affect phase-structure in coatings?

How does the feedstock affect the final coating (starting from amorphous powder)?

What are the potential metastable phases?

Can we achieve tetragonal prime phases in oxides?

The objective was to plasma spray three compositions of interest; pyrochlore oxide compositions within the chemical formula of $Y_{2-x}Ti_2Zr_xO_{7+x/2}$, Ti-YSZ and YSZ tetragonal phase structures with a focus on the coating microstructure and properties. The contribution will be to understand the affect of starting material (un-reacted starting materials) and their effect on coating microstructure and properties.

This chapter will investigate the following in plasma spray coatings:

- Detailed phase-structure in coatings and compare to powder phase evolution study
- Investigate phase development of coatings deposited by un-reacted (amorphous) powders
- Investigate morphological stability of coatings as a function of temperature
- Investigate thermal conductivity and coating microstructure
- Present mechanical properties of APS tetragonal phase oxides

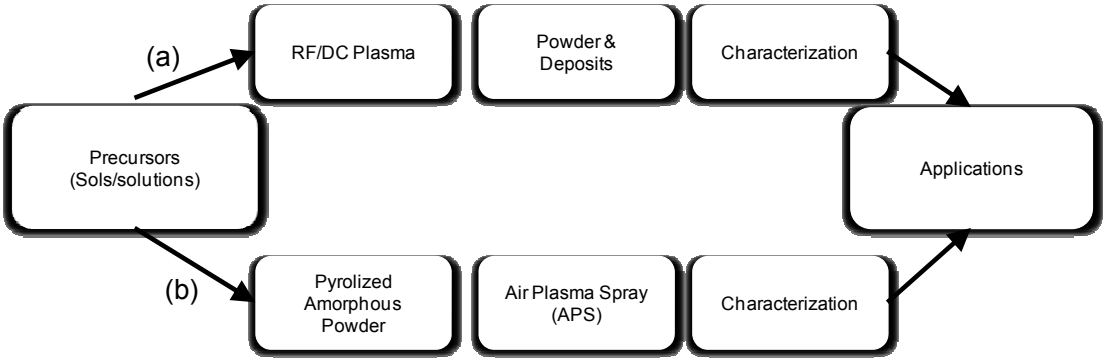

Figure 60 Development of coatings from precursors (a) Thermal spray by RF plasma allowing direct deposit of coating from sols/solutions (b) Precursors are pyrolyzed in order to fabricate powder feedstock for APS. (Courtesy of Dr. Sanjay Sampath and Dr. B.G. Ravi)

5.1.2. Process Complexities

As binary material compositions move toward ternary and multi-phased oxides controlling processing conditions by thermal spray becomes critical. Predicting phase selection in plasma sprayed coatings is complex when oxides are multi-phased (1-3 possible equilibrium phases). Process parameters and large thermal gradients ultimately affect the coating phase, microstructure and properties by materials deposited by plasma spray. Thermal sprays of functional oxides require precise chemistries; therefore the following issues are critical:

- Precursor chemistry and concentration
- Both thermo-physical and thermo-chemical interaction between droplet/powder and thermal plasma
- Short time scales / particle size / particle morphology / splat morphology
- Reaction with surrounding gases
- Starting material feedstock; effect of reacted versus un-reacted powders

5.1.3. Plasma Spray Coating of Functional Oxides Compositions within the Y_2O_3-ZrO_2-TiO_2 System

Three compositions selected for plasma spraying are marked (red solid circles) in the ternary diagram (Figure 61). As noted in the diagram, composition (*i*) is of yttria-stabilized zirconia (YSZ) with the compositions of 7.6 mol% of $YO_{1.5}$ (*ii*) $7.6YO_{1.5}$-$15.2TiO_2$-$77.2ZrO_2$ (Ti-YSZ), composition (*iii*) is near $Y_2Ti_2O_7$, (pyrochlore-phase). The two compositions are promising because the tetragonal and pyrochlore oxides have been proven to have low thermal conductivity values. The results presented in this chapter compare the standard composition of 7.6YSZ to Ti-YSZ for phase stability, mechanical properties and micro-structure.

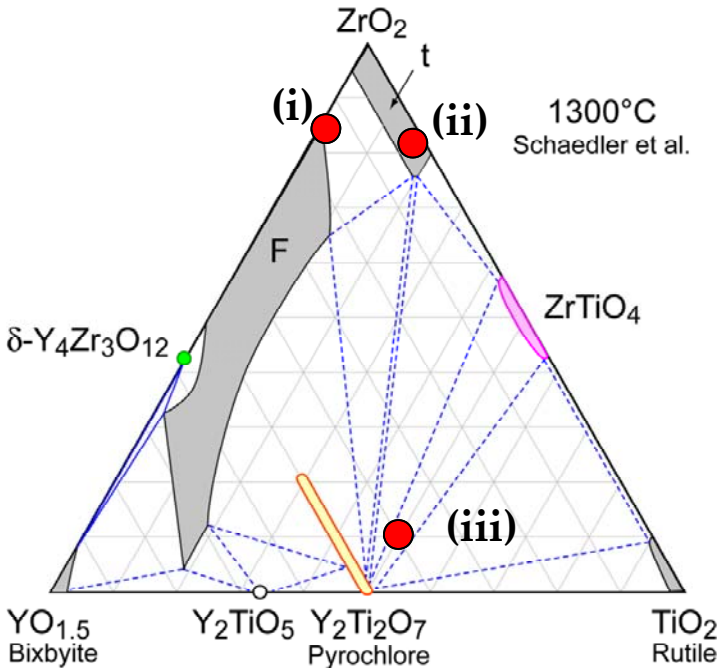

Figure 61 Equilibrium ternary diagram of ZrO_2-$YO_{1.5}$-TiO_2.[60] Compositions of plasma sprayed coatings (i) YSZ (ii) Ti-YSZ (iii) Pyrochlore-region

5.2. (A) Results and Discussion for Pyrochlore Oxides:

5.2.1. Microstructure and Structural Analysis of Pyrochlore Oxide Coatings

In our first series of thermal spray experiments, we successfully deposited coatings of pyrochlore compositions of $Y_2Ti_2O_7$ by direct deposition utilizing a RF plasma process for coatings from solution. Figure 62, illustrates a pyrochlore composition sprayed by DC/RF plasma. Results were promising because RF plasma spray coatings from precursor resulted in the desired pyrochlore oxide phase. Although the characterization by XRD confirmed that by plasma spray was viable in depositing the desired pyrochlore phase in a single processing step, solutions to coatings, the coating microstructure was composed of loose agglomerates of cylindrically shaped particles. The coating microstructure illustrated in Figure 64 showed that the samples did not adhere well to neighboring particles. The coatings were not dense and hindered our ability to measure mechanical and thermal properties. An alternative to directly depositing precursor to coating was to pyrolyze solution precursors at low temperature (600˚C) to produce large batches of amorphous powders. Details on precursor development are in the experimental section (chapter three) of this thesis. Figure 63 is the XRD spectra of starting powder feedstock with low pyrolizing temperature of precursors and as-sprayed coating for the chemical formula of $Y_{1.6}Ti_2Zr_{0.4}O_{7.2}$. The starting powder feedstock was amorphous; however, the as-sprayed coating was indexed as a pyrochlore phase oxide. The results proved that plasma spray can produce metastable phases in this system by amorphous oxide feedstock. At equilibrium, for the composition of $Y_{1.6}Ti_2Zr_{0.4}O_{7.2}$ the ternary diagram anticipates a three phase system of pyrochlore; zirconia-titanate and rutile. However, by the experimental results, the intermediate phases are from amorphous oxides are fluorite, pyrochlore,

pyrochlore and rutile. The XRD spectrum of $Y_{1.6}Ti_2Zr_{0.4}O_{7.2}$ amorphous powder had the metastable pyrochlore phase. This is a result of the fast quench rates in the thermal spray process yielding a metastable phase. After plasma spraying the amorphous oxide powders, the powders were thermally sprayed the same composition ($Y_{1.6}Ti_2Zr_{0.4}O_{7.2}$); however, the powder was heat treated at high temperature ensuring of a crystalline material. Phase analysis for the heat treated powders, Figure 63, was two phase comprising of rutile and pyrochlore. With identical plasma spray process conditions, the XRD spectrum was the pyrochlore phase with small presence of rutile indexed with the main (311) peak in comparison to feedstock powder with multiple rutile peaks. The results suggested that that a majority of powder particle are melted; however there are also some unmelts that may contribute to rutile phase formation. In comparison,

Figure 63, starting powder feedstock was of two phase, rutile and pyrochlore phase. Figure 65 is the SEM micrograph for the composition of $Y_{0.4}Ti_2Zr_{1.6}O_{7.8}$ illustrating the fracture surface of the oxide. From the microstructure micrograph, we can easily distinguish between the splat boundaries and globular pores. Table 1 is the Air Plasma Spray (APS) conditions used in order to fabricate the free standing coatings of $Y_{1.6}Ti_2Zr_{0.4}O_{7.2}$. Processing variables have the potential to vary coating microstructure and phase. Variations include standoff distance; substrate temperature and carrier gas. Ultimately, variations in process conditions affect the powder particle temperature and velocity resulting in changes in coating properties. Figure 66 is a cross section of the $Y_{1.6}Ti_2Zr_{0.4}O_{7.2}$ coating deposited on YSZ. The micrographs illustrate globular pores and crack networks throughout the coating. Additional observations include light and dark regions as illustrated in Figure 68 and Figure 69. EDS show that the white regions are in fact rich in zirconia while the dark regions are

rich in TiO_2. EDS results suggest that there are may be segregation in APS because starting powders were well mixed at low temperatures. APS with its high temperature, velocity and the variation of particle size may cause segregation in coatings. In Figure 69 there is evidence of white band formation during each pass of the air plasma spray gun over the sample further suggesting segregation in coatings. The white banks were between the splats boundaries there are layers of lighter colored regions through EDS are shown to be rich in ZrO_2. Figure 70, is a summary of XRD results for a composition, $Y_2Ti_{0.8}Zr_{1.2}O_7$, with B-cation substitution representing the substitution of Ti^{4+} for Zr^{4+}. For this composition, the ternary diagram predicts that the phase will be either fluorite, pyrochlore or a combination of both phases. Figure 70 is a comparison of the RF spray and APS coatings. The RF plasma spray of precursors resulted in fluorite phase. According to the equilibrium diagram the phase should be pyrochlore. We also observed the fluorite phase in as-sprayed coating from amorphous powders. However, the XRD spectrum revealed a more crystalline spectrum in plasma spray coatings in comparison to RF sprayed materials where the peaks were broader. For the powder compositions of $Y_2Ti_{0.8}Zr_{1.2}O_7$ heat treated in furnace for three hours for 1500˚C, the XRD spectrum showed well resolved pyrochlore peaks for the indices of (311) (222) and (400). Efforts were taken to obtain thermal conductivity values of pyrochlore composition. Conductivity measurements were taken for temperature ranges from 700˚C to 1200˚C at room temperature. The samples were sintered pellets, fired at temperature for one hour. Results showed thermal conductivity values under 0.7 W/mk for temperatures of 1000˚C and less. After 1000˚C, the conductivity reached approximately 1.6 W/mk.

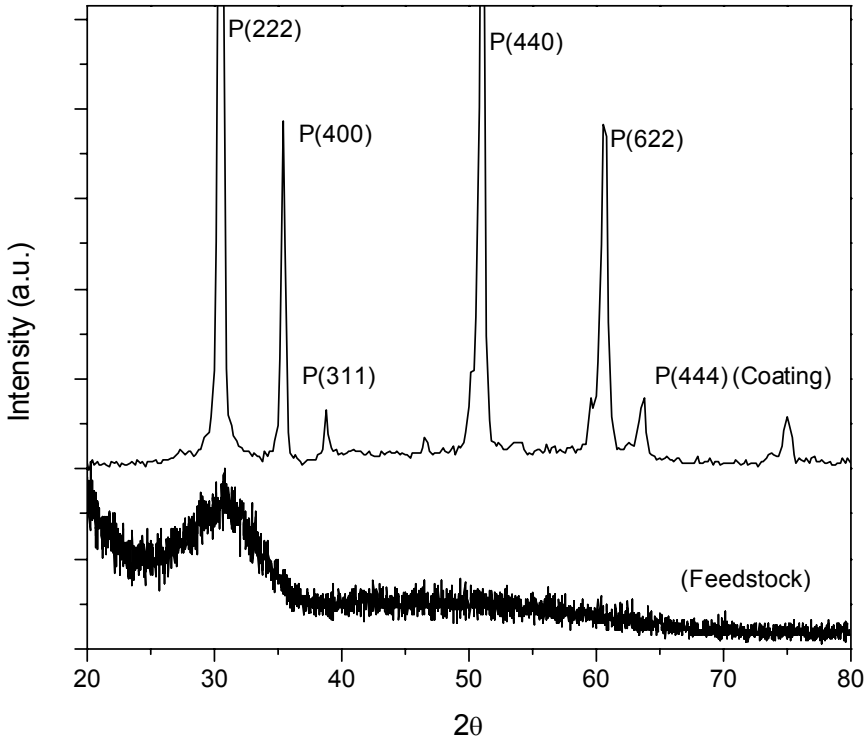

Figure 62 XRD patterns of thermally sprayed $Y_{1.6}Ti_2Zr_{0.4}O_{7.2}$ coatings and precursor derived feedstock powder

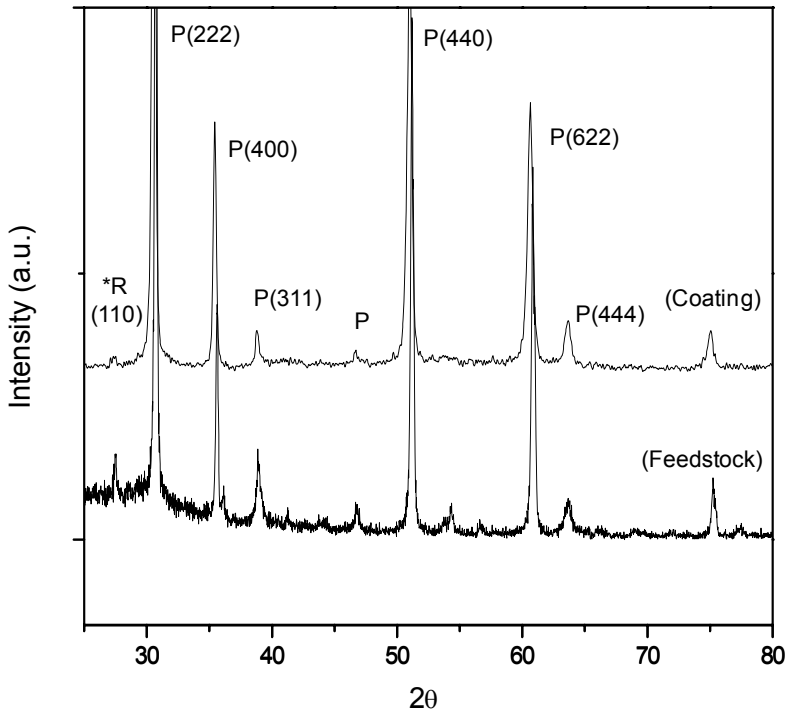

Figure 63 XRD patterns of thermally sprayed $Y_{1.6}Ti_2Zr_{0.4}O_{7.2}$ coatings and precursor derived powder heat treated at 1100°C (P = pyrochlore phase)

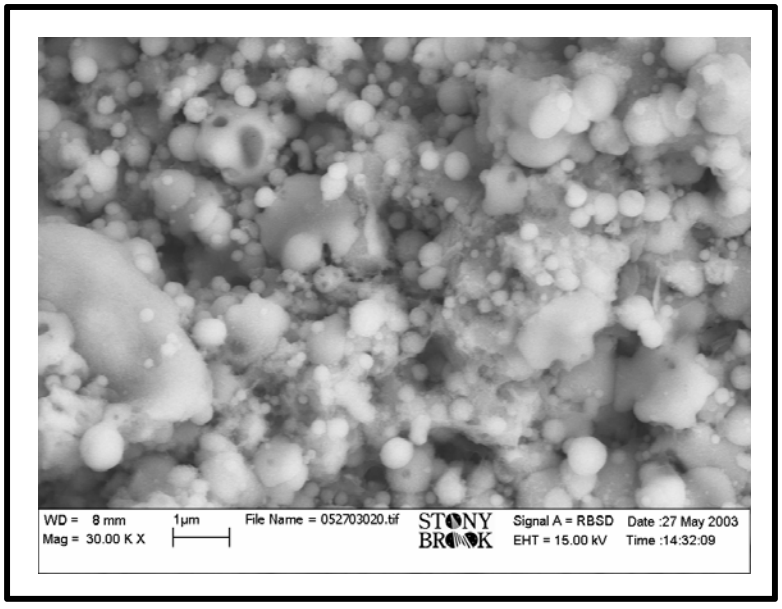

Figure 64 Radio Frequency (RF) sprayed $Y_2Ti_{0.8}Zr_{1.2}O_7$ on Alumina. SEM image depicts top surface view of coating

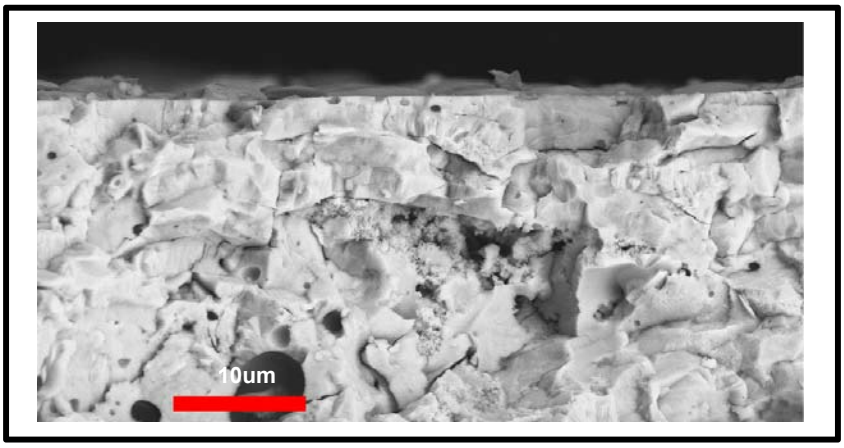

Figure 65 Fracture Surface of Air plasma Sprayed (APS) $Y_{1.6}Ti_2Zr_{0.4}O_{7.2}$ coating illustrates splat boundaries and pores within coating material.

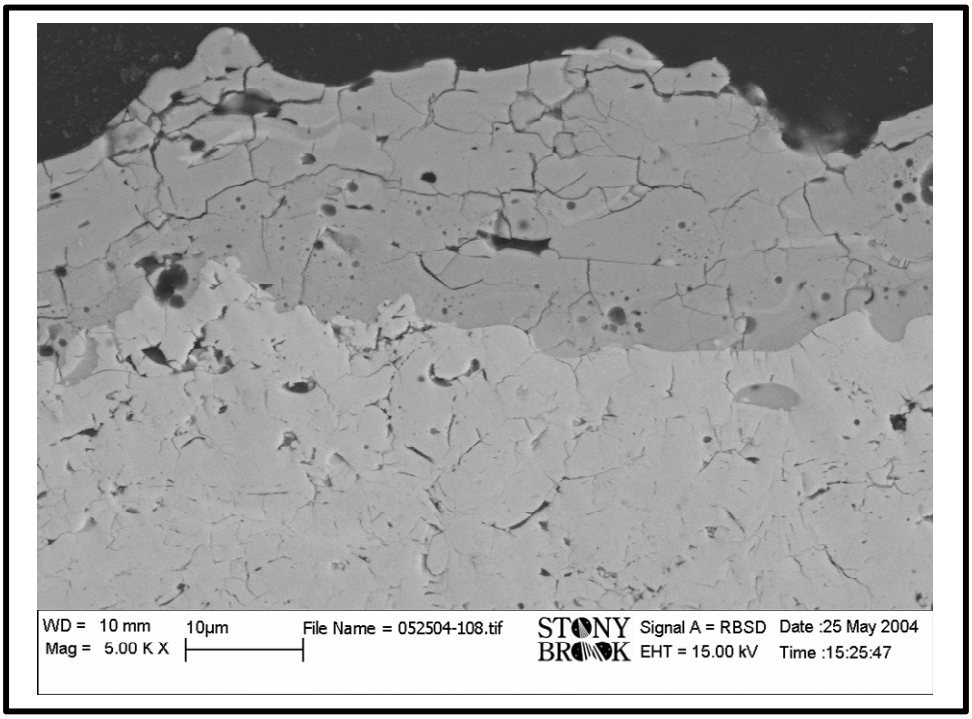

Figure 66 Amorphous powder deposited of $Y_{1.6}Ti_2Zr_{0.4}O_{7.2}$by Air Plasma Spray on YSZ substrate. Cross-section of sample illustrates a morphology that includes porosity and inter-laminar cracks.

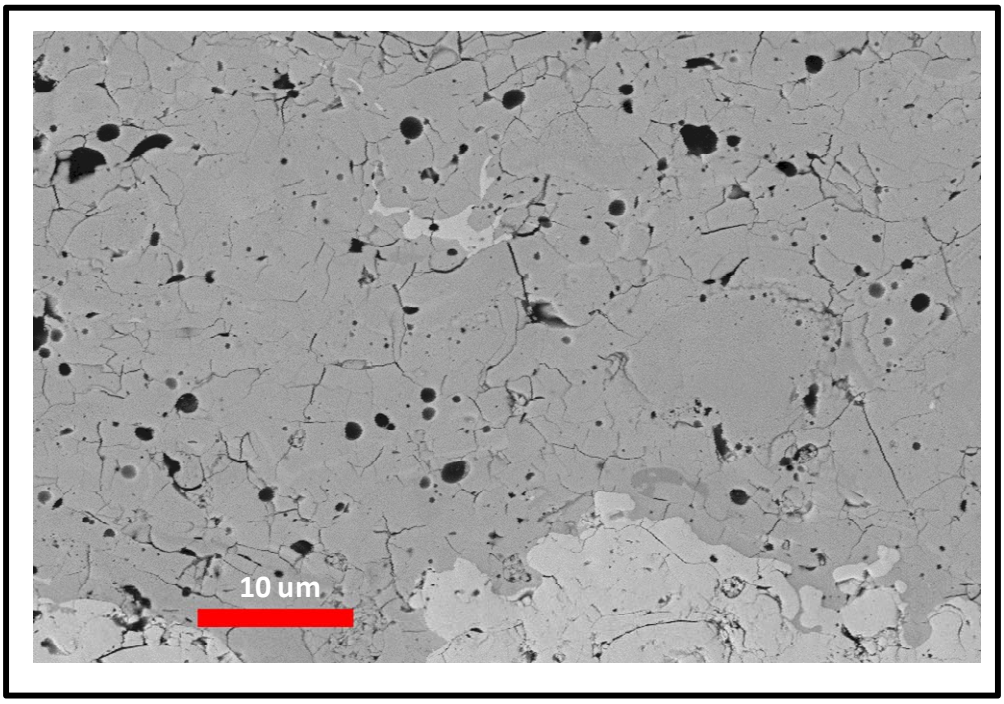

Figure 67 Cross-section of air plasma sprayed coating of $Y_{1.6}Ti_2Zr_{0.4}O_{7.2}$ with YSZ substrate. High magnification SEM Illustrates globular –pores, micro-cracks and interlamanar pores within coating.

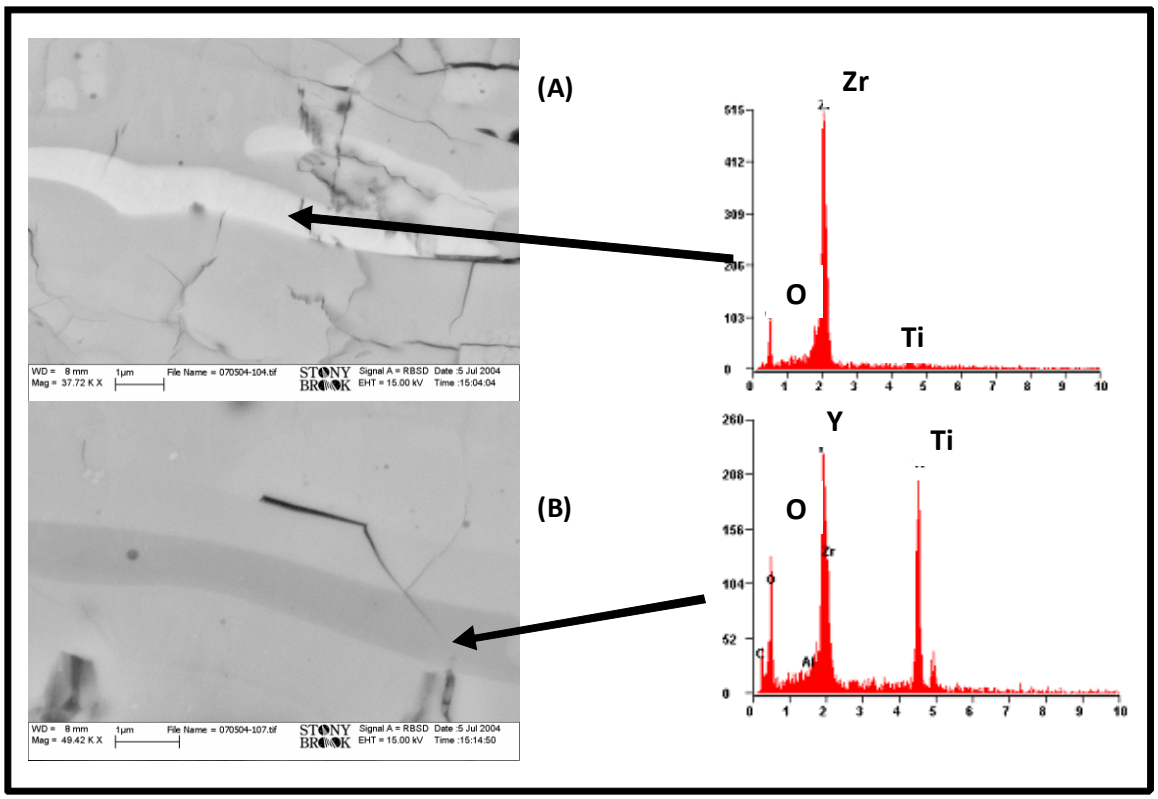

Figure 68 Magnified image from Figure 67 illustrating Zirconia rich regions shown in (a) and Titanium rich (b) regions within the Air Plasma Spray Coating.

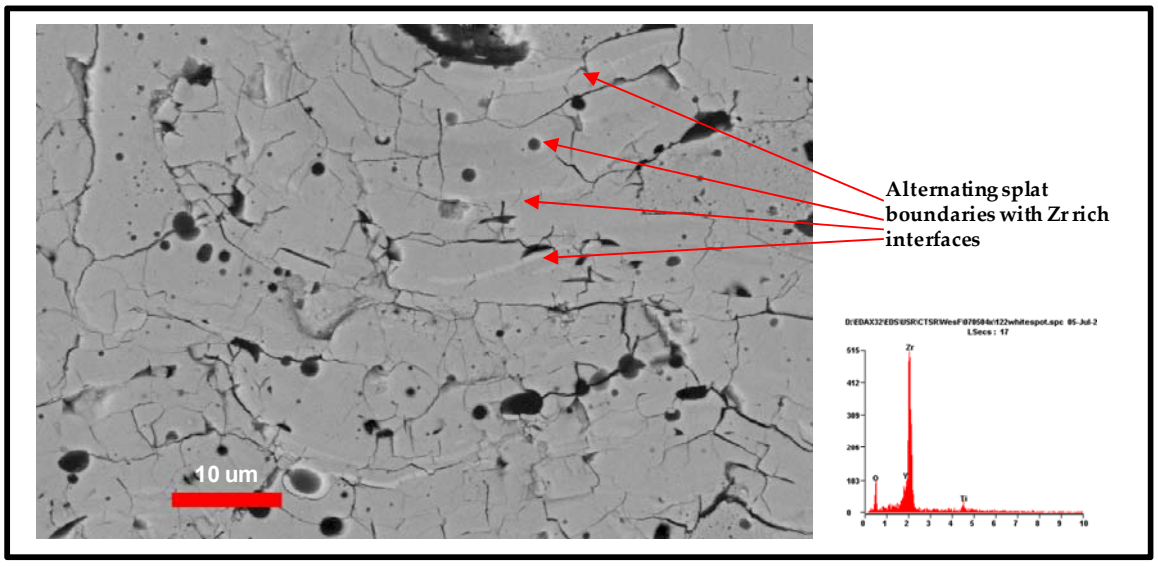

Figure 69 Thermal spray coating of 50Ti-40Y-10Zr ($Y_{1.6}Ti_2Zr_{0.4}O_{7.2}$). Figure illustrates with arrows regions with white bands at splat boundaries. EDS determined that these regions are rich with zirconia Partitioning in coatings observed.

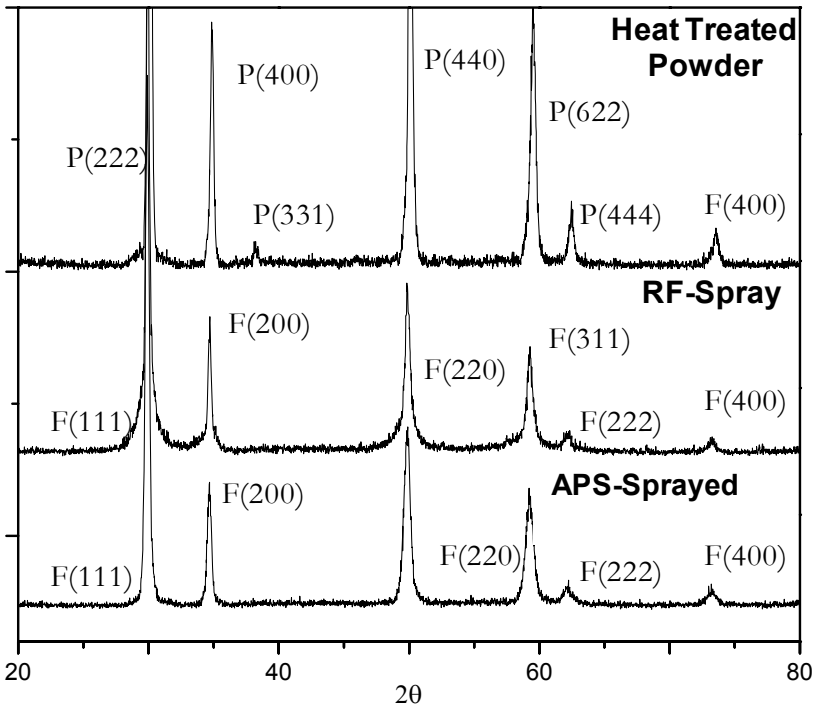

Figure 70 Comparison of APS as-sprayed, Precursor as-sprayed and static pyrolyzed powders at 1500˚C/3hr XRD patterns for composition of $Y_2Ti_{0.8}Zr_{1.2}O_7$

5.2.2. Phase Analysis of Pyrochlore Splats

Splat morphologies were investigated by optical microscopy for pyrochlore composition of $Y_{1.6}Ti_2Zr_{0.4}O_{7.2}$ deposited on stainless steel and glass samples to observe splat morphology. Optical images revealed disk shaped splats that were in agreement with Zygo measurements with three dimensional images with average diameters on the order of 30-40 microns in diameter. Splat samples had higher thickness in edges and were circular in comparison with lower thicknesses in the center. At the edges the splats were approximately 0.60 microns and the center of the splats were 0.2-0.4 microns. GAADS ZEED diffraction patterns were measured for splats of $Y_{1.6}Ti_2Zr_{0.4}O_{7.2}$. The indices of (222), (400) and (440) were of the fluorite phase. The XRD spectrum showed that the splats were a mixture of amorphous and fluorite phase. The ternary diagram predicts that the equilibrium diagram for the select composition should be pyrochlore; however, we observed the metastable fluorite phase. The long range order of the pyrochlore phase was suppressed by the plasma spray process. Phase analysis results suggest the difficulty of cation ordering migration in coatings.

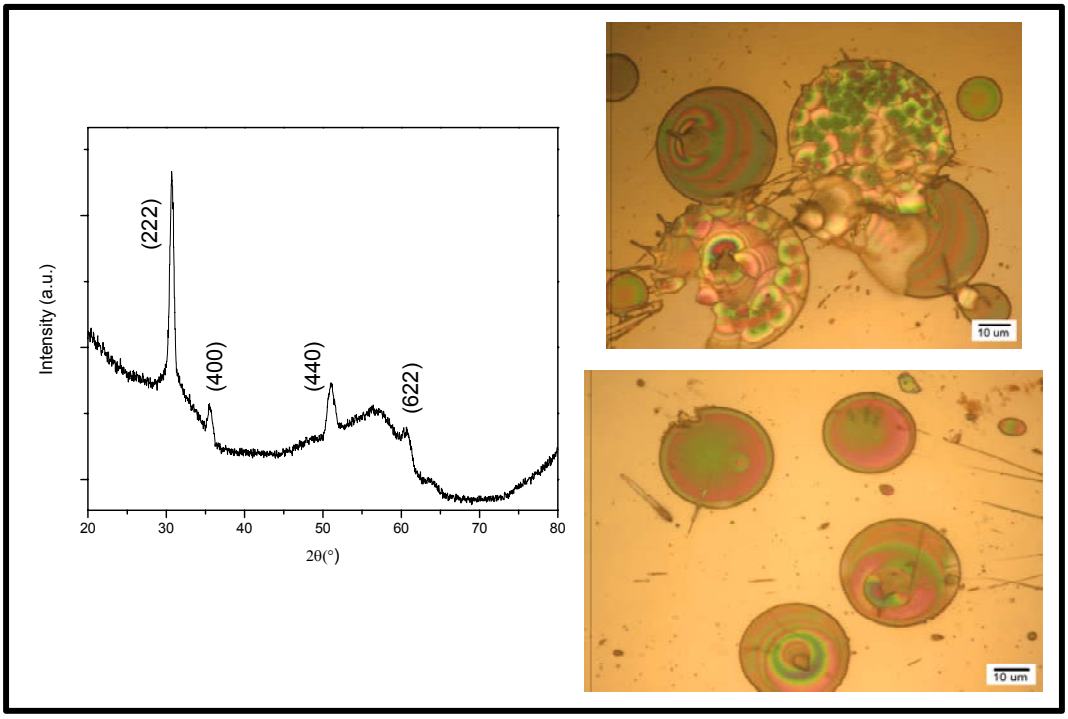

Figure 71 GAADS diffraction pattern for $Y_{1.6}Ti_2Zr_{0.4}O_{7.2}$ composition (left); Splats deposited on aluminum (right) Fluorite phase in splats deposited from precursor derived powders

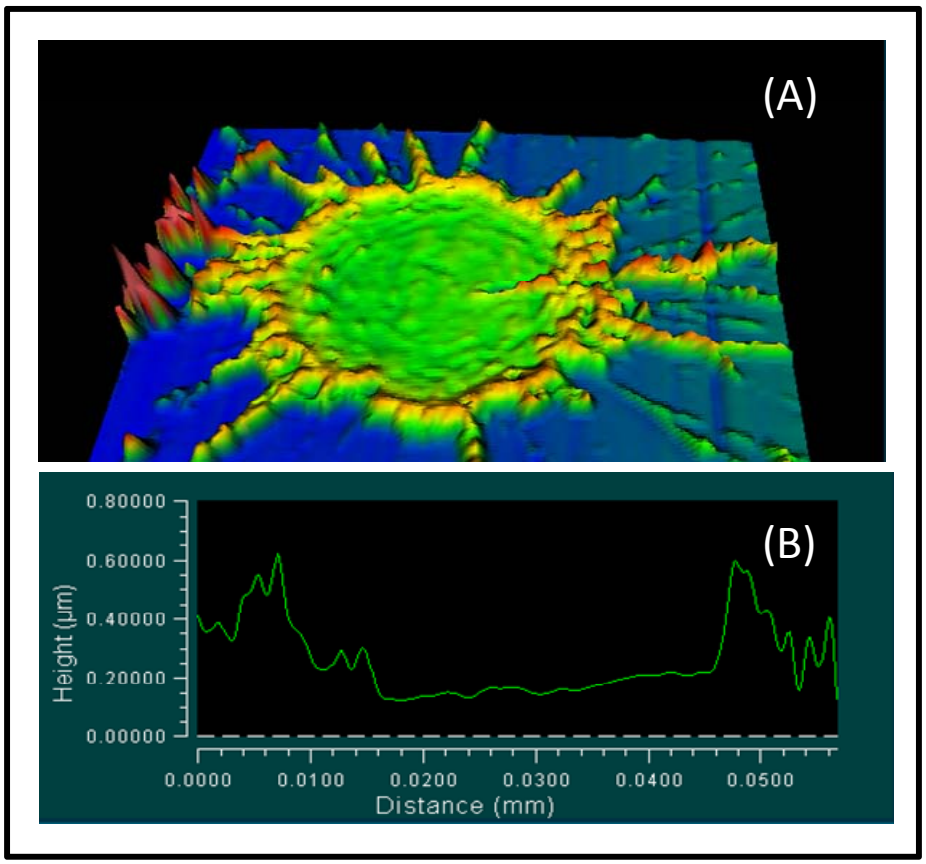

Figure 72 (A) Zygo three-dimensional images of spat deposits for YSZ prepared by precursor methods. (B) Splat widths and height measurements

(B) Results and Discussion for Tetragonal Oxides:

This section presents the microstructural characteristics, phase analysis and properties of plasma sprayed coatings of YSZ and Ti-YSZ from powders derived from soft chemistry. In plasma spray coatings, there exist pores (globular and/or interlamellar), micro-cracks, interlayer interface and inter splat boundaries that affect properties, which include thermal conductivity and elastic modulus. The objective is to provide an understanding to the affects of starting material (soft chemistry derivation of feedstock powder) and understand the affect of co-doping of zirconia with Ti^{4+} on coating microstructure and phase. Experiments will also include the influence of heat treatments on micro-structural change in the coatings of YSZ and co doped coatings. The experimental results are summarized as follows: coating microstructure relationship of YSZ and Ti-YSZ, thermal conductivity of thermally cycled coatings, modulus measurements and detailed phase analysis.

5.2.3. High Temperature Phase Stability of YSZ/Ti-YSZ Coatings

Figure 73 illustrates the starting XRD spectrum of YSZ and Ti-YSZ as amorphous oxides with a fluorite peak hump at (111). The pyrolization temperature used to synthesize the powders was approximately 550°C. The significance of starting with low pyrolization is that it we can investigate phase selection in coatings with a starting amorphous oxide. We can determine if in fact the starting structure has a significant role in coating microstructure or an effect of processing conditions (influence of temperature and velocity). Figure 74 is the full spectrum diffraction pattern of YSZ as-sprayed coating from the initial amorphous powders from precursor synthesis. Detailed structural analysis for select two-theta diffraction angles on both low angle (25-40°) and high angle (72-76°) were used in order to identify monoclinic/cubic and tetragonal/tetragonal prime phases respectively. For detailed structural analysis, we focused on peak indices at (400)/(004) and (111)/(222) peak. From the XRD spectrum we identify the cubic phase. For as-sprayed coatings, we identified cubic phase (111)/(220) and a small monoclinic peak in the range of 25-40°. Utilizing deconvolution techniques[71], the tetragonal prime phase at (400)/(004) for angles between 72-76° were identified. From an XRD spectrum, the tetragonal prime phase is identified by the main (400) indice with a smaller reflection of (004). For plasma spray coatings of Ti-YSZ, we identified indices for the cubic and fluorite structure. Figure 76 is the XRD full spectrum of (20-80°) for as-sprayed coating of Ti-YSZ by APS. We identified indices for cubic phases by the (111), (200) and (220). For as-deposited coatings, there were no discernable peaks at 004/400 and 002/200 for the tetragonal/tetragonal prime phase (Figure 77). Investigations of the spectra at low angle, 25-40, we are able to detect monoclinic phase m(111) and rutile phase r(110). XRD results suggest that coatings have small degree of partitioning into two phase system. Therefore, as-sprayed coatings of YSZ and

Ti-YSZ under the same process conditions; YSZ had tetragonal prime however, Ti-YSZ the separation of peaks were not clear. There appears to be slower partitioning kinetics in YSZ in comparison to Ti-YSZ. In addition, for Ti-YSZ, based on the equilibrium diagram we expect to have only the tetragonal phase. Results suggest segregation occurring in powders and/or during thermal spray process.

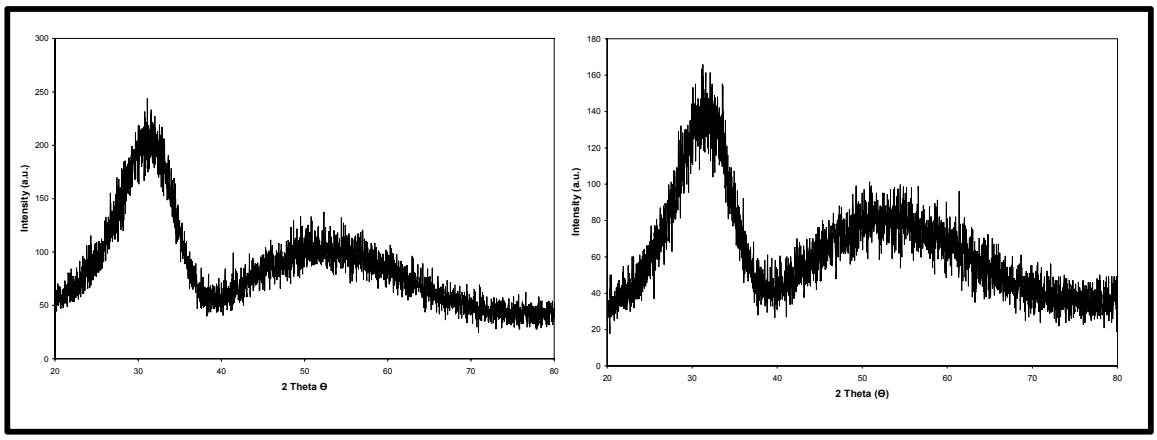

Figure 73 XRD pattern of pyrolyzed powder prepared by reverse co-precipitation processing at 550°C (left) YSZ (right) Ti-YSZ

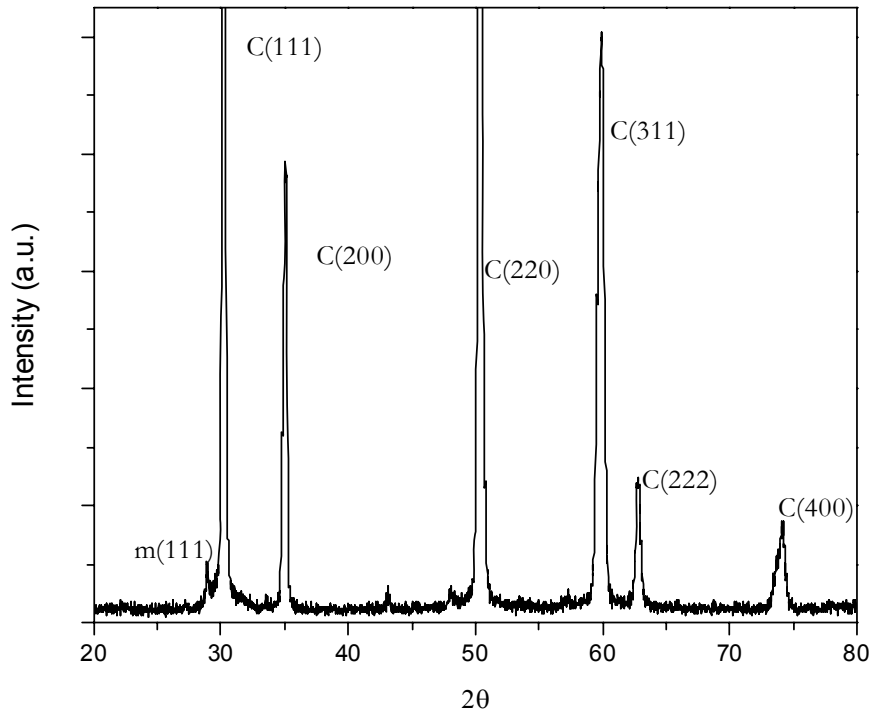

Figure 74 Plasma spray coating of YSZ coating prepared from precursor processing. Full spectrum between 20-80° illustrating primarily cubic phase.

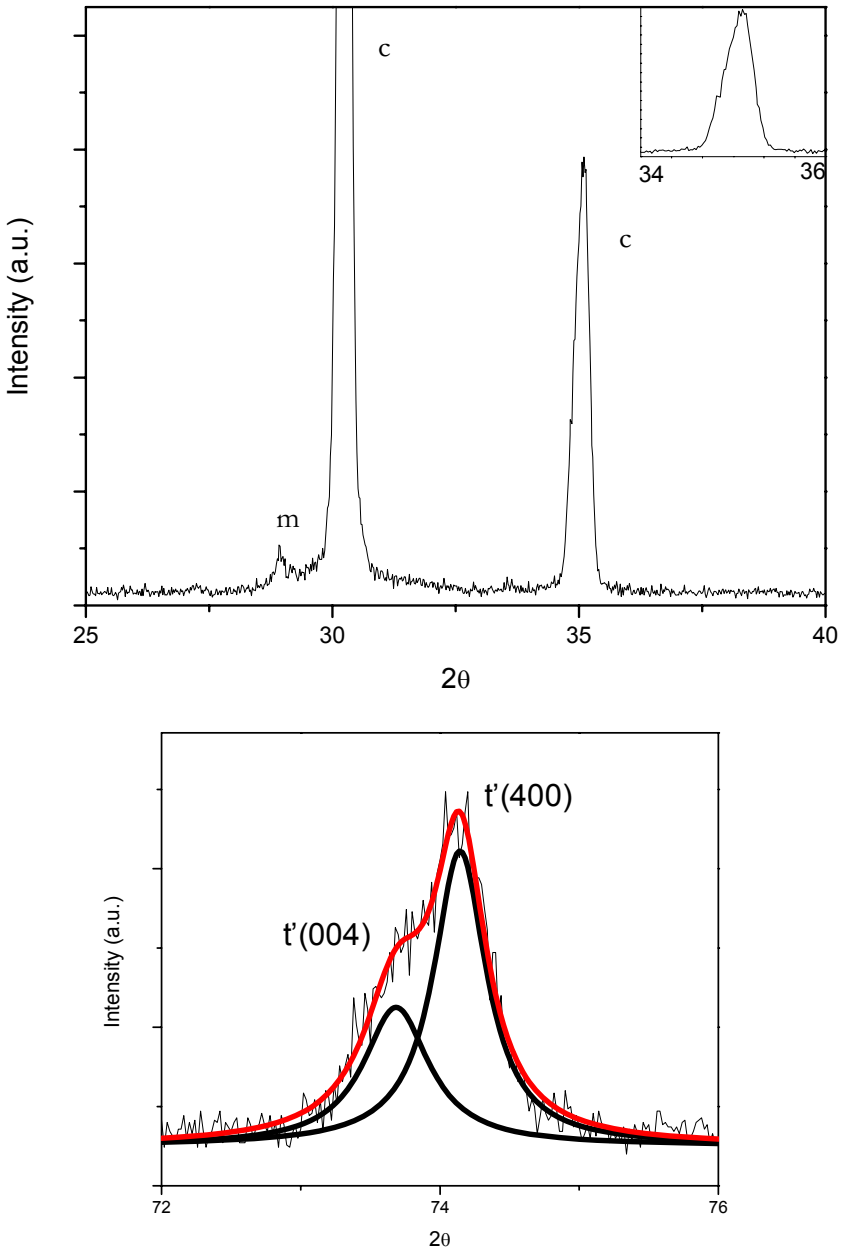

Figure 75 (Top) XRD spectrum of As-deposited YSZ coating 25-40°. (Bottom) Detailed evaluation of tetragonal indices for peaks between 72-76°

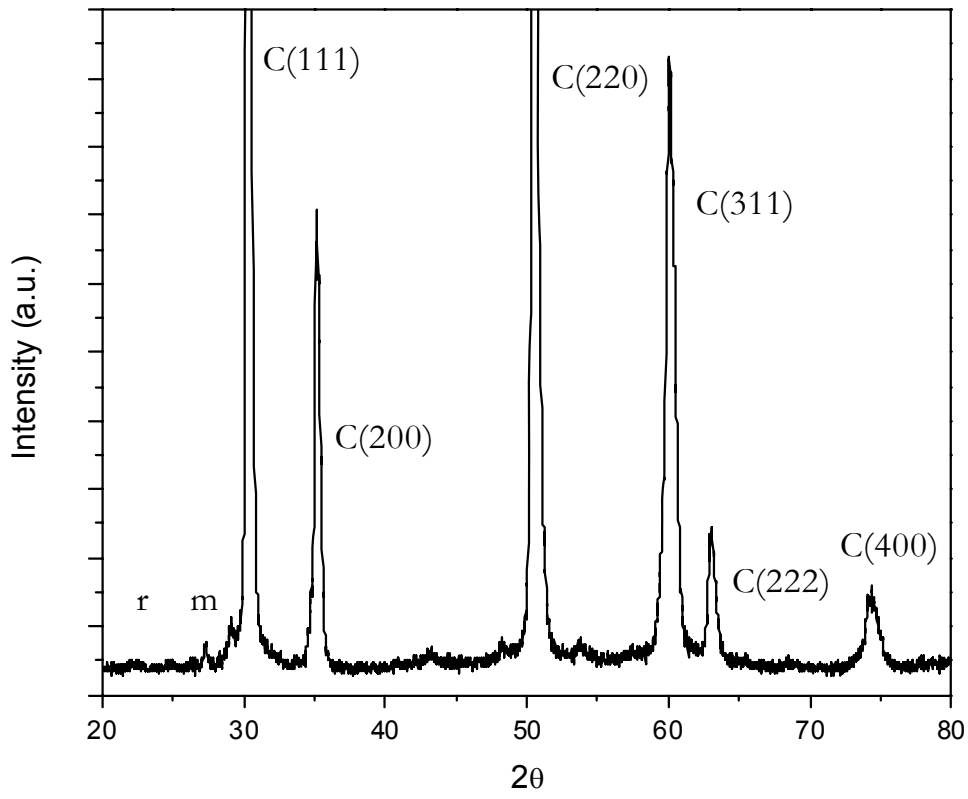

Figure 76 As-deposited Plasma spray coating of Ti-YSZ from reverse co-precipitation precursor synthesis. Cubic, monoclinic and rutile peaks were indexed.

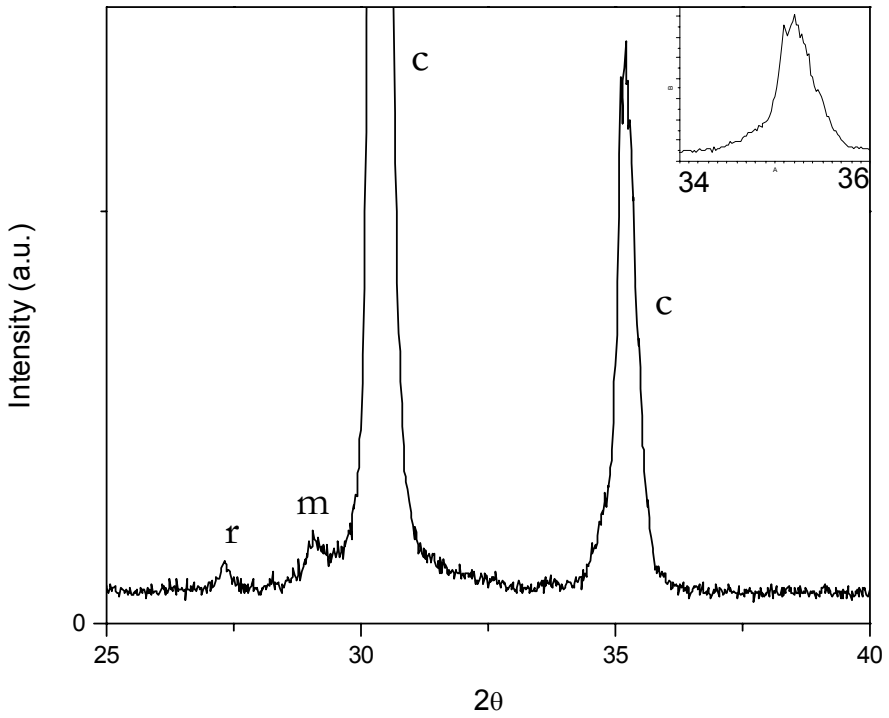

Figure 77 XRD spectrum of as-deposited coatings of Ti-YSZ between 25-40°. For as-deposited conditions, deconvolution of peaks between 34-36° were non-discernable for cubic and/or tetragonal indices.

5.2.3.1. Thermal Cycled and Isothermal Heat-Treatment of Coatings

This section investigates coatings at high temperate to report high temperature phase stability. Figure 78 is the XRD spectrum for YSZ coatings heat-treated at 1400˚C. Deconvolution techniques for XRD peaks between 72-76˚ for 200/002 indices revealed, the tetragonal and cubic phases. Results suggest moderate partitioning in YSZ coatings. There was also minute amount of monoclinic peaks present in heat treated coatings. In samples of Ti-YSZ, Figure 79, with heat-treatment of 1400˚C for twenty-four hours, there was a higher degree of partitioning in comparisons to YSZ coatings. Small amounts of rutile phase were present with no monoclinic phase present. Results imply slower partitioning kinetics in YSZ compared to Ti-YSZ at high temperatures. First we investigated YSZ at 1400˚C by using deconvolution techniques. We observed the tetragonal and cubic phases for between 34-36˚ for samples heat treated for one hour. More notably, after heat treated of YSZ coatings at 1400˚C for twenty-four hours, Figure 80 shows that both coatings of YSZ and Ti-YSZ had complete partitioning into the cubic and tetragonal phase. However, the monoclinic phase was not detected in the spectrum of YSZ and Ti-YSZ. The XRD spectrum of Ti-YSZ in comparison to YSZ has a higher degree of partitioning of phases into cubic and tetragonal. There was also no monoclinic or rutile peaks present at low angle. Figure 81 compares the 004/400 peaks for both YSZ and Ti-YSZ coatings. Lattice parameter results are summarized on Table 8. Results further suggest slower partitioning kinetics in YSZ at temperatures at 1400˚C. Phase diagram suggest that there should not be any partitioning of the cubic phase into tetragonal up to equilibrium temperatures. For the second isothermal study, we introduced longer heat treatments for YSZ and Ti-YSZ at 1400˚C. Results for YSZ are consistent with the equilibrium diagram for compositions of 7.6YSZ. The

equilibrium diagram predicts for the material composition to partition into cubic and tetragonal phase. The equilibrium diagram for the composition of Ti-YSZ predicts that the phase should be a single tetragonal phase. The results suggest that either phase field is not consistent or that coatings during the thermal spray process shifted compositions becoming yttria-rich, therefore, falling within two phase region. The results suggest that the initial tetragonal phase field in the ternary diagram is narrower than initially expected.

Figure 82 and Figure 83 summarize the as-sprayed and thermally cycled YSZ. As-sprayed coatings have small amounts of monoclinic peaks present. However, in figure 71, it is clear through detailed analysis that it as-sprayed material is in fact tetragonal prime phase. Results are promising from industrial stand-point for thermal barrier coatings because oxides with tetragonal prime phase were found to have longest cycle life and the ability to resist partitioning in comparison to other stabilizers. After five thermal cycles, it is apparent that that the t'(004) and t'(400) peaks begin to segregate. The results of the lattice parameters are summarized on Figure 84 is the XRD spectrum for Ti-YSZ coatings of as-sprayed powder that was thermally cycled. Deconvolution of peaks were performed for (400)/(004) region of the XRD spectra. For Ti-YSZ, the as-sprayed peaks were not discernable; however, after heat treatment the tetragonal prime phase was well resolved. Results indicate that as the as-sprayed coatings after heat treatments of 1100°C for 30 minutes immediately showed the tetragonal prime structure. The monoclinic and rutile peaks were reduced as the material was thermally cycled. Table 8 summarizes the lattice parameter values for YSZ and Ti-YSZ thermal cycled samples. Figure 78 illustrated the tetragonality (c/a) versus heat treatments of coatings. Results show that the Ti-YSZ had higher tetragonality values than YSZ. Concurrently, the values of YSZ and Ti-YSZ increased as the materials were thermally cycled. Values for YSZ

coatings ranged from 1.005 to 1.0067. Tetragonality values for Ti-YSZ ranged from 1.018 to 1.028.

$$\%YO_{1.5} = \left(\frac{a-3.5963}{0.00227}\right) \quad (26)$$

Figure 87, are the results of yttria content (YO1.5 mol. %) in as sprayed and thermally cycled YSZ coatings. As-sprayed coatings resulted in yttria content of 6.66 and decreased to 6.60 mol. % at 1400˚C. Results suggest that the coatings are yttria-rich (tetragonal) in the as-deposited state. Thermal cycling resulted in decreasing the mole percent. Chemically, the starting material was synthesized to have a mol.% of 7.6. The yttria concentrations in the tetragonal phase were computed by equation 26 by Toraya[72]. The values of the lattice parameters are found on Table 8.

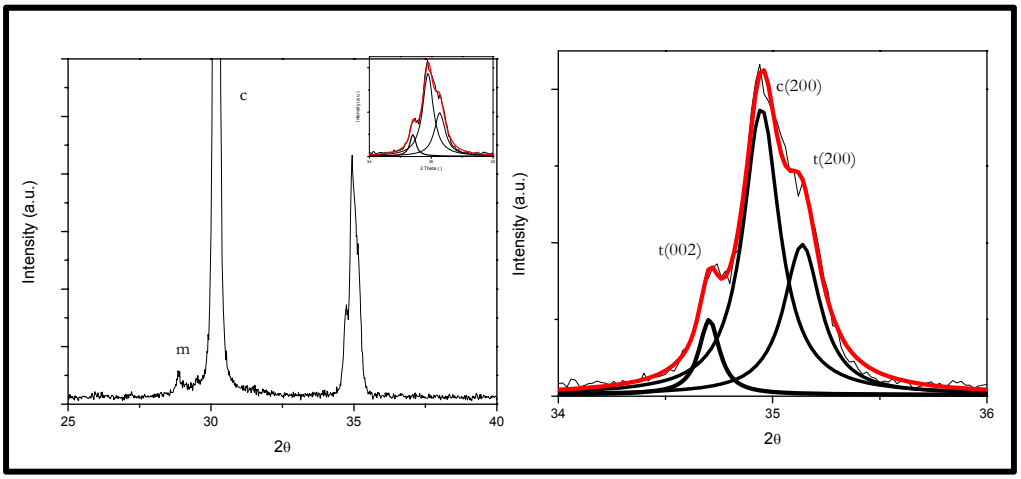

Figure 78 XRD spectrum of YSZ coating isothermal heat-treatment at 1400˚C for ten hours (left) spectrum from 20-40˚ and de-convoluted peaks evaluated between 34-36˚ (right)

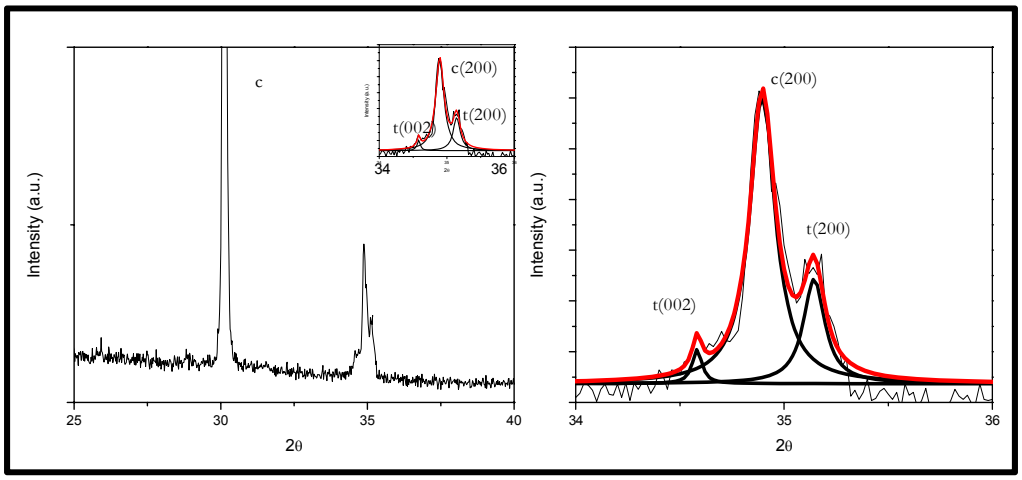

Figure 79 XRD spectrum of Ti-YSZ isothermal heat-treatment at 1400˚C for ten hours (left) spectrum from 20-40˚ and de-convoluted peaks evaluated between 34-36˚ (right)

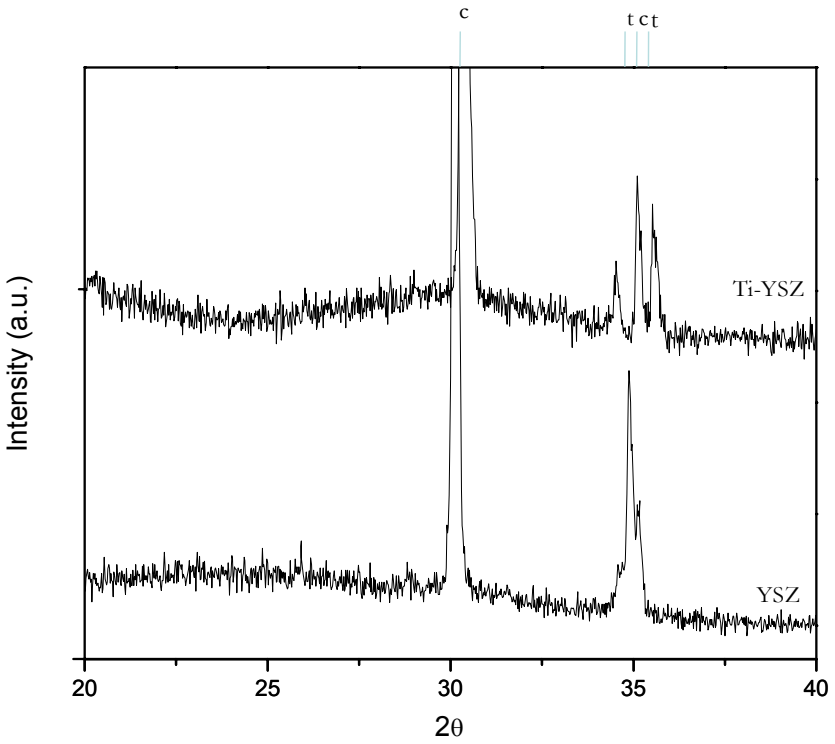

Figure 80 XRD spectrum of free-standing coating of Ti-YSZ and YSZ heat-treated to 1400˚C for 24 hours

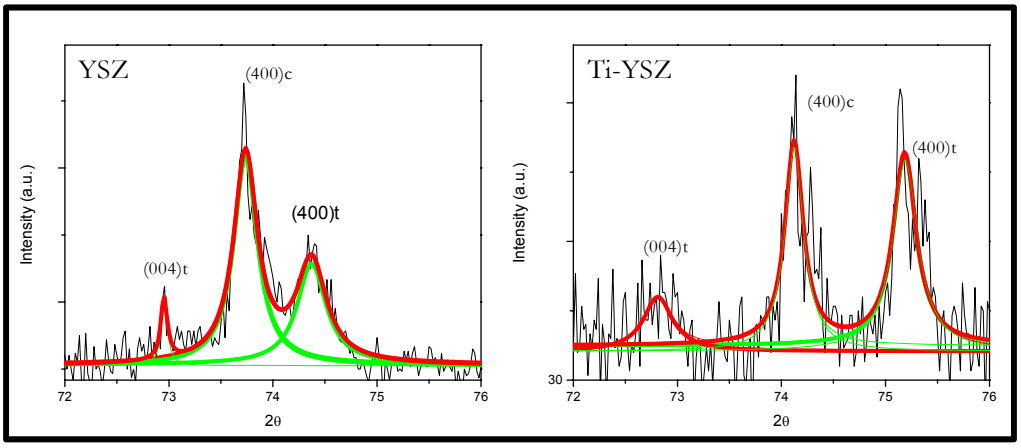

Figure 81 XRD spectrum from 72-76˚ for plasma sprayed coatings of YSZ (left) and Ti-YSZ (right) Post-treated to 1400˚C for 24hrs; both coating with two-phase; tetragonal and cubic.

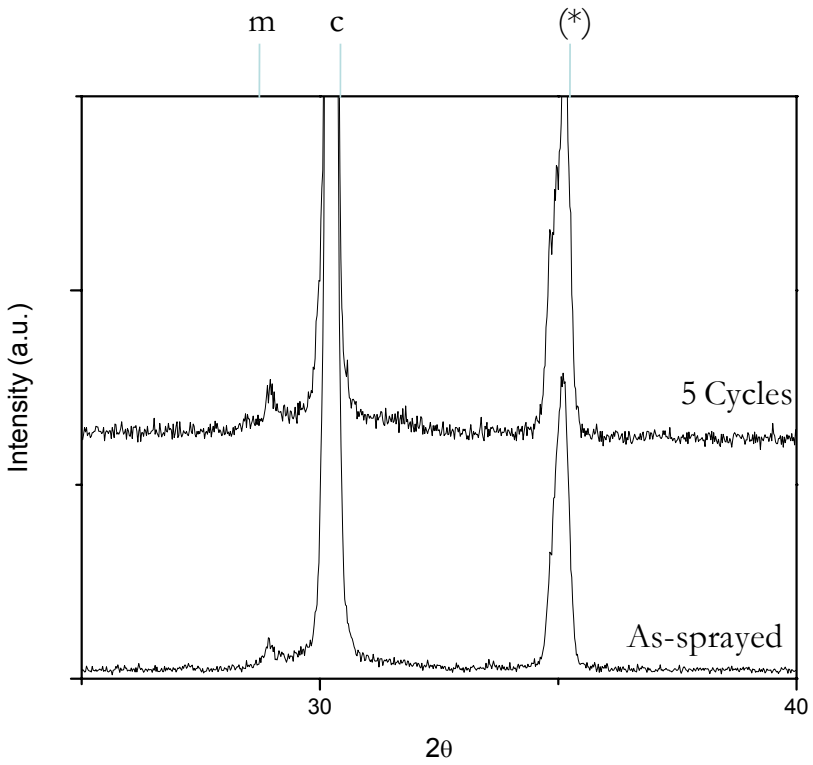

Figure 82 XRD spectrum between 20-40° of YSZ coating As-sprayed and thermally cycled; (*) indiscernible peak of cubic/tetragonal

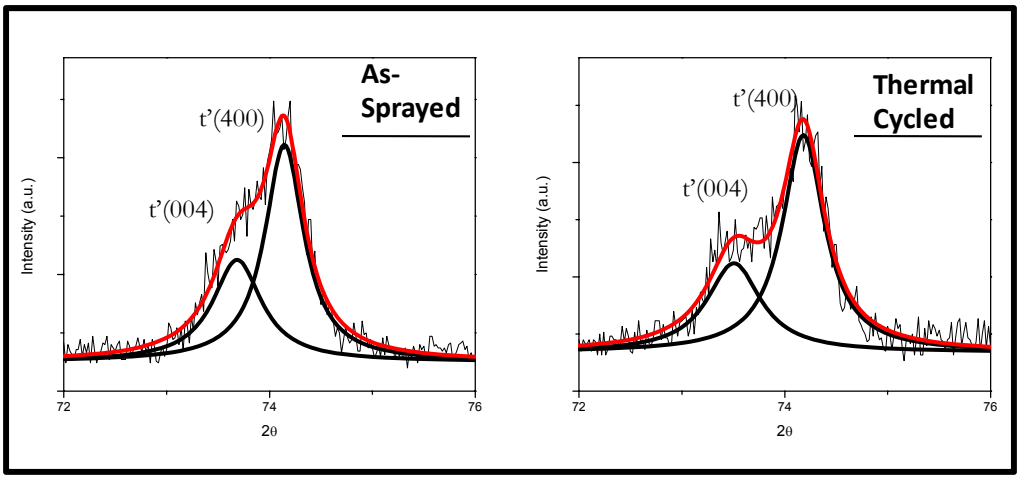

Figure 83 XRD spectrums between 72-76° for as-deposited coating and coating thermally cycled five times

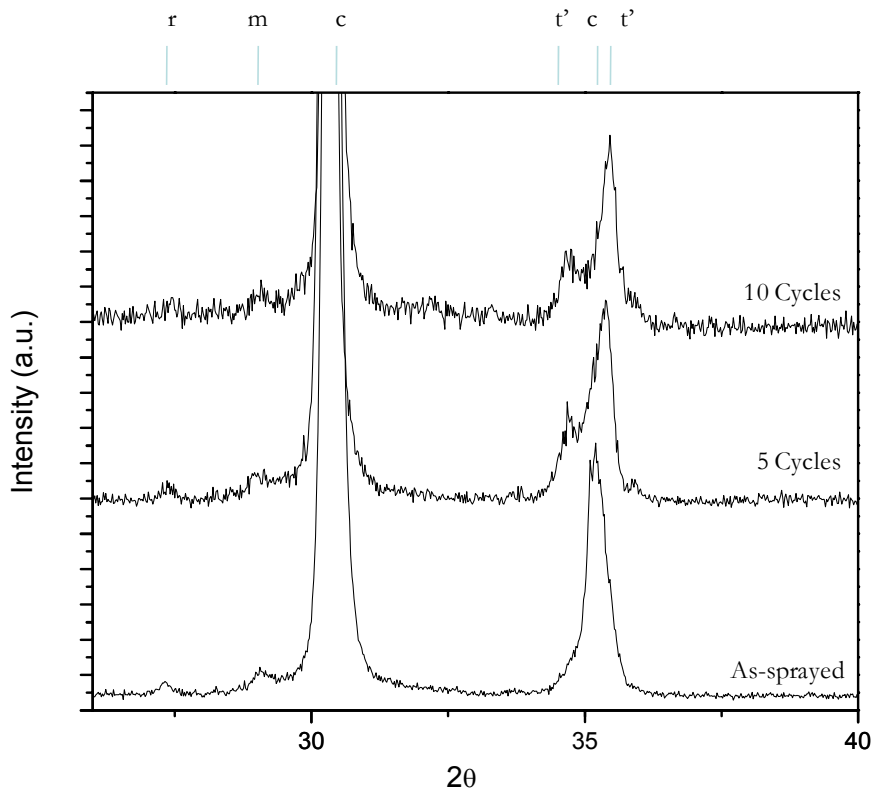

Figure 84 XRD low angle spectrum with range between 20-40°; Ti-YSZ; As-sprayed, five and ten cycles (at 1150° C for 30min)

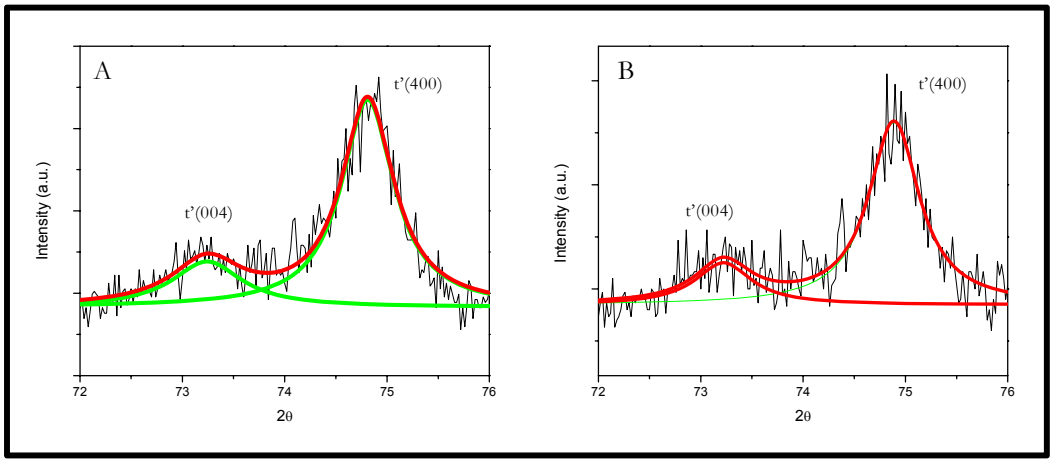

Figure 85 XRD spectrum of Ti-YSZ from 72-76° (A) Coating cycled five times (B) Coating cycled ten times

Table 8 Summary of lattice parameters for APS coatings of YSZ and Ti-YSZ

Powder Heat Treatment	Coating Material	Identified Phase	d_t(400) (A)	d_t(004) (A)	c (A)	a (A)	c/a
As-deposited	YSZ	t'	1.284	1.277	5.136	5.108	1.005
	Ti-YSZ	C	-	-	-	-	--
5 Cycles	YSZ	t'	1.286	1.276	5.15	5.106	1.008
	Ti-YSZ	t'	1.267	1.291	5.165	5.069	1.019
10 Cycles	YSZ	-	-	-	-	-	-
	Ti-YSZ	t'	1.266	1.291	5.165	5.066	1.020
Isothermal 24hrs 1400C	YSZ	C+t	1.273	1.294	5.09	5.18	1.017
	Ti-YSZ	C+t	1.297	1.262	5.190	5.049	1.028

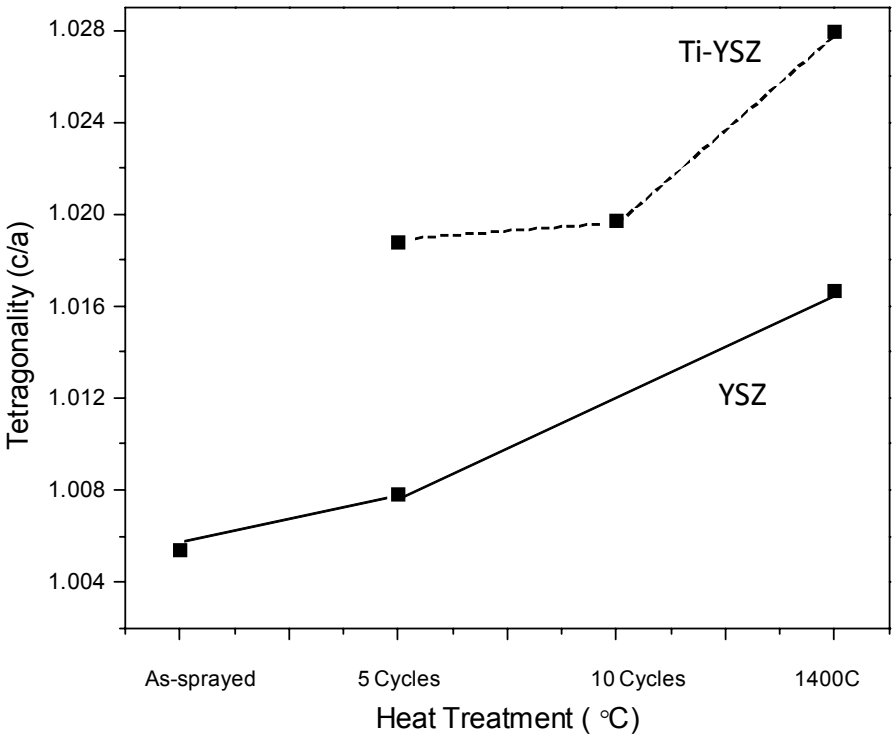

Figure 86 Tetragonality (c/a) versus heat heat-treatment for YSZ and Ti-YSZ plasma sprayed coatings

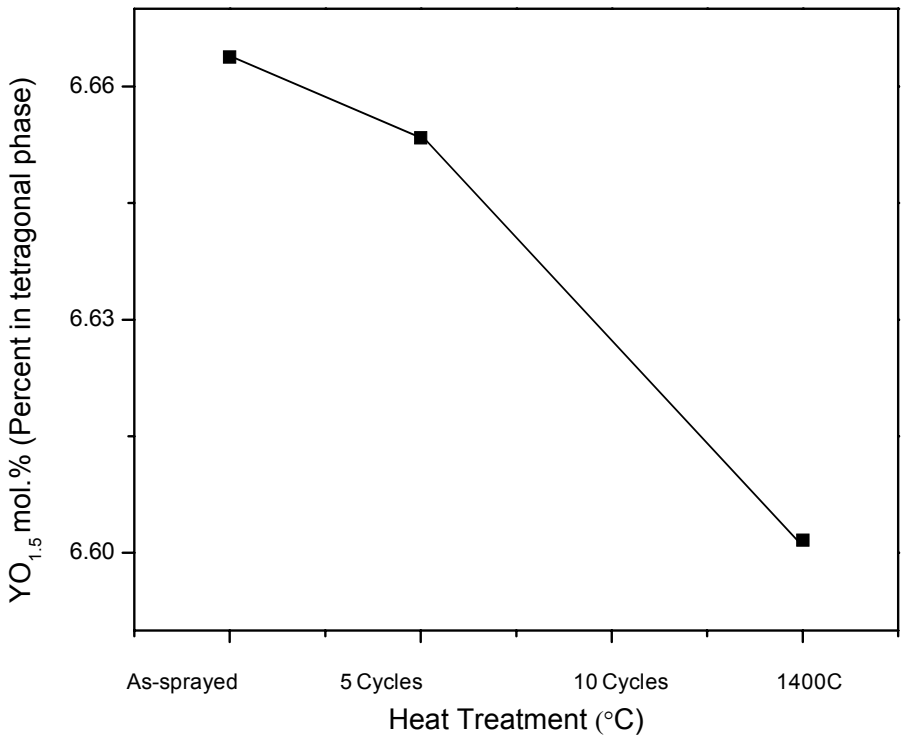

Figure 87 Calculated $YO_{1.5}$ mol.% of tetragonal phase coatings in YSZ based on heating regiments. Tetragonal molar percentage decreases with increased thermal cycles resulting in phase transformations in coatings.

5.2.4. Thermal Conductivity of Plasma Sprayed Coatings

Thermal conductivity measurements, Figure 88, were taken for the cases of as-sprayed coatings and thermal cycled coating materials. Unique to this study is that coatings of Ti-YSZ and YSZ were derived from precursor processing techniques. Results compared Ti-YSZ to YSZ which is the premier commercially available thermal barrier coating material. As-sprayed coatings of 7YSZ had a thermal conductivity of 0.925 W/mK and Ti doped YSZ had a thermal conductivity value of 1.015 W/mK. From Table 9, we report the average density for YSZ was approximately 4.6 for 7YSZ; however, there was a decrease in density for Ti-YSZ from 4.445 for as-sprayed, 4.427 for 5 cycles to 4.323. Thermal conductivity results of precursor prepared 7YSZ were less than those produced by commercially available powders.

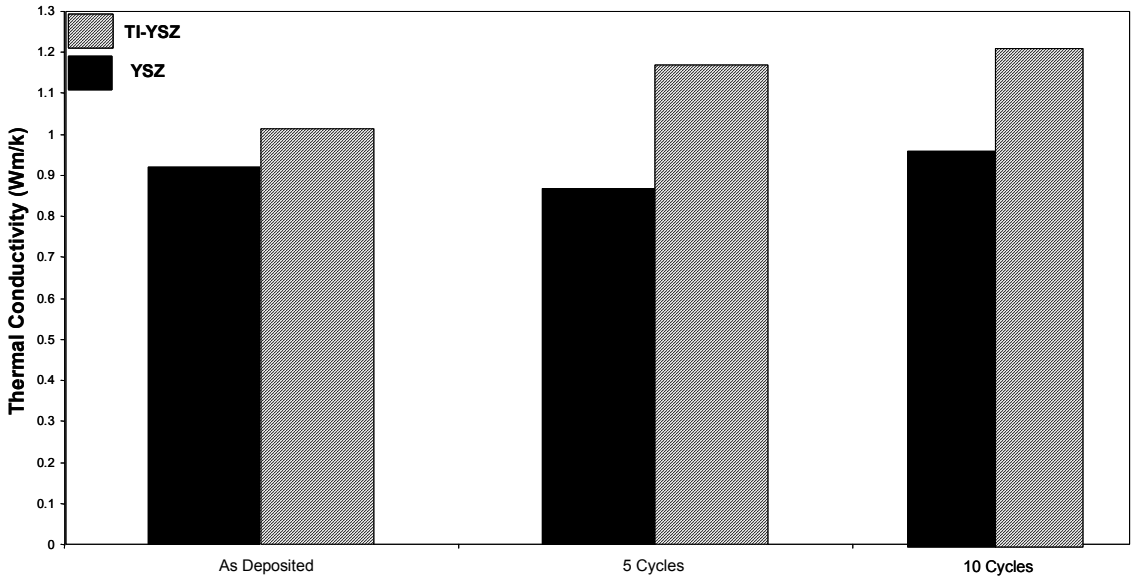

Figure 88 Thermal conductivity values for thermally cycled coatings of Ti-YSZ and YSZ powders reverse co-precipitation processing

Table 9 Thermal properties of as-deposited and thermally cycled coatings

Condition	Coating Material	Diffusivity (m^2/s)	Cp (J/(Kg K))	Density (kg/m^3)	Conductivity (W m/K)
As-Deposited	YSZ	0.00448	0.449	4.601	0.925
	Ti-YSZ	0.00526	0.434	4.445	1.015
5 Cycles	YSZ	0.00497	0.375	4.647	0.866
	Ti-YSZ	0.00637	0.41	4.427	1.167
10 Cycles	YSZ	0.00497	0.453	4.589	1.037
	Ti-YSZ	0.00669	0.452	4.323	1.308

5.2.5. Mechanical Properties of YSZ/Ti-YSZ Coatings

The mechanical properties of YSZ and Ti-YSZ of APS coatings are reported in this section with emphasis on microstructural variations due to heat treatments and their affect on coating properties. Micro-indentation for the measurement of the mechanical properties was taken for YSZ and Ti-YSZ APS coatings. The coatings were subjected to thermal cycles for temperatures of 1150˚C for 30 minutes followed by cooling in air for 15 minutes to observe the mechanical properties on thermal cycling. Coating materials were deposited on mild steel. Mechanically bending mild steel debonded the coating from the substrate material resulting in free standing materials. Table 9 shows that in the case of YSZ there is a decrease in the thermal conductivity from the as-sprayed coating to the coating cycled five times. The values for thermal conductivity were from 0.925 W/mK to 0.866 W/ mK and the modulus increased from 15.92 to 79.855 GPa. Figure 85 is a load versus displacement curve for YSZ and Ti-YSZ for as-sprayed coatings and samples that were thermal cycled five times. There

was less displacement in as-sprayed coating of Ti-YSZ compared to YSZ. The modulus for YSZ was 15.92 and after thermal cycling the modulus increased to 79.85. Based on this result it is possible that the increase is based on larger spacing in the as-sprayed coatings between splats and inter lamellar pores causing higher plastic depth and lower modulus. Heat treatment increased the sintering and densification rate therefore causing an increase in modulus. Ti-YSZ had less spacing between splats and was a denser coating in the as-sprayed state. However, the dominate defect in Ti-YSZ was globular pores in comparison to YSZ coatings. There was also less inter-splat spacing in comparison to YSZ.

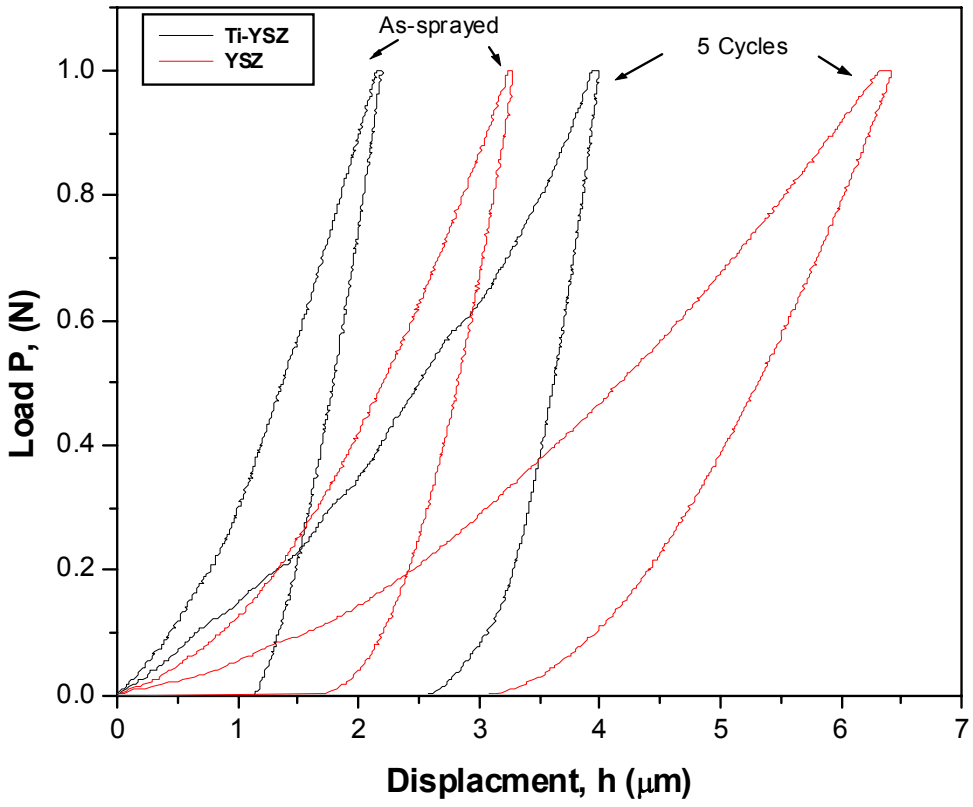

Figure 89 Micro-indentation of Ti-YSZ and YSZ freestanding coatings of as deposited and thermal cycled oxides

Table 10 Micro indentation measurements of as-sprayed deposits of Coatings. (differences in modulus results in YSZ in comparison to Ti-YSZ are the result of microstructural differences in coatings as explained in the following section)

	Max (Depth) (nm)	Plastic Depth (nm)	Max. Load (mN)	Hardness (GPa)	Er (GPa)	
YSZ	6584.23	4645.66	1000.45	1.92	15.92	*Mean*
	734.01	366.91	0.29	0.33	4.85	*S.D.*
Ti-YSZ	3416.90	2855.30	1001.49	5.37	85.33	*Mean*
	410.60	459.20	0.97	1.78	6.74	*S.D.*

Table 11 Micro indentation measurements of thermal cycled deposits

	Max (Depth) (nm)	Plastic Depth (nm)	Max. Load (mN)	Hardness (GPa)	Er (GPa)	
YSZ	3514.13	2933.17	1001.22	4.8583	79.855	*Mean*
	281.43	284.75	0.986	0.8529	9.44	*S.D.*
Ti-YSZ	3106.43	2621.48	1001.79	7.15	112.22	*Mean*
	623.20	652.19	0.988	3.818	24.60	*S.D.*

5.2.6. Microstructural Characterization of YSZ/Ti-YSZ Coatings

The objective of this section was to report the coating architecture of powders that were initially prepared by soft chemistry routes resulting in amorphous oxides due to low pyrolizing temperatures. In addition to as-sprayed coatings, coatings that were thermally cycled at 1100 C for one hour and rapidly quenched in air were investigated. Finally, the morphological stability of coatings as a function of thermal cycling were investigated. Approach was to use YSZ as standard and compare to effects of doped Ti-YSZ as well as influence and effects on thermal conductivity in coating materials.

Objective of microstructural investigations in coatings is to report:

- Phase relations in ternary system and affect on coating
- Morphological stability in coatings
- Observation of phase segregation in coating
- Coating architecture
- Correlate coating microstructure to thermal conductivity
- Correlate microstructure with mechanical strength of coatings

5.2.6.1. Morphological Stability in YSZ and Ti-YSZ

Figure 90 (A-B) shows SEM micrograph of as-sprayed YSZ and Ti-YAZ coatings. At low magnification, the microstructure has globular pores and regions that appear to be affects of small powder clustering. At high magnification, we observe interlamellar pores, intrasplat cracks and areas of un-melts. The defects associated with the coatings are classical characteristics of other YSZ coatings. After five thermal cycles, Figure 91 (A-B), there was less clusters and the reduction of some of the splat interfaces. Columnar equiaxed grains were also observed within the splats. After fifteen thermal cycles, Figure 93 (A-B), there is a reduction in the coating porosity; however the splat boundaries are still preserved. There was also an increase in grains with regions with clustering of un-melted particles increased sintering. Figure 94 illustrates air plasma sprayed coatings that were heat treated at 1400°C for 24 hours followed by rapid quenching in air. We also observed sintering of splat boundaries and a large reduction of pores. Figure 90 (C-D) is the micrograph of as-sprayed Ti-YSZ coating. The microstructure for Ti-YSZ was very unique in comparison to that of YSZ coating. In the high magnification image of as-sprayed Ti-YSZ we observe of the splat boundaries and interconnecting vertical cracks in the coating microstructure. However, the interlamellar pore structure is less in comparison to YSZ. Within the coating, we observe unique regions with clusters. We report that as-sprayed coatings of Ti-YSZ had are denser than as-sprayed YSZ coatings. Also, as-spray coating Ti-YSZ was denser than YSZ. Figure 91 (C-D), after the coating of Ti-YSZ was cycled five times; the coating has become denser in comparison to as-sprayed material. The splat boundaries are not observed; hence the material has experienced a degree of sintering. In the high magnification images, we can observe a unique level of crack networks.

The cracks network is random and they appear to be directly linked to the remaining pores of the coating structure. Another distinctive coating microstructure of Ti-YSZ is that there are observed "*clusters*" in the coating. The clusters ranged in sizes between 4-8 microns. The smaller circles within the clusters were in the range of sub- 0.5 microns. The clusters are circular, with many smaller cylindrical circles within them. As we increase the number of thermal cycles, it is observed in the low magnification images of an increased number of clusters (Figure 91, C-D). For the coating with 10 thermal cycles, it is also observed that the cluster sizes increased to greater than 10 microns with some clusters reaching nearly 60 microns in diameter. Within the larger clusters, there are cylindrical grains with sizes of approximately 0.5-1 micron. Some of the smaller clusters that averaged six microns or less and their microstructures are reported in Figure 92 (C-D). The smaller clusters are very porous. The inner cores have fine agglomerated particles with spherical dimensions. After 15 cycles Figure 93 (C-D), we observe an increase in the number of large clusters. There is no clear and visible indication of any splat boundaries and there is also little variation in the pore dimensions. In the micrographs, we also observe an increase in the grain size. The inner grains diameters doubled in comparison to coatings cycled five times.

In Figure 94 (C-D), we observe the microstructure of Ti-doped YSZ heat treated to 1400˚C and rapidly quenched in air. We did not observe any splat boundaries or micro cracks however, we do observe globular pores in the microstructure. Moreover, there is the observance of regions with dark phase fields that are non-cylindrical and average approximately one micron in length. Figure 100 is a high resolution image of Ti-YSZ. In the top eight microns of the coating, in the SEM micrograph, we observe the coating microstructure comprising of a large number of un-melted particles. The un-melted particles on

the surface of the coating are were less than three microns. The powder particles are in the shape of round spheres. In the center of the micrograph we observe a splat boundary in the center of the image. There appears to be a large white band at the splat interface. Under the white band we observe a unique microstructure. From the images we observe large clusters in coatings as observed in Figure 102 and Figure 103. However, with high resolution SEM within the clusters, we observe smaller particles. Clusters appear to be quenched in state by the plasma spray process and not un-melted particles. The results suggest that clusters are the result of segregation of the titania phase from the solid solution of the tetragonal phase (Figure 102). Figure 103 is a high resolution micrograph with a pore within the cluster. The image is of a globular pore; however we observe sub micron size particles near particle boundaries. Figure 103 is an SEM image at a splat interface. We observe a lamellae structure above the interface along with two un-melted particles. Below the splat interface we observe the clustering phenomenon.

Figure 98 and Figure 99 are the analysis of SANS measurements were for Ti-YSZ and YSZ coating conducted at the National Institute of Standards and Testing (NIST). The results show that the specific surface area for Ti-YSZ was higher than YSZ for the as-sprayed coatings. After the coating of Ti-YSZ was cycled five times, there was a reduction of the specific surface area from 2.7 to 1.7 m^2/cm^3. For 20 thermal cycles, the specific surface area remained about the same as the coating cycled 5 times (~1.5 m^2/cm^3). For the coating of YSZ, Figure 98, there was a small increase in the specific surface area from 0.55 m^2/cm^3 to 0.7 m^2/cm^3 for as-sprayed coating to five thermal cycled YSZ. For 20 cycles of YSZ, the surface area reduced from 0.7 to 0.6 m^2/cm^3. Results indicate that the reduction in surface area corresponds to the coating sintering. The SANS results provides information for the constituent porosity, opening dimensions and

orientation distribution of the void components. SANS results suggest low levels of anisotropy in coatings due to the contributions of voids or cracks along the spray direction (Figure 97).

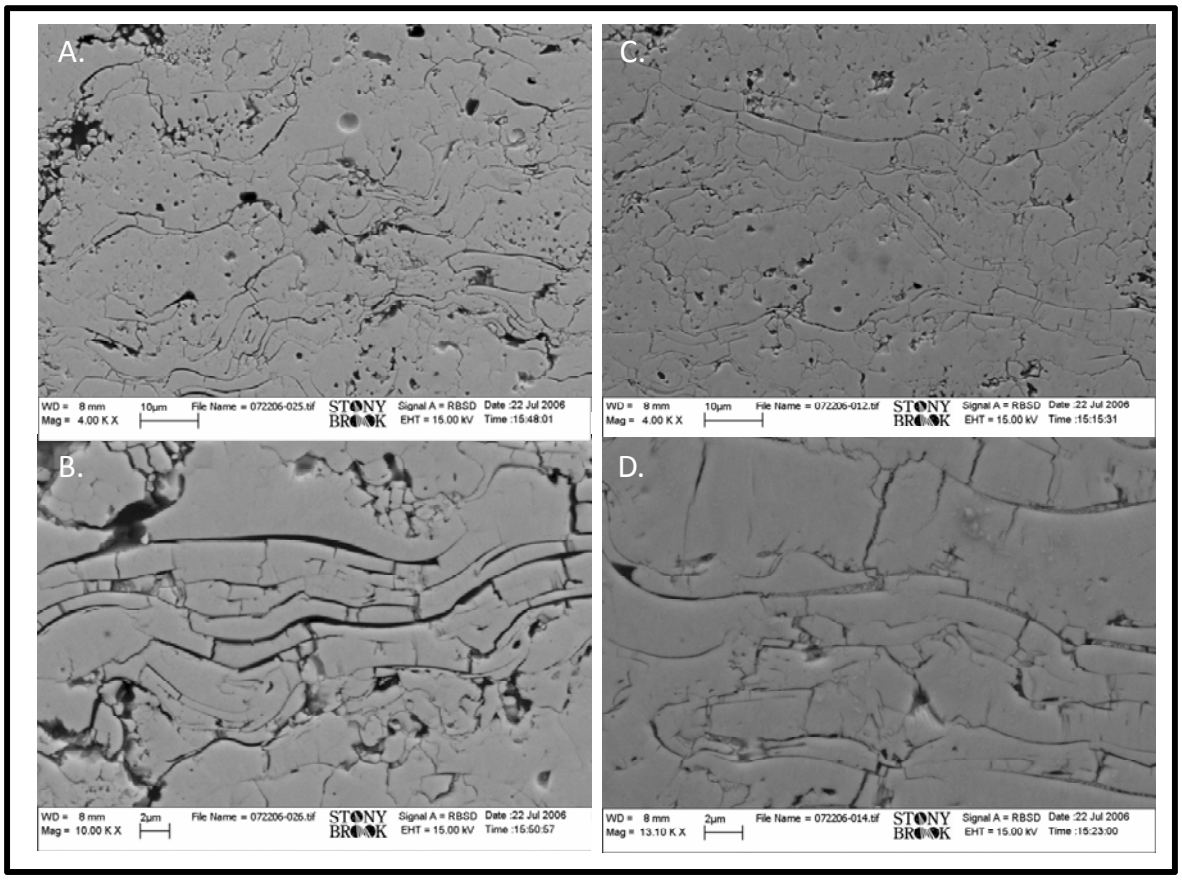

Figure 90 Low and High magnification images of as-sprayed YSZ ((A.) and (B.)) coating and Ti-YSZ ((C.) and (D.)) respectively. (Pore open dimensions are a lot smaller in Ti-YSZ in comparison to YSZ which explains sintering rate)

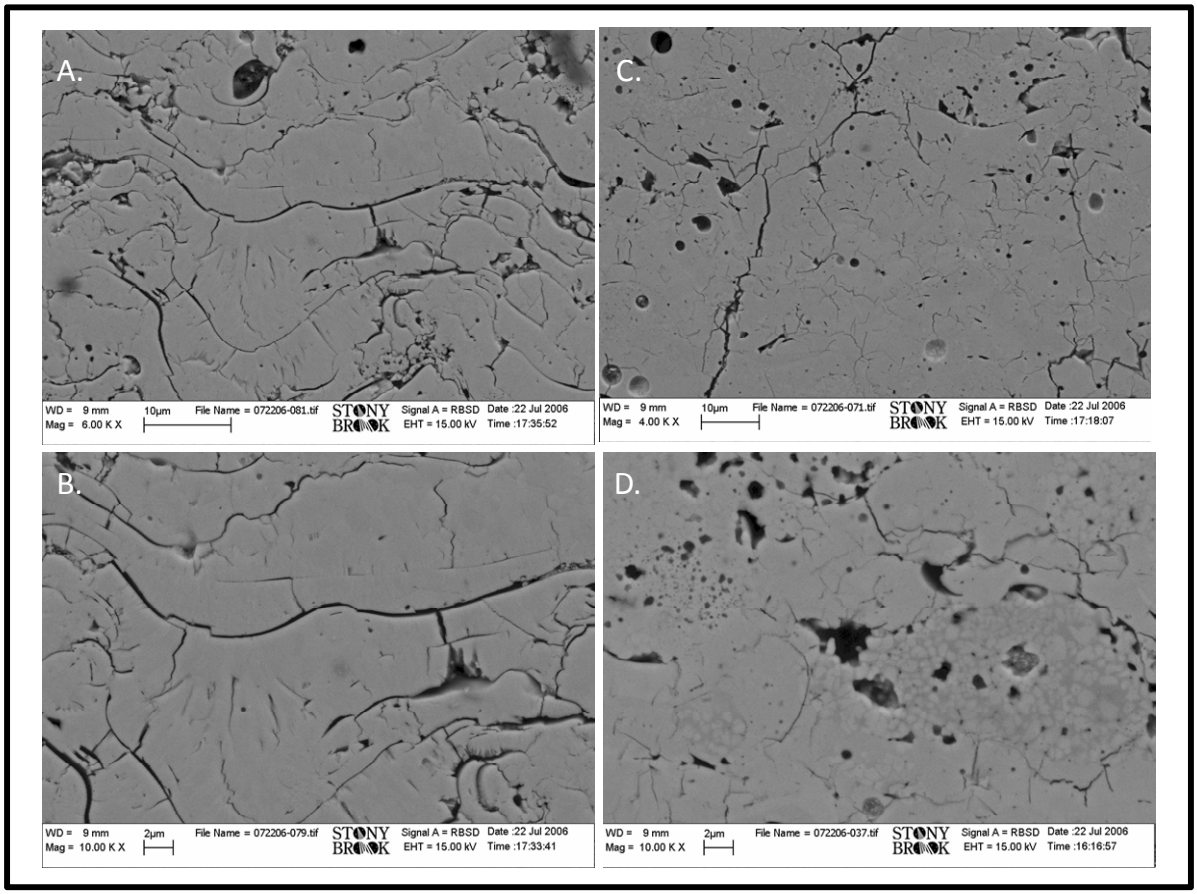

Figure 91 Low and High magnification images of coatings cycled five times for YSZ ((A.) and (B.)) coating and Ti-YSZ ((C.) and (D.)) respectively.

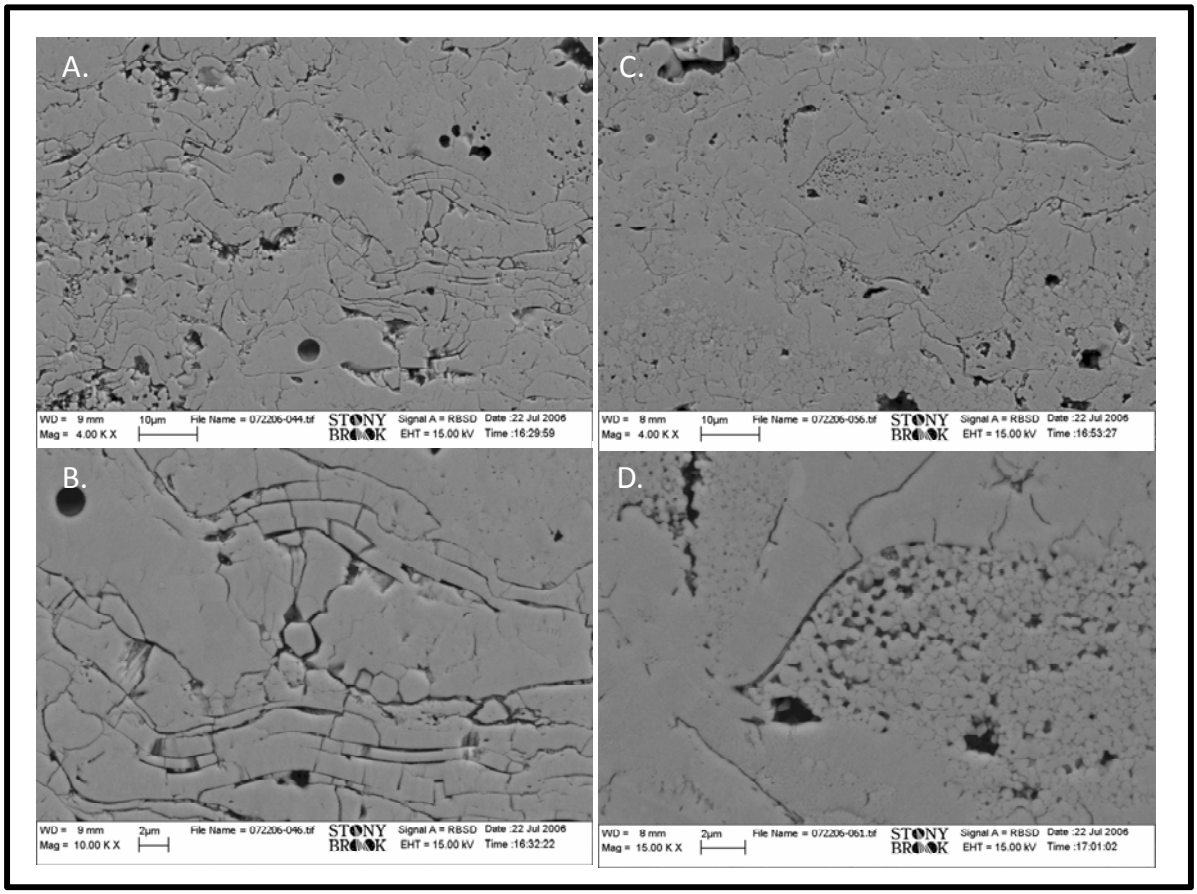

Figure 92 Low and High magnification images of coatings cycled ten times for YSZ ((A.) and (B.)) coating and Ti-YSZ ((C.) and (D.)) respectively.

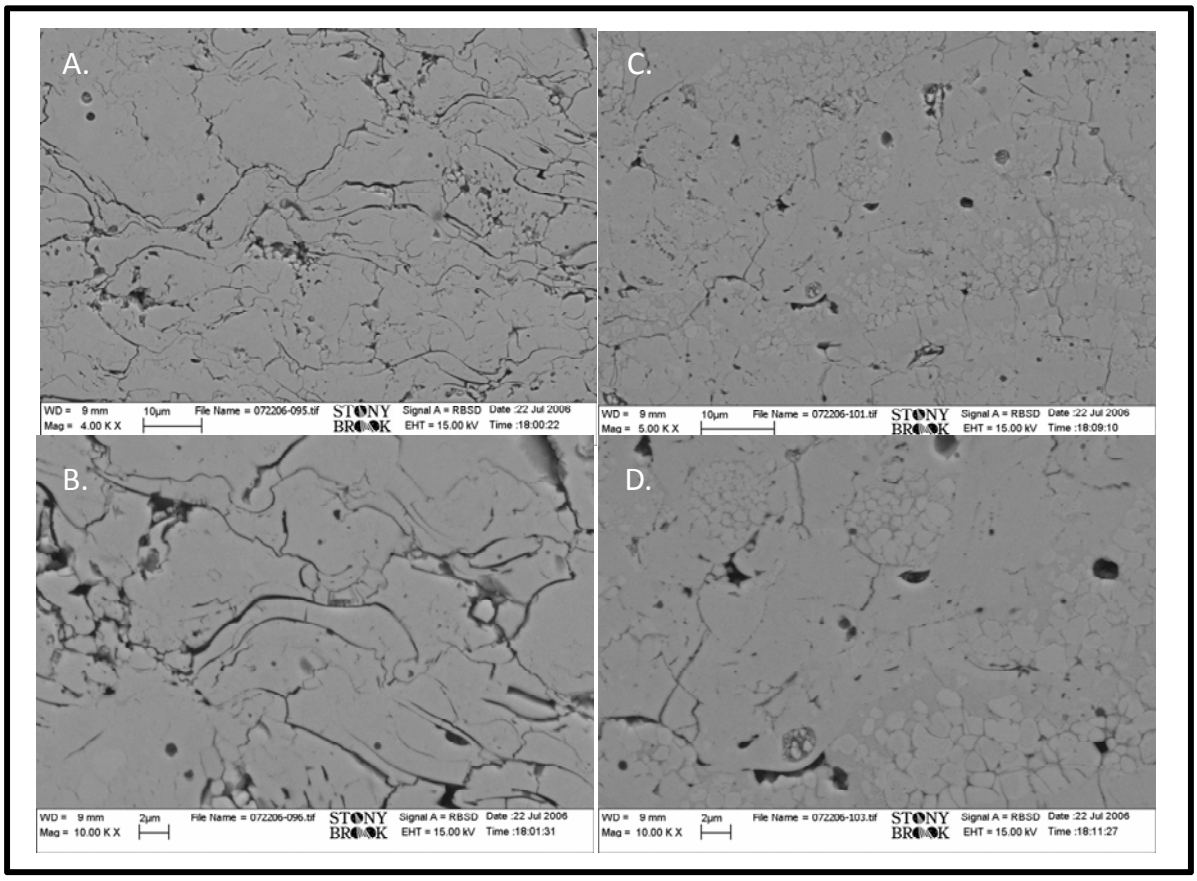

Figure 93 Low and High magnification images of coatings cycled fifteen times for YSZ ((A.) and (B.)) coating and Ti-YSZ ((C.) and (D.)) respectively.

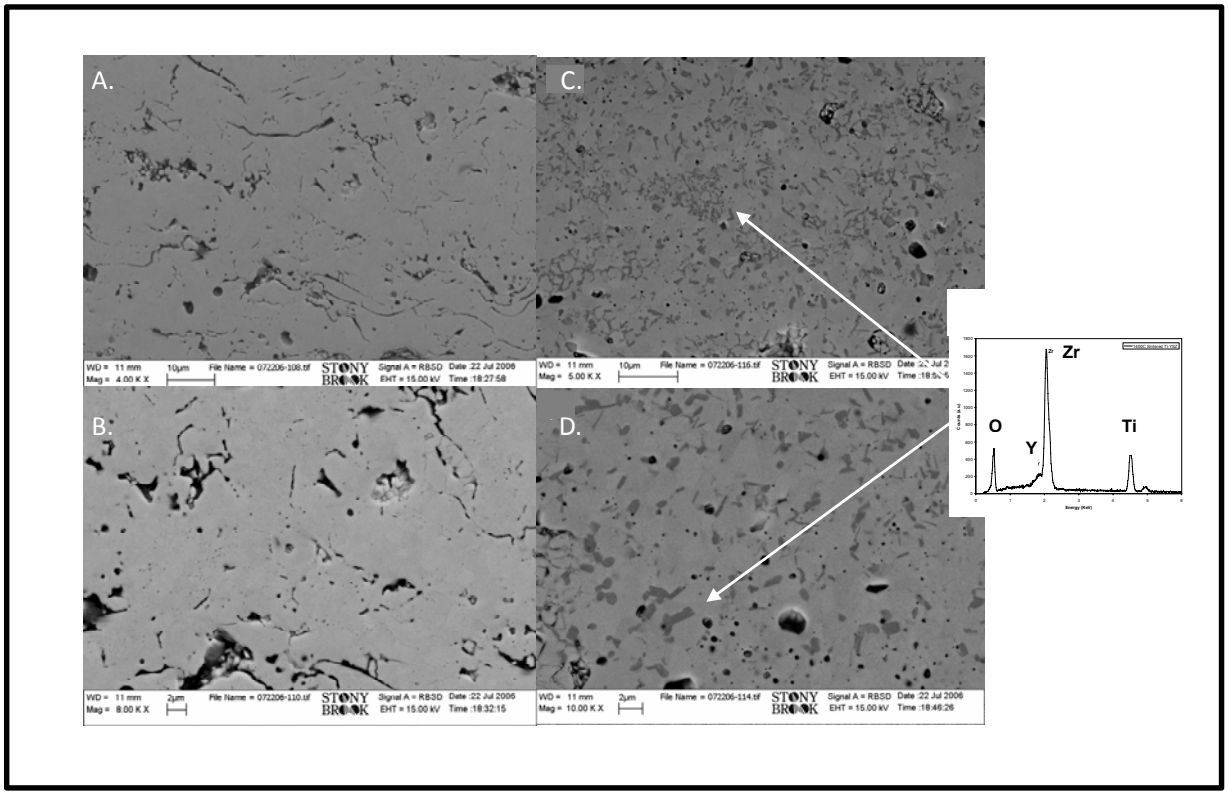

Figure 94 Low and High magnification images of coatings sintered at 1400˚C for YSZ ((A.) and (B.)) coating and Ti-YSZ ((C.) and (D.)) respectively.

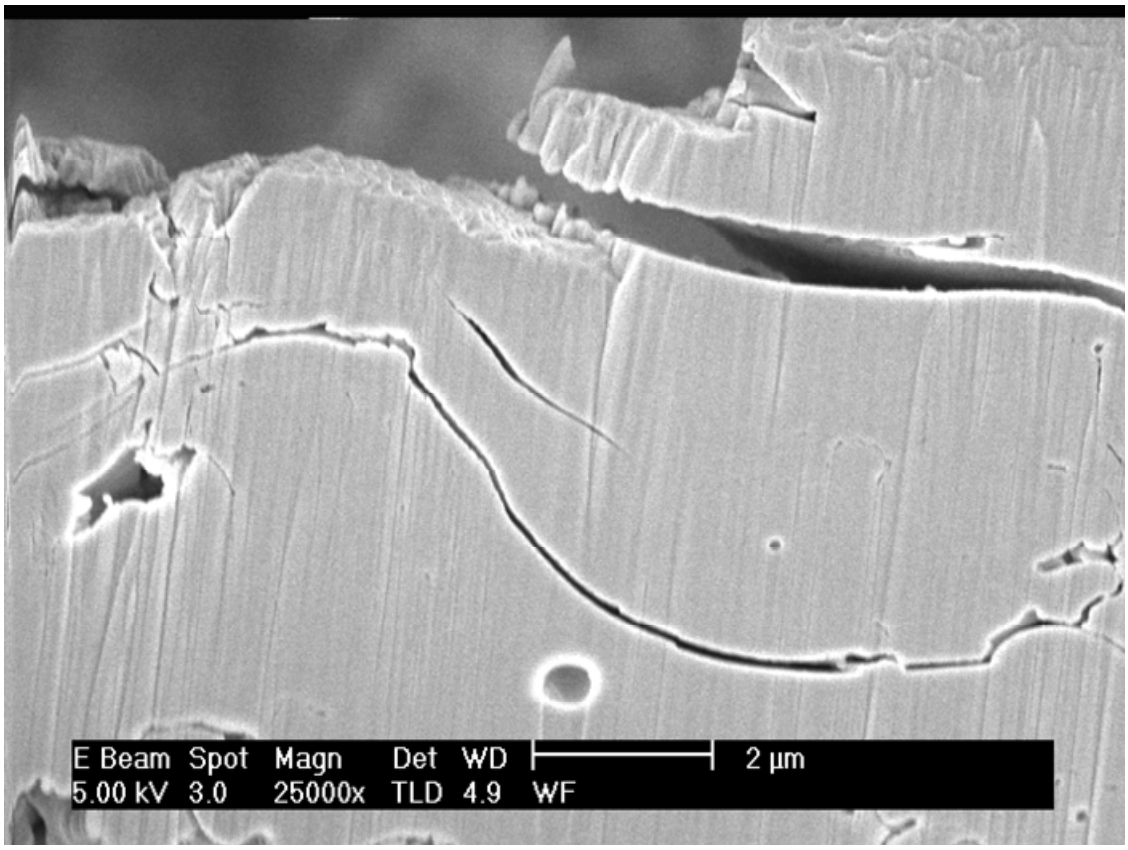

Figure 95 High resolution SEM micrograph of YSZ coating deposited by APS. Vertical columnar structure observed at interfaces of splat boundaries.

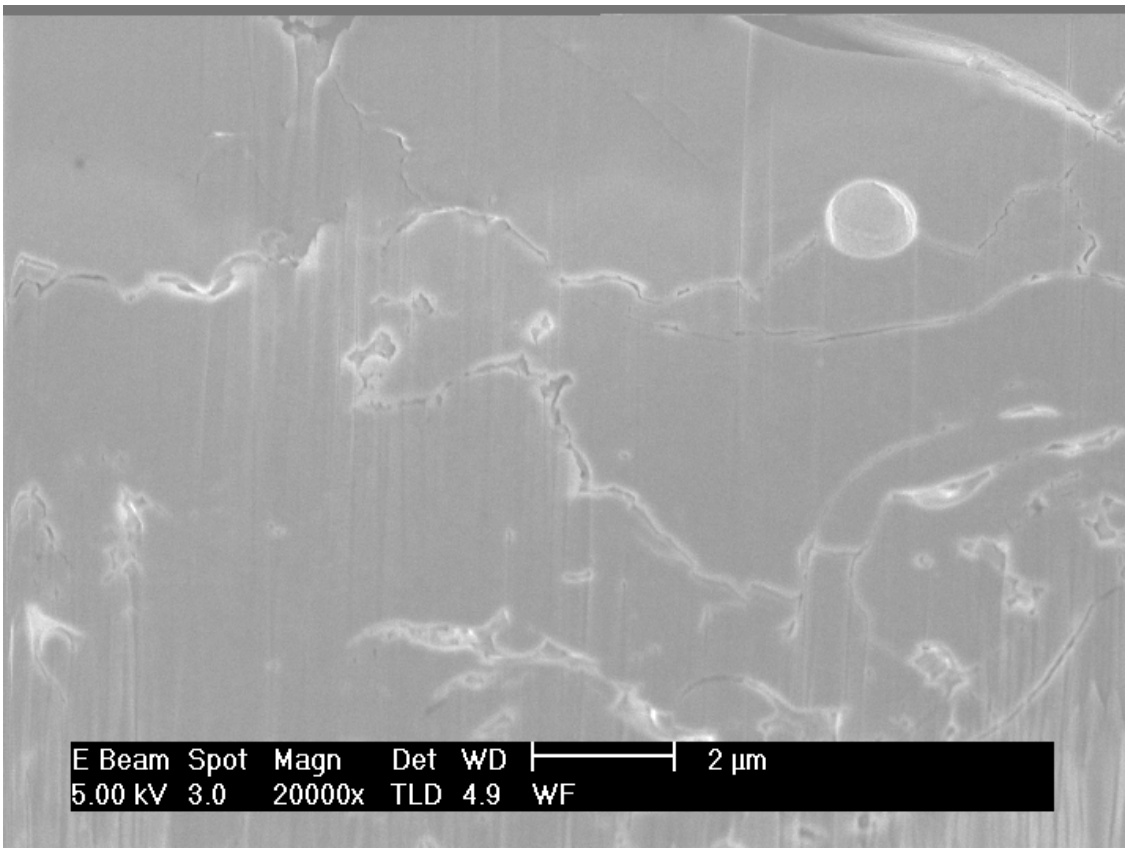

Figure 96 High resolution SEM micrograph of YSZ as-sprayed coatings

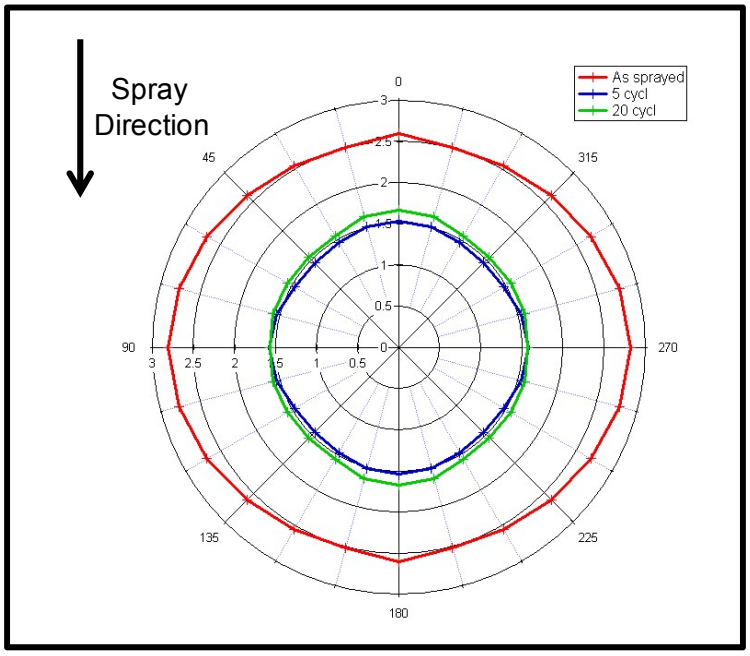

Figure 97 SANS Ti-YSZ for as-sprayed coatings and samples thermally cycled (five and twenty cycles)

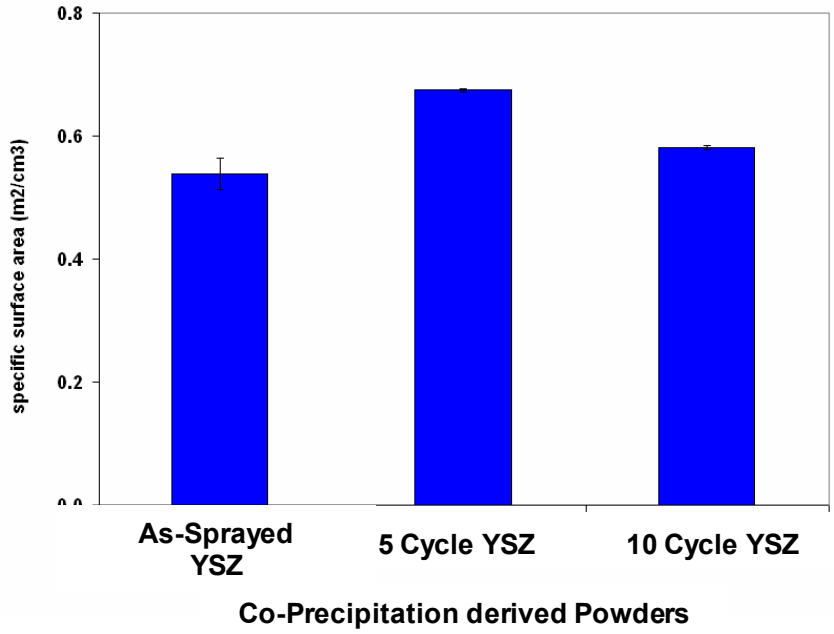

Figure 98 Specific surface areas (m^2/cm^3) of plasma spray coatings of YSZ. Measurements are of as-sprayed, five and twenty thermal cycles.

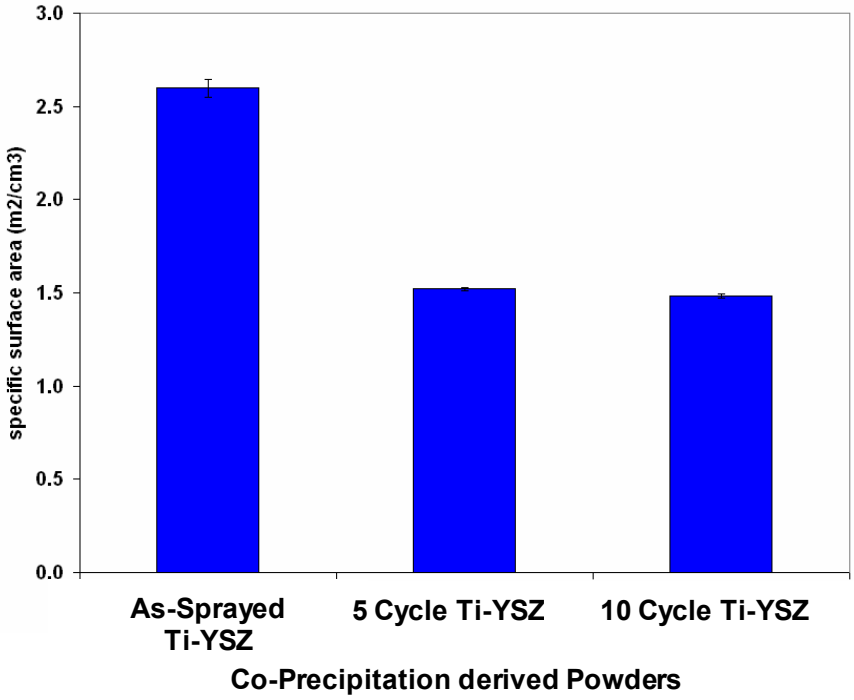

Figure 99 Specific surface areas (m^2/cm^3) of plasma spray coatings of Ti-YSZ. Measurements are of as-sprayed, five and twenty thermal cycles.

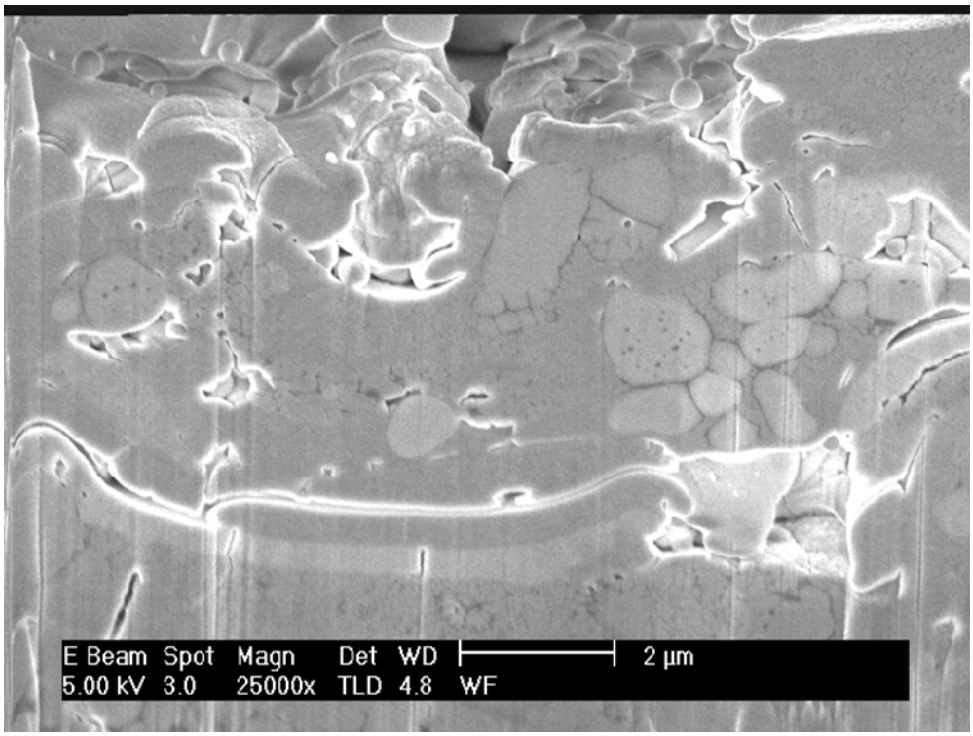

Figure 100 SEM micrograph of Ti-YSZ deposited by APS. Cross section of coating with un-melted particles near surface

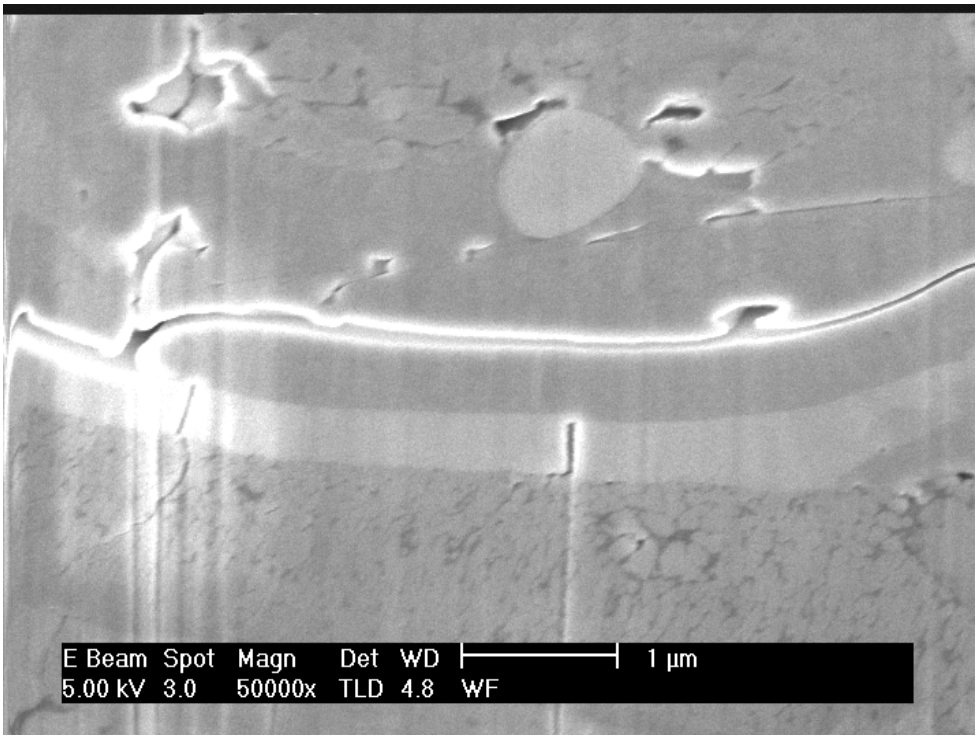

Figure 101 High resolution SEM micrograph of Ti-YSZ plasma spray coating at splat interface. (Phase segregation in coatings)

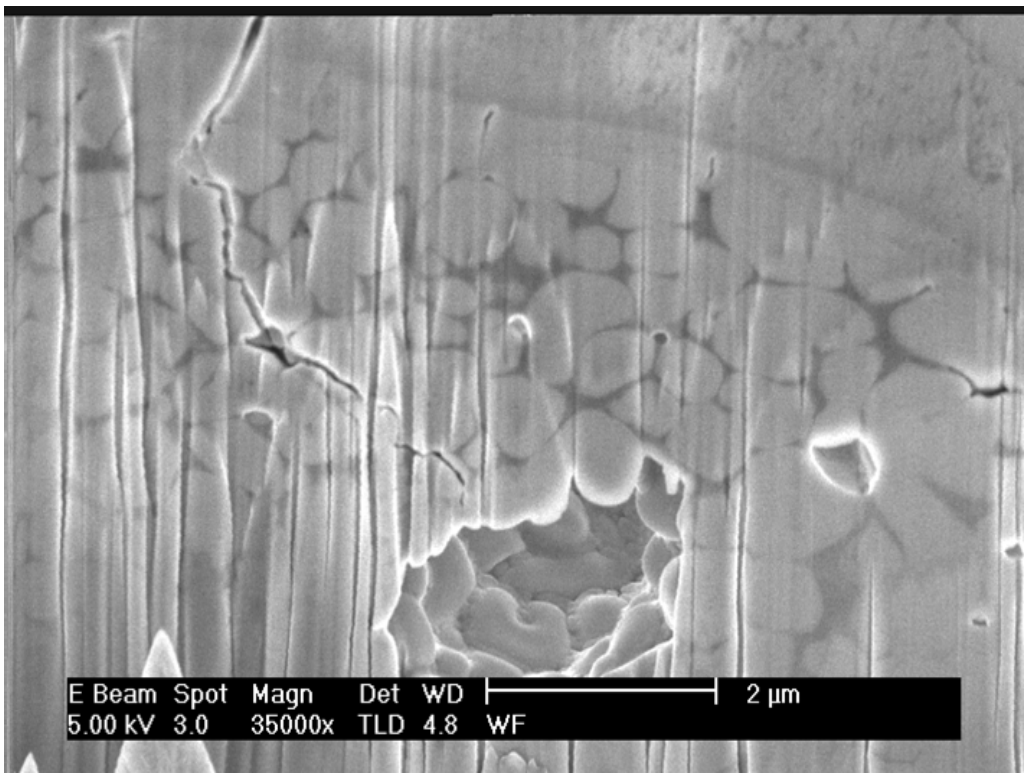

Figure 102 High resolution SEM micrograph of Ti-YSZ deposited by APS. Globular pore within coating. First stages of partitioning in Ti-YSZ coatings along grains.

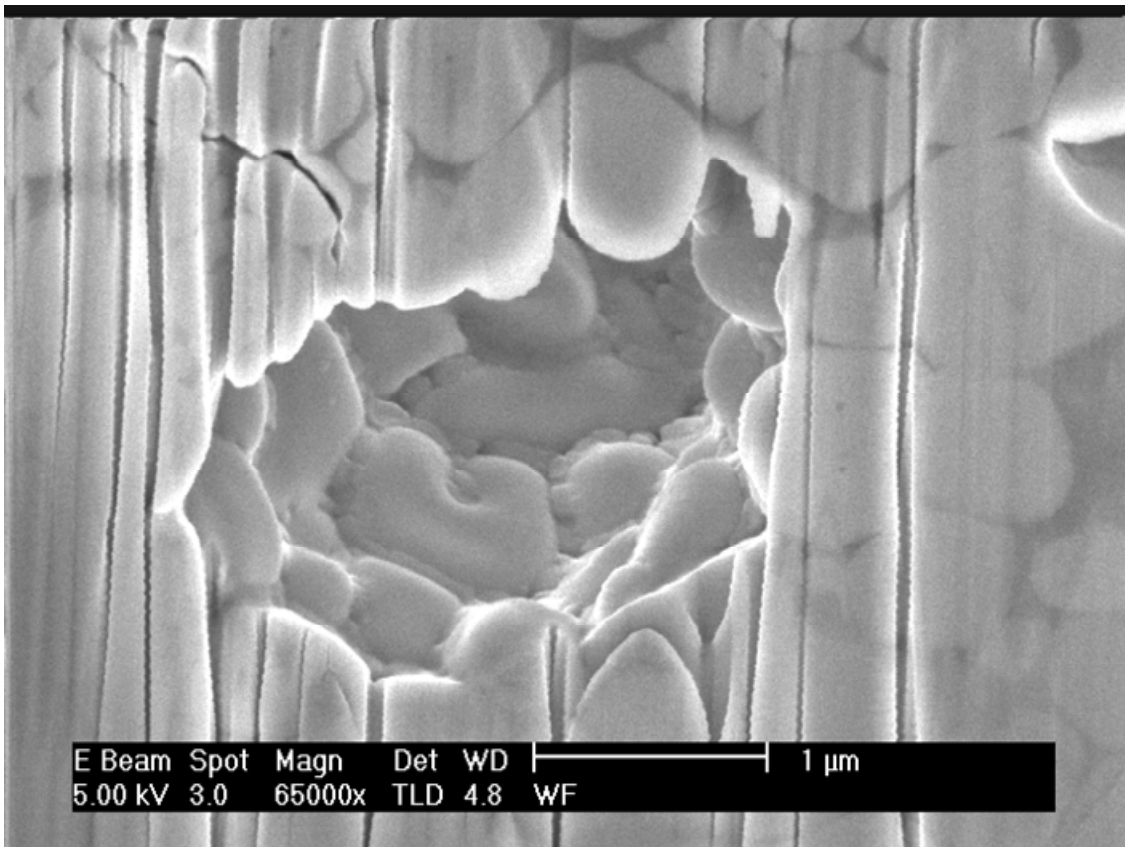

Figure 103 High resolution micrograph of globular pore in Ti-YSZ

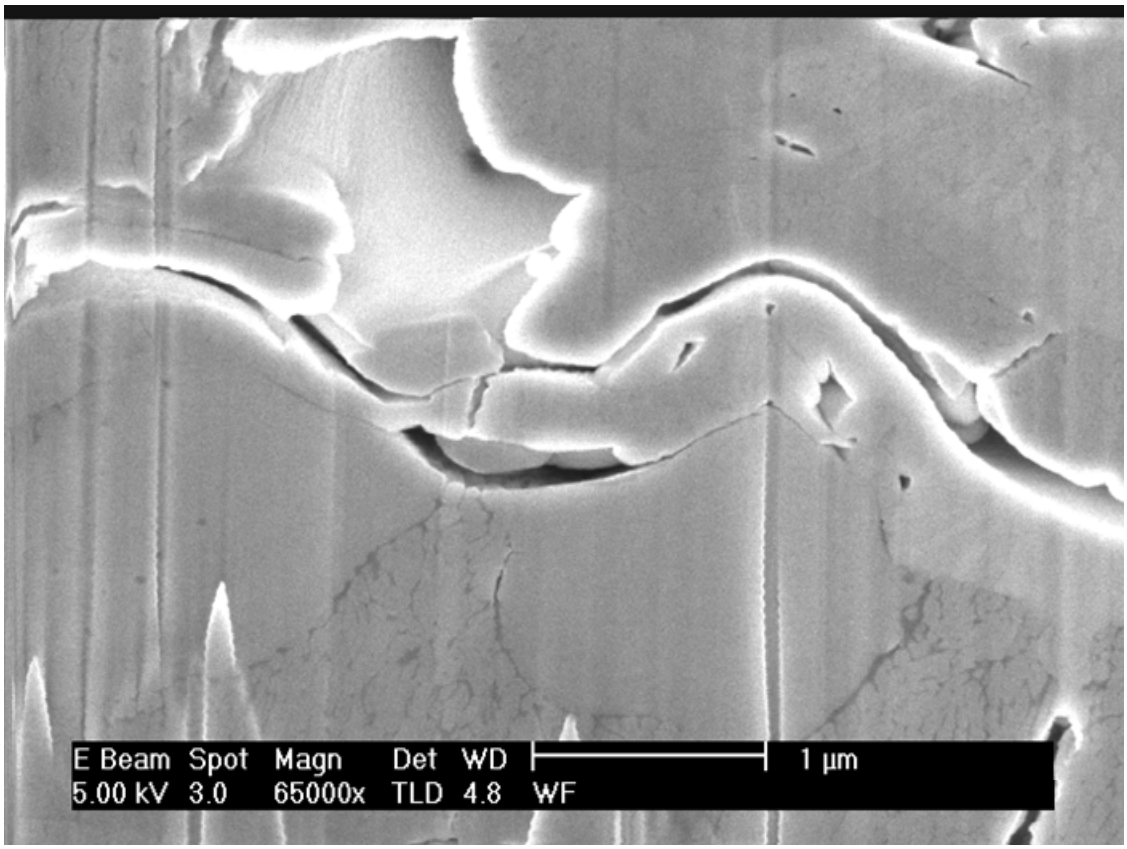

Figure 104 High resolution SEM micrograph of Ti YSZ coating. Observed splat boundary is in center of image. Particle un-melts observed and unique grain structure

5.2.7. TEM Characterization of As-sprayed Coatings

Bright-field TEM micrograph shown in Figure 105, is low magnification image of edge of splat in YSZ coating. Image depicts columnar grains that are 0.1 μm in width by 0.2 μm in height. Figure 106 is a TEM micrograph of inter-splat boundary and a micro-pore. At higher magnification Figure 106 (bottom), lamellae structure is clearly visible. Lamellae columnar grains extended approximately 1.0 μm in length and were less than 0.1 μm in width. In select regions of coatings, TEM micrographs showed polycrystalline grains. Grain diameters were approximately 150-200nm. The splats were one micron in thickness and approximately four microns in length. The grains have texture due to crystal orientation differences. We also observe inter-splat pores in the TEM micrograph. In Figure 106, we observe small cracks in coatings and equixaed grains. For higher magnification images, figure 98 (bottom) we observe the lamellae structure with alternating grain textures and non-textured grains near splat edges and pores. Examination of the TEM micrograph for the microstructure of the non-crystalline powder had the presence of equiaxed grains and columnar grains. Fine equiaxed grains are a result from homogenous nucleation of a highly under-cooled melt, while the columnar grains growth are from heterogeneous nucleation at splat boundaries where higher gradient of cooling rate exist.

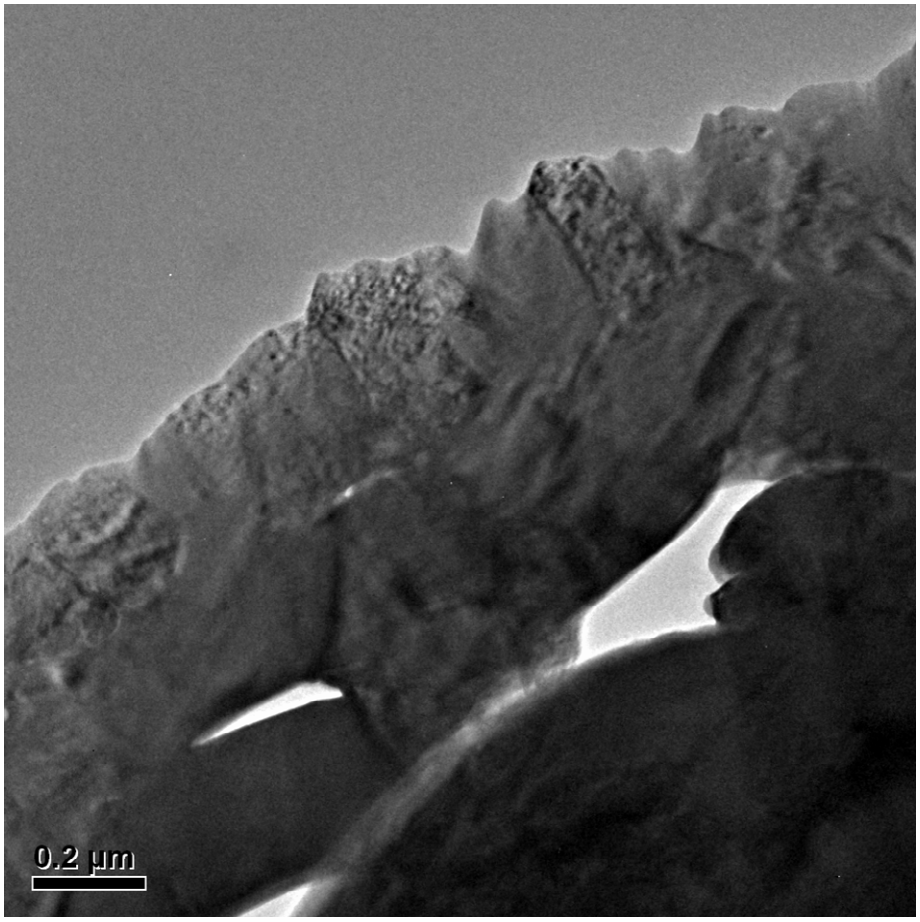

Figure 105 High resolution TEM micrograph of YSZ coating illustrating splat interface, grains and lamellae structure

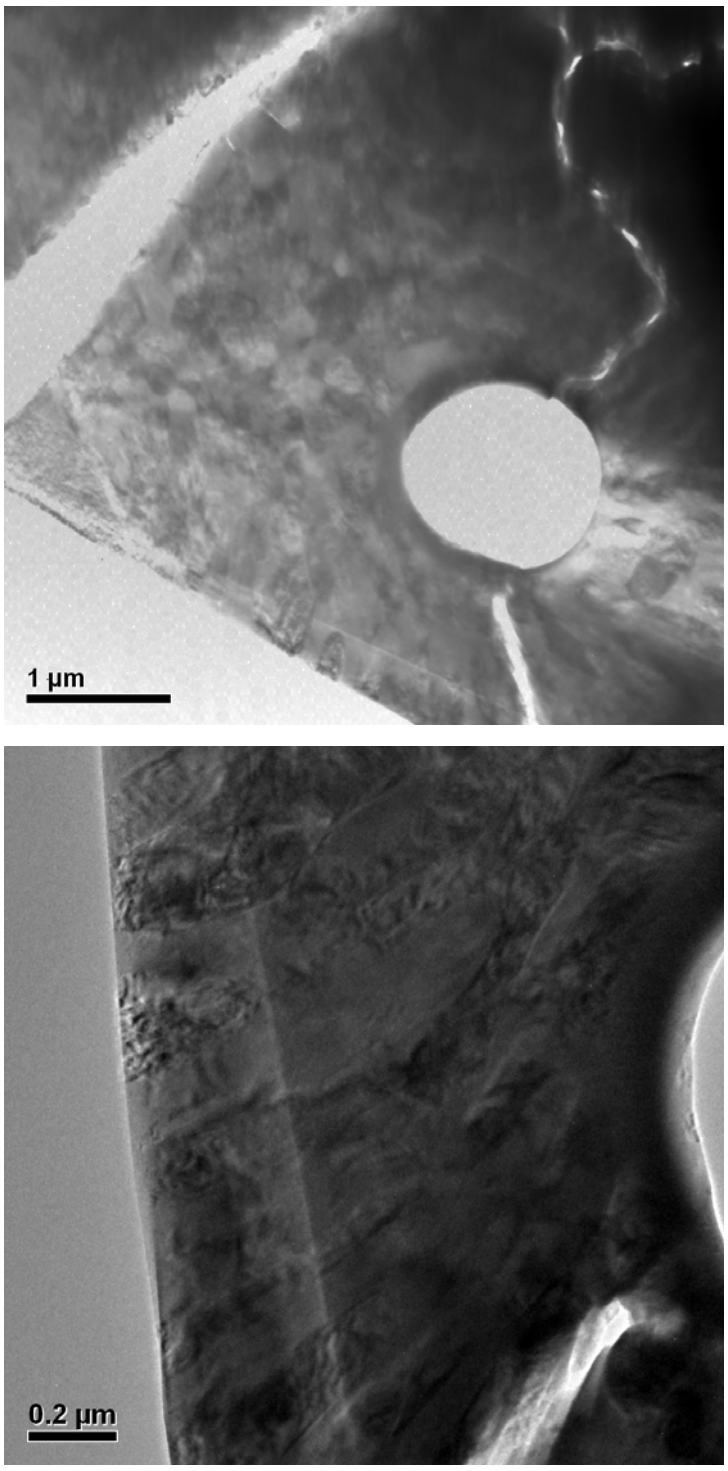

Figure 106 (Top) TEM micrograph near pore (Bottom) High magnification of select region to illustrate lamellae grains

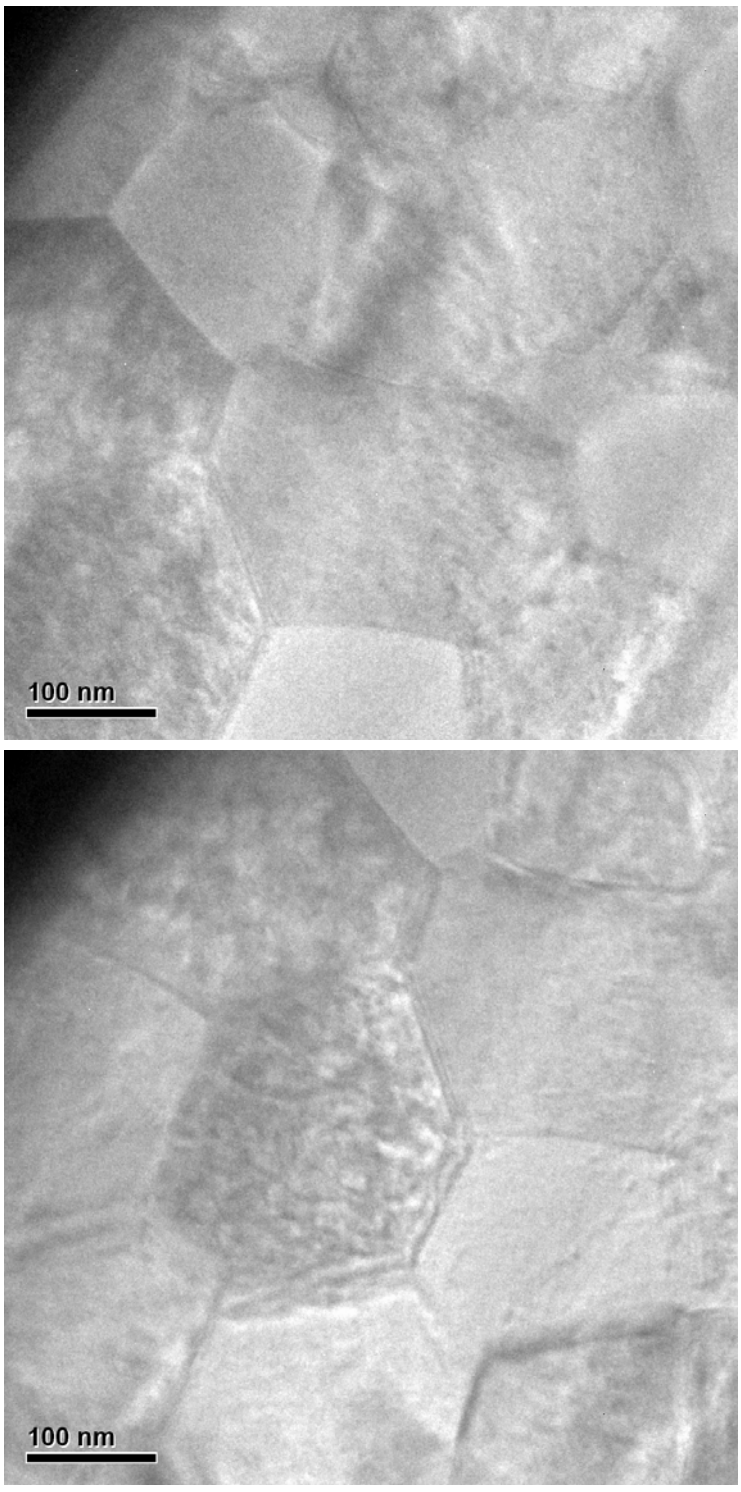

Figure 107 TEM Bright-field micrographs of polycrystalline grains in YSZ coatings

5.3. Conclusion and Summary

This chapter demonstrated that the functional oxides of pyrochlore and tetragonal phase oxides (YSZ and Ti-YSZ) investigated in this dissertation were successfully deposited by plasma spray from amorphous powders. The microstructure, properties, morphological stability of coatings and phase evolution of the coatings are summarized in the following sections for microstructure properties, morphological stability and structural evolution of coatings. The motivation was to investigate coatings that were synthesized by soft chemistry routes prepared at Stony Brook University Center for Thermal Spray research (CTSR). Our objective for this investigation was to: (1) synthesize powders by precursor processing to create homogenous compositions of YSZ, Ti-YSZ and pyrochlore oxides. (2) Use low pyrolizing temperatures to keep compositions in amorphous state and study the affect of starting materials compositions on coating properties. (3) Study micro-structure and phase of oxides. (4) Investigate the mechanical and thermal properties for select compositions as a potential TBC material.

5.3.1. Plasma Spray Coating of Pyrochlore Oxides

This study investigates two series of compositions by thermal spray; (I) Chemical formula for compositions in tie-line $Y_2Ti_{2-y}Zr_yO_7$ referring to pyrochlore and fluorite phase transitions (Zr for Ti). (II) Chemical formula for a second tie-line, $Y_{2-x}Ti_2Zr_xO_{7+x/2}$, substituting for Y and Ti. For compositions along the first tie-line (I) we were successful in depositing RF spray for compositions near pyrochlore region. The final coating phase was fluorite. For the chemical formula of $Y_{1.6}Ti_2Zr_{0.4}O_{7.2}$, plasma coatings revealed that starting material feedstock phases affects the final coating microstructure. Powders with starting

phase of amorphous oxides were of pyrochlore phase, however, when starting phase was pyrochlore and rutile, the final coating structures was that of pyrochlore and rutile. SEM micrographs of as-sprayed coatings of amorphous powders revealed porous coatings with large globular pores. There were also observations of segregation in coating structures between splat boundaries. EDS results determined that there were regions of zirconium-rich and titanium-rich. RF Sprayed coatings showed fluorite structures with As-sprayed coatings compared to APS coatings that lead to pyrochlore phase. For the composition of $Y_{1.6}Ti_2Zr_{0.4}O_{7.2}$ (II) we addressed the difficulties of measuring attainable material properties caused by the loose structure of RF sprayed coatings. As a secondary option, we synthesized powders that were in the amorphous state by using precursor processing and pyrolizing oxides at low temperature. Our results showed that the starting powder phase influences final coating phase in complex oxide systems.

5.3.2. Plasma Spray of Tetragonal Phase Oxides: YSZ and Ti-YSZ

5.3.2.1. Phase Formation in Coatings

Zirconia stabilized with yttria as-sprayed coatings revealed that deposited phase was tetragonal prime (t') oxide. Peaks between $72^\circ<\theta<76^\circ$ to distinguish the tetragonal prime and the cubic phase were not discernable for as-sprayed coatings Ti-YSZ ($7.6YO_{1.5}$-TiO_2-77.2 ZrO_2). However, after heat-treatments the metastable tetragonal phase was observed. In APS coatings of as-sprayed coatings ions are randomly distributed. Annealing samples of YSZ cause Y^{3+} ions to diffuse due to lower free energy and partition into regions with Y^{3+} ion depleted regions (tetragonal zirconia) and into regions with excess Y^{3+} ions (cubic). With thermal cycling temperatures of 1100°C we observed partitioning in both YSZ and Ti-YSZ into the cubic and tetragonal phase. The transformation

kinetics was slower in YSZ in comparison to Ti-YSZ. In the as-sprayed coating we observed a secondary phase of rutile, however, as the heat treatments increased the rutile peak reduced. Possible explanation is that the rutile phase re-mixed into the structure. At high temperatures of 1400°C coatings of YSZ and Ti-YSZ partitioned into the cubic and tetragonal phase. However, no monoclinic phases were detected in both material systems. The degree of partitioning was higher in Ti-YSZ compared to YSZ as illustrated by the separation of the (400)/(004) cubic and tetragonal peaks. According to the ternary diagram, the composition of Ti-YSZ should be tetragonal at equilibrium. In coating materials, the composition of Ti-YSZ did not transform to the equilibrium phase. Suggest that when samples are annealed, they redistribute and partition into regions of rutile, tetragonal and cubic phases. A promising result was that the tetragonality in Ti-YSZ was higher than YSZ.

5.3.2.2. Microstructural Characterization of Coatings

The microstructure of YSZ coatings by amorphous oxides complimented findings of previous studies of non-amorphous coatings. We observed microstructure with typical coatings characteristics that include interlamellar pores and cracks. In the second scenario of fabricating Ti-YSZ coatings, powders were synthesized and thermally sprayed using the exact same procedures as YSZ. Although both oxides were prepared under the same conditions, Ti-YSZ had vastly different microstructures. Ti-YSZ suffered from clusters in the coatings. We observed the onset of segregation in starting oxides in the form of small clusters. We presume that clustering was an affect of the thermal spray process and a function of particle size and shape variations. In the SEM micrographs we observed that smaller particles tend to adhere to large powders during plasma spray. The combination of un-melts and melted particles appear to be regions

where clustering in coatings were observed. After heat-treatment samples, clustering regions increased. We presume that Ti^{4+} redistributes into regions to form TiO_2 in coatings.

5.3.2.3. Thermal Conductivity of Coatings

The addition of titanium caused an increase in the thermal conductivity of coating deposits and thermal cycled coatings. YSZ as-deposited coatings had a thermal conductivity value of (0.925 W/mK) compared to 1.015 (W/mK) for Ti-YSZ. Comparisons of the thermal conductivity values showed a slight decrease in the thermal conductivity value of YSZ from the as-sprayed coatings to the coating that was cycled five times. Comparisons of the thermal conductivity values of the as deposited and thermally cycled coatings were made. It was found in all three cases that Ti-YSZ had slightly higher thermal conductivity values than YSZ. Results for higher thermal conductivity may be explained due to the influence of the smaller atomic mass of Ti 4+ in comparison to Zr^{4+}. The increase is likely due to densification and less scattering sites of the material as it was heat-treated.

Chapter 6: Conclusion

6.1. Synthesis of the Current Work: Linkage of Precursor Development of Powders with Plasma Spray Coatings

The results presented in this dissertation demonstrate that thermal spray is a viable technique to deposit functional oxides of zirconia with the addition of titania system and pyrochlore oxides. The results also suggest the possibilities to use solution directly deposited by RF spray with producing oxide materials with pyrochlore, tetragonal and perovsikite structures. The primary motivation of this work was to investigate novel composition by using diffraction techniques to interpret phases up to the equilibrium temperatures and translate the structural work to thermal spray coatings. The ternary oxide system of $YO_{1.5}$-ZrO_2-TiO_2 offer compositions with various electrochemical properties. Research has shown that compositions having pyrochlore crystal structures exhibit low thermal conductivity and mixed electronic-ionic conductivity. Until now, very few compositions of this ternary phase system have been unexplored. Traditional solid state synthesis methods of complex oxides require heat treatment of Y_2O_3, TiO_2 and ZrO_2 at temperatures greater than 1500˚C for several days. Soft chemical approach such as chemical precipitation offers excellent opportunities to synthesis these oxides with homogeneous compositions at low temperatures. For this dissertation, synthesized powders include a pyrochlore oxide ($Y_{2-x}Ti_2Zr_xO_{7+x/2}$), baseline YSZ (7.6 mol% Y^{3+}) and Ti-YSZ. A detailed structural investigation was essential to determining the validity of the currently available equilibrium diagram that is based on theoretical computational methods. Our findings have led to a better understanding of phase development in compositions of interest. These results are summarized in phase evolution maps.

Some remarks on the phase evolution maps:

- A comprehensive study on phase formation for all temperature and compositions from an amorphous precursor to its final equilibrium phase
- The extent of metastability in precursor derived powder
- A guideline for phase formation for plasma sprayed compositions providing information on thermal history.
- The effect of substitutions on phase formation
- The structural changes that may occur with compositional variations in a solid solution

Fundamentally, the phase evolution studies contributed to our structural understanding for chemical compositions in the $YO_{1.5}$-ZrO_2-TiO_2 system. In addition, provide guidelines on phase stability at low temperatures; understand the kinetic phase transformation and the effect of substitutions and/or co-doping on crystallization. The motivation of the phase evolution study was to determine how structural changes in this system influence coating development in plasma spray coatings. The thesis presented a detailed analysis of the structure of the $Y_{2-x}Ti_2Zr_xO_{7+x/2}$ pyrochlore oxide and Ti-YSZ ($7.6YO_{1.5}$-$15.2TiO_2$-$77.2ZrO_2$.). Emphasis on synchrotron based *time-resolved* XRD was compiled for pyrochlore compositions. Moreover, *time-resolved* synchrotron diffraction was used to observe the phase evolution of this system and to study the hierarchy of phase selection in these synthesized powders.

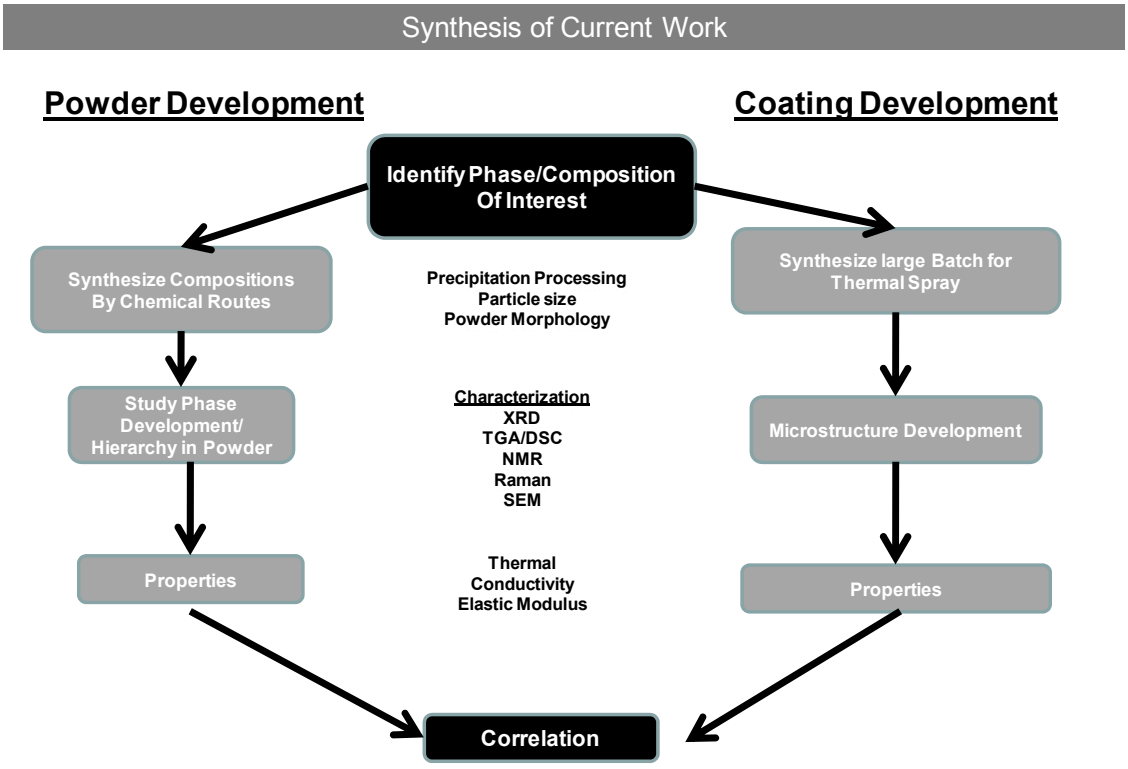

Figure 108 Diagram illustrating synthesis of this dissertation representing correlation between powder developments and coating development with $YO_{1.5}$-TiO_2-ZrO_2 ternary diagram

6.2. Contributions of this Dissertation in the System of $YO_{1.5}$-TiO_2-ZrO_2

Today, there remain many challenges for fabricating functional oxides. In particular, when depositing by rapid quench techniques such as plasma spray, processing parameters and phase stability of desired chemical compositions are critical to coating durability and life-predictions[61]. Equilibrium phase diagrams, representing compositions in ternary oxide systems, are crucial; however, they do not represent possible metastable phase states and transformations paths of crystallization for different chemistries/compositions. One of the conventional approaches for developing thermal barrier coatings materials is by utilizing compositions that are thermally stable at high temperatures. The current TBC utilize 6-8 wt% yttria-stabilized zirconia is approaching its high temperature stability limit. However, the system of $YO_{1.5}$-ZrO_2-TiO_2 is highly unexplored and it has phases (pyrochlore and tetragonal) that are promising as a potential replacement material in TBC and solid oxide fuel cells. Although the chemistries are complex, plasma spray powders of precursors were able to achieve desired phases. In thermal spray, due to its high cooling rates, stabilized metastable states have proven to be critical in enhancing material properties in areas such as thermal barrier coatings. As thermal barrier coatings oxides chemistries become more complex, the relationship between precise starting feedstock and coatings becomes important. Among these concerns, is addressing the difficulties of depositing these multifaceted oxides by plasma spray.

In this dissertation, we identified the phase stability limits of compositions with the ternary system. The results contributed to a novel phase diagram with modified phase fields in $YO_{1.5}$-TiO_2-ZrO_2. In order to develop these oxides in coating systems, we must understand the structure/phase development in

powders and how they pertain to final coating structure and properties. This dissertation also demonstrated the versatility in thermal spray to produce coating materials of pyrochlore, perovskite and tetragonal oxides with precise chemistries from powders synthesized from soft chemistry methods. The following sections detail findings in candidate phases of interest. This dissertation was divided into two sections; identifying candidate material compositions and evaluating coating properties derived by soft chemistry synthesized powders. Furthermore, we identified the thermal stability and phase fields of select oxide compositions. Our results contributed to modifications of the phase diagram of $YO_{1.5}$-TiO_2-ZrO_2 that was originally proposed on theoretical values in comparison to our experimental results. The following sections highlight the contributions of the pyrochlore and tetragonal oxide powder evolution studies and coating evaluations.

(i) Phase evolution in Pyrochlore Oxides

Chemical co-precipitation methods were used to synthesize the powders in the system $Y_{2-x}Ti_2Zr_xO_{7+x/2}$. One of the major contributions of this work was to us chemical precipitation methods to synthesis these oxides with homogeneous compositions at low temperatures. Results from the phase evolution of pyrochlore oxides contributed to modifications of $YO_{1.5}$-TiO_2-ZrO_2 ternary phase diagram, originally based on theoretical studies in comparison to our new experimental values. The novel phase fields were re-drawn reflecting our findings. Because of low synthesizing temperatures, our experimentations revealed a large range of metastable (non-equilibrium phases) compositions of pyrochlore, fluorite and amorphous phases. This work also contributed to proving experimentally the low thermal conductivity values obtained for compositions with A and B cation substitutions in $Y_{2-x}Ti_2Zr_xO_{7+x/2}$. The values

were lower than YSZ, thus the potential candidate material for pyrochlore oxides in $YO_{1.5}$-TiO_2-ZrO_2 as a thermal barrier coating.

(ii) Thermal Sprayed Coatings of Pyrochlore Oxides

In this dissertation, pyrochlore oxides were deposited by RF spray (directly from precursor) and by the plasma spray process. When stoichiometric compositions of pyrochlore precursors were deposited by the RF system, we were able to successfully deposit the pyrochlore phase of interest in a single deposition step.

(iii) Phase Evolution of Ti-YSZ (TiO_2 Substitutions in 7YSZ)

Comparisons were made between standard zirconia doped with yttria (7YSZ) and zirconia 7YSZ with Ti-YSZ. The current equilibrium ternary diagram, of $YO_{1.5}$-TiO_2-ZrO_2 has a single tetragonal phase field. This region is promising in studying as a potential candidate material (composition) for TBC materials. Some contributions of this work showed that there were slower partitioning kinetics in Ti-YSZ compared to YSZ oxide powders. In principle, oxide compositions of Ti-YSZ should not have partitioning in this system based on the equilibrium diagram. Ti-YSZ had higher tetragonality in comparison to 7YSZ, hence illustrating higher transformability temperatures in tetragonal prime structures.

(iv) Thermal Sprayed Coatings of Ti-YSZ and 7YSZ

Structural analysis of Ti-YSZ as-deposited coatings showed no distinguishable phase between the cubic or tetragonal phase. However, after a low heat treatment the tetragonal prime (t') phase was observed. As-deposited coatings of 7YSZ yielded the tetragonal prime phase, as expected for results obtained by industrial powder feedstock. Both oxides of YSZ and Ti-YSZ were able to maintain the tetragonal prime phase when thermal cycled. However, at temperature of 1400°C, Ti-YSZ and YSZ de-stabilized into cubic and tetragonal phase. Detailed structural analysis work revealed that Ti-YSZ had higher tetragonality (c/a) in comparison to YSZ. Thus, we expect Ti-YSZ to have higher toughness. High-resolution images revealed that very little changes were observed in the pore morphology of YSZ below 1200°C. However, for Ti-YSZ, microstructure suffered from densification at temperatures less than 1200°C. Results also showed that there was segregation in coatings into rutile and tetragonal phase. Thermal conductivity values were approximately 10-15% higher in Ti-YSZ. The higher thermal conductivity is the result of coating densifications (high sintering of coating oxide). The densification of coatings was also responsible for increased elastic modulus and hardness. Thermal spray has been proven to be a very promising for depositing functional oxides. However, the complexity of the system, rapid powder heating and high quenching rates, require further understanding into the competing phases within ternary systems.

Chapter 7: Suggestions for Future Work

The results in this dissertation demonstrate that thermal spray is a viable candidate for the deposition of solutions or precursor-derived powders by single step deposition technique for producing coatings of functional oxide materials. Results also suggest the myriad of chemical composition to study and directly deposit coatings by RF- spray. The primary motivation of this work was to integrate results of novel compositions in powders and relate it the effect on microstructure and properties. The current knowledge provides input on properties and structure of novel compositions in thermal spray. The following sections are designed as suggestions to broadening our understanding of these complex functional oxides.

7.1. Oxide Deposition by Precursor Plasma Spray

Thermal spray of precursors plasma spray (PPS) is a relatively new processing method compared to the conventional powder feedstocks. PPS is very attractive process because it allows the fabrication of advanced ceramic coatings that are highly important especially for the recent demands of compositionally complex functional oxides. By monitoring the feedstock precursor and RF deposition parameters we can explore different compositions and the microstructural variations in a combinational manner in order to access non-equilibrium structures that offer practical opportunities in areas such as TBCs and SOFCs and investigate their scientific importance to the thermal spray community[27, 73]. The PPS synthesis research will link process understanding with phase selection maps in order to enhance our knowledge base for future

technological implementation. However, this method has not been explored compared to more mature thermal spray techniques such as APS. One of the main differences in SPPS is that the precursor is injected directly into the flame. Spraying of precursor is also vital because nanomaterials exhibit unique properties (Figure 109). The synthesis and study of these materials as they pertain to the development of nanomaterials is critical. Other competing technologies are flame processing, vapor deposition, laser ablation, reverse co-precipitation processing and microwave plasma synthesis.

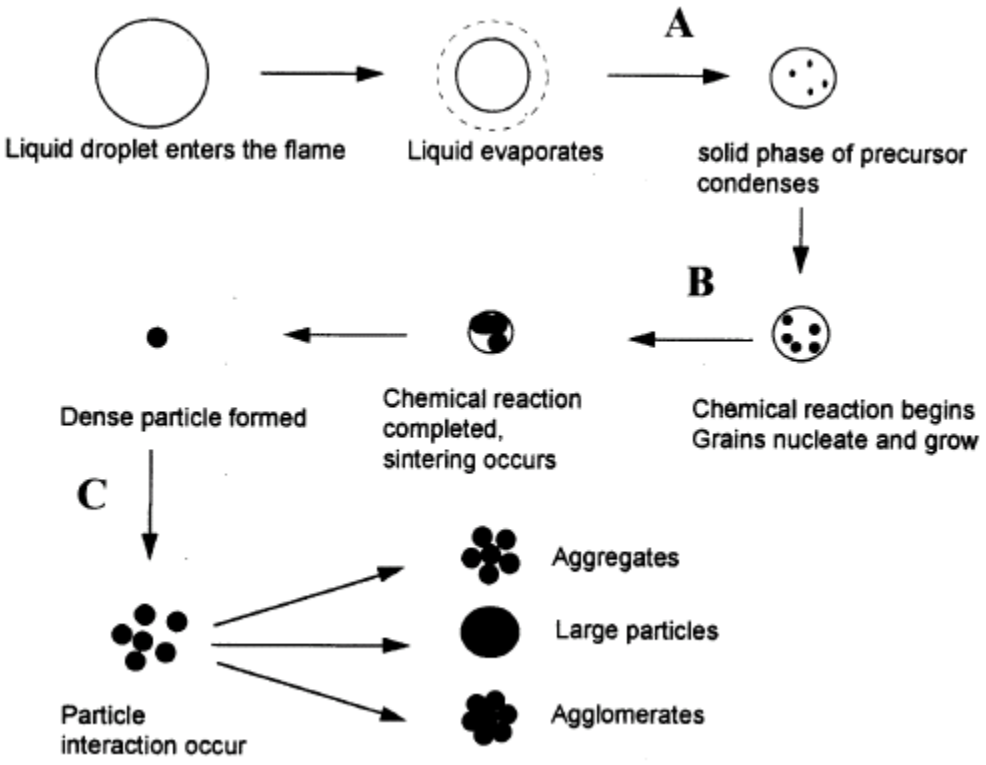

Figure 109 Liquid precursor evolution in plasma plume[74]

In summary, PPS offers greater flexibility in with material systems such as Y_2O_3-TiO_2-ZrO_2 and their compositions. One of the major advantages over other thermal spray processes is the ability to reduce the processing steps in powder processing associated with traditional powder preparation. This includes

avoiding screening for particle sizes etc. The advantages also include long dwell times, based on the 250 mm nozzle that plays an important role in the high heating rates. Hence, the opportunity to yield unique thermal histories that may not have possible compared to conventional plasma spray.

7.1.1. Recent advances in Radio Frequency Thermal Spray

As a secondary method to fabricate thermal spray deposits, Radio Frequency (RF) plasma spray, offered a unique avenue to create deposits. The technique offers reduced contamination of the coatings that are usually found as a result of arc erosion of the DC electrodes in plasma spraying. Chemically, the RF plasma spray technique has the capability of handling reactive gases, which are not possible with the APS technique due to the chemicals would normally consume the DC electrode. Other instrumentation advantages include a vertical injection of the solution precursor feedstock. This result in increased deposit efficiency (D.E) compared to radial injected by APS systems. Coatings were deposited using a TECKNA RF torch. Comparative to APS, RF plasma spray has axial injection and longer dwell times on the order of $100ms^{-1}$. In particular the RF system at the Center of Thermal Spray Research (CTSR) at Stony Brook utilizes a system that has instrument parameters that include control of carrier/atomizer gas flow rate, torch nozzle diameter, chamber operating pressure and total plasma gas flow rate. The options in the plasma torches include variations in plasma discharge diameters of either 50 or 75 mm with a length of approximately 250mm. The temperature range is estimated to be around 8000 to 10500 K with temperature variations attributed by controlling the plasma and particle velocity.

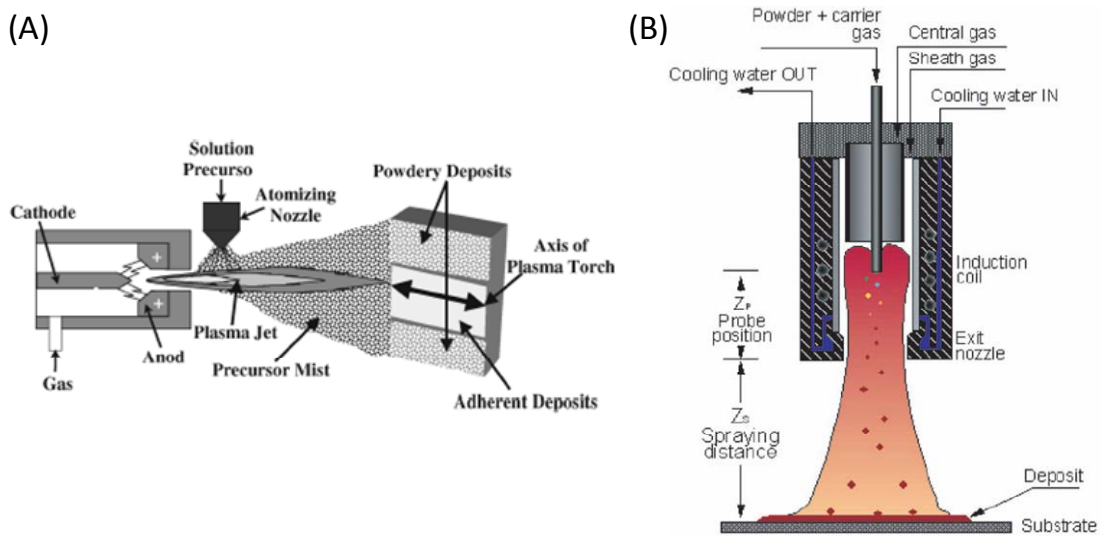

Figure 110 (A) Solution precursor plasma spray[28] (B) illustration of RF plasma spray [75]

7.2. Mixed Ionic Conducting Oxides

Mixed oxygen ion-electronic conductors are receiving special interest because of their potential use in fuel electrodes, in high temperature electrochemical devices such as solid oxide fuel cells (SOFCs), as catalytic materials, and oxygen permeable membranes. In particular, the ternary oxide system, $YO_{1.5}$-ZrO_2-TiO_2 offers excellent compositions with ionic conducting fluorite and mixed ion-conducting pyrochlore phases at high temperatures. For example $Y_2Zr_{1.2}Ti_{0.8}O_7$ with a disordered fluorite structure, has been shown to have an ionic conductivity σ, greater than 10^{-2} S/cm at 1000°C, comparable to the values found for yttria stabilized cubic zirconia. Yttrium titanate, $Y_2Ti_2O_7$ has a pyrochlore structure and exhibited mixed ion-electronic conduction at 1000°C. However the ternary system, $YO_{1.5}$-ZrO_2-TiO_2 is fairly unexplored, including the possible metastable phases that may be present during phase transformation.

A detailed phase evolution study of the system $Y_{2-x}Ti_2Zr_xO_{7+x/2}$ was implemented to observe the structural transformations from powders synthesized by chemical precipitation method. This processing method allows for the complete homogeneous mixing of these complex oxides. Moreover, the precipitation processing technique results in an amorphous starting material that allows for the complete study of phase selection upon crystallographic transformations as the composition is heat treated to its final equilibrium temperature. Another important aspect of this work is to form ceramic coatings of ionic and/or electronic properties by thermal spray. This has excellent technological applications because thermal spray is a unique process that allows for the fabrication of metastable phases. We suggest measuring ionic conductivity in coating materials for pyrochlore and fluorite oxides deposited by thermal spray.

7.3. Compositionally Graded Coatings

Films and compositionally graded coatings may be processed in order to incorporate functionality to exploit the properties of interest in the most promising compositions[76]. Coatings of the composition $Y_2Ti_{1.2}Zr_{0.8}O_7$ were synthesized by RF plasma spraying of reverse co-precipitated colloidal suspension, as a demonstration of this concept. Appropriate doping results in either predominantly p or n type electronic conduction in $Y_2(Zr_yTi_{1-y})_2O_7$, which makes it ideally suitable for monolithic fuel cells. $Y_2(Zr_yTi_{1-y})_2O_7$ system undergoes a gradual transformation from pyrochlore structure to a fluorite structure with an increase in conductivity of three orders. The system $Y_2(Zr_yTi_{1-y})_2O_7$ has been shown to have an ionic conductivity σ, greater than 10^{-2} S/cm at 1000°C, comparable to the values found for stabilized cubic zirconia. Pyrochlore ordering is seen in a wide range of compositions. This is interesting from the

standpoint of order-disorder transformation of crystal chemistry and material applications as in fuel cell systems. Therefore utilizing thermal spray as an avenue to create graded coating is necessary.

7.4. Applications of RF Precursor Spray for Solid Oxide Fuel Cells (SOFC)

Precursor RF Plasma Spray offers a single step approach to synthesis and deposition of oxides. Thermal spray technique coupled with precursor solution chemistry is expected to offer excellent opportunities in making such a monolithic (thin/thick film) fuel cells. For SOFCs, there are many opportunities to investigate structure-properties of anodes, cathodes and electrolytes by plasma/RF spray. Some of the primary areas for future work in materials reside in studying ionic conductivity and phase stability of oxides. Electrolytes in SOFCs require dense zirconia oxides while anode and cathodes require porous oxides.

In this dissertation, we have successfully deposited anode and cathode compositions for the application of by RF precursor spray. In the system of Y_2O_3-TiO_2-ZrO_2 compositions within $Y_2(Zr_yTi_{1-y})_2O_7$ were synthesized by precursor solutions methods for compositions when (y=0.6, 0.9 and 1.0) sprayed on alumina and Stain less steel substrates (6 cm x 2.5 cm x 0.2 cm) using a RF plasma torch (Model 66, Tafa, Concord, NH). Structural characterizations of thee coatings revealed that desired phases were possible however, more investigation into enhancing processing parameters in order to create dense coatings. The current RF spray parameters that resulted in the optimal coating parameters are listed in Table 12.

Table 12 Optimized RF spray conditions for 5.5-7 wt.% LSM and pyrochlore compositions

Parameter	Value
Feed rate	10 ml/min
Substrate Torch Distance	8 cycles(15 sec/cycle)
Traverse Speed	12 cm/s
Atomizing Gas	Helium
Plasma gas Composition	Ar/He (60/40)
Chamber Pressure	100 torr

7.4.1. SOFC Cathode: Lanthanum Strontium Manganites (LSM)

Lanthanum Strontium Manganites (LSM) is scientifically and technologically important perovskite oxide materials. Depending on chemistry, LSM oxides have shown properties that range from magnetic semiconductors and mixed ionic-electronic conduction at high temperature. LSM oxides, have been recently investigated for applications in the areas of cathode materials for Solid Oxide Fuel Cells[77]; High magneto-caloric effect (useful for magnetic refrigeration), Magneto-Resistive (MR sensors).

In this dissertation, we fabricated coatings of LSM oxides by RF precursor spray. Coatings deposited by RF precursor spay offer a single deposition step to synthesize oxides. Preliminary experiments focused on the fabrication of LSM coatings by RF precursor spray. The initial experimentation was based on trial and error, however Table 12 presents the optimal conditions for the fabrication of the functional oxides. Figure 111Figure 112 are micrographs for the unique microstructure of LSM oxides deposited by RF precursor spray. The microstructure of the LSM structure is an open three-dimensional network with *branch-like* oxides with diameters ranging between 0.5 - 1.0 microns. The structures are presumably a function of the interaction of the precursor droplets, evaporation of precursor and low droplet velocity. In comparison to traditional

plasma spray coatings, there are no splats or two-dimensional porosity. Figure 111 is the top down micrographs of LSM for as-deposited and heat treated oxides. The differences in coatings is that in that after coatings are heat treated resulted in reduction of the precursor droplets and a small decrease in the *branch-like* network. The results suggest that the shrinkage may be caused by excess precursor evaporation with post treatment. Another contribution of this study is that we were able to deposit the crystalline perovskite phase of LSM in a single deposition step. The feedstock was a homogenous solution precursor mixture described in the materials and methods second of this dissertation. Figure 113 is the XRD spectrum of LSM oxides of as-deposited and heat treated coatings. The as-deposited spectrum is primarily the perovskite phase with a small amorphous hump at an angle of approximately 27 degrees. After post-treatment, the coating was a single phase of perovskite oxide. Results were very promising and illustrated the feasibility of RF precursor spray to produce porous cathode material for fuel cell applications.

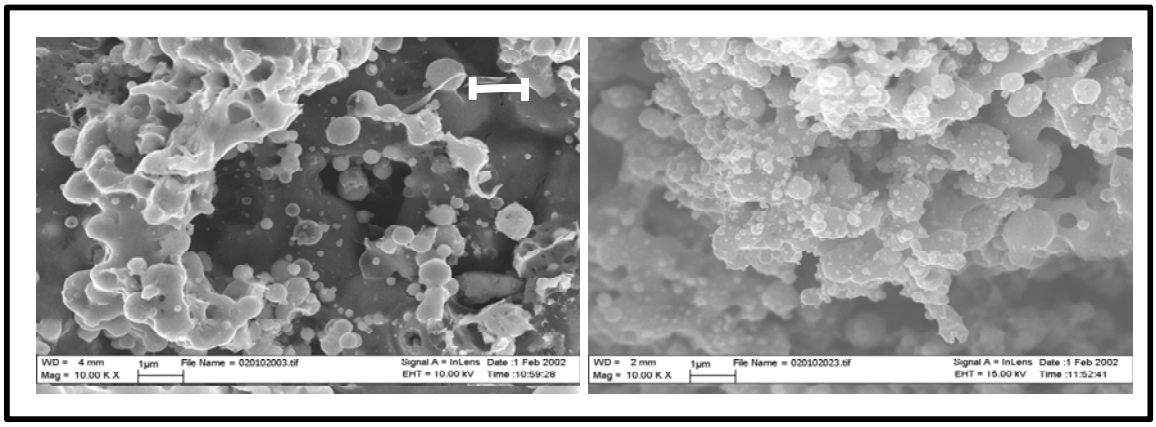

Figure 111 SEM Top down images of (a) as-deposited by RF plasma spray (b) Post treatment of LSM coating (1200 ˚C)

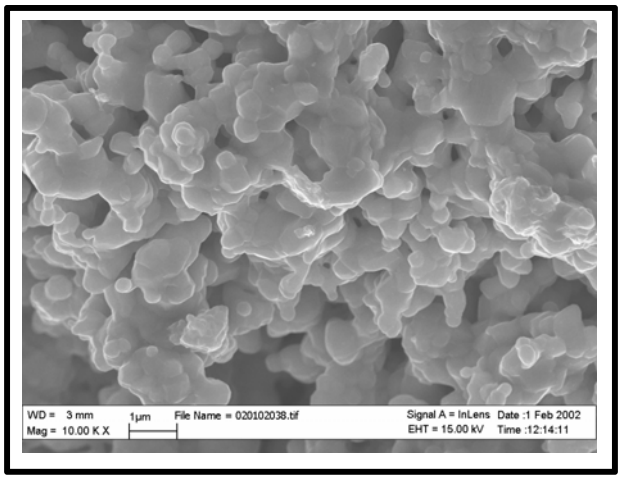

Figure 112 LSM post treatment 800˚C for 6hrs deposited by RF plasma spray

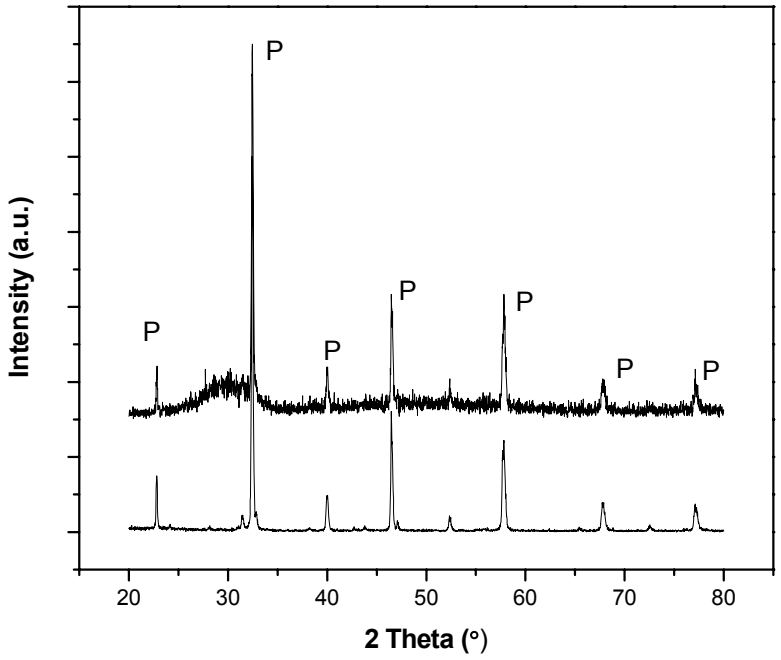

Figure 113 XRD spectrum (Top) RF sprayed LSM from precursor (Bottom) LSM precursor derived powder heat treated at 1200°C for 12hrs for single phase perovskite (P)

7.5. Process Map Studies in Ternary System Oxide Composition

Due to the complexity of the chemistries of functional oxides, advancing our understanding of processing parameters and their effect on material properties is important to understanding of next generation material systems. Our results suggest that there is a need for process maps because they may elucidate the correlation between structure complexity and phase segregation in coatings. Therefore, experiments are necessary to report the variations in parameters of plasma power, spray distance, powder size/shape and substrate temperature and how they affect the chemistry, morphology, microstructure and phase content of coating. In addition, experiments are needed for process maps that compare structural results and coating properties for air plasma and RF plasma spray.

References

[1] Dongming Zhu RAM. Thermal-Barrier Coatings for Advanced Gas- Turbine Engines. MRS BULLETIN 2000:43.

[2] N. Shibata JK, A. Kuwabara, Y. Ikuhara, T. Sakuma. instability and resulting phase transition of cubic zirconia. Materials Science and Engineering A 2001;312:90.

[3] Scott HG. Phase-relationships in the zirconia-yttria system. Journal of Materials Science 1975;10:1527.

[4] Subhash L. Shindé JG. High Thermal Conductivity Materials: Springer, 2006.

[5] Kittel C. ‘‘Interpretation of the Thermal Conductivity of Glasses. Phys. Rev. 1949;75:972.

[6] D.R. Clarke CGL. Materials design for the next generation thermal barrier coatings. Annual Review of Materials Research 2003;33:383.

[7] Kingery WD. Introduction to Ceramics. New York: Wiley Interscience, 1976.

[8] Michael R. Winter DRC. Oxide Materials with Low Thermal Conductivity. J. Am. Ceram. Soc., 2007;90:533.

[9] Slack GA. The Thermal Conductivity of Nonmetallic Crystals. Solid State Physics 1979;34:1.

[10] D. G. Cahill ROP. Lattice Vibrations and Heat Transport in Crystals and Glasses. Annu. Rev. Phys. Chem. 1988;39:93.

[11] Maloney MJ. Thermal barrier coating systems and materials. vol. 6,177,200. US: United Technologies Corporation, 2001. p.1.

[12] J. Wu XW, N.P. Padture, P.G. Kelmens, M. Gell, E. Garcia, P. Mirzano and M.I. Osendi. Low thermal-conductivity rare-earth zirconates for potential thermal barrier coating applications. Journal of American Ceramic Society 2002;85.

[13] M.A. Subramanian GA, G.V. Subba Rao. Rare Earth Pyrochlores. Prog. Solid State Chemistry 1983;15:56.

[14] C. Heremans BJW. Fast-Ion Conducting Y2(ZryTi1-y)2O7 Pyrochlores: Neutron Rietveld Analysis of Disorder Induced by Zr Substitution. Journal of Solid State Chemistry 1994;117:108.

[15] Tae-Hwan Yu HLT. Ionic conduction and disorder in the $Gd_2Sn_2O_7$ pyrochlore system. Solid State Ionics 1996;96:177.

[16] J.T.S. Irvine DPF, J. Labrincha, F.M.B. Marques. Development of novel anodes for solid oxide fuell cells. Catalysis Today 1997;38:467.

[17] S. Lutique RJMK, V.V. Rondinella, J. Somers, T. Wiss. The thermal conductivity of $Nd_2Zr_2O_7$ pyrochlore and the thermal behaviour of pyrochlore-based inert matrix fuel. Journal of Alloys and Compounds 2003;352.

[18] K. E. Sickafus LM, R. W. Grimes, J. A. Valdez,M. Ishimaru, F. Li, K. J. McClellan, T. Hartmann. Radiation Tolerance of Complex Oxides. Science 2000;289:4.

[19] A.V. Shlyakhtina AVK, M.V. Boguslavski, S.Yu. Stefanovich, D.V. Peryshkov, I.V. Kolbanev, L.G. Shcherbakova. Effects of the synthesis procedure, doping and non-stoichiometry on the order–disorder transformation in Ln2Ti2O7 (Ln=Tm–Lu) oxygen-ion conductors. Solid State Ionics 2005;176:2297

[20] H. Takamura HT. Ionic conductivity of Gd_2GaSbO_7-$Gd_2Zr_2O_7$ solid solution with structural disorder. Solid State Ionics 2000;134:67.
[21] Glicksman ME. Diffusion in Solids: field theory, solid-state principles, and applications. New York: John Wiley & Son, 2000.
[22] P.J. Wilde CRAC. Defects and diffusion in pyrochlore structured oxides. Solid State Ionics 1998;112:173.
[23] M. Kato NM. Asahi Garasu Kogyo Gijutsu Shoreikai 1976;29:35.
[24] Norby T. oxygen ion conductors from doped to ordered systems. J. Mater. Chem 2001;11.
[25] Herman H. Plasma Sprayed Coatings. Sci. America 1988;259:112.
[26] R.L. Jones DM. Improved tetragonal phase stability at 1400°C with Scandia yttria-stabilized zirconia. Surface and Coatings Technology 1996;86-87:94.
[27] D.Chen MG. Thermal Stability of Air Plasma Spray and Solution Precursor Plasma Spray Thermal Barrier Coatings. J. Am. Ceram. Soc. 2007;90:3160.
[28] L. Xie a EHJ, N.P. Padture, M. Gell Phase and microstructural stability of solution precursor plasma sprayed thermal barrier coatings. Materials Science and Engineering A 2004;381:189.
[29] H. Yokokawa NS, T. Kawada, and M. Dokiya. Chemical Potential Diagrams for Rare Earth-Transition Metal-Oxygen Systems: I. Ln-V-O and Ln-Mn-O Systems. J. Am. Ceram. Soc. 1990;73:649.
[30] M.Ciftcioglu MM, J. Mayo. Processing of Nanocrystalline Ceramics. In: Society MR, editor. Materials Research Society Symposium Processding, vol. 196, 1990. p.77.
[31] Newton RG. Scattering Theory of Waves and Particles: Second Edition: Published by Courier Dover Publications, 2002.
[32] Kissinger HE. Reaction Kinetics in Differential Thermal Analysis. Analytical Chemistry 1957;29:1702.
[33] E.G. Herberta GMP, W.C. Oliver, B.N. Lucas, J.L. Hay. On the measurement of stress–strain curves by spherical indentation. Thin Solid Films 2001;398 –399:331.
[34] W.C. Oliver GMP. An Improved Technique tbr Determining Hardness and Elastic Modulus Using Load and Displacement Sensing Indentation Experiments. Journal of Materials Research 1992;7:1564.
[35] G.M. Pharr WCO, F.R. Brotzen. On the Generality of the Relationship Among Contact Stiffness, Contact Area, and Elastic Modulus during Indentation. Journal of Materials Research 1992;7:613.
[36] D.B. Marshall TN, A.G. Evans. A Simple Method for Determining Elastic-Modulus-to-Hardness Ratios Using I_aoop Indentation Measurements. Journal of American Ceramic Society 1982;65:175.
[37] M.F. Doerner WDN. A Method for Interpreting the Data from Depth-Sensing Indentation Instruments. Journal of Materials Science 1986;1:601.
[38] Sneddon N. The relation between load and penetration in the axisymettric boussinesq problem for a punch of arbritury profile. International journal of engineering science 1965;3:47.
[39] Yu Gu TN, Lubos Prchlik, Sanjay Sampath, Jay Wallace. Micro-indentation and inverse analysis to characterize elastic-plastic graded materials. Materials Science and Engineering A 2003;345:223.

[40] J. Alcala´ FG, S. Suresh, S. Sampath. Instrumented spherical micro-indentation of plasma-sprayed coatings. Materials Science and Engineering A 2001;316:1.
[41] W.C. Oliver GMP. Measurement of hardness and elastic modulus by instrumented indentation: Advances in understanding and refinements to methodology. J. Mater. Res., 2004;19:3.
[42] A. Kulkarni JG, S. Sampath, A. Goland, W.B. Lindquist,, H. Herman AJA, B. Dowd. Studies of the microstructure and properties of dense ceramic coatings produced by high-velocity oxygen-fuel combustion spraying. Materials Science and Engineering A 2004;369:124.
[43] Pavel Strunz GS, Robert Vassen, Albrecht Wiedenmann. In situ SANS study of pore microstructure in YSZ thermal barrier coatings. Acta Materialia 2004;52:3305.
[44] Blanchard CR PR. J Mater Sci 1998;33:5049.
[45] Harjo S MY, ┌Saroun J, Ryukthin V, Strunz P, Baron M, et al. Mater Sci Forum 2004;447–448::67.
[46] Levi CG. Metastability and Microstructure evolution in the sythesis of Inorganics from Precursors. Acta Material 1998;47.
[47] Leckie RMR RN, Yang JC, Levi. C. Surf. Coat. Technol. In press 2003.
[48] H. Yamamura HN, K. Kakinuma, K. Nomura. Electrical Conductivity anomaly around fluorite-pyrochlore phase boundary. Solid State Ionics 2002;158:359.
[49] J.J. Sprague OP, H.L. Tuller. Mixed conducting gas sensors: atmosphere dependent electrode impedance. Sensors and Actuators B 1996;35:348.
[50] B.D. Begg NJH, W.J. Weber, R. Devanathan, J.P. Icenhower, S. Thevuthasan, B.P. McGrail. Heavy-ion irradiation effects on structures and acid dissolution of pyrochlores. Journal of Nuclear Materials 2000:208.
[51] B.J Wuensch KE, C Heremans, E. Ku, P. Onnerud, J.K. Stalick. Connections between oxygen-ion conductivity of pyrochlore fuel cell materials and structural change with composition and temperature. Solid State Ionics 2000;129.
[52] McCauley R. Structural characteristics of pyrochlore formation. Journal of Applied Physics 1980;51:290.
[53] N. Kim CPG. 17O MAS NMR study of the oxygen local environments in the anionic conductors Y2(B1-xB'x)1O7 (B,B' = Sn, Ti, Zr). Journal of Solid State Chemistry 2003:110.
[54] M. Glerup OFN, F.W. Poulsen. The Structural Transformation from the Pyrochlore Structure, $A_2B_2O_7$ to the fluorite AO_2, Studied by Raman Spectroscopy and Defect Chemistry Modeling. Journal of Solid State Chemistry 2001:25.
[55] E. Granado PGP, J. A. Sanjurjo, and C. Rettori. Phonon Raman scattering in $A_2Mn_2O_7$ (A=Tl,In,Y) . PHYSICAL REVIEW B 1999;60:6513.
[56] K. Taniguchi TK, S. Iguchi, Y. Taguchi, H. Takagi, Y. Tokura. Raman study of the metal-insulator transition in pyrochlore Mo oxides. PHYSICAL REVIEW B 2004;70:1.
[57] H.C. Gupta SB, N. Rani, V.B. Gohel. A lattice dynamical investigation of the Raman and the infrared frequencies of the cubic $A_2Sn_2O_7$. Journal of Inorganic Materials 2001;3:983.
[58] F.W. Poulsen MG, P. Holtappels. Structure, Raman spectra and defect chemistry modelling of conductive pyrochlore oxides. Solid State Ionics 2000:595.

[59] N. J. Hess BDB, S. D. Conradson, D. E. McCready, P. L. Gassman, W. J. Weber. Spectroscopic Investigations of the Structural Phase Transition in $Gd_2(Ti_{1-y}Zr_y)_2O_7$ Pyrochlores. J. Phys. Chem. B 2002;106:4663.
[60] Tobias A. Schaedler WF, Ashutosh S. Gandhi, Clare P. Grey,Sanjay Sampath, Carlos G. Levi. Phase evolution in the YO1.5–TiO2–ZrO2 system around the pyrochlore region. Acta Materialia 2005;53:2957.
[61] A.G. Evans DRM, J.W. Hutchinson, G.H. Meier and F.S. Pettit. Mechanics controlling the durability of thermal barrier coatings. Progress in Materials Science 2001;46:505.
[62] S. Tekeli AG. Sintering, phase stability and room temperature mechanical properties of c-ZrO_2 ceramics with TiO_2 addition. 2007;28.
[63] R. A. Miller RGG, J. L. Smialek. Phase Distributions in Plasma-Sprayed Zirconia–Yttria. journal of American Ceramic Society 1983;62:1355.
[64] F.R. Chen FJU, V. Prakash and H. Heurer. Stress induced martensitic transformation and ferroeleastic deformation adjacent microhardness indents in tetragonal zirconia single crystals. Acta material 1998;46:2151.
[65] Mercer C, J. R. Williams, D. R. Clarke and A. G. Evans. On a ferroelastic mechanism governing the toughness of metastable tetragonal-prime (t ‘) yttria-stabilized zirconia. Proc. R. Soc. A 2007;463:1393.
[66] Fang Daining AKS, Liu Jinxi. ELECTROMECHANICAL DEFORMATION AND FRACTURE
OF PIEZOELECTRIC/FERROELECTRIC MATERIALS. ACTA MECHANICA SINICA 2001;17:193.
[67] Oates WS. FRACTURE OF FERROELECTRIC MATERIALS. Mechanical Engineering, vol. Doctor of Philosophy: Georgia Institute of Technology, 2004. p.179.
[68] T.Tien. Toughned Ceramics. vol. 4,886,768. US: Board of Regents Acting for and on Behalf of the University of Michigan; Ann Arbor, Mich, 1989. p.1.
[69] Spitsberg I. Thermal Barrier Coatings with improved impact and erosion resistant. vol. 6,869,703. US: General Electric Company, 2005. p.1.
[70] Rebollo NR, A.S. Gandhi and C.G. Levi. Phase stability issues in emerging TBC systems. Electrochemical Society Proceedings vol. PV-2003-16, 2003. p.431.
[71] Lughi. V DRC. Transformation of Electron-Beam Physical Vapor-Deposited 8 wt% Yttria-Stabilized Zirconia Thermal Barrier Coatings. J. Am. Ceram. Soc. 2005;88:2552.
[72] Toraya H. Effect of $YO_{1.5}$ Dopant on Unit-Cell Parameters of ZrO_2 at Low Contents of $YO_{1.5}$. Journal of the American Ceramic Society 1988;72:662.
[73] N. P. Padture KWS, T. Bhatia, A. Ozturk, B. Cetegen, E. H. Jordan, M. Gell, S. Jiang, T. D. Xiao, P. R. Strutt, E. Garcia, P. Miranzo and M. I. Osiendi. Towards durable thermal barrier coatings with novel microstructures deposited by solution-precursor plasma spray. Acta Material 2001;49:2251.
[74] J. Karthikeyan CCB, J. Tikkanen, J. Y. Wang, A. H. King , H. Herman. Preparation of nanophase materials by thermal spray processing of liquid precursors. Nanostructured Materials 1998;9:137.
[75] Fauchais P. Understanding plasma spraying. Journal of Physics D: Applied Physics 2004;37:86.

[76] K.A. Khor ZLD, Y.W. Gu. Plasma sprayed functionally graded thermal barrier coatings. Materials Letter 1999;38:437.
[77] J. Heberlein RH, T. Ishigaki, and T. Yoshida. Integrated Fabrication Processes for Solid-Oxide Fuel Cells Using Thermal Plasma Spray Technology. MRS Bulletin 2000.